

DELIVERABLE D70.4

Results of the Optimization of EST Design Based on CFD Analysis

I. Numerical Methods, Simulations and Interpolation Codes.....	3
II. EST Telescope Environment Preliminary Thermal Analysis II.....	53
II. EST Thermal Analysis - Observations Out of the Sun.....	107
IV. EST Telescope Structure - Analysis Report.....	132

WP 70 Wavefront Control: Turbulence Characterization and
Correction

1ST Reporting Period

November 2014

PROJECT GENERAL INFORMATION

Grant Agreement number: 312495

Project acronym: SOLARNET

Project title: High-Resolution Solar Physics Network

Funded under: FP7-INFRASTRUCTURES: INFRA-2012-1.1.26 - Research Infrastructures for High-Resolution Solar Physics

Funding scheme: Combination of Collaborative Project and Coordination and Support Action for Integrating Activities

From: 2013-04-01 to 2017-03-31

Date of latest version of Annex I against which the assessment will be made: **13/02/2013**

Periodic report: 1st 2nd 3rd 4th

Period covered: from **01/04/2013** to **30/09/2014**

Project's coordinator: Dr. Manuel Collados Vera, IAC.

Tel: (34) 922 60 52 00

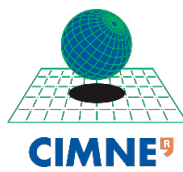
Fax: (34) 922 60 52 10

E-mail: mcv@iac.es

Project website address: <http://solarnet-east.eu/>

SOLARNET. WP70

CIMNE CONTRIBUTION



SUMMARY

The report is divided in three parts. In the first part of we present new developments in the numerical methods for the estimation of atmospheric seeing in the atmosphere, which have been investigated in the Solarnet project. The material presented there corresponds to the paper "Variational multiscale based dissipation models for the estimation of atmospheric seeing", by J. Baiges and R. Codina, and that has accepted for publication in the journal *Computers & Fluids* (acknowledgement of Solarnet is made in the paper). In the second part we present the results of the numerical simulations for the evaluation of atmospheric seeing at the EST sites. Finally, in the third part we present a very brief description of the interpolation code, which has been implemented for reading the boundary conditions for the numerical simulations.

1 Variational Multiscale Methods for the estimation of Atmospheric Seeing

1.1 Introduction

It is clear that being able to evaluate the suitability of an observation site or a telescope facility design prior to the telescope construction is key for getting the best possible performance out of the telescope. Also, it is convenient to be able to quantify the characteristics of the adaptive optics mechanism to be installed in the telescope beforehand. Due to this, several efforts have been devoted recently to the quantification of atmospheric seeing parameters through numerical simulation.

One of the first numerical models for the quantification of the temperature structure function was presented in [20]. In [29, 30] an atmospheric Meso-Nh numerical model was used to compute atmospheric seeing in an observation site in Cerro Paranal, Chile. Soon after, the same methodology was applied to the simulation of another observation site at the Roque de Los Muchachos, Canary Islands, Spain [31]. In [7, 8, 6] a Large Eddy Simulation (LES) model run on a weather forecast simulation software was used to characterize near-surface optical turbulence under different climatic conditions in observation sites. A seeing model which makes use of the turbulent kinetic energy provided by a planetary boundary layer simulation software was used to compute seeing in Mauna Kea, Hawaii in [10, 9]. In [22] a weather forecasting model was used together with the statistical parametrization of the refraction index structure constant C_n^2 presented in [35] in order to forecast the seeing conditions in the Roque de Los Muchachos, Canary Islands, Spain. A numerical weather prediction tool was used in [1] to compute various turbulence parameters which allow to characterise C_n^2 in the islands of Maui and the Big Island, Hawaii, and a similar methodology was presented in [21].

All of these methodologies have in common the use of numerical weather prediction tools for the simulation of seeing conditions, where the expression for C_n^2 is derived from different mesoscale turbulence models. In [13] we presented a strategy for the computation of atmospheric seeing parameters, which, to our knowledge, is the first computational method capable of simulating seeing conditions at a local level; that is, by using a finite element

computational fluid dynamics simulation with a resolution ranging from decimeters to few meters instead of using mesoscale simulation tools with a coarse resolution. The proposed model for the computation of the refraction index structure function C_n^2 is based on a Large Eddy Simulation of the incompressible flow and temperature fields, and has been successfully applied to the design phase of the *Advance Technology Solar Telescope* (ATST) [28] and the *European Solar Telescope* (EST) [3, 5].

In this work we present a model for the numerical simulation of the C_n^2 function which is computed from a variational multiscale (VMS) [26] based turbulence model. For finite element analysis, the basic idea of VMS is to split the unknowns into their finite-element part and a subgrid scale component, the subscale. The approximation adopted for the subscale defines the numerical model. The interesting feature about VMS is that it is capable of providing, at the same time, a numerical stabilization mechanism for the studied equations (in this case, the incompressible Navier-Stokes equations) and a turbulence model which takes into account the under-resolved scales (those which cannot be captured by the finite element mesh). This has been studied in several works [27, 18, 14, 15, 23] with successful results. The advantage of using this kind of approach is that there is no interference between the numerical stabilization and the turbulence models because both issues are taken care of by the numerical subgrid scales.

The method used in the present work is the Orthogonal Subgrid Scale VMS method (OSS). Its particularity is that it models the numerical subscales in a rich manner: the subscales are considered to be transient in time, non-linear, and orthogonal to the finite element space. A theoretical analysis of the orthogonal-subscales VMS turbulence model is presented in [24], and an extensive campaign of numerical experiments is presented in [19]. The conclusions of these experiments are that VMS turbulence models can provide an accurate representation of turbulent phenomena at a competitive computational cost, with the particular feature that the turbulence model arises from numerical reasoning only. In this work we use the kinetic energy and thermal turbulent dissipations which arise from the OSS turbulence model in order to quantify the refraction index structure function.

1.2 Incompressible Navier-Stokes equations

i Problem statement

In this section we summarize the Orthogonal Subgrid-Scale (OSS) approach applied to the incompressible Navier-Stokes equations described in [11]. Let us consider the transient incompressible Navier-Stokes equations, which consist of finding $u : \Omega \times (0, T) \rightarrow \mathbb{R}^3$ and $p : \Omega \times (0, T) \rightarrow \mathbb{R}$ such that:

$$\partial_t \mathbf{u} - 2\nu \nabla \cdot \nabla^s \mathbf{u} + \mathbf{u} \cdot \nabla \mathbf{u} + \nabla p = \mathbf{f} \quad \text{in } \Omega, \quad (1)$$

$$\nabla \cdot \mathbf{u} = 0 \quad \text{in } \Omega, \quad (2)$$

$$\mathbf{u} = \bar{\mathbf{u}} \quad \text{on } \Gamma_D, \quad (3)$$

$$-pn + \nu \mathbf{n} \cdot \nabla \mathbf{u} = \mathbf{0} \quad \text{on } \Gamma_N. \quad (4)$$

for $t > 0$, where $\partial_t u$ is the local time derivative of the velocity field and $\nabla^s u = \frac{1}{2}((\nabla u)^T + \nabla u)$. $\Omega \subset \mathbb{R}^3$ is a bounded domain, ν is the viscosity, and f the given source term. Γ_D is the Dirichlet boundary, where velocity boundary conditions are applied. In the case of the numerical simulation of aerodynamics of telescopes, it corresponds to the inflow boundary and the ground and telescope surfaces. Γ_N is the Neumann boundary, where conditions on the value of the tractions are applied. In aerodynamics of telescopes simulations, it corresponds to the outflow boundary. Appropriate initial conditions have to be appended to this problem. In the numerical examples section, the source term f is due to the Boussinesq buoyancy forces, which appear due to temperature gradients and are of the form:

$$\mathbf{f} = \alpha \mathbf{g}(\theta - \theta_0),$$

where α is the thermal expansion coefficient, \mathbf{g} is the gravity acceleration vector, θ_0 is a reference temperature and θ the temperature of the fluid.

ii Finite element approximation

Let us now consider the finite element approximation of equations (1)-(4). We define $V = H^1(\Omega)^d$, and $V_0 = \{\mathbf{v} \in V \mid \mathbf{v} = \mathbf{0} \text{ on } \Gamma_D\}$. Let also $Q = L^2(\Omega)$ and $D^0(0, T; Q)$ be the distributions in time with values in Q . The variational problem consists of finding $[u, p] \in L^2(0, T; V) \times D^0(0, T; Q)$ such that:

$$(\mathbf{v}, \partial_t \mathbf{u}) + \langle \mathbf{v}, \mathbf{u} \cdot \nabla \mathbf{u} \rangle + 2\nu (\nabla^s \mathbf{v}, \nabla^s \mathbf{u}) - (p, \nabla \cdot \mathbf{v}) = \langle \mathbf{v}, \mathbf{f} \rangle \quad \forall \mathbf{v} \in V_0, \quad (5)$$

$$(q, \nabla \cdot \mathbf{u}) = 0 \quad \forall q \in Q, \quad (6)$$

with

$$\mathbf{u} = \bar{\mathbf{u}} \quad \text{on } \Gamma_D.$$

Here, (\cdot, \cdot) stands for the $L^2(\Omega)$ inner product and $\langle \cdot, \cdot \rangle$ for the integral of the product of two functions, not necessarily in $L^2(\Omega)$. Let us also define

$$B([\mathbf{v}, q], [\mathbf{a}; \mathbf{u}, p]) := \langle \mathbf{v}, \mathbf{a} \cdot \nabla \mathbf{u} \rangle + 2\nu (\nabla^s \mathbf{v}, \nabla^s \mathbf{u}) - (p, \nabla \cdot \mathbf{v}) + (q, \nabla \cdot \mathbf{u}),$$

where \mathbf{a} represents the convective velocity. When the Galerkin finite element approximation is used, it is well known that the semilinear form B suffers from stability issues due to the convective nature of the flow, but also requires a compatibility between the velocity and pressure approximation spaces due to the classical LBB inf-sup condition.

Many stabilization methods have been developed to deal with these issues in the past decades. Amongst them, one of the stabilization approaches which has received more interest in recent years is the variational multiscale (VMS) method. The most interesting feature of VMS

is that the stabilization terms are not derived from purely numerical reasons, but are motivated from a *physical* point of view. This physical approach comes from the introduction of a decomposition of a general solution of the problem of interest into its finite element part and the part of the solution which cannot be captured by the finite element mesh. In order to introduce the subscale concept in the weak form (5), let us consider the finite element partition $T_h := \{K\}$ defined over domain Ω , h denoting the element size. To simplify the exposition, we consider T_h quasi-uniform. From this partition we construct the finite element spaces $V_h \subset V$, $Q_h \subset Q$. We will seek for approximate solutions $u_h \in C^1(0, T; V_h)$ and $p_h \in C^0(0, T; Q_h)$.

The variational multiscale method is derived by introducing the subscales space for the velocity field \tilde{V} such that:

$$V = V_h \oplus \tilde{V}.$$

This implies that the velocity solution field and the velocity test functions can also be decomposed into the finite element part and the fine scale part:

$$\begin{aligned} \mathbf{u} &= \mathbf{u}_h + \tilde{\mathbf{u}}, \\ \mathbf{v} &= \mathbf{v}_h + \tilde{\mathbf{v}}. \end{aligned}$$

The same decomposition can be applied to the pressure field by introducing the pressure subscales space \tilde{Q} , as described in [12]:

$$\begin{aligned} Q &= Q_h \oplus \tilde{Q}, \\ p &= p_h + \tilde{p}, \\ q &= q_h + \tilde{q}. \end{aligned}$$

Also, we consider the subscales to vanish on the element boundaries, although their contribution in the element faces can also be taken into account, as described in [17]. Introducing this splitting in equation (5), and after integrating by parts some of terms, the discrete variational problem we obtain is to find $[u_h, p_h] \in V_h \times Q_h$, for each $t \in [0, T]$ and $\tilde{u} \in \tilde{V}$, $\tilde{p} \in \tilde{Q}$ for each $t \in [0, T]$, such that:

$$\begin{aligned}
& (v_h, \partial_t u_h) + B([v_h, q_h], [u; u_h, p_h]) \\
+ \sum_K \langle v_h, \partial_t \tilde{u} \rangle_K + \sum_K \langle -\nu \Delta v_h - u \cdot \nabla v_h - \nabla q_h, \tilde{u} \rangle_K - \sum_K \langle \nabla \cdot v_h, \tilde{p} \rangle_K &= \langle v_h, f \rangle, \\
\sum_K \langle \tilde{v}, \partial_t u_h - \nu \Delta u_h + u \cdot \nabla u_h + \nabla p_h \rangle_K \\
+ \sum_K \langle \tilde{v}, \partial_t \tilde{u} - \nu \Delta \tilde{u} + u \cdot \nabla \tilde{u} + \nabla \tilde{p} \rangle_K &= \langle \tilde{v}, f \rangle, \\
\sum_K \langle \tilde{q}, \nabla \cdot u_h \rangle_K + \sum_K \langle \tilde{q}, \nabla \cdot \tilde{u} \rangle_K &= 0,
\end{aligned}$$

for all test functions $v_h, q_h, \tilde{v}, \tilde{q}$, and where $\langle \cdot, \cdot \rangle_K$ stands for the integral of the product of two functions in K . Note that, for incompressible flows, $\nabla \cdot u = \Delta u$. Equation (8) is the subscales equation, which will be used to provide a closure for the expressions of the velocity and pressure subscales, \tilde{u} and \tilde{p} . Following the steps in [18] we first consider the equation for the velocity subscales, omitting the contribution of the pressure subscales. This allows us to formulate a simpler method, and it implicitly assumes that the velocity subscales are due to the residual of the momentum equations, instead of being driven by the incompressibility constraint. The second term in equation (8) can be modeled as follows:

$$\sum_K \langle \tilde{v}, -\nu \Delta \tilde{u} + u \cdot \nabla \tilde{u} \rangle_K \simeq \tau_K^{-1} \langle \tilde{v}, \tilde{u} \rangle_K, \quad \tau_K^{-1} = \left(c_1 \frac{\nu}{h^2} + c_2 \frac{|u|}{h} \right), \quad (10)$$

where c_1 and c_2 are algorithmic constants. The approximation of the subscales operator as a scalar term times the product \tilde{v}, \tilde{u} can be justified by means of a Fourier analysis of the problem for the subscales [12]. Replacing this expression in the equation for the subscales we obtain:

$$\sum_K \langle \tilde{v}, \partial_t u_h - \nu \Delta u_h + u \cdot \nabla u_h + \nabla p_h \rangle_K + \sum_K \langle \tilde{v}, \partial_t \tilde{u} \rangle_K + \sum_K \tau_K^{-1} \langle \tilde{v}, \tilde{u} \rangle_K = \langle \tilde{v}, f \rangle. \quad (11)$$

Equation (11) yields an expression for the subscales in the element interiors in terms of the finite element component, as long as \tilde{V} is approximated by a space of discontinuous functions:

$$\partial_t \tilde{u} + \tau_K^{-1} \tilde{u} = P_{\tilde{V}} (f - (\partial_t u_h - \nu \Delta u_h + u \cdot \nabla u_h + \nabla p_h)), \quad (12)$$

where $P_{\tilde{V}}$ denotes the projection onto the subscales space. Equation (12) implicitly defines a \tilde{u} as a function of u_h, p_h and t :

$$\tilde{u} = \phi_{\tilde{u}}(u_h, p_h, t). \quad (13)$$

There are several possible choices for the space of subscales, which yield different projection operators $P_{\tilde{V}}$. A typical choice is $P_{\tilde{V}} = I$, which results in the Algebraic Subgrid-Scale formulation (ASGS). The formulation we favor in our VMS model is to take the subscale space to be orthogonal to the finite element space:

$$\tilde{V} = V_h^\perp \cap V,$$

and as a consequence:

$$P_{\tilde{V}} = I - P_h,$$

where P_h is the $L^2(\Omega)$ projection onto the finite element space. This formulation is called the Orthogonal Subgrid Scale (OSS) formulation. It usually results in sharper, less diffusive solutions than the ASGS method.

This provides the required expression for the subscales in terms of the finite element unknowns. Note that equation (12) involves the time derivative of the velocity subscales. As a consequence, the subscales will need to be tracked in time and a time discretization scheme for them will be required. Note also that the velocity in all the convective terms is $u = u_h + \tilde{u}$, leading to a non-linear expression for the velocity subscales. The pressure subscales can be modeled as:

$$\tilde{p} = \phi_{\tilde{p}}(\mathbf{u}_h) := \tau_p \tau_K^{-1} P_{\tilde{Q}}(\nabla \cdot \mathbf{u}_h), \quad \tau_p = c_3 h^2, \quad (14)$$

following a procedure similar to the one described for the velocity subscales in equation (10). Again, \tilde{Q} is taken to be orthogonal to Q :

$$\tilde{Q} = Q_h^\perp \cap Q.$$

Note that both equation (12) and (14) need to be solved at the numerical integration points, since the subscales are needed there to compute (numerically) the integrals appearing in (7).

This final formulation of the incompressible Navier-Stokes equations can be proven to be stable for a proper choice of the stabilization constants c_1 and c_2 . Equally important, the motivation for the stabilizing terms has arisen from taking into account the contribution of the part of the solution which cannot be captured by the finite element mesh. This is the reason why many authors [27, 18, 14, 15, 23] have decided to use these numerical subscales not only as a stabilizing mechanism, but also as a model for the physics undergoing below the spatial and temporal resolution of the finite element mesh. In the case of the Navier-Stokes equations this corresponds to the modeling of turbulence.

iii Turbulent viscous dissipation for the OSS Navier-Stokes equations

Let us now focus on the numerical dissipation (and also turbulent, if we attend to the physical meaning of the subscales) of the scheme. We define the kinetic energy per unit volume inside the computational domain as:

$$W := \frac{1}{2} \rho |\mathbf{u}|^2.$$

The balance of kinetic energy for the continuous problem can be obtained by taking the test function v equal to the velocity u , the test function q equal to the pressure p , and multiplying (5) and (6) by the density ρ . After some manipulations we arrive to:

$$\frac{\partial}{\partial t} \int_{\Omega} W + \int_{\partial\Omega} \mathbf{n} \cdot \mathbf{u} W = \langle \mathbf{u}, \rho \mathbf{f} \rangle - 2\mu (\nabla^s \mathbf{u}, \nabla^s \mathbf{u}), \quad (15)$$

where μ is the dynamic viscosity. Equation (15) is saying that the variation of kinetic energy in the computational volume $\int_{\Omega} W$ is due to the flux of kinetic energy through the domain boundaries $\int_{\partial\Omega} \mathbf{n} \cdot \mathbf{u} W$, the increment of kinetic energy due to body forces $\langle \mathbf{u}, \rho \mathbf{f} \rangle$ (external power) and the decrement of kinetic energy due to the viscous dissipation $\epsilon = \mu (\nabla^s \mathbf{u}, \nabla^s \mathbf{u})$. The discrete counterpart of (15) is obtained by taking $v_h = u_h, q_h = p_h$ in (7):

$$\begin{aligned} \frac{\partial}{\partial t} \int_{\Omega} W_h + \int_{\partial\Omega} \mathbf{n} \cdot (\mathbf{u}_h + \tilde{\mathbf{u}}) W_h &= \langle \mathbf{u}_h, \rho \mathbf{f} \rangle - 2\mu (\nabla^s \mathbf{u}_h, \nabla^s \mathbf{u}_h) - \sum_K \langle \rho \mathbf{u}_h, \partial_t \tilde{\mathbf{u}} \rangle_K \\ &+ \sum_K \langle \mu \Delta \mathbf{u}_h + \rho (\mathbf{u}_h + \tilde{\mathbf{u}}) \cdot \nabla \mathbf{u}_h + \rho \nabla p_h, \tilde{\mathbf{u}} \rangle_K + \sum_K \langle \rho \nabla \cdot \mathbf{u}_h, \tilde{p} \rangle_K, \end{aligned} \quad (16)$$

with:

$$W_h := \frac{1}{2} \rho |\mathbf{u}_h|^2.$$

The terms involving the subscales in the right-hand side of equation (16) constitute the viscous numerical dissipation:

$$\begin{aligned} D_{\text{num}} &:= \sum_K \int_K \epsilon_{\text{num}} \\ \epsilon_{\text{num}} &:= \rho \mathbf{u}_h \cdot \partial_t \tilde{\mathbf{u}} - (\mu \Delta \mathbf{u}_h + \rho (\mathbf{u}_h + \tilde{\mathbf{u}}) \cdot \nabla \mathbf{u}_h + \rho \nabla p_h) \cdot \tilde{\mathbf{u}} - \rho \nabla \cdot \mathbf{u}_h \tilde{p}. \end{aligned} \quad (17)$$

On the other hand, we have the dissipation due to the finite element part of the solution:

$$\begin{aligned} D_h &= \int_{\Omega} \epsilon_h, \\ \epsilon_h &:= 2\mu |\nabla^s \mathbf{u}|^2. \end{aligned}$$

ϵ_{num} appears due to the contribution of the stabilization terms and, at the same time, it is taking into account the dissipation due to the subscales. In order to show this, let us study a simplified problem where we neglect the contribution of the pressure subscales \tilde{p} . Let us also neglect the contribution of $\mu \Delta \mathbf{u}_h$ (which is reasonable if highly turbulent flows are considered, or exact if a linear interpolation space is chosen for u_h). Furthermore, we take into account that, if $\tilde{V} \subset V_h \cap V$, then:

$$\sum_K \langle \rho \mathbf{u}_h, \partial_t \tilde{\mathbf{u}} \rangle_K = 0.$$

Let us also define the kinetic energy of \tilde{u} :

$$\tilde{W} := \frac{1}{2} \rho |\tilde{\mathbf{u}}|^2$$

the dissipation of \tilde{u} :

$$\tilde{D} = \sum_K \int_K \tilde{\epsilon}, \quad \tilde{\epsilon} = \tau_K^{-1} |\tilde{\mathbf{u}}|^2,$$

and the external power on u_h and $u^{\tilde{}}$:

$$\mathcal{P}_h := \langle \mathbf{u}_h, \rho \mathbf{f} \rangle, \quad \tilde{\mathcal{P}} := \langle \tilde{\mathbf{u}}, \rho \mathbf{f} \rangle.$$

Let us multiply (8) by ρ and take $v^{\tilde{}} = u^{\tilde{}}$. In this case from (8) and (16) we have:

$$\frac{\partial}{\partial t} \int_{\Omega} W_h + \int_{\partial\Omega} \mathbf{n} \cdot \mathbf{u} W_h + D_h + D_{\text{num}} = \mathcal{P}_h, \quad (18)$$

$$\frac{\partial}{\partial t} \int_{\Omega} \tilde{W} + \tilde{D} - D_{\text{num}} = \tilde{\mathcal{P}}. \quad (19)$$

It can be seen from equations (18)-(19) that D_{num} is in charge for the transfer of energy from the large (finite element) scales to the subgrid scales. Due to this, D_{num} can be understood as the dissipation caused by the turbulent effects of the flow (see [19, 24]).

Another interesting observation can be done if we plug the equation for the subscales (12) into the expression for ϵ_{num} (17) (again taking into account the orthogonality of the subscales and neglecting \tilde{p} and $\mu \Delta u_h$):

$$\begin{aligned} D_{\text{num}} &= \rho \sum_K \tau_K \langle P_{\tilde{V}}(\mathbf{u} \cdot \nabla \mathbf{u}_h + \nabla p_h), P_{\tilde{V}}(\mathbf{u} \cdot \nabla \mathbf{u}_h + \nabla p_h) \rangle_K \\ &\quad + \rho \sum_K \tau_K \langle P_{\tilde{V}}(\mathbf{u} \cdot \nabla \mathbf{u}_h + \nabla p_h), \partial_t \tilde{\mathbf{u}} \rangle_K. \end{aligned} \quad (20)$$

The first term in the right-hand side of (20) is always positive. The second term only appears if dynamic subgrid scales are considered. It is shown in [16] that it can be locally (in space and time) negative, although the average in time of D_{num} is proved to be positive. Locally negative values of D_{num} represent a transfer of energy from the small scales to the large scales, a phenomenon known as backscatter, which is observed in physical turbulent flows. After the decomposition of the unknowns into the contributions of the finite element scales and the subgrid scales, taking into account the temporal derivatives of the subscales allows the OSS method to model backscatter. Let us stress that this backscatter model arises from the numerical decomposition of the unknown and not from a physical modeling of the phenomena. See the numerical examples section where dissipation values and their average are shown for a convective boundary layer case. Another numerical example can be found in [16].

Finally, the total pointwise dissipation which accounts for the numerical and large scale dissipation:

$$\epsilon = \epsilon_h + \epsilon_{\text{num}}, \quad (21)$$

is going to be used for the computation of quality of seeing estimators.

iv Discretization in time

For the discretization in time, we rely on a finite difference time discretization. We consider a uniform partition of $[0, T]$ of size δt . We denote a time dependent function f approximated at $t^n = n\delta t$ as f^n and δf^n the approximation to $\partial_t f$ at t^n . Introducing this notation, the time discrete

problem is: find $[u_h, p_h] \in V_h \times Q_h$, for each $t \in [0, T]$ and $\tilde{u} \in V, \tilde{p} \in \tilde{Q}$ for each $t \in [0, T]$, such that:

$$\begin{aligned} & (\mathbf{v}_h, \delta_t \mathbf{u}_h^{n+1}) + B([\mathbf{v}_h, q_h], [\mathbf{u}_h^{n+1}; \mathbf{u}_h^{n+1}, p_h^{n+1}]) + \sum_K \langle \mathbf{v}_h, \delta_t \tilde{\mathbf{u}}^{n+1} \rangle_K \\ & + \sum_K \langle -\nu \Delta \mathbf{v}_h - \mathbf{u}^{n+1} \cdot \nabla \mathbf{v}_h - \nabla q_h, \tilde{\mathbf{u}}^{n+1} \rangle_K - \sum_K \langle \nabla \cdot \mathbf{v}_h, \tilde{p}^{n+1} \rangle_K = \langle \mathbf{v}_h, \mathbf{f}^{n+1} \rangle. \end{aligned} \quad (22)$$

In order to approximate $\delta_t \mathbf{u}_h^{n+1}$, a second order backward differences scheme is used:

$$\delta_t \mathbf{u}_h^{n+1} = \frac{\frac{3}{2} \mathbf{u}_h^{n+1} - 2 \mathbf{u}_h^n + \frac{1}{2} \mathbf{u}_h^{n-1}}{\delta t}.$$

On the other hand, a first order backward Euler scheme is used to integrate the subscales in time:

$$\delta_t \tilde{\mathbf{u}}^{n+1} = \frac{\tilde{\mathbf{u}}^{n+1} - \tilde{\mathbf{u}}^n}{\delta t}.$$

This is sufficient for the approximation of the subscales, since:

$$\tilde{\mathbf{u}} = \mathcal{O}(\tau_K (\mathbf{f} - (\partial_t \mathbf{u}_h - \nu \Delta \mathbf{u}_h + \mathbf{u} \cdot \nabla \mathbf{u}_h + \nabla p_h))),$$

and $\tau_K = \mathcal{O}(\delta t)$.

v Fractional step splitting

In order to minimize the computational time inverted in solving (22), we rely on a fractional step splitting technique. This decomposes the solution of the monolithic system into the solution of several simpler problems: a convection-diffusion equation for the velocity unknown, a pressurepoisson equation and a projection step. We start by noting that, for the choice $\tilde{V} = V_h^\perp \cap V$:

$$\sum_K \langle \mathbf{v}_h, \delta_t \tilde{\mathbf{u}}^{n+1} \rangle_K = 0.$$

We introduce an intermediate velocity $\hat{\mathbf{u}}_h^n$, for which we consider:

$$\begin{aligned} \hat{\mathbf{u}}_h^n &= \mathbf{u}_h^n, \\ \hat{\mathbf{u}}_h^{n-1} &= \mathbf{u}_h^{n-1}, \end{aligned}$$

and the intermediate velocity and pressure subscales $\hat{\mathbf{u}}_h^{n+1}$ and \hat{p}_h^{n+1} . The steps of the fractional step method are:

1. Convection-diffusion equation. We solve for the intermediate quantities $\hat{\mathbf{u}}_h^{n+1}$, $\hat{\mathbf{u}}_h^{n+1}$ and \hat{p}_h^{n+1} :

$$\begin{aligned}
& (\mathbf{v}_h, \delta_t \hat{\mathbf{u}}_h^{n+1}) + B([\mathbf{v}_h, 0], [\hat{\mathbf{u}}^{n+1}; \hat{\mathbf{u}}_h^{n+1}, p_h^n]) \\
& + \sum_K \left\langle -\nu \Delta \mathbf{v}_h - \hat{\mathbf{u}}^{n+1} \cdot \nabla \mathbf{v}_h, \hat{\mathbf{u}}^{n+1} \right\rangle_K - \sum_K \left\langle \nabla \cdot \mathbf{v}_h, \hat{p}^{n+1} \right\rangle_K = \langle \mathbf{v}_h, \mathbf{f}^{n+1} \rangle,
\end{aligned}$$

where $\hat{\mathbf{u}}^{n+1}$ is the solution of:

$$\hat{\mathbf{u}}^{n+1} = \phi_{\tilde{\mathbf{u}}}(\hat{\mathbf{u}}_h^{n+1}, p_h^n, t^{n+1})$$

as defined in (13) and \hat{p}^{n+1} is the solution of:

$$\hat{p}^{n+1} = \phi_{\tilde{p}}(\hat{\mathbf{u}}_h^{n+1}),$$

as defined in (14).

2. Pressure Poisson equation. We solve for p_h^{n+1} and \tilde{u}^{n+1} :

$$(q_h, \nabla \cdot \hat{\mathbf{u}}_h^{n+1}) - \sum_K \langle \nabla q_h, \tilde{\mathbf{u}}^{n+1} \rangle_K = -\frac{2\delta t}{3} (\nabla(p_h^{n+1} - p_h^n), \nabla q_h),$$

where \tilde{u}^{n+1} is the solution of:

$$\tilde{\mathbf{u}}^{n+1} = \phi_{\tilde{\mathbf{u}}}(\hat{\mathbf{u}}_h^{n+1}, p_h^{n+1}, t), \quad (23)$$

as defined in (13). For the temporal integration of (23), we consider $\tilde{u}^n = \tilde{u}^{n-1}$. In this way only the intermediate subscale velocity needs to be tracked in time.

3. Projection step: We solve for u_h^{n+1} :

$$\frac{3}{2\delta t} (\mathbf{v}_h, \mathbf{u}_h^{n+1} - \hat{\mathbf{u}}_h^{n+1}) + (\mathbf{v}_h, (\nabla p_h^{n+1} - \nabla p_h^n)) = 0.$$

1.3 Heat transfer equation

i Problem statement

In this section we summarize the finite element approximation of the heat transfer equation using the OSS approach. Let us consider the transient heat transfer equation, which consists of finding $\theta : \Omega \times (0, T) \rightarrow \mathbb{R}^3$ such that:

$$\begin{aligned}
\partial_t \theta + \mathbf{u} \cdot \nabla \theta - \kappa \Delta \theta &= q & \text{in } \Omega, \\
\theta &= \bar{\theta} & \text{on } \Gamma_{D\theta}, \\
\mathbf{n} \cdot \nabla \theta &= 0 & \text{on } \Gamma_{N\theta},
\end{aligned} \quad (24)$$

where θ is the temperature field, κ is the thermal diffusivity and q is now the heat source term. Initial conditions have to be appended to this problem.

ii Finite element approximation

Let us define $\Psi = H^1(\Omega)$, and the finite element space defined through the finite element partition $\Psi_h \subset \Psi$. The Galerkin finite element approximation of equation (24) consists of finding $\theta_h \in C^1(0, T; \Psi_h)$ such that:

$$(\psi_h, \partial_t \theta_h) + (\psi_h, \mathbf{u} \cdot \nabla \theta_h) + \kappa (\nabla \psi_h, \nabla \theta_h) = \langle \psi_h, q \rangle \quad \forall \psi_h \in \Psi_h, \quad (25)$$

with the corresponding initial and boundary conditions. Similarly to the Navier-Stokes problem, the finite element approximation (25) suffers from instability problems caused by the convective term. Stabilization is required, and again physically based numerical stabilization can be obtained by using the VMS method. Following a process analogous to the one presented in Section 2, the subscales can be modeled as a function of the finite element part of the temperature solution field, θ_h :

$$\partial_t \tilde{\theta} + \tau_{\theta K}^{-1} \tilde{\theta} = P_{\tilde{\Psi}} (q - (\partial_t \theta_h - \kappa \Delta \theta_h + \mathbf{u} \cdot \nabla \theta_h)), \quad (26)$$

with

$$\tau_{\theta K} = \left(c_{\theta 1} \frac{\kappa}{h^2} + c_{\theta 2} \frac{|\mathbf{u}|}{h} \right)^{-1}.$$

$c_{\theta 1}$ and $c_{\theta 2}$ are algorithmic constants, which in practice coincide with c_1 and c_2 in equation (10). Again, several choices are possible for the space of subgrid scales. As in the Navier-Stokes equations, we advocate for the use of Orthogonal Subgrid Scales, that is, we choose the space for temperature subscales $\tilde{\Psi}$ to be:

$$\tilde{\Psi} = \Psi_h^\perp \cap \Psi.$$

The stabilized finite element heat transfer problem is obtained by introducing the scale splitting in equation (25) and replacing the subscales by its approximation (26):

$$\begin{aligned} & (\psi_h, \partial_t \theta_h) + (\psi_h, \mathbf{u} \cdot \nabla \theta_h) + \kappa (\nabla \psi_h, \nabla \theta_h) \\ & + \sum_K \langle \psi_h, \partial_t \tilde{\theta} \rangle_K + \sum_K \langle -\kappa \Delta \psi_h - \mathbf{u} \cdot \nabla \psi_h, \tilde{\theta} \rangle_K = (\psi_h, q) \quad \forall \psi_h \in \Psi_h. \end{aligned} \quad (27)$$

iii Turbulent thermal dissipation for the OSS heat transfer equation

As done for the Navier-Stokes equations, we now deal with the numerical-turbulent dissipation of the OSS scheme for the heat transfer equation. We start by defining the thermal energy per unit volume in the computational domain Ω as:

$$H = \frac{1}{2} \rho c_p \theta^2,$$

where c_p is the heat capacity and ρ the density of the fluid. The continuous thermal energy balance equation can be obtained by taking $\psi = \theta$ in equation (25), and multiplying the equation by ρc_p . After some manipulations, and taking into account the incompressibility of u , we obtain:

$$\frac{\partial}{\partial t} \int_{\Omega} H + \int_{\partial \Omega} \mathbf{n} \cdot \mathbf{u} H = \langle \theta, \rho c_p q \rangle - \rho c_p \kappa (\nabla \theta, \nabla \theta). \quad (28)$$

In this case, the variation of thermal energy $\frac{\partial}{\partial t} \int_{\Omega} H$ in the computational domain is due to the convective flux of thermal energy through the domain boundary $\int_{\partial\Omega} \mathbf{n} \cdot \mathbf{u} H$, the increment of thermal energy caused by the heat source $\int_{\Omega} \rho c_p q$ and the decrement of thermal energy caused by the thermal dissipation $\chi = \rho c_p \kappa (\nabla \theta, \nabla \theta)$. The discrete counterpart of equation (28) is obtained by taking $\psi_h = \theta_h$ in equation (27):

$$\begin{aligned} \frac{\partial}{\partial t} \int_{\Omega} H_h + \int_{\partial\Omega} \mathbf{n} \cdot \mathbf{u} H_h &= \langle \theta_h, \rho c_p q \rangle - \rho c_p \kappa (\nabla \theta_h, \nabla \theta_h) \\ &- \sum_K \langle \rho c_p \theta_h, \partial_t \tilde{\theta} \rangle_K + \sum_K \langle \rho c_p \kappa \Delta \theta_h + \rho c_p \mathbf{u} \cdot \nabla \theta_h, \tilde{\theta} \rangle_K, \end{aligned} \quad (29)$$

with:

$$H_h = \frac{1}{2} \rho c_p \theta_h^2.$$

The two last terms in the right-hand side of equation (29) are called the thermal numerical dissipation:

$$E_{\text{num}} = \sum_K \int_K \chi_{\text{num}} \quad (30)$$

$$\chi_{\text{num}} = \rho c_p \theta_h \partial_t \tilde{\theta} - (\rho c_p \kappa \Delta \theta_h + \rho c_p \mathbf{u} \cdot \nabla \theta_h) \tilde{\theta}. \quad (31)$$

χ_{num} appears due to the contribution of the stabilization terms and, as χ_{num} in the Navier-Stokes equations, is modeling the contribution to the dissipation due to the subscales. As a consequence, it can be considered as a model for the turbulent effects of the flow. Note that, contrary to other models, the turbulent Prandtl number which relates turbulent viscosity and turbulent thermal diffusivity is not required in this variational multiscale based turbulence model for the heat transfer equation. The total thermal dissipation is now modeled as:

$$\chi = \chi_h + \chi_{\text{num}} \quad (32)$$

with:

$$\chi_h = \rho c_p \kappa |\nabla \theta_h|^2.$$

iv Discretization in time

The associated time discrete problem is: find $\theta_h \in \Psi_h$ for each $t \in [0, T]$ such that:

$$\begin{aligned} &(\psi_h, \delta_t \theta_h^{n+1}) + (\psi_h, \mathbf{u}^{n+1} \cdot \nabla \theta_h^{n+1}) + \kappa (\nabla \psi_h, \nabla \theta_h^{n+1}) \\ &+ \sum_K \langle \psi_h, \delta_t \tilde{\theta}^{n+1} \rangle_K + \sum_K \langle -\kappa \Delta \psi_h - \mathbf{u}^{n+1} \cdot \nabla \psi_h, \tilde{\theta}^{n+1} \rangle_K = (\psi_h, q) \quad \forall \psi_h \in \Psi_h. \end{aligned} \quad (33)$$

A second order backward difference scheme is used to approximate $\delta_t \theta_h^{n+1}$ and a first order backward Euler scheme is used to approximate the subscales derivative with respect to time, $\delta_t \bar{\theta}_{n+1}$.

1.4 Atmospheric seeing parameters

In this section we describe the parameters which quantify the atmospheric seeing of a facility or observation site. We also relate them to the numerical approximations described in Sections 2 and 3. We focus especially on the relation with the turbulent dissipations ϵ_{num} and χ_{num} which appear in the stabilized discrete finite element equations due to the energy transfer to the non-resolved scales of the Kolmogorov cascade.

The final optical parameters we aim to simulate numerically are the Fried parameter r_0 and the Greenwood frequency f_G . The Fried parameter is essential in adaptive optics. In the case of telescopes it allows to determine the number of segments into which a segmented mirror has to be split, or the distance between actuators for a continuous deformable mirror, by prescribing an admissible RMS distortion of a wavefront [2]. But the design of their actuators is also based on the so called *Greenwood frequency*, which is an indication of how fast the atmosphere is changing and defines the bandwidth of the servo control for an adaptive optics system (see [33] for more details). However, both parameters are a function of the integral along the optical path of light beams of the structure constant C_n of the refractive index of a medium, $n(x,t)$. See [13] for a detailed description of the relationship between r_0 , f_G and C_n .

This structure function can be related to the structure function of the temperature, the humidity and their joint structure parameter (see [32]). However, we will consider the humidity effects negligible. Thus, if we write the temperature dependence of n as $n = n(\theta)$, we have

$$C_n = \frac{dn}{d\theta} C_\theta,$$

where C_θ is the structure function of the temperature. Assuming pressure equilibrium it is found that [34]

$$C_n = \frac{79 \times 10^{-6}}{\bar{\theta}^2} \bar{p} C_\theta, \quad (34)$$

where p is assumed to be measured in millibars and θ is the absolute temperature. Here and below, θ , p and u denote the solution of the continuous problems defined in equations (4) and (24) and the overbars denote mean quantities in the observation period.

In view of (34), the problem is to compute C_θ . Once again in the inertial range of the Kolmogorov spectrum and assuming the temperature to be a passive quantity, it can be shown that (see [33])

$$C_\theta^2 = a^2 \bar{\chi}_m \bar{\epsilon}_m^{-1/3}, \quad (35)$$

where a is an empirical value called Obukhov-Corrsin constant (see [25, 36] for extensions and a discussion about Obukhov-Corrsin constants and on the validity of this approximation). In (35), $\bar{\chi}_m$ denotes the mean molecular thermal diffusive dissipation and $\bar{\epsilon}_m$ the mean molecular dissipation of kinetic energy of the flow. These parameters are given by

$$\bar{\chi}_m := \rho c_p \kappa \overline{|\nabla \theta|^2}, \quad \bar{\epsilon}_m := 2\mu \overline{|\nabla^s \mathbf{u}|^2}. \quad (36)$$

The problem is now closed: using (36) in (35) and the result back in (34) we have an expression to compute C_n in terms of the flow variables u, p, θ at each point.

Some questions remain open when we want to numerically apply the previous approximations for C_n and C_θ . The first issue is that, instead of working with $u, p,$ and θ , we are going to be working with $u_h, p_h,$ and θ_h , and a model for the velocity and temperature under-resolved scales \tilde{u} and $\tilde{\theta}$ given by equations (12) and (26). The first point to consider is the relation between the averaged quantities $\bar{u}, \bar{p},$ and $\bar{\theta}$, and their finite element approximations. To this end we will recall that filtered unknowns in LES models need to maintain the mean of the original variables. Due to the close relationship of the presented VMS turbulence model to LES filtering, we will assume this to be true also for the finite element variables $u_h, p_h,$ and θ_h . This means that we will consider

$$\bar{\mathbf{u}} \approx \bar{\mathbf{u}}_h, \quad \bar{p} \approx \bar{p}_h, \quad \bar{\theta} \approx \bar{\theta}_h. \quad (37)$$

The second point is how to compute the average kinetic and thermal energy dissipations $\bar{\epsilon}_m$ and $\bar{\chi}_m$. In order to do this we will make use of the definitions in equations (21) and (32), and we will compute the averaged dissipations as

$$\bar{\epsilon} = \bar{\epsilon}_h + \bar{\epsilon}_{\text{num}}, \quad \bar{\chi} = \bar{\chi}_h + \bar{\chi}_{\text{num}}, \quad (38)$$

We assume that $\bar{\epsilon} \approx \bar{\epsilon}_m, \bar{\chi} \approx \bar{\chi}_m$, that is, the model accounts properly for the molecular dissipation. This is proved in particular in [24] in a simplified setting. That the mean dissipation approximates the molecular dissipation is the general assumption of LES models.

Using approximations (37) and (38) in (35) and inserting the result in (34) it is found that:

$$C_n = 79 \times 10^{-6} \bar{\theta}_h^{-2} \bar{p}_h a \bar{\chi}^{1/2} \bar{\epsilon}^{-1/6}. \quad (39)$$

Equation (39) is the expression we were looking for. It allows us to compute the structure function of the refractive index in terms of the flow variables resulting from a VMS numerical simulation.

1.5 Numerical examples

i Convective boundary layer

The first numerical example consists of a convective boundary layer. This example was first presented in [8] where a method for the estimation of atmospheric seeing using the Dutch Atmospheric LES method (DALES) is presented. We use it here to compare the optical parameters obtained by using the VMS based dissipation model against the ones obtained using the Smagorinsky based dissipation model presented in [13], and a dissipation model based on the WALE subgrid scale model. The simulation domain is a parallelepiped whose base is a square with a 10 km side and a height of 2 km. Air flow is caused by the presence of a heat flux through the inferior base (0.1 K m s^{-1}) and an horizontal body acceleration term ($9.4325 \cdot 10^{-5} \text{ m s}^{-2}$). Boundary conditions are periodic in the lateral boundaries and no fluid is allowed to trespass the superior and inferior boundaries of the domain. Also a wall law boundary

condition [4] is used in the inferior boundary, which causes the presence of the boundary layer for this example. Initial conditions are given by a vertical temperature gradient set to 3 K km^{-1} and air at rest. The numerical simulation is run for 10000 seconds, with a time step of 1 second. The finite element mesh is a uniform structured tetrahedra mesh totaling 1.8 million elements. The mesh resolution is 150 m horizontally and 150 m vertically.

Fig. 1 shows the averaged temperature and velocity profiles along the vertical dimension. In the temperature profile the expected increase in mean temperature due to the heat flux in the inferior boundary is observed. At a greater height, the temperature values get closer to the initial condition temperature profile. Regarding the horizontal velocity profile, a boundary layer behavior is recovered with a large velocity gradient close to the floor. Moreover, a slight decrease in the average velocity is observed in the region where the temperature joins the initial constant vertical gradient (1000 m height). Fig. 2 shows a snapshot of the velocity and temperature fields at the end of the simulation. The velocity snapshot allows to see how hot air in the ground tends to be convected up due to the Boussinesq forces. The temperature field, on the other hand, is smooth, large temperature gradients appear only in the ground where the heat flux causes bubbles of hot air to appear. Finally Fig. 3 shows a plot of the dissipation values for the kinetic energy balance at the end of the simulation obtained using the OSS Variational Multiscale Method. The top plot corresponds to dissipation values computed at numerical integration points and its extrapolation to the nodes of each element. Elements with a partially white area correspond to elements where the dissipation at some of the numerical integration points is negative (or the dissipation extrapolated to the nodes of the element is negative). In the bottom plot the nodally averaged (through a lumped L^2 projection) is shown. The nodally averaged dissipation values are positive everywhere. This is in agreement with the expected behavior for the modeling of backscatter, where dissipation values can be locally negative (accounting for the transmission of energy from the small scales to the large scales), but need to be positive when averaged in space and time.

Fig. 4 shows a comparison of the C_n^2 fields obtained by using the OSS based model for the computation of the viscous and thermal dissipations and the structure constants, the Smagorinsky and the WALE models. It can be observed that the three models yield qualitatively similar results: the magnitude of the structure constant C_n^2 is large close to the ground, where large temperature gradients exist due to the thermal heat flux. After the first few meters, the C_n^2 value starts to diminish with height (as the cyan regions denote), although the C_n^2 coefficient magnitude is larger in those regions where there is a hot air bubble moving up (vertical yellow patches close to the ground). In the mid-height region of Fig. 4 (corresponding to a height of 1000 m) the hot bubbles disappear due to the effect of the dominant horizontal flow. In this region, an increase of the C_n^2 values is observed. At a height of 1500 m, the C_n^2 values diminish again. Due to the non-trespassing boundary condition, an spurious increase of the C_n^2 values is observed in the top wall. This increase appears due to the fact that large gradients of the velocity are obtained in this top non-trespassing boundary condition, and would not be there in a real open-flow boundary condition (which we cannot reproduce at the numerical level). It must also be noted that the C_n^2 field is smoother for the Smagorinsky and WALE models than for the OSS model. This is probably caused by the fact that the Smagorinsky and WALE models for the dissipations are based on the gradients of the recovered fields, while the dissipations for the OSS model are based on the component of the residual orthogonal to the finite element space, which is undoubtedly less smooth. Finally, Fig. 5 shows a comparison of the horizontally averaged C_n^2 values at the end of the simulation, including the results of [8] using the DALES

model. It is clear that the presented results and the results in [8] are qualitatively similar. However, the increase in the C_n^2 at mid-height occurs at a lower height in the results from [8]. The largest differences are obtained in the region close to the ground. This can be caused by the fact that the C_n^2 parameter is very sensitive to small variations in the temperature gradients. The bottom region presents the largest temperature gradients, and small deviations in the computed temperature gradients can cause large variations in the obtained C_n^2 values. In spite of this, the results presented here are in good agreement with the results in [8], since, in most of the height (except for the bottom region very close to the ground), they lay within one standard deviation of the mean of the distribution of results statistically collected in [8].

This results allow to state that the C_n^2 values obtained through the Orthogonal Subgrid Scale model show a distribution which is qualitatively the same as the one obtained through physically based LES models (Smagorinsky, WALE and the DALES model in [8]). Since the C_n^2 values depend on the turbulent dissipation of the model, it means that the viscous and thermal turbulent dissipations obtained in the OSS method are qualitatively the same as the ones in the physically based LES models. This is remarkable, because the expressions for these dissipations were motivated exclusively by numerical arguments in the case of OSS, which contrasts with the physically based arguments used to derive the LES turbulent dissipations.

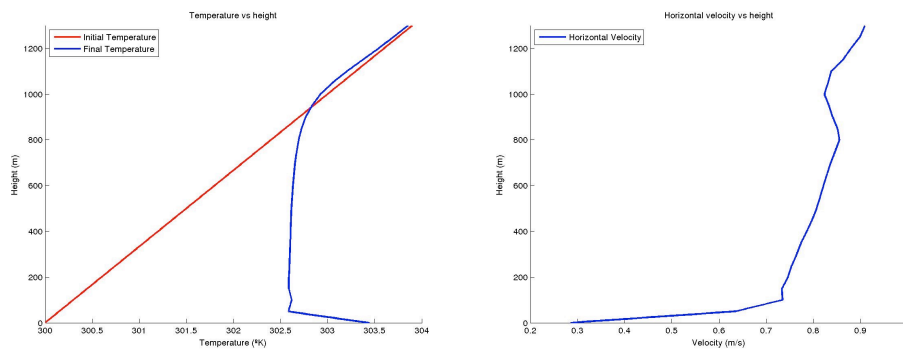
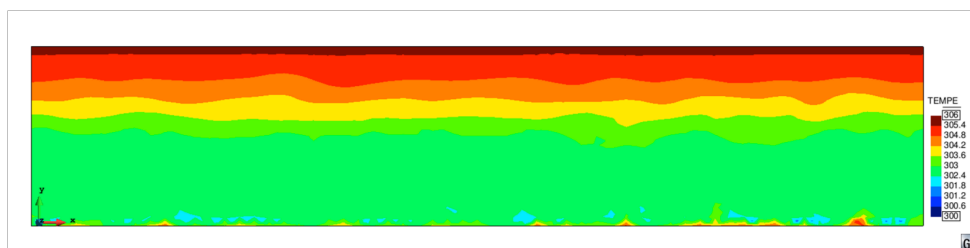


Figure 1: Temperature (left) and horizontal velocity (right) averaged profiles



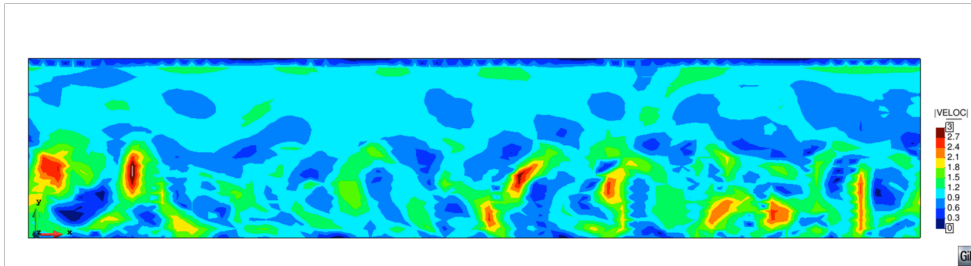


Figure 2: Temperature in K (top) and Velocity (bottom) snapshots at the end of the simulation

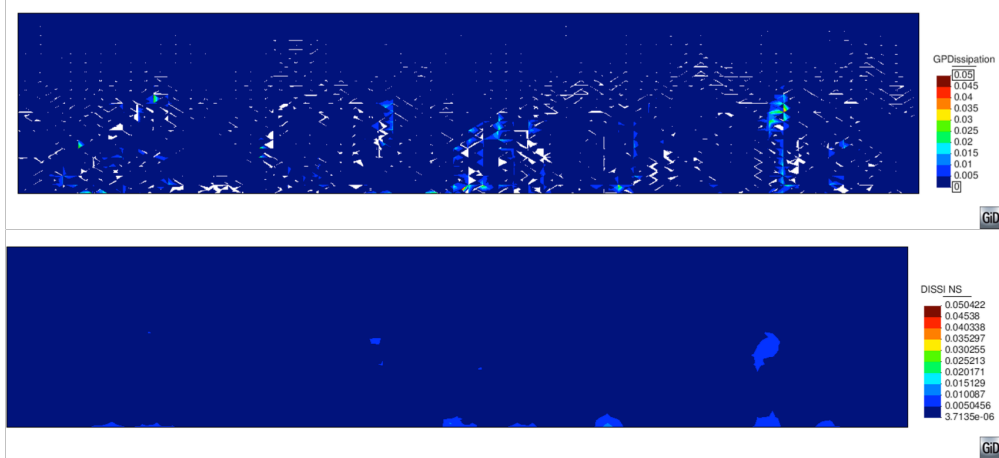
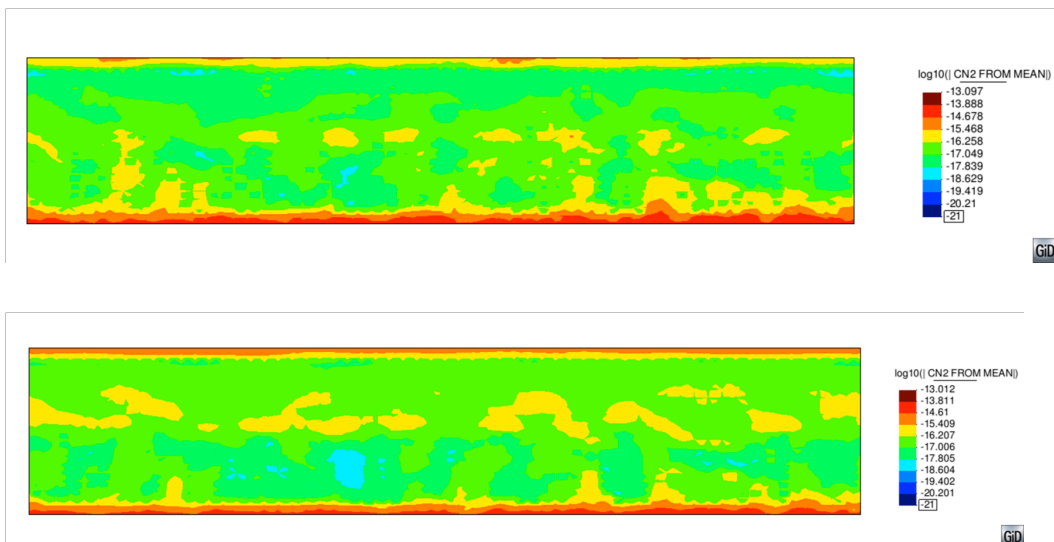


Figure 3: Dissipation values for the kinetic energy balance: numerical integration points (top) and nodally averaged (bottom) values.



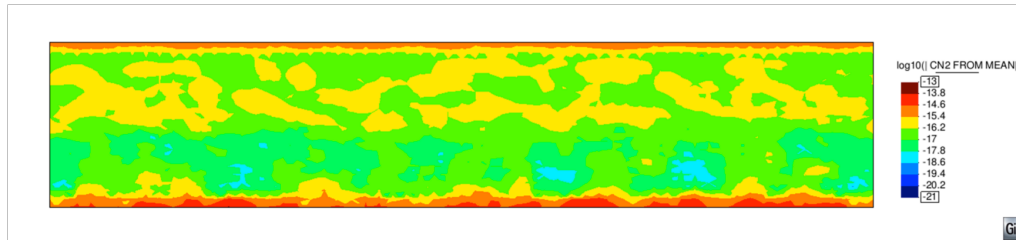


Figure 4: C_n^2 snapshots at the end of the simulation. From top to bottom: Variational Multiscale, Smagorinsky, WALE model.

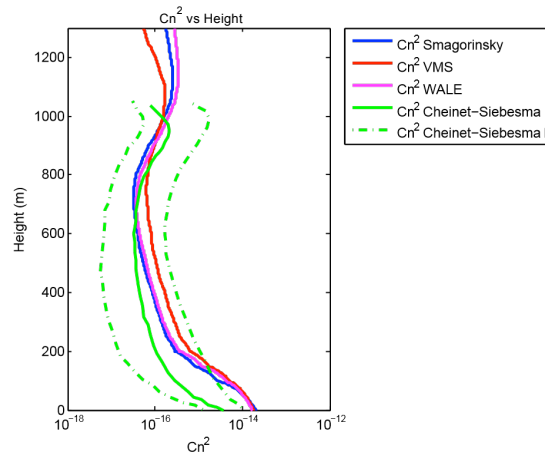


Figure 5: Averaged (horizontally) C_n^2 values at the end of the simulation. Comparison with the results in [8]. The green dotted lines represent the values which lie within one standard deviation in the statistical data collected in [8].

ii Transfer optics and Coudé room

The second example corresponds to a transfer optics chamber and Coudé room. The geometry and boundary conditions for this case were provided by the Astrophysical Institute of the Canary Islands during the design phase of the European Solar Telescope (EST). Fig. 6 shows the geometry and boundary conditions of the case. The spheres in the plot represent concentrated heat loads, which consist of 300 mm and provide a heat source of 2W (7.0738 W/m²). The thermal control system consists of air plenums blowing air at ambient temperature (20 °C), vertical velocity equal to 1 m/s, in the vertical direction from the top of the chamber (plenum area = 22.1 m²). Return air plenums are placed at the lower part of the chamber (plenum area = 314.16 m²). The objective of this case is to analyze the seeing degradation in the transfer optics chamber.

Velocity boundary conditions in the lateral walls and the heating spheres correspond to a wall-law condition. Inflow velocity is set to 1 m/s, and outflow velocity is left free. The numerical simulation is run for 100 seconds, after which the flow is considered to be

completely developed. The time step is set to 0.2 seconds. The finite element mesh is composed of 3.4 million tetrahedra, with a local refinement in the regions close to the heating spheres (element size equal to 0.03 m) and larger elements in the regions far from them (element size equal to 0.3 m).

Fig. 7 shows a velocity and temperature snapshot after the flow has been completely developed. The velocity is larger in the central region, where most of the injected air flow is circulating. The heating spheres oppose to the flow, which causes some boundary layers to appear. This will have a negative effect in the resulting seeing conditions. Regarding the temperature, the largest temperatures and temperature gradients are found on the surface of the heating spheres, and hot air jets are found following the path of the vertical air inflow.

Fig. 8 shows a comparison of the C_n^2 values in the transfer optics room, obtained by using

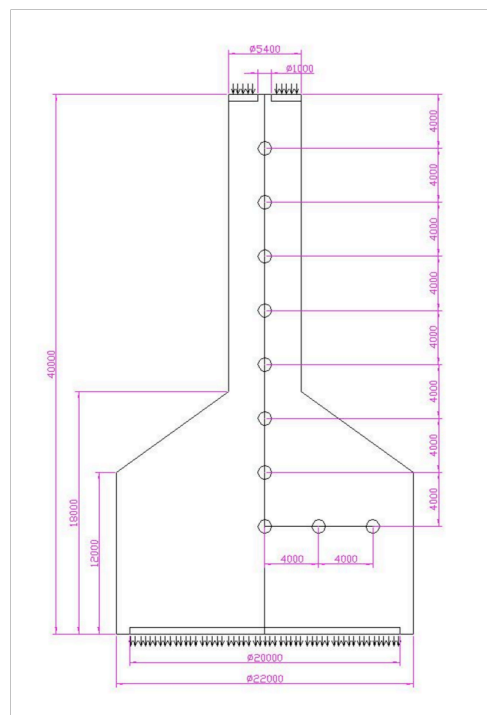


Figure 6: Geometry of the transfer optics and Coudé room (distances in mm)

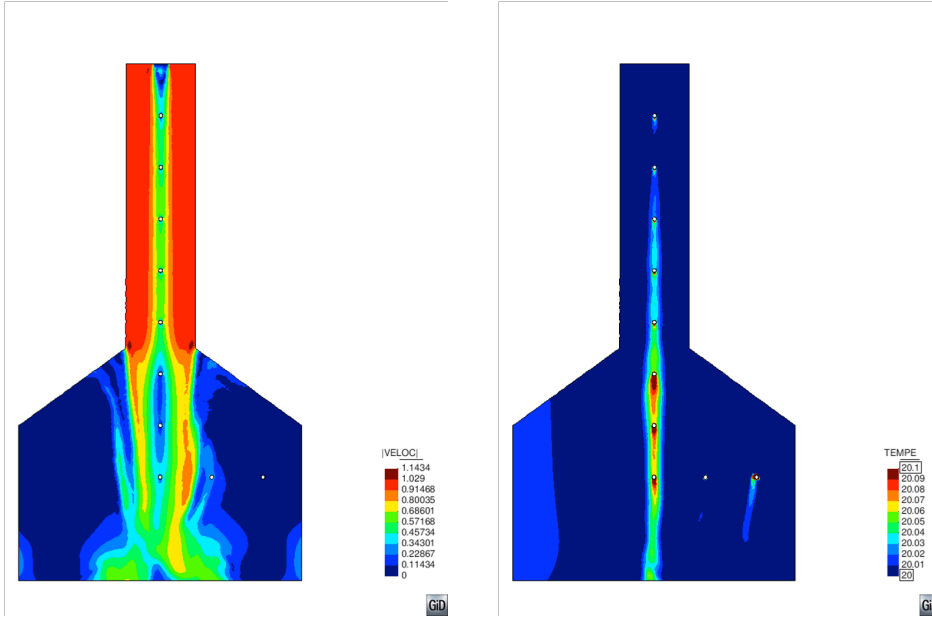


Figure 7: Velocity (left) and temperature in °C (right) snapshots at the transfer optics and Coudé room.

the OSS, the Smagorinsky and the WALE models. It is clear that these models provide very similar results in this case, the C_n^2 field being less smooth for the OSS case.

iii Flow around a telescope enclosure

In the last example we simulate the atmospheric seeing around a telescope enclosure. In particular, this corresponds to one of the tentative designs of the European - Extremely Large Telescope (E-ELT) enclosure. Fig. 9 shows the geometry of the enclosure. The objective of this simulation was to evaluate the effect of a frontal wind shield in the atmospheric seeing. The enclosure has 4 meter sized windows which facilitate the natural ventilation of the building. The enclosure diameter is 85 m, with a maximum height of 79 m. The external domain for the simulation is a $600 \times 600 \times 1500 \text{ m}^3$ box. The finite element mesh is composed of 3.3 million tetrahedra, with element sizes ranging from 1 m (close to the telescope) to 20 m (in the open flow region).

A wall-law velocity boundary condition [4] is set on the ground and building surfaces, while a non-trespassing boundary condition is set on the lateral walls of the bounding box. The inflow velocity is set to 1 m/s. Regarding temperature boundary conditions, we impose the following expression for temperature as a function of height:

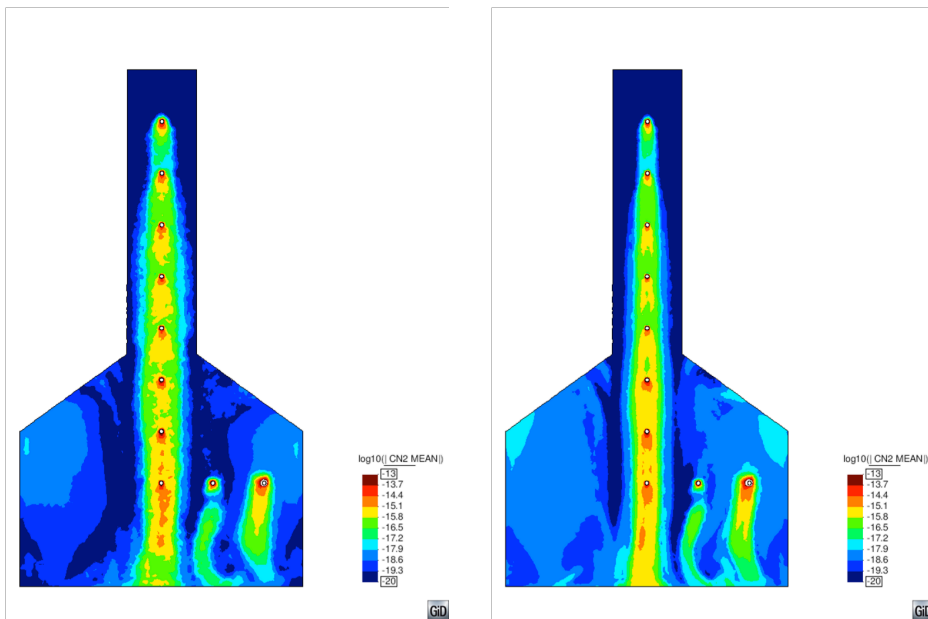
$$\theta = 12 - 0.7 \ln \left(\frac{z + 0.01}{0.02} \right)$$

where the height z is expressed in meters and the resulting temperature is expressed in °C. The initial temperature profile is depicted in Fig. 10.

Fig. 11 shows the velocity and temperature fields at a cut along the stream-wise direction after the flow has been fully developed. Turbulent vortexes appear behind the telescope, the largest velocity gradients occurring on the surface of the telescope. The maximum absolute value velocity appears after the flow has been detached from the telescope enclosure, and a low-speed recirculation zone can be observed leeward from the telescope. Regarding the temperature field, the maximum temperature and temperature gradients are again found on the surface of the telescope. The interior of the telescope shows larger temperatures when compared to the exterior domain, despite the large ventilation windows put in place in order to minimize temperature gradients. Intermediate temperature values are also found in the recirculation area behind the telescope.

Fig. 12 shows a comparison of the C_n^2 profiles obtained by using the OSS, Smagorinsky and WALE dissipation models. As in the previous cases, maximum values for the C_n^2 parameter are found in the regions where the velocity and temperature gradients are larger, which coincide with the terrain ground, the telescope enclosure surface and the area where the detachment of the flow occurs. The low speed recirculation zone behind the telescope also shows large values for the C_n^2 parameter, which is due to the large temperature gradients. If we compare the results of the various models, results are again qualitatively equivalent, the results being smoother for the Smagorinsky and WALE models.

Let us say again that this agreement is remarkable if we take into account that the expressions for the calculation of dissipations were motivated by physical arguments in the case of the LES models and, on the contrary, by numerical arguments in the case of the OSS variational multiscale method.



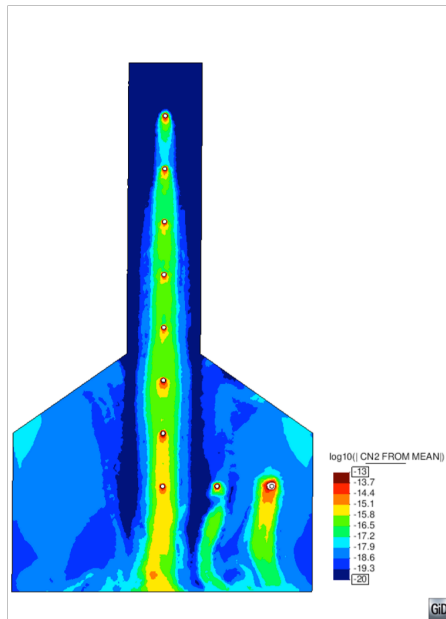


Figure 8: C_n^2 snapshots for the Coud'e room. Variational Multiscale (top left), Smagorinsky (top right) and WALE (bottom) models.

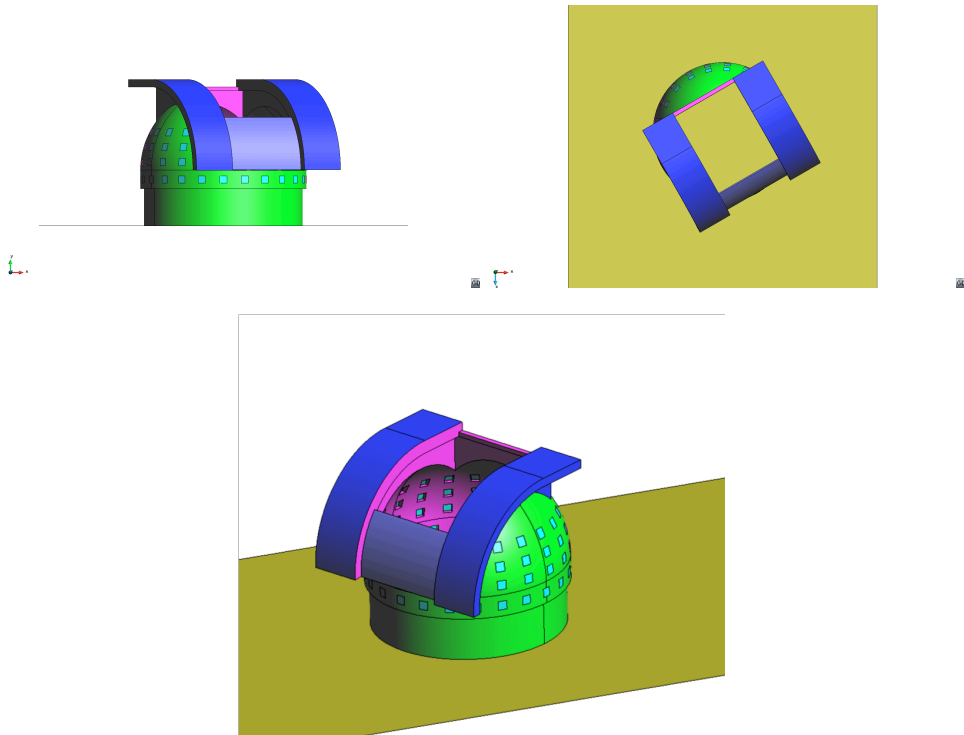


Figure 9: External geometry for the E-ELT enclosure. Front, top and perspective views.

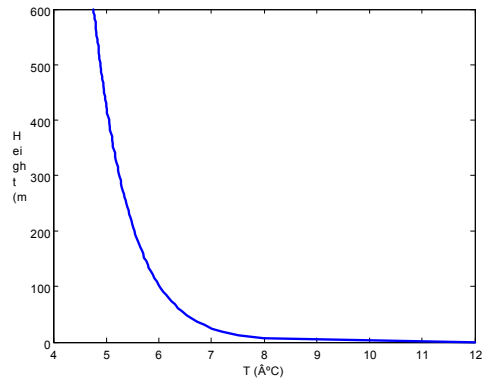


Figure 10: Temperature inflow boundary condition as a function of height

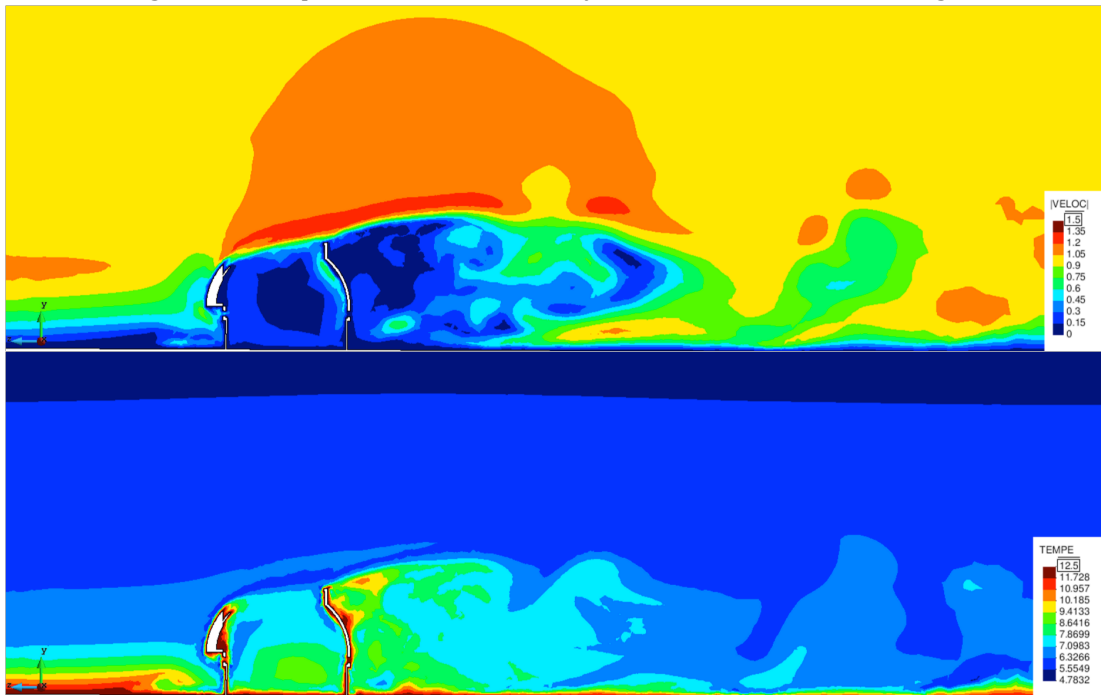


Figure 11: Velocity and temperature fields for the flow around a telescope enclosure

1.6 Conclusions

In this work we have presented a numerical model for the estimation of atmospheric seeing in observation sites. The main feature of the proposed model is that it is based on the numerical dissipations which arise from a particular version of the Variational Multiscale Method, the Orthogonal Subgrid Scale method. The advantage of using this kind of models relies on the fact that, by decomposing the fields of interest into coarse and fine scales, they are able to deal simultaneously with the sources of numerical instabilities and the modeling of turbulent

effects. In the present work we have summarized the properties of our variational multiscale method, which is based on modeling the numerical subscales in an as complete as possible manner: the subscales are considered to be transient in time, non-linear, and orthogonal to the finite element space. This leads not only to the resolution of numerical stability issues (advection and the use of arbitrary interpolations for velocity and pressure), but also to a rich representation of turbulent phenomena. Based on this turbulence model, we have developed the expressions for the viscous and thermal dissipations, ν_{num} and χ_{num} , which have been used for evaluating the constant of structure of the refraction index C_n^2 following the classical model developed by Tatarski.

In the numerical examples section we have tested the performance of the method in three practical cases, namely a convective boundary layer, the flow inside a transfer optics room, and the flow around a telescope enclosure. In all three cases we have compared our model with the results obtained by using a Smagorinsky and WALE models for evaluating the viscous and thermal dissipations, and, in the convective boundary layer case, with the results presented in [8]. The numerical examples show that the method is capable of doing an accurate estimation of the C_n^2 coefficients. This fact does not only provide us with a new numerical tool for the

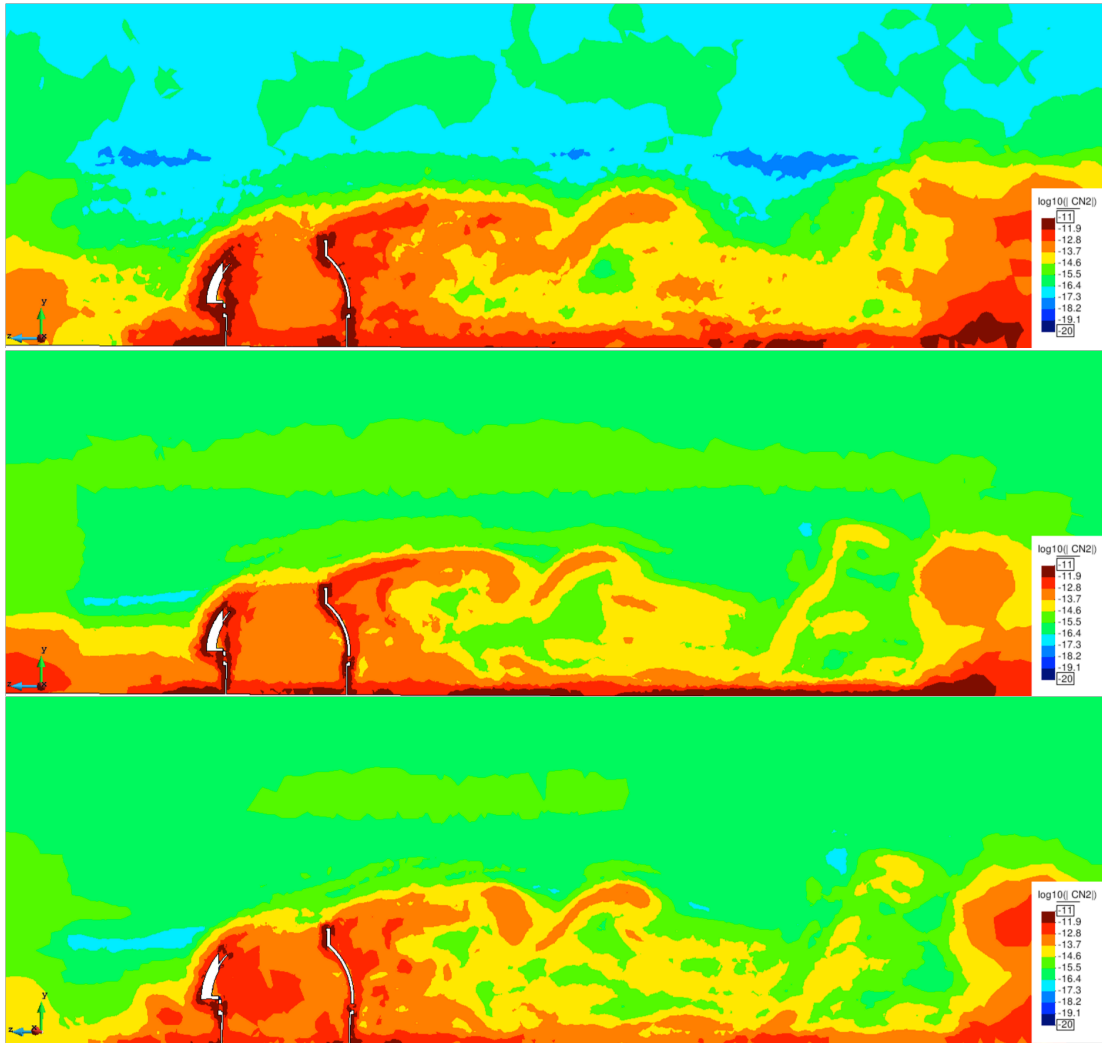


Figure 12: C_n^2 field for the flow around a telescope enclosure. From top to bottom: Variational Multiscale, Smagorinsky and WALE models.

evaluation of the atmospheric seeing but it also adds arguments in favor of the viability of implicit LES methods which rely on the numerical stabilization mechanisms for the modeling of turbulence.

References

- [1] R.J. Alliss and B.D. Felton. Validation of optical turbulence simulations from a numerical weather prediction model in support of adaptive optics design. In *Advanced Maui Optical and Space Surveillance Technologies Conference*, volume 1, page 54, 2009.
- [2] J.M. Beckers. *Adaptive optics for astronomy: Principles, Performance and Applications*. Annual Reviews in Astronomy and Astrophysics, 1993.
- [3] FCM Bettonvil, R Codina, RH Hammerschlag, APL J'agers, JNM Kommers, SJ Van Leverink, G Sliepen, and S Visser. The enclosure for the European Solar Telescope (EST). In *SPIE Astronomical Telescopes and Instrumentation: Observational Frontiers of Astronomy for the New Decade*, pages 773333–773333. International Society for Optics and Photonics, 2010.
- [4] Peter Bradshaw and George P Huang. The law of the wall in turbulent flow. *Proceedings of the Royal Society of London. Series A: Mathematical and Physical Sciences*, 451(1941):165–188, 1995.
- [5] L Cavaller, M Collados, and J Castro. Performance simulations for the conceptual design of the European Solar Telescope (EST). In *Proc. of SPIE Vol*, volume 8336, pages 83360G–1, 2011.
- [6] S. Cheinet, A. Beljaars, K. Weiss-Wrana, and Y. Hurtaud. The use of weather forecasts to characterise near-surface optical turbulence. *Boundary-Layer Meteorology*, 138:453–473, 2011.
- [7] S. Cheinet and A. P. Siebesma. The impact of boundary layer turbulence on optical propagation. In *Optics in Atmospheric Propagation and Adaptive Systems X. Proc. of SPIE Vol. 6747*, pages 1–12, 2007.
- [8] S. Cheinet and A. P. Siebesma. Variability of local structure parameters in the convective boundary layer. *J. Atmos. Sci.*, 66:1002–1017, 2009.
- [9] T. Cherubini and S. Businger. An operational perspective for modeling optical turbulence, in *Seeing Clearly: The impact of Atmospheric Turbulence on the Propagation of Extraterrestrial Radiation*, T. Cherubini and S. Businger (Eds.). VBW Publishing, 2010.
- [10] T. Cherubini, S. Businger, and R. Lyman. Modeling optical turbulence and seeing over Mauna Kea: Verification and algorithm refinement. *J. Appl. Meteor. Climatol.*, 47:3033–3043, 2008.
- [11] R. Codina. A stabilized finite element method for generalized stationary incompressible flows. *Computer Methods in Applied Mechanics and Engineering*, 190:2681–2706, 2001.
- [12] R. Codina. Stabilized finite element approximation of transient incompressible flows using orthogonal subscales. *Computer Methods in Applied Mechanics and Engineering*, 191:4295–4321, 2002.
- [13] R. Codina, J. Baiges, D. P'erez-S'anchez, and M. Collados. A numerical strategy to compute optical parameters in turbulent flow: Application to telescopes. *Computers & Fluids*, 39(1):87 – 98, 2010.
- [14] R. Codina and J. Principe. Dynamic subscales in the finite element approximation of thermally coupled incompressible flows. *International Journal for Numerical Methods in Fluids*, 54:707–730, 2007.

- [15] R. Codina, J. Principe, and M. Avila. Finite element approximation of turbulent thermally coupled incompressible flows with numerical sub-grid scale modelling. *International Journal of Numerical Methods for Heat & Fluid Flow*, 20(5):492–516, 2010.
- [16] R. Codina, J. Principe, and S. Badia. Dissipative structure and long term behavior of a finite element approximation of incompressible flows with numerical subgrid scale modeling. In *Multiscale Methods in Computational Mechanics*, pages 75–93. Springer, 2011.
- [17] R. Codina, J. Principe, and J. Baiges. Subscales on the element boundaries in the variational twoscale finite element method. *Computer Methods in Applied Mechanics and Engineering*, 198:838– 852, 2009.
- [18] R. Codina, J. Principe, O. Guasch, and S. Badia. Time dependent subscales in the stabilized finite element approximation of incompressible flow problems. *Computer Methods in Applied Mechanics and Engineering*, 196:2413–2430, 2007.
- [19] O. Colomés, S. Badia, R. Codina, and J. Principe. Assessment of variational multiscale models for the large eddy simulation of turbulent incompressible flows. *Submitted*.
- [20] A.F. de Baas and M. Sarazin. The temperature structure function for a complex terrain. *Eighth Symposium on turbulent shear flows.*, pages 1–6, Munich September 9-11, 1991.
- [21] R. Frehlich, R. Sharman, F. Vandenberghe, W. Yu, Y. Liu, J. Knievel, and G. Jumper. Estimates of Cn2 from Numerical Weather Prediction Model Output and Comparison with Thermosonde Data. *Journal of Applied Meteorology and Climatology*, 49(8):1742–1755, 2010.
- [22] C. Giordano, J. Vernin, H. Vázquez Ramió, C. Muñoz-Tunón, AM Varela, and H. Trinquet. Atmospheric and seeing forecast: Wrf model validation with in situ measurements at orm. *Monthly Notices of the Royal Astronomical Society*, 430(4):3102–3111, 2013.
- [23] V. Gravemeier. The variational multiscale method for laminar and turbulent flow. *Archives of Computational Mechanics—State of the Art Reviews*, 13:249–324, 2006.
- [24] O. Guasch and R. Codina. Statistical behavior of the orthogonal subgrid scale stabilization terms in the finite element large eddy simulation of turbulent flows. *Computer Methods in Applied Mechanics and Engineering*, 261:154–166, 2013.
- [25] R.J. Hill. Structure functions and spectra of scalar quantities in the inertial-convective and viscousconvective ranges of turbulence. *Journal of the atmospheric sciences*, 46:2245–2251, 1989.
- [26] T.J.R. Hughes, G.R. Feijóo, L. Mazzei, and J.B. Quincy. The variational multiscale method—a paradigm for computational mechanics. *Computer Methods in Applied Mechanics and Engineering*, 166:3–24, 1998.
- [27] T.J.R. Hughes, L. Mazzei, and K.E. Jansen. Large eddy simulation and the variational multiscale method. *Computing and Visualization in Science*, 3:47–59, 2000.
- [28] S.L. Keil, T.R. Rimmele, and J. Wagner. Advanced technology solar telescope. *Earth, Moon, and Planets*, 104(1-4):77–82, 2009.
- [29] E. Masciadri, J. Vernin, and P. Bougeault. 3D mapping of optical turbulence using an atmospheric numerical model. Part I. *Astron. Astrophys. Suppl. Ser.*, 137:185–202, 1999.
- [30] E. Masciadri, J. Vernin, and P. Bougeault. 3D mapping of optical turbulence using an atmospheric numerical model. Part II. *Astron. Astrophys. Suppl. Ser.*, 137:203–216, 1999.

- [31] E. Masciadri, J. Vernin, and P. Bougeault. 3D numerical simulations of optical turbulence at the Roque de Los Muchachos Observatory using the atmospheric model Meso-Nh. *Astronomy & Astrophysics*, 365:699–708, 2001.
- [32] L.J. Peltier and J.C. Wyngaard. Structure function parameters in the convective boundary layer from large eddy simulation. *Journal of the atmospheric sciences*, 52:3641–3660, 1995.
- [33] F. Roddier. *Adaptive optics in astronomy*. Cambridge University Press, 2004.
- [34] V.I. Tatarski. *Wave propagation in a turbulent medium*. Dover Publications, INC, 1961.
- [35] H. Trinquet and J. Vernin. A statistical model to forecast the profile of the index structure constant. *Environ Fluid Mech*, 7:397–407, 2007.
- [36] L.P. Wang, S. Chen, and J.G. Brasseur. Examination of the hypothesis in the Kolmogorov refined turbulence theory through high resolution simulations. Part 2. Passive scalar fields. *Journal of Fluid Mechanics*, 400:163–197, 1999.

2 Numerical simulations at the European Solar Telescope Sites

The next step within the Solarnet project is the evaluation of the seeing degradation produced by the European Solar Telescope facilities, once obtained the temperature distributions in different moments in the day.

In order to evaluate the seeing degradation produced by telescope facilities three different configurations, under the same conditions, have been generated:

- Site without facilities (Site)
- Site with facilities without telescope structure (Facilities)
- Site with facilities and telescope structure (Telescope)

The analysis have been performed in different moments in the day, since the ambient temperature, the ground temperature and the temperature of the facilities changes along the day, hence the seeing degradation will change also.

The site models (Tenerife and La Palma) include the topography and roughness of the selected site.

2.1 Objectives

The main objective of these simulations is to analyze the seeing degradation produced by the EST facilities and summarize their main results. This analysis consists in to obtain the C_n^2 distribution for each case.

2.2 Description of the computational domains

The generation of the 3D model has been carried out taking into account that the computational domain is large enough to ensure that their boundaries are placed sufficiently far from the computational domain (Facilities/Telescope), so that they do not affect the results inside it.

Taking into account the three different configurations (Site / Facilities / Telescope); the two site models (Tenerife / La Palma) and the two building orientation (West / South) a 12 different computational domains are possible within this study.

2.3 Geometry

The three different geometries that take part within these CFD simulations are described in the following sub-sections.

Computational Domain

The computational domains (Tenerife and La Palma) include the terrain description and the boundaries of the domain. The terrain has been generated directly from the contour lines, and the telescope has been placed in its location following the indications provided by IAC (Instituto de Astrofísica de Canarias) to CIMNE.

These computational domains are rectangles, and the main dimensions of each location are summarized in the next Table.

	TENERIFE	LA PALMA
Length	2600 m	2900 m
Width	2600 m	4000 m
Height	900 m	1500 m

Telescope facilities

The geometry of the telescope facilities, that has been considered to carry out the numerical simulations, has been provided by IAC (Instituto de Astrofísica de Canarias) to CIMNE. Two different telescope facilities (building west / building south) have been created. The difference between them is only the orientation of the adjacent building. The whole dimensions remain the same for both cases.

Its main dimensions are summarized in the next Figure.

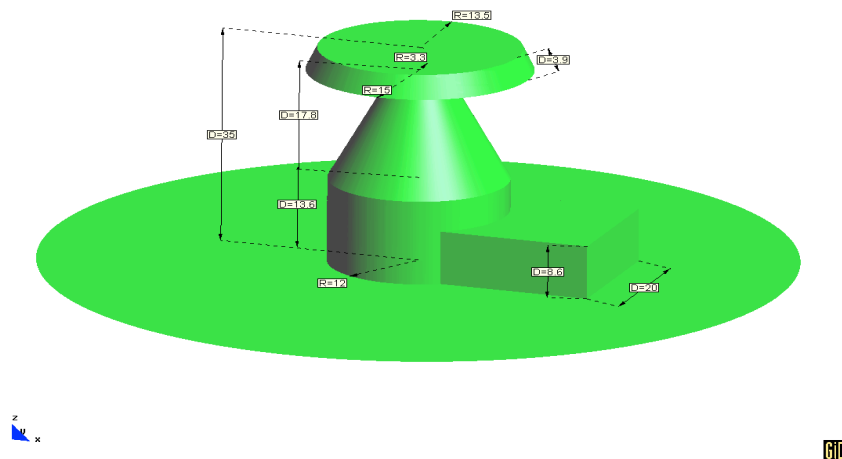
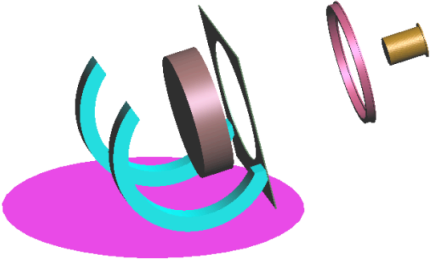
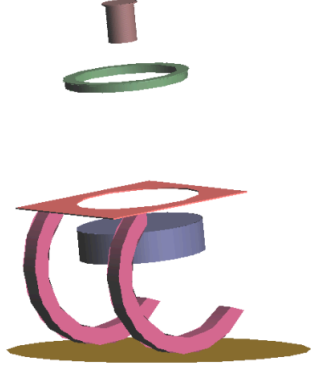
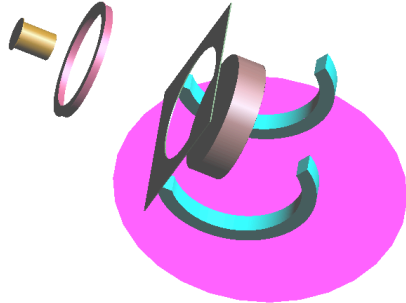


Figure 4. Telescope Facilities main dimensions

Telescope structure

The geometry of the telescope structure, that has been considered to carry out the numerical simulations, has been provided by IAC (Instituto de Astrofísica de Canarias) to CIMNE. The

main dimensions of this geometry are the same that we have shown in the previous subsection. And the three provided geometries are presented in the following figures.

 <p>A 3D CAD model showing a complex assembly. It features a cyan ring-like structure on a magenta circular base. A dark grey cylindrical component is positioned vertically through the center. To the right, a separate assembly consists of a pink ring and a small gold cylindrical pin. A coordinate system with x, y, and z axes is visible in the bottom-left corner. A small red 'GID' logo is in the bottom-right corner.</p>	<p>Case 18 and Case 19</p>
 <p>A 3D CAD model showing a complex assembly. It features a blue cylindrical component on a dark blue base. Two pink curved components are positioned around the base. Above the assembly, a green ring and a small brown cylindrical pin are shown. A coordinate system with x, y, and z axes is visible in the bottom-left corner. A small red 'GID' logo is in the bottom-right corner.</p>	<p>Case 20</p>
 <p>A 3D CAD model showing a complex assembly. It features a cyan ring-like structure on a magenta circular base. A dark grey cylindrical component is positioned vertically through the center. To the left, a separate assembly consists of a pink ring and a small gold cylindrical pin. A coordinate system with x, y, and z axes is visible in the bottom-left corner. A small red 'GID' logo is in the bottom-right corner.</p>	<p>Case 21</p>

2.4 Boundary conditions

Over the different computational domains several velocity and temperature conditions have been applied.

The temperatures of the facilities have been obtained for winter and summer conditions and for two different wind speeds (5m/s, 2m/s) and one wind direction (North). In order to perform an exhaustive analysis it would be necessary to analyze the 3 proposed configurations for the two proposed sites (Tenerife and La Palma), for winter and summer conditions, for 3 moments during the day.

An example of the temperature maps, provided by IAC, obtained using NASTRAN is shown in the next figure. These temperature boundary conditions are interpolated to the generated mesh as temperature boundary conditions.

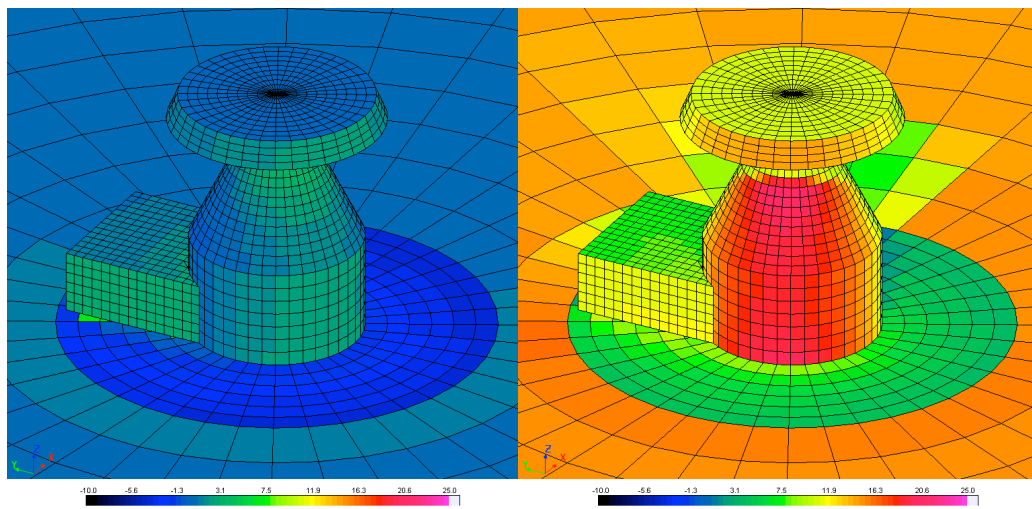


Figure 5. Examples of temperature maps at Sunrise (left) and Noon (right). South view.

Another example of temperature maps, but now in the figure the NASTRAN results and its interpolation over the CFD mesh that was used to the calculations are shown.

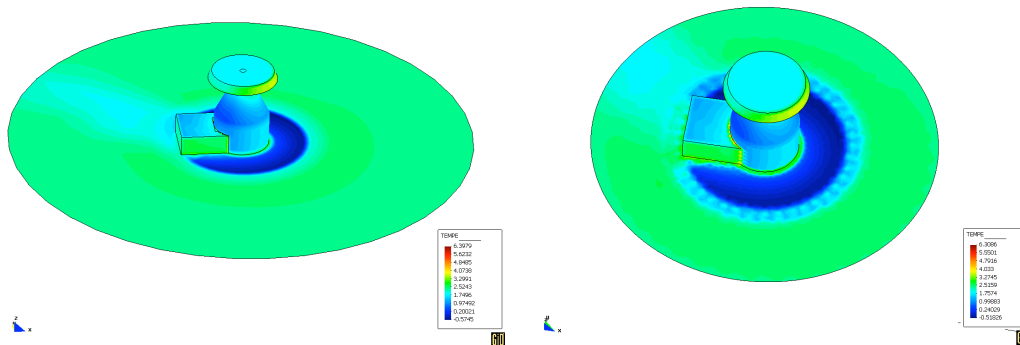


Figure 6. Example of temperature maps of NASTRAN (left) and its interpolation into GiD (right). South view.

2.5 Physical properties

The fluid used into the simulations is air at the temperature prescribed for each case (see Boundary Conditions Table in section *CFD Simulation*). The physical properties used are:

PHYSICAL PROPERTY	AIR TEMPERATURE			
	24.3 °C	21.1 °C	15.7 °C	3.9 °C
Density (kg/m ³)	1.1873	1.2002	1.2227	1.2750
Dynamic viscosity (kg/m·s)	1.8410E-5	1.8258E-5	1.7998E-5	1.7424E-5
Specific Heat (J/kg·K)	1.0062E+3	1.0061E+3	1.0060E+3	1.0057E+3
Conductivity (W/m·K)	0.025917	0.025678	0.025272	0.024374

2.6 CFD simulation

In the following sub-sections we provide an overview of the main results of the CFD simulations for all the cases defined. The represented results are the following:

- Pressure distribution (N/m²)
- Kinetic Energy field
- Velocity field (m/s)
- Velocity vectors distribution (m/s)

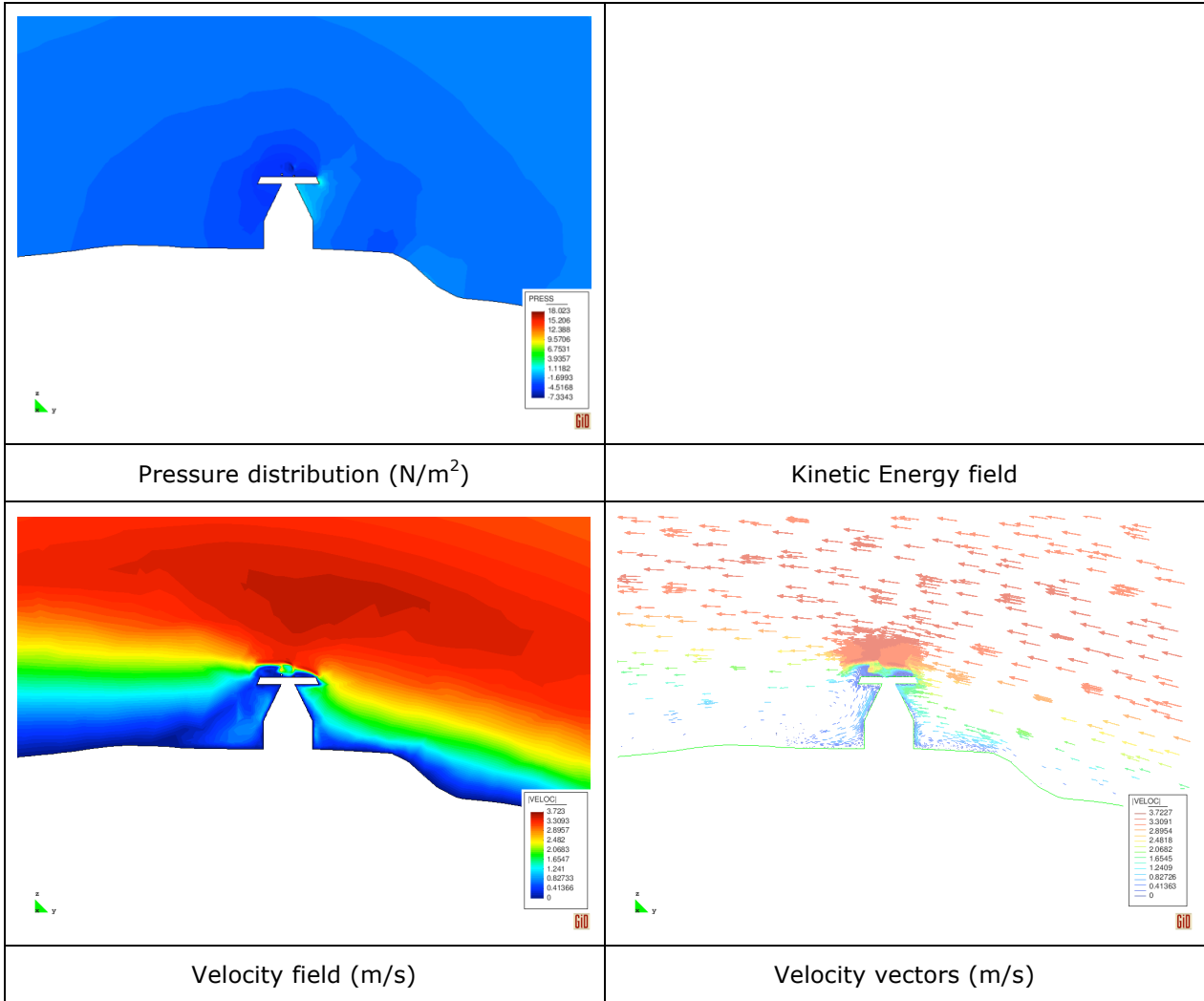
A part from these results, the analysis consists in to obtain the Cn² distribution for each case and from this distribution to obtain the seeing degradation along 100m (TBC) of the primary mirror light beam in terms of θ_{FWHM} (arcsec) . The light beam is oriented in azimuth and elevation in each case according the moment of the day which is analysed. In the cases without telescope, the position of the primary mirror is assumed 5m above the telescope platform (40m above the ground level

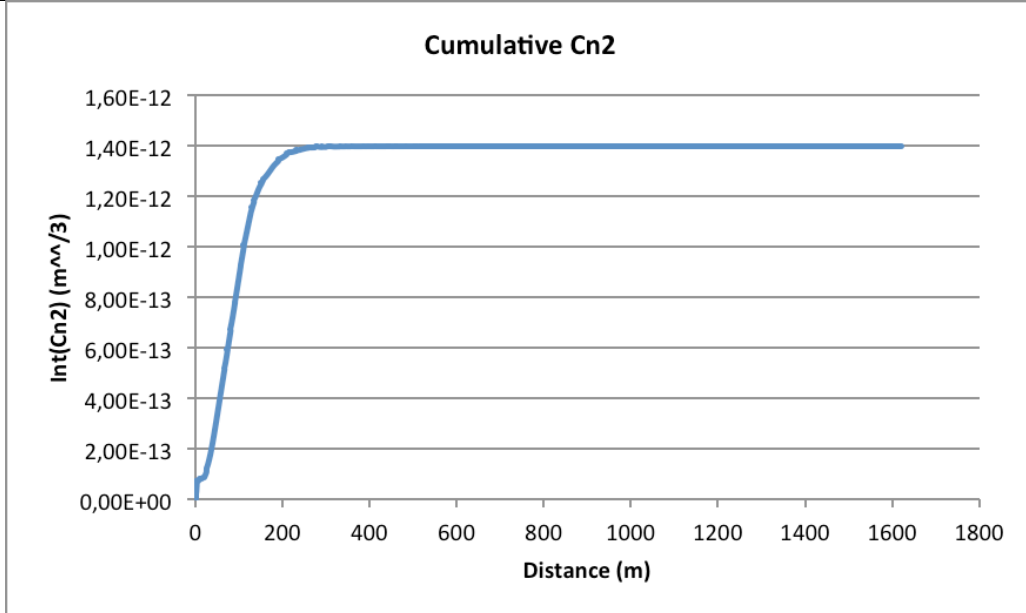
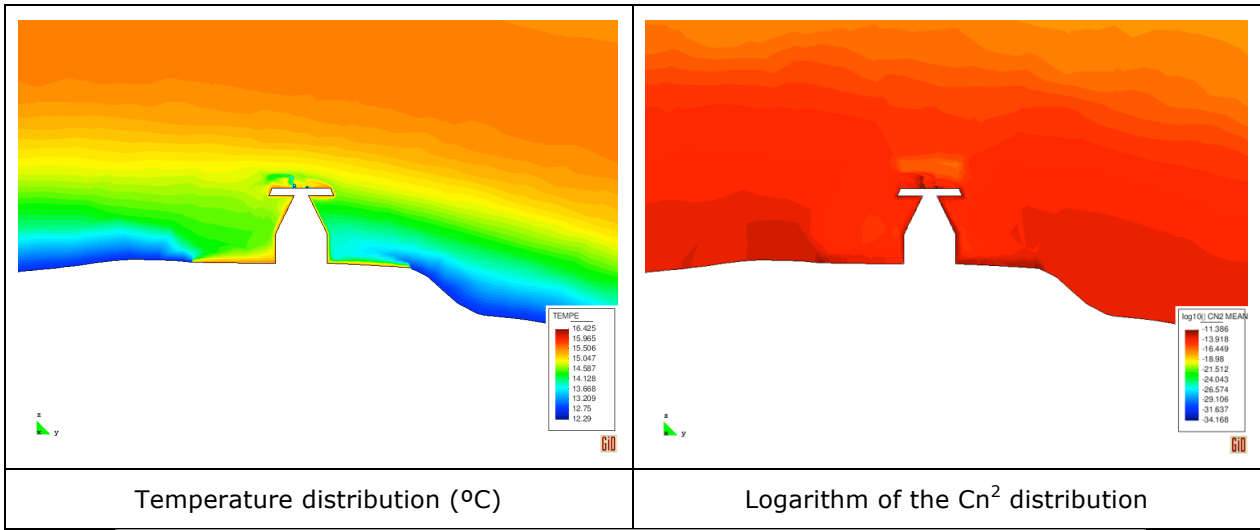
2.7 Summary of the calculated cases

Some numerical results of the cases described are presented in the following pictures. They have all been computed with an in-house CFD code in which the formulation presented in Part 1 of this report has been implemented.

Case 18

Results over vertical section

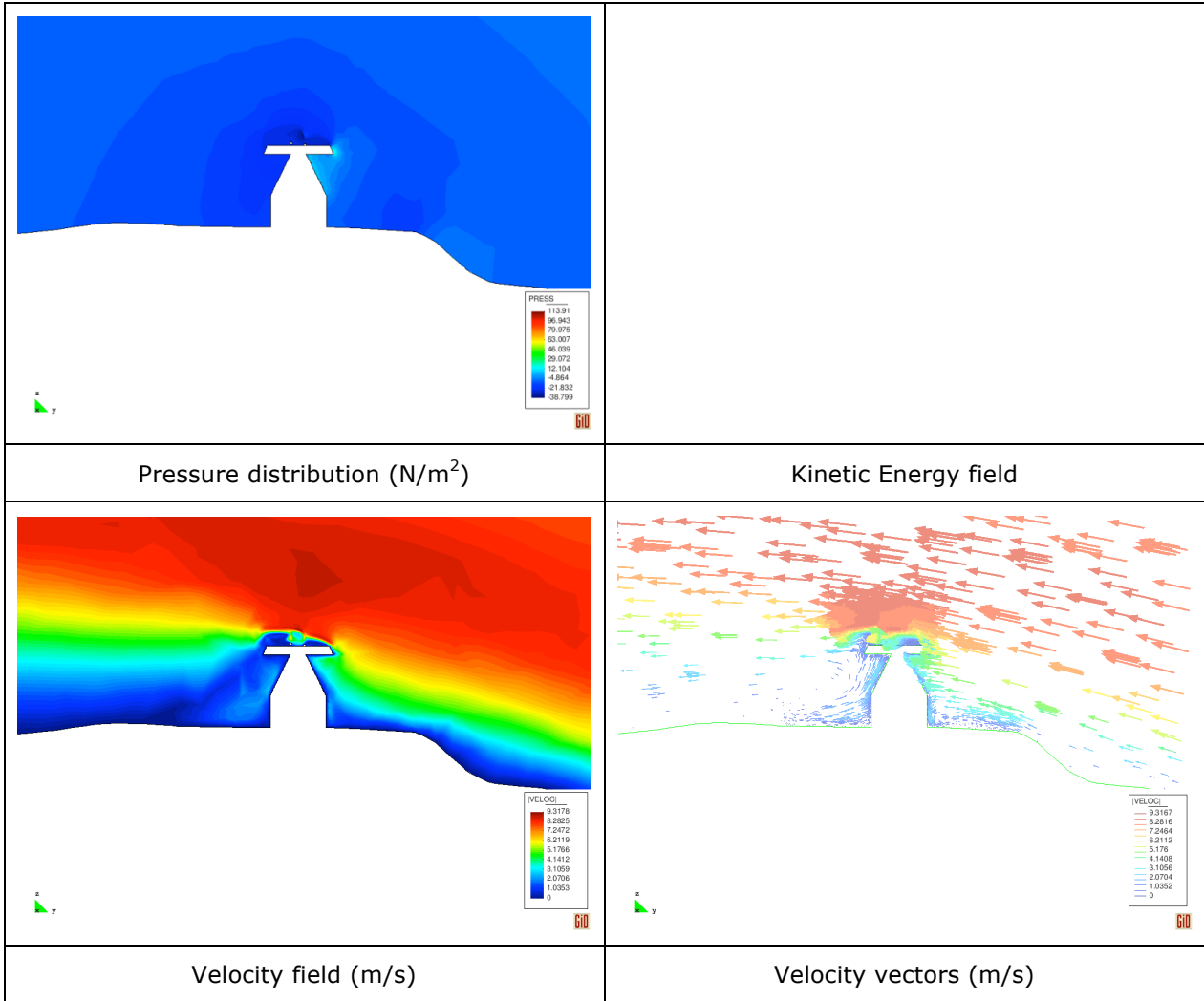


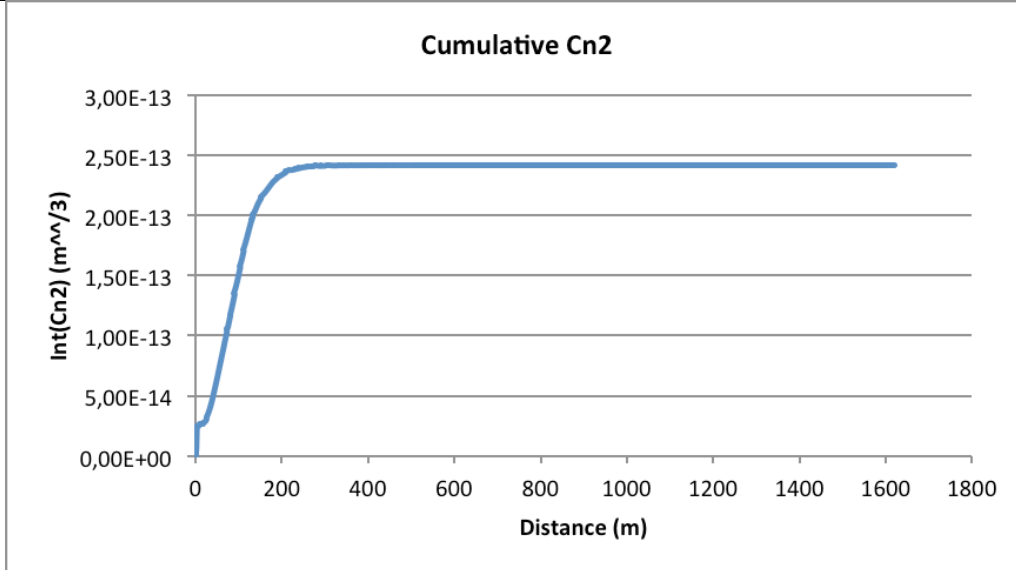
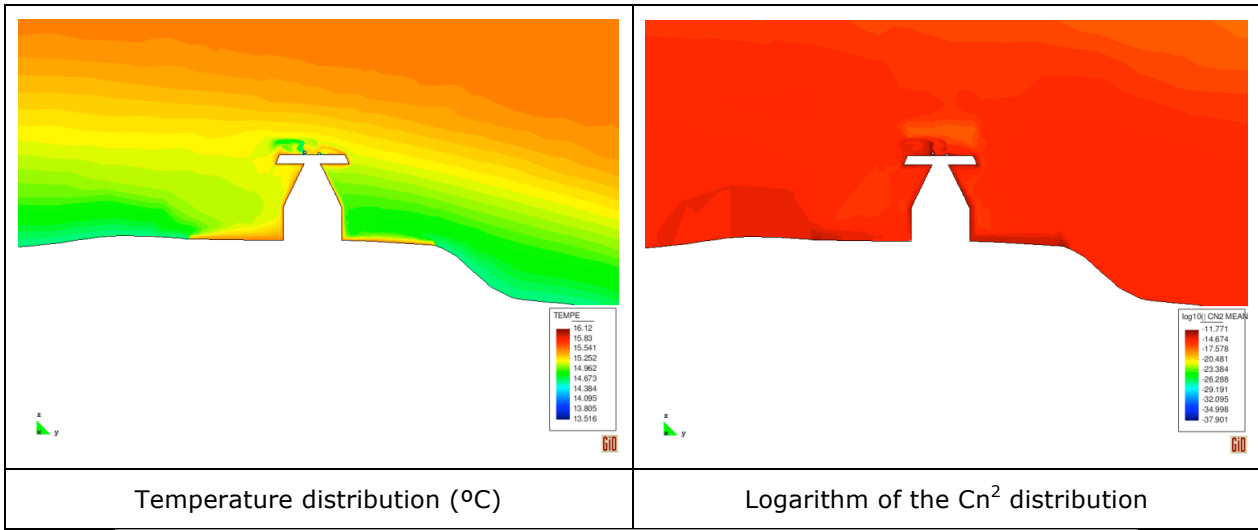


The integral of the Cn₂ coefficient in the computational domain is around 1.42e-12. According to Barnetti et al., the integral of the Cn₂ coefficient in the region which goes from a 3 km height to the outer atmosphere is 2.8e-13. The total integral of the Cn₂ coefficient along the light beam is the sum of both integrals, which is around 1.7e-12.

Case 19

Results over vertical section

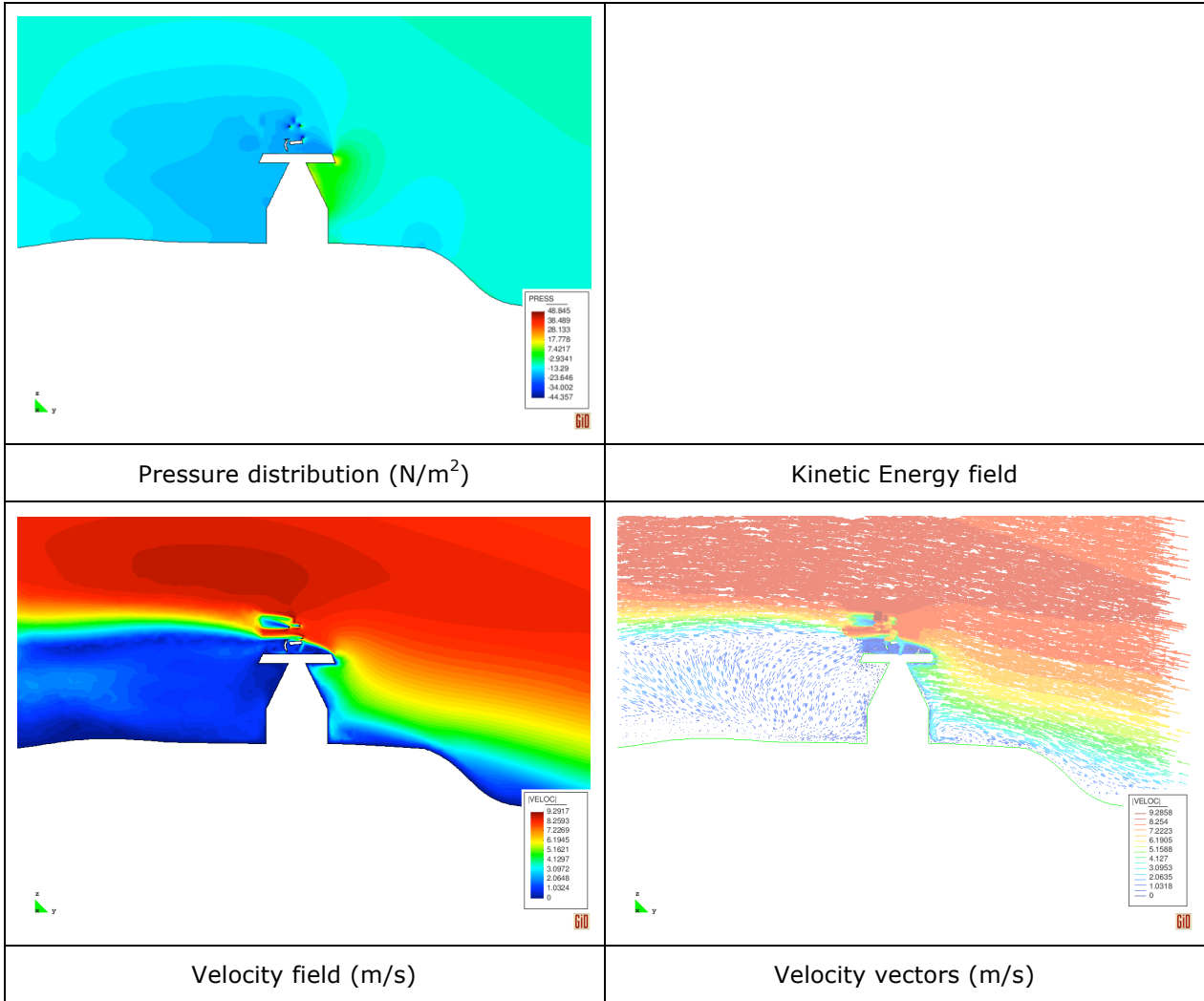


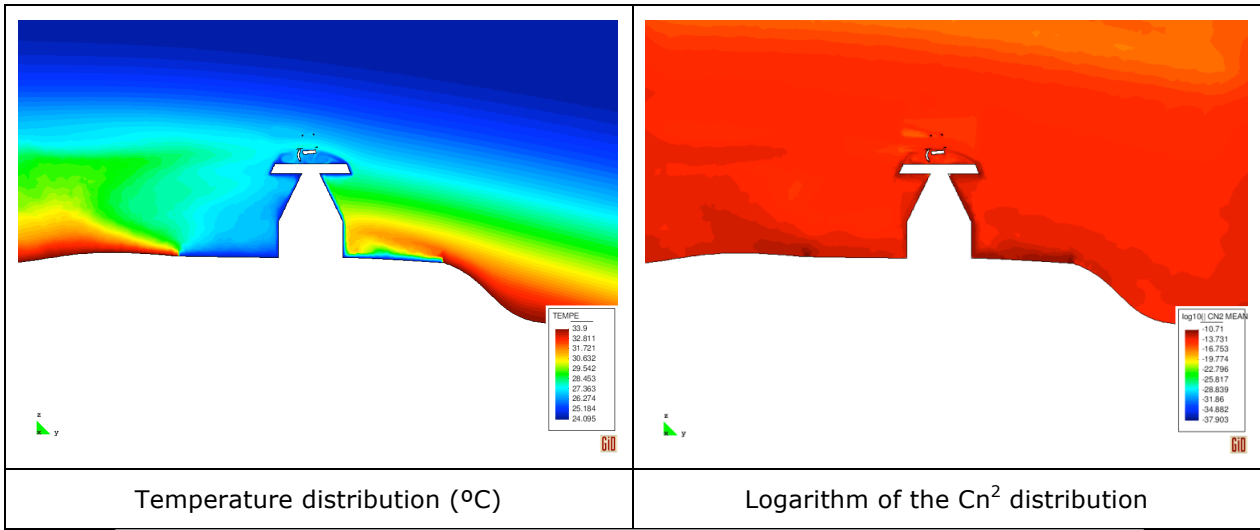


The integral of the Cn² coefficient in the computational domain is around 2.33e-13. According to Barnetti et al., the integral of the Cn² coefficient in the region which goes from a 3 km height to the outer atmosphere is 2.8e-13. The total integral of the Cn² coefficient along the light beam is the sum of both integrals, which is around 5.13e-13.

Case 20

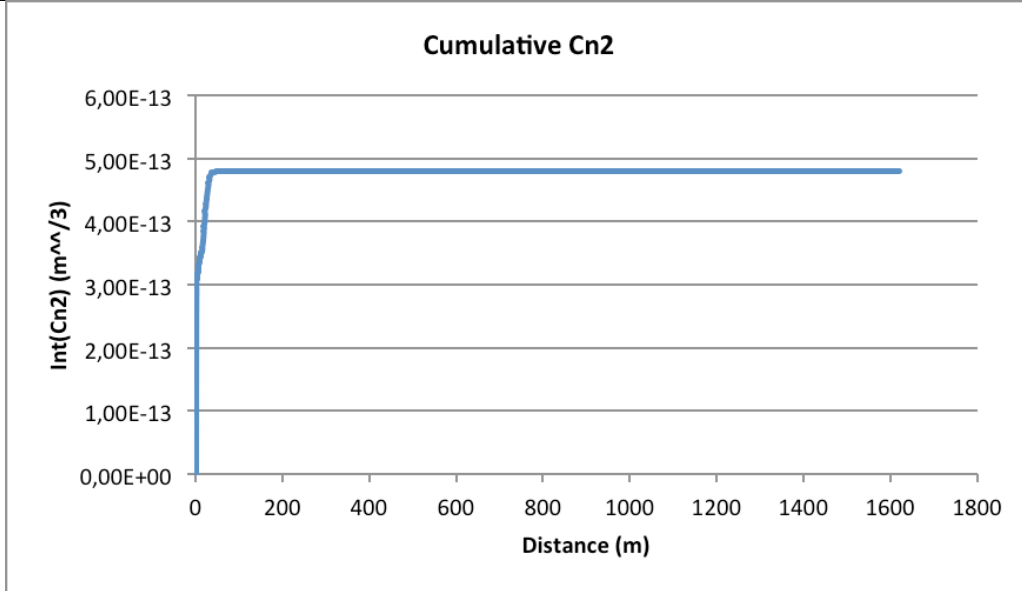
Results over vertical section





Temperature distribution (°C)

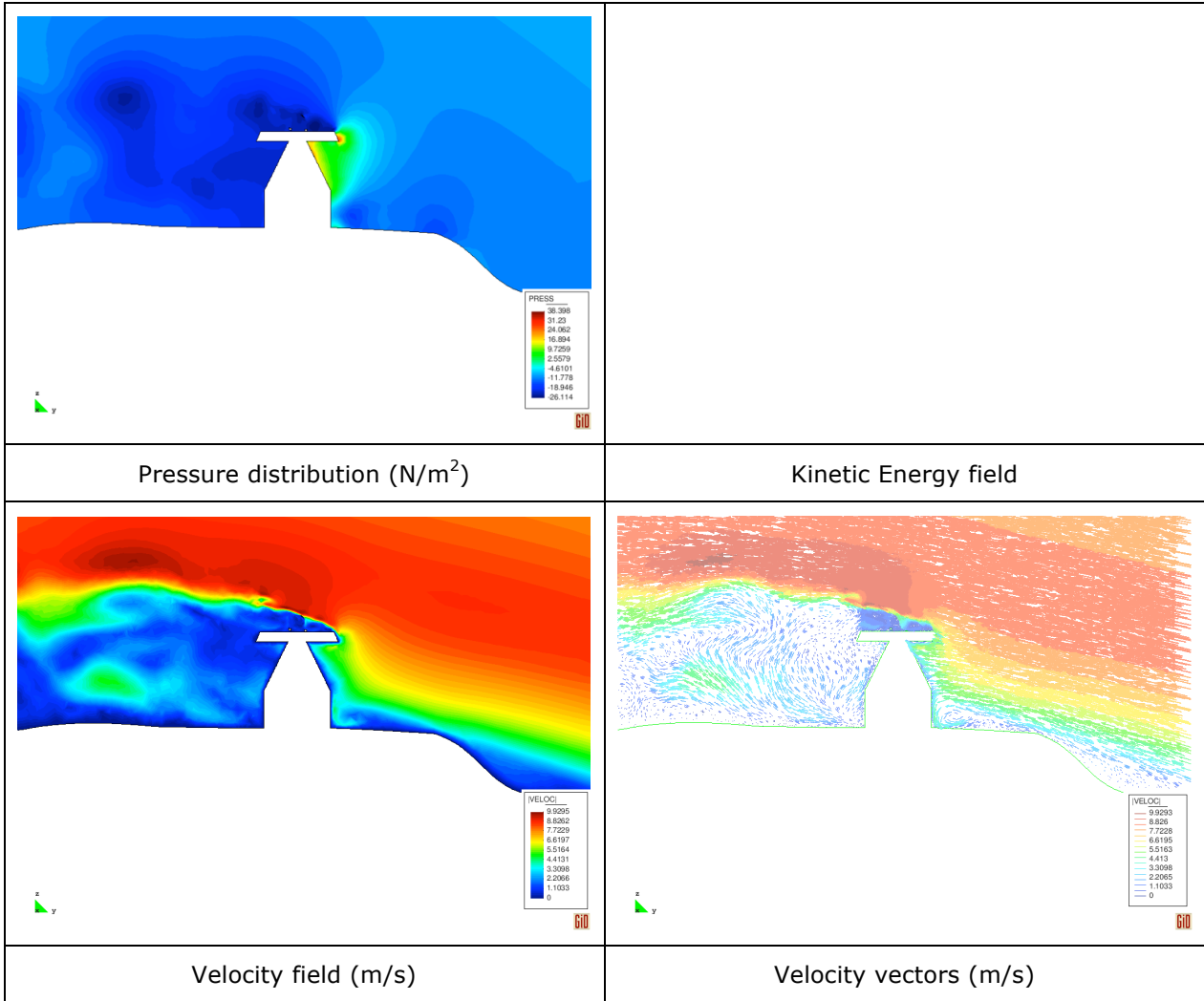
Logarithm of the Cn² distribution

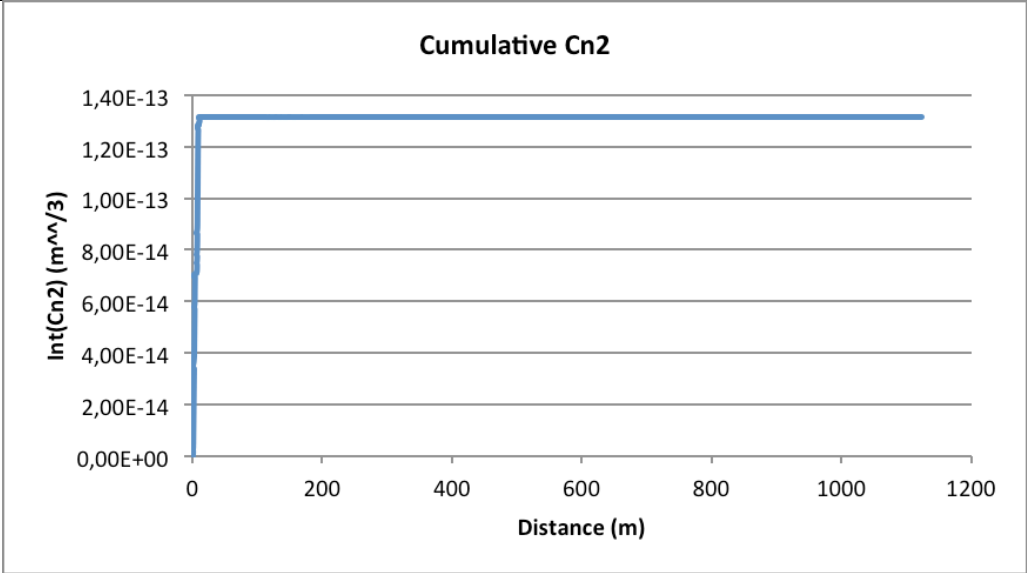
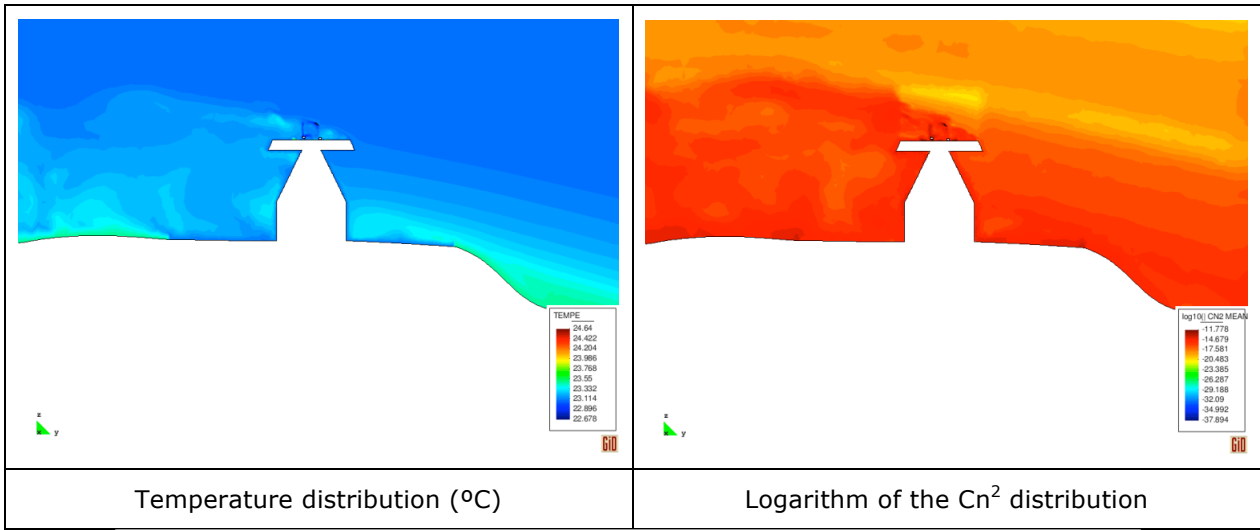


The integral of the Cn₂ coefficient in the computational domain is around 4.81e-13. According to Barnetti et al., the integral of the Cn₂ coefficient in the region which goes from a 3 km height to the outer atmosphere is 2.8e-13. The total integral of the Cn₂ coefficient along the light beam is the sum of both integrals, which is around 7.61e-13.

Case 21

Results over vertical section

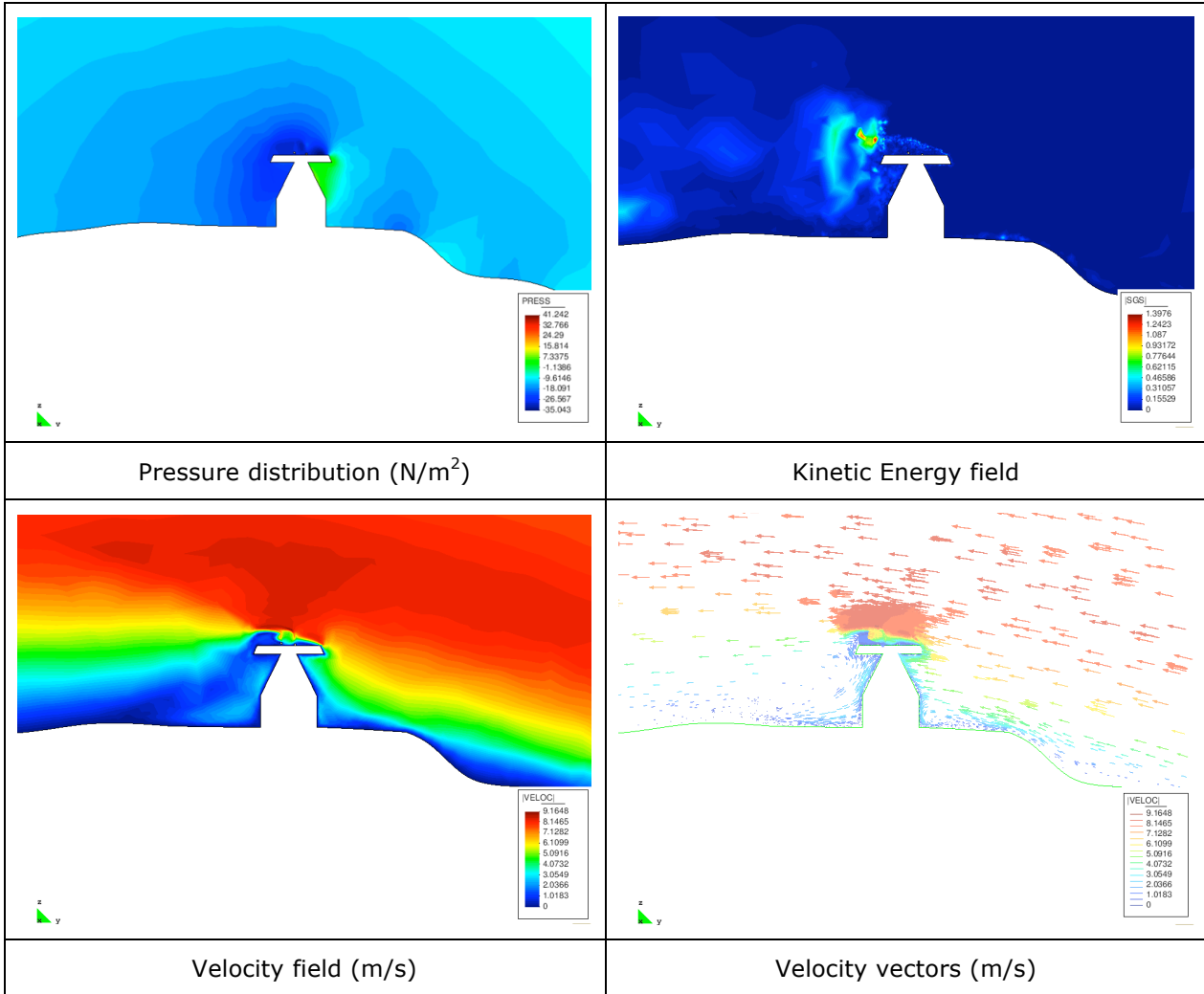


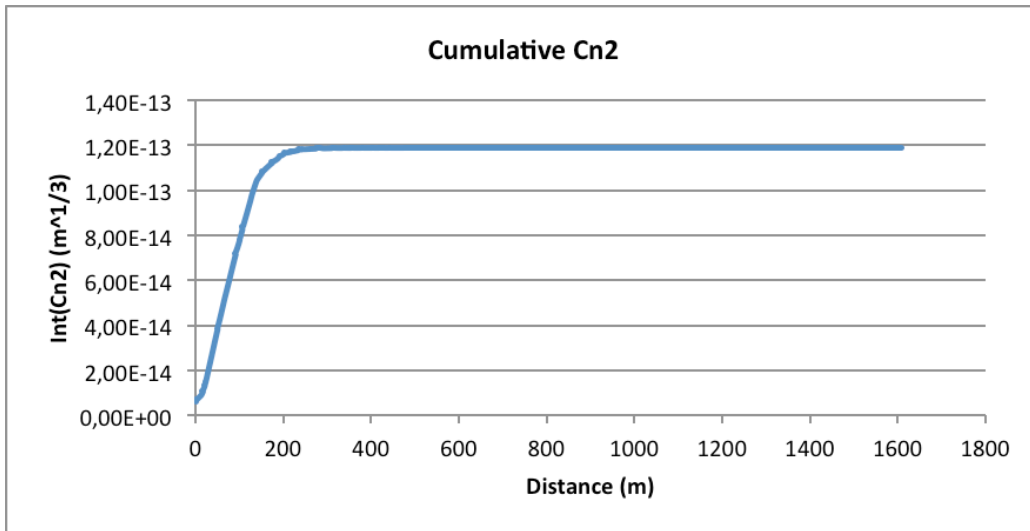
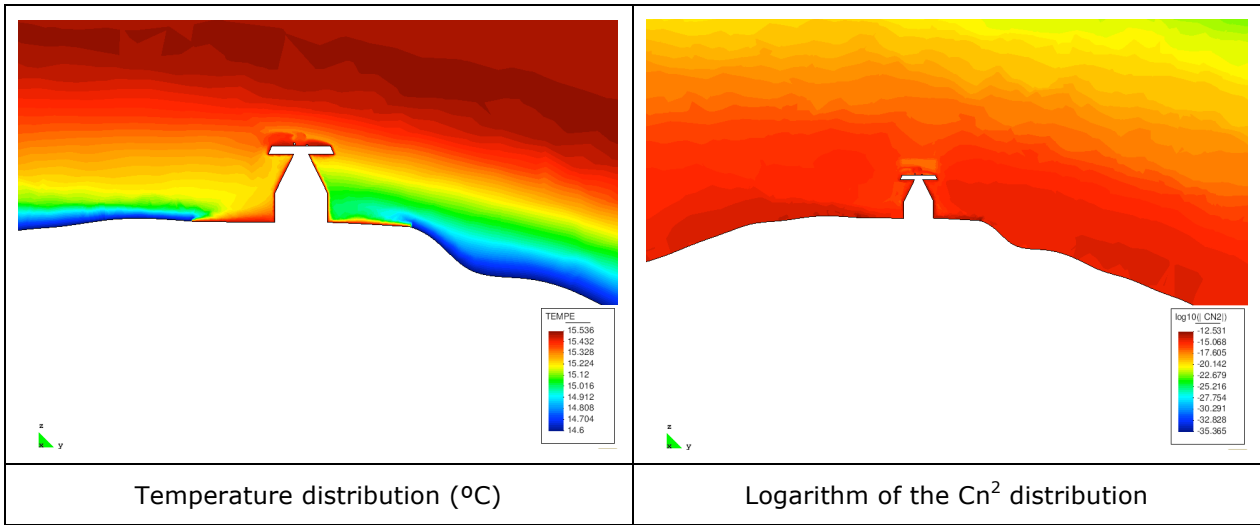


The integral of the Cn2 coefficient in the computational domain is around 1.27e-13. According to Barnetti et al, the integral of the Cn2 coefficient in the region which goes from a 3 km height to the outer atmosphere is 2.8e-13. The total integral of the Cn2 coefficient along the light beam is the sum of both integrals, which is around 4.07e-13.

Case 24

Results over vertical section

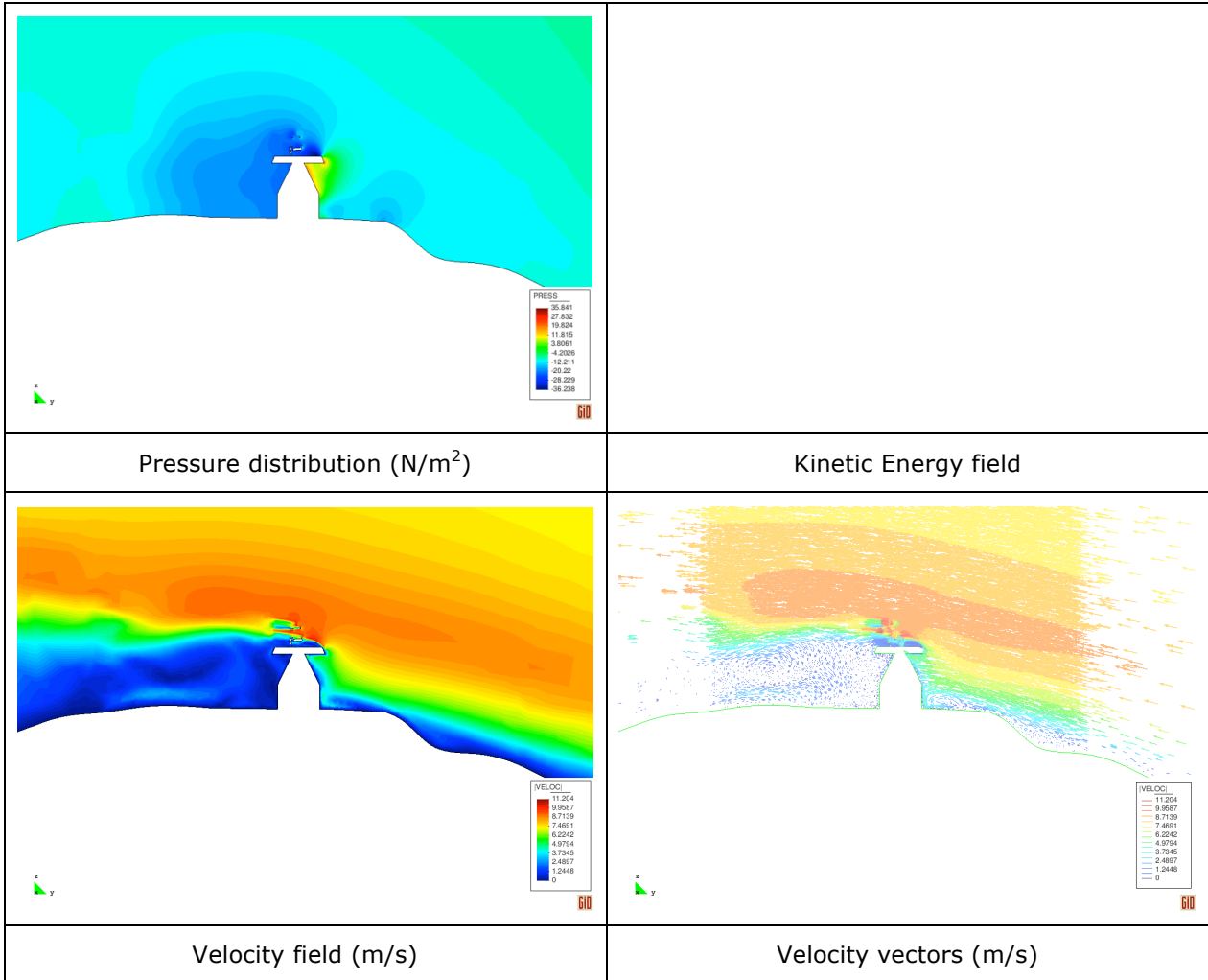


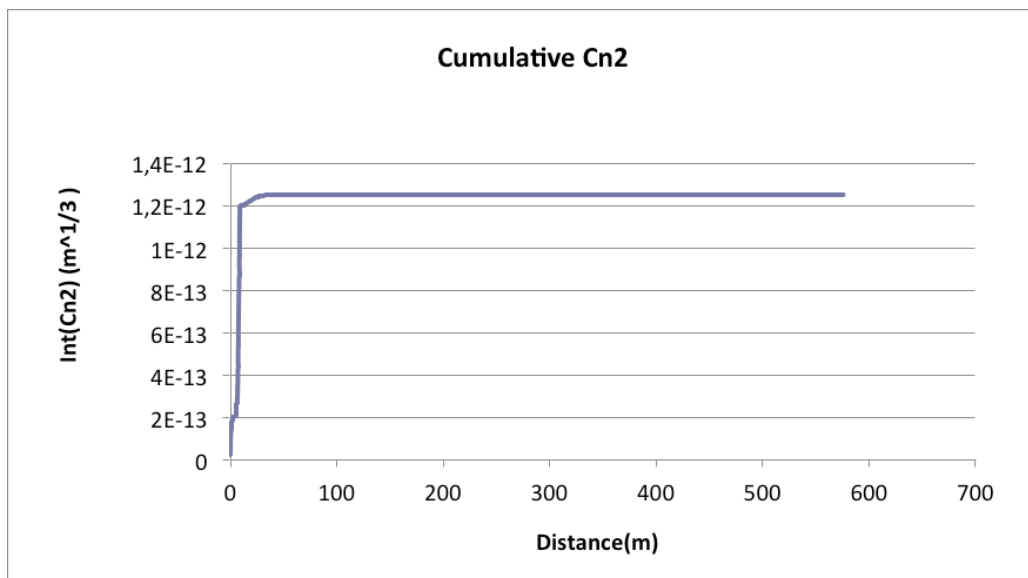
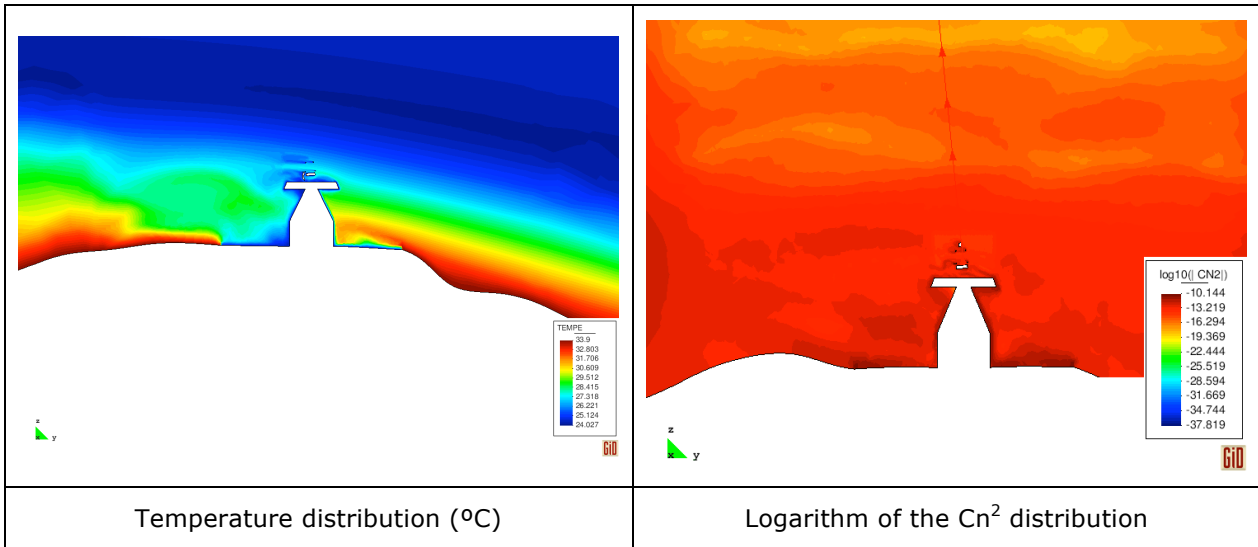


The integral of the Cn2 coefficient in the computational domain is around 1.2e-13. According to Barnetti et al., the integral of the Cn2 coefficient in the region which goes from a 3 km height to the outer atmosphere is 2.8e-13. The total integral of the Cn2 coefficient along the light beam is the sum of both integrals, which is around 4.0e-13.

Case 25

Results over vertical section

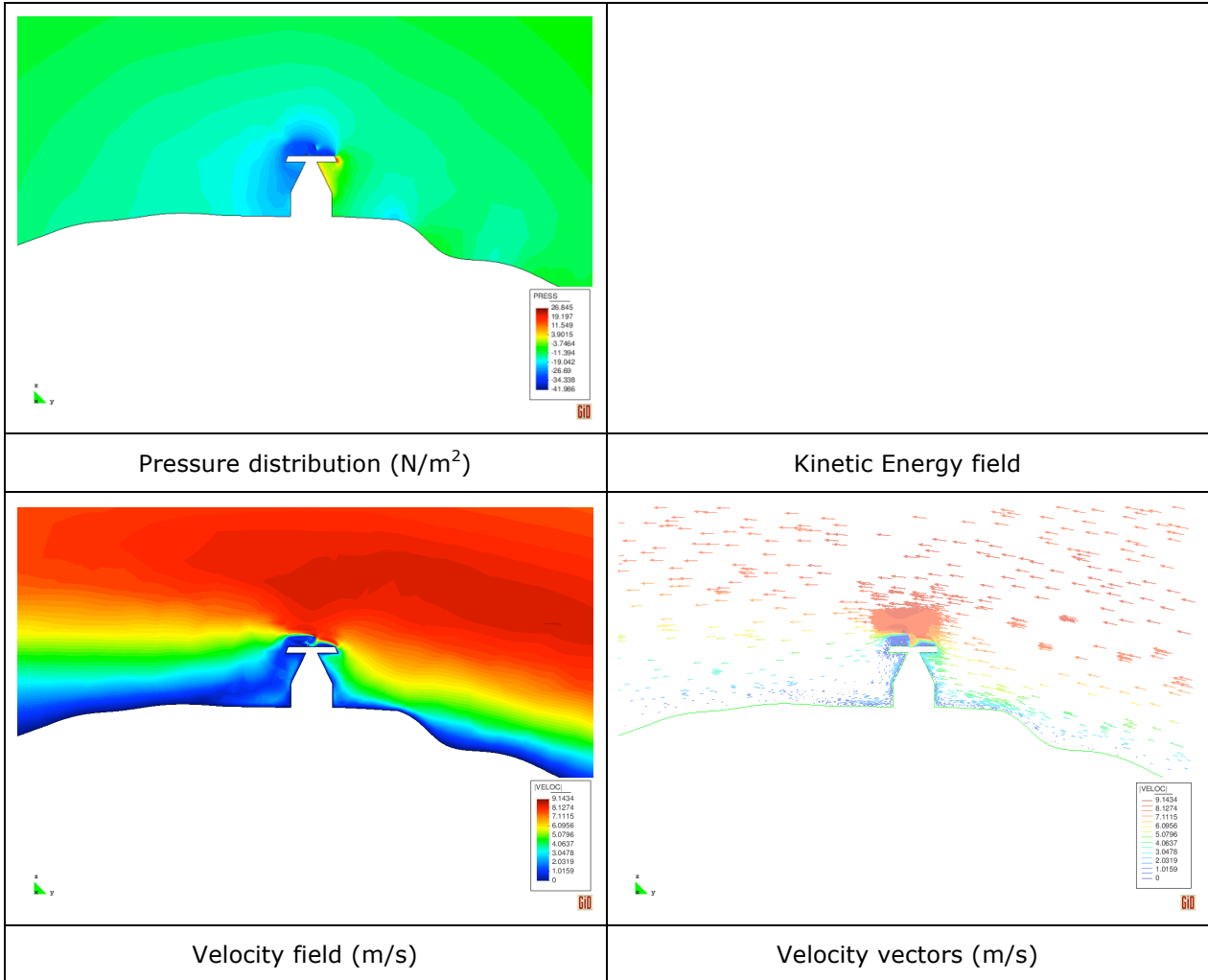


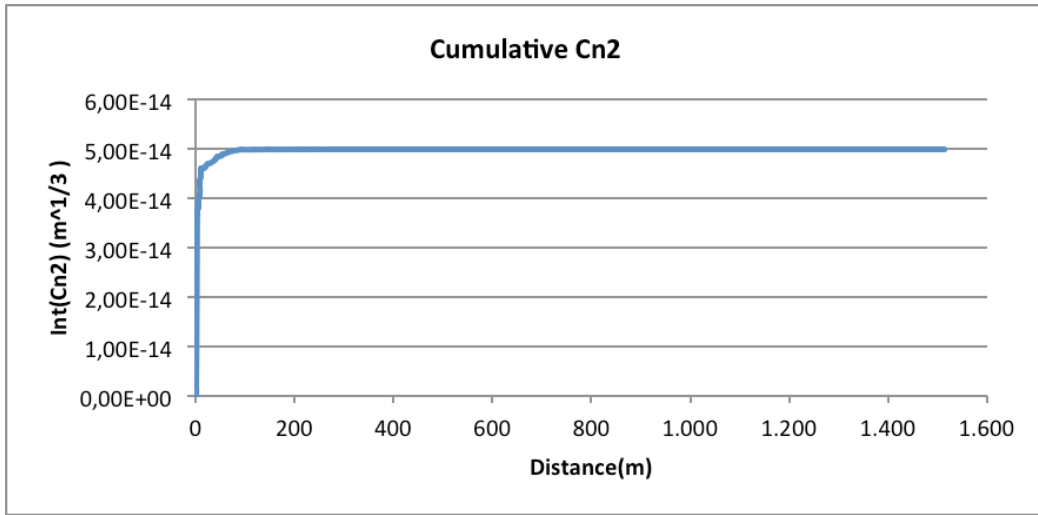
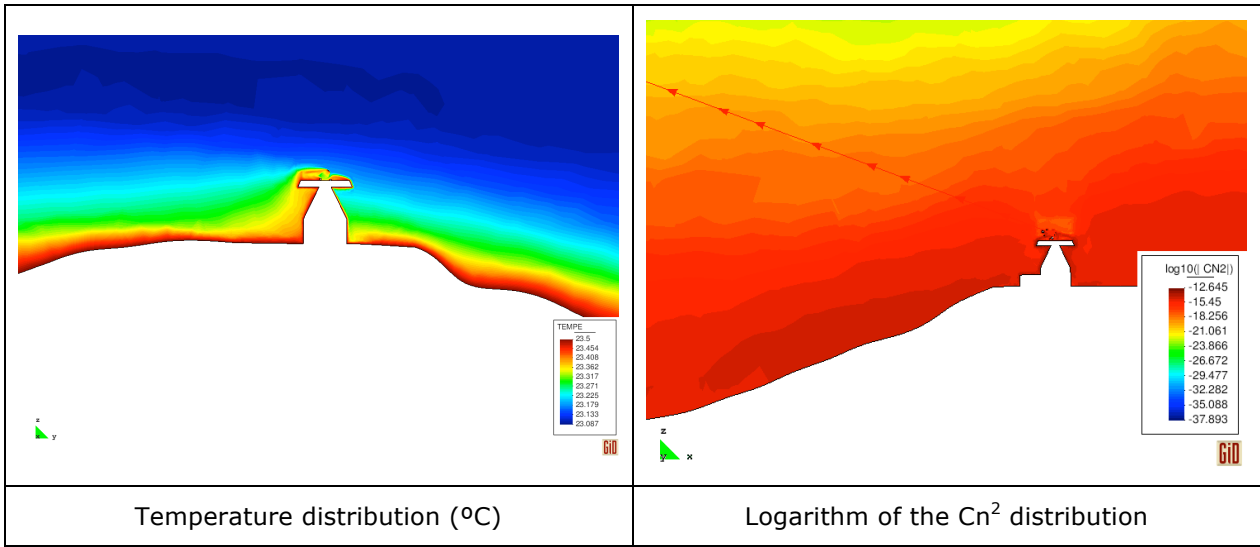


The integral of the C_n^2 coefficient in the computational domain is around $1.36e-12$. According to Barnetti et al., the integral of the C_n^2 coefficient in the region which goes from a 3 km height to the outer atmosphere is $2.8e-13$. The total integral of the C_n^2 coefficient along the light beam is the sum of both integrals, which is around $1.64e-12$.

Case 26

Results over vertical section





The integral of the Cn2 coefficient in the computational domain is around 4.78e-14. According to Barnetti et al., the integral of the Cn2 coefficient in the region which goes from a 3 km height to the outer atmosphere is 2.8e-13. The total integral of the Cn2 coefficient along the light beam is the sum of both integrals, which is around 3.28e-13.

2.8 Main calculated seeing parameters

In the following table we summarize the computed seeing parameters (Fried parameter r_0 , Greenwood frequency f_g , FWHM).

Case	R_0 (m) $\lambda = 500$ nm	FWHM(arcsec)	f_g (Hz)
18	0.059	1.72	24.49
19	0.120	0.84	29.04
20	0.095	1.06	23.21
21	0.138	0.73	17.91
22	--	--	--
23	--	--	--
24	0.139	0.72	24.84
25	0.060	1.68	42.07
26	0.158	0.64	15.32

3 Numerical ingredients for the imposition of boundary conditions in atmospheric seeing simulations

IAC has provided CIMNE with 3D surface meshes of the telescope building and the surrounding topography, as well as the corresponding temperature boundary conditions of the structure. However, the in-house multiphysics code FEMUSS is not able to load such meshes and requires volume meshes for 3D computations. Therefore, a conversion of this mesh into a volume 3D mesh has been performed with the GiD preprocessor. Moreover, an interpolator between meshes has been developed by CIMNE in order to guarantee the proper transmission of the temperature boundary conditions from the original mesh to the final one. This tool is based on a search octree which links each coordinate of the new mesh with a box of elements or nodes of the old one. Another subroutine brings the coordinate into the isoparametric space and checks to which element it belongs. Since the data format and the numbering provided by IAC are not compatible with the GiD preprocessor, the interpolator, which was originally based on a pure nodal interpolation, had to be modified into a coordinate-based least-squares interpolation or a closest point projection. This interpolator can project results between different kinds of elements, including high-order. The following figures show the transmission of temperature boundary conditions performed by the interpolator.

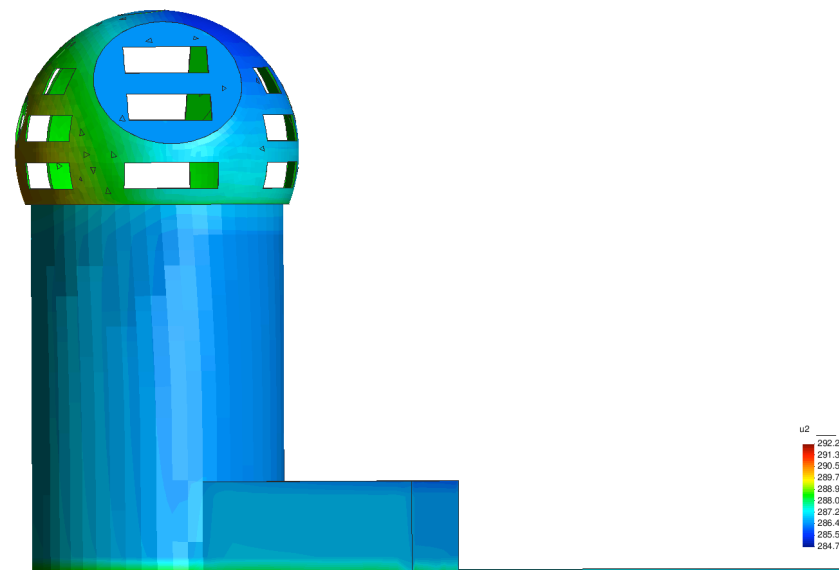


Fig. 1. Temperature boundary conditions in a 3D surface mesh ($^{\circ}\text{K}$).

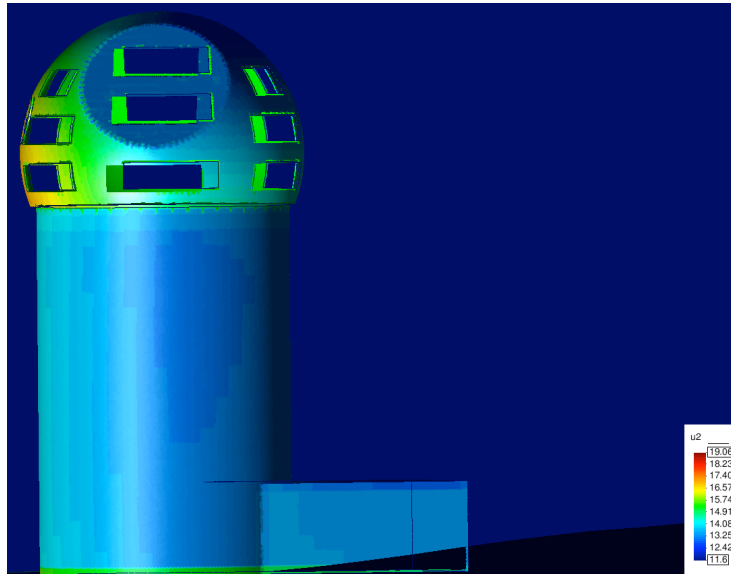


Fig. 2. Interpolated temperature boundary conditions in a 3D volume mesh using closest point projection (°C).



IAC TECHNOLOGY DIVISION

DM/TN-SNT/011v.1

DMTNSNT_011V1

October 14, 2014

Project Ref.: 312495

PROJECT / DESTINATION:

SOLARNET

TITLE:

**EST TELESCOPE ENVIRONMENT PRELIMINARY THERMAL
ANALYSIS II**

INSTITUTO DE ASTROFISICA DE CANARIAS

38200 La Laguna (Tenerife) - ESPAÑA - Phone (922)605200 - Fax (922)605210

EST TELESCOPE ENVIRONMENT PRELIMINARY THERMAL ANALYSIS II	Page: 2 of 54 Date: November 13, 2014
Code: DM/TN-SNT/011v.1	File: DELIVERABLE70_4B.DOCX

AUTHOR LIST

Name	Function
Nauzet Vega Reyes	Mechanical Engineer

DOCUMENT CHANGE RECORD

Issue	Date	Change Description
01	07/10/2014	Initial Issue

APPROVAL CONTROL

Control	Name	Function
Revised by:	Lluís Cavaller	System Engineering
Approved by:	Christine Grivel	Project Manager
Authorised by:	Manuel Collados	Project Coordinator

EST TELESCOPE ENVIRONMENT PRELIMINARY THERMAL ANALYSIS II	Page: 3 of 54 Date: November 13, 2014
Code: DM/TN-SNT/011v.1	File: DELIVERABLE70_4B.DOCX

SUMMARY

The aim of this document is to describe the results of the thermal analysis of the telescope environment (conventional dome, platform, pier, building, ground,...) according to RD.1, as a continuation of the analysis performed in RD.2, RD.3 and RD4, in order to evaluate the local seeing effect produced by the telescope facilities.

In this document are analysed different configurations for the telescope facilities with a conventional dome (Closed Configuration) and facilities with windshield (Open Configuration), in summer, for North wind of 5 m/s, in order to select the optimal configuration. The objective is to keep the temperature of the surfaces of the facility as close as possible to the ambient temperature so as to minimize the local seeing effect.

Once obtained the temperature maps for the selected configuration, CFD analysed will be performed to evaluate the local seeing degradation. CFD results obtained for these environment configurations will be compared to the previous configurations analysed.

EST TELESCOPE ENVIRONMENT PRELIMINARY THERMAL ANALYSIS II	Page: 4 of 54 Date: November 13, 2014
Code: DM/TN-SNT/011v.1	File: DELIVERABLE70_4B.DOCX

TABLE OF CONTENTS

AUTHOR LIST	2
DOCUMENT CHANGE RECORD	2
APPROVAL CONTROL	2
SUMMARY	3
TABLE OF CONTENTS	4
1. PREVIOUS ANALYSIS	5
2. ANALYSES PERFORMED	6
2.1 WEATHER CONDITIONS	9
2.2 CLOSED CONFIGURATION	11
2.2.1 <i>DOME WITHOUT THERMAL CONTROL</i>	13
2.2.2 <i>DOME WITH THERMAL CONTROL</i>	14
2.2.3 <i>DOME - HEAT STOP</i>	16
2.3 OPEN CONFIGURATION WITH WINDSHIELD	19
3. RESULTS	23
3.1 RESULTS SUMMARY	23
3.2 TEMPERATURE MAPS	25
3.3 RESULTS ANALYSIS	33
3.3.1 <i>Closed Configuration</i>	33
3.3.1.1 Dome without Thermal Control.	33
3.3.1.2 Dome with Thermal Control.	37
3.3.1.3 Dome Heat Stop.	39
3.3.2 <i>Open Configuration with Windshield</i>	44
4. CONCLUSIONS	47
5. ANNEXES	48
5.1 LIST OF REFERENCE DOCUMENTS	48
5.2 LIST OF RADTHERM FILES	49
5.3 LIST OF CFD INPUT FILES.....	54

LIST OF ABBREVIATIONS

EST	European Solar Telescope
CIMNE	Centre Internacional de Mètodes Numèrics en Enginyeria
CFD	Computational Fluid Dynamics
Cn ²	Turbulence profile
HR	Heat Rejecter
HS	Heat stop

EST TELESCOPE ENVIRONMENT PRELIMINARY THERMAL ANALYSIS II	Page: 5 of 54 Date: November 13, 2014
Code: DM/TN-SNT/011v.1	File: DELIVERABLE70_4B.DOCX

1. PREVIOUS ANALYSIS

Analyses performed at the EST conceptual design study phase are included in the table below which shows different configurations analysed under the same conditions.

- Site without facilities (Site)
- Site with facilities without telescope structure (Facilities)
- Site with facilities and telescope structure (Telescope)

The main objective of these simulations is to analyse the seeing degradation produced by the EST facilities, in different moments in the day, since the ambient temperature, the ground temperature and the temperature of the facilities changes along the day. CFD analysis consists in to obtain the C_n^2 distribution for each case once obtained the temperature maps and have been performed at CIMNE.

Case	Configuration	Site	Season	Wind	Time	Sun Orientation	Tair	T Ground
1 ✓	Site without facility	Izaña	Summer	2m/s North	Morning	72º North 15.9º Elev	15.7ºC	12.7ºC
2 ✓	Site without facility	Izaña	Summer	5m/s North	Morning	72º North 15.9º Elev	15.7ºC	14.6ºC
3 ✓	Site without facility	Izaña	Summer	5m/s North	Noon	192.3º North 84.6 Elev	24.3ºC	33.9ºC
4 ✓	Site without facility	Izaña	Summer	5m/s North	Afternoon	289º North 13.8º Elev	21.1ºC	23.5ºC
5 ✓	Site without facility	Izaña	Winter	5m/s North	Morning	125.8º North 13.7º Elev	3.9ºC	3ºC
6 CANCEL	Site without facility	ORM	Summer	5m/s North	Morning	72º North 15.9º Elev	15.7ºC	14.6ºC
7 ✓	Facility build. West	Izaña	Summer	2m/s North	Morning	72º North 15.9º Elev	15.7ºC	12.7ºC
8 ✓	Facility build. West	Izaña	Summer	5m/s North	Morning	72º North 15.9º Elev	15.7ºC	14.6ºC
9 ✓	Facility build. West	Izaña	Summer	5m/s North	Noon	192.3º North 84.6 Elev	24.3ºC	33.9ºC
10 ✓	Facility build. West Steel Platf.	Izaña	Summer	5m/s North	Afternoon	289º North 13.8º Elev	21.1ºC	23.5ºC
11 ✓	Facility build. West Concrete Platform	Izaña	Summer	5m/s North	Afternoon	289º North 13.8º Elev	21.1ºC	23.5ºC
12 ✓	Facility build. West	Izaña	Winter	5m/s North	Morning	125.8º North 13.7º Elev	3.9ºC	3ºC
13 CANCEL	Facility build. West	ORM	Summer	5m/s North	Morning	72º North 15.9º Elev	15.7ºC	14.6ºC
14 CANCEL	Facility build. South	Izaña	Summer	2m/s North	Morning	72º North 15.9º Elev	15.7ºC	12.7ºC
15 ✓	Facility build. South	Izaña	Summer	5m/s North	Morning	72º North 15.9º Elev	15.7ºC	14.6ºC
16 ✓	Facility build. South	Izaña	Summer	5m/s North	Noon	192.3º North 84.6 Elev	24.3ºC	33.9ºC
17 ✓	Facility build. South	Izaña	Summer	5m/s North	Afternoon	289º North 13.8º Elev	21.1ºC	23.5ºC
18 ✓	Telescope + Platform	Izaña	Summer	2m/s North	Morning	70.9º North 13.9º Elev	15.5ºC	12.7ºC
19 ✓	Telescope + Platform	Izaña	Summer	5m/s North	Morning	70.9º North 13.9º Elev	15.5ºC	14.7ºC
20 ✓	Telescope + Platform	Izaña	Summer	5m/s North	Noon	214.3º North 83.8º Elev	24.5ºC	33.9ºC
21 ✓	Telescope + Platform	Izaña	Summer	5m/s North	Afternoon	286.1º North 20.1º Elev	23.1ºC	23.5ºC
22 CANCEL	Telescope + Platform	Izaña	Winter	5m/s North	Morning	124.6º North 11.9º Elev	3.4ºC	3ºC
23 CANCEL	Telescope + Platform	ORM	Summer	5m/s North	Morning	70.9º North 13.9º Elev	15.5ºC	14.6ºC
24 ✓	Telescope(Tamb)+ Platform	Izaña	Summer	5m/s North	Morning	70.9º North 13.9º Elev	15.5ºC	14.7ºC
25 ✓	Telescope(Tamb)+ Platform	Izaña	Summer	5m/s North	Noon	214.3º North 83.8º Elev	24.5ºC	33.9ºC
26 ✓	Telescope(Tamb)+ Platform	Izaña	Summer	5m/s North	Afternoon	286.1º North 20.1º Elev	23.1ºC	23.5ºC

Table 1: Seeing simulations performed based on the thermal analysis of the EST DS phase.

<p align="center">EST TELESCOPE ENVIRONMENT PRELIMINARY THERMAL ANALYSIS II</p>	<p>Page: 6 of 54 Date: November 13, 2014</p>
<p align="center">Code: DM/TN-SNT/011v.1</p>	<p>File: DELIVERABLE70_4B.DOCX</p>

2. ANALYSES PERFORMED

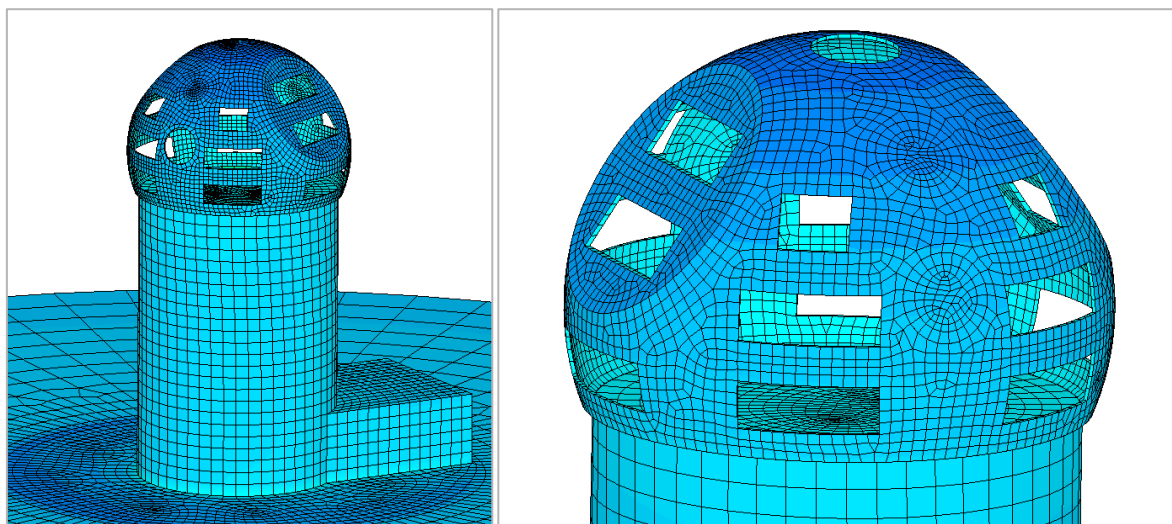
These analysis have been performed for different configurations of the telescope facilities with a conventional dome (Closed Configuration) and windshield (Open Configuration), for complete day-night cycles comprising two consecutive days in summer for North wind of 5 m/s. Second day results are considered the significant results of this analysis, assuming that the first day is used to stabilize the model. For each configuration temperature maps of the facilities are obtained for different moments of day, morning, noon and afternoon.

These analysis have been performed with RadTherm software from ThermoAnalytics, Inc. . using a lineal convection model which provides estimations of the convection heat transfer coefficient based on the McAdam's plate model ($h = 5.7 + 3.8 \cdot v$), which results in a convection coefficient of 24.7W/m²K for 5m/s.

The daily air temperature and irradiance profiles considered correspond to the profiles measured at GREGOR telescope (RD.6), assuming the averaged July 99 day as the summer day conditions. The effective sky radiation temperature has been obtained directly by Radtherm from the summer environmental data assumed from GREGOR telescope measurements.

Two different groups of configurations have been performed:

1. "Closed Configuration": Telescope with a conventional dome (Analysis 30 to



41).

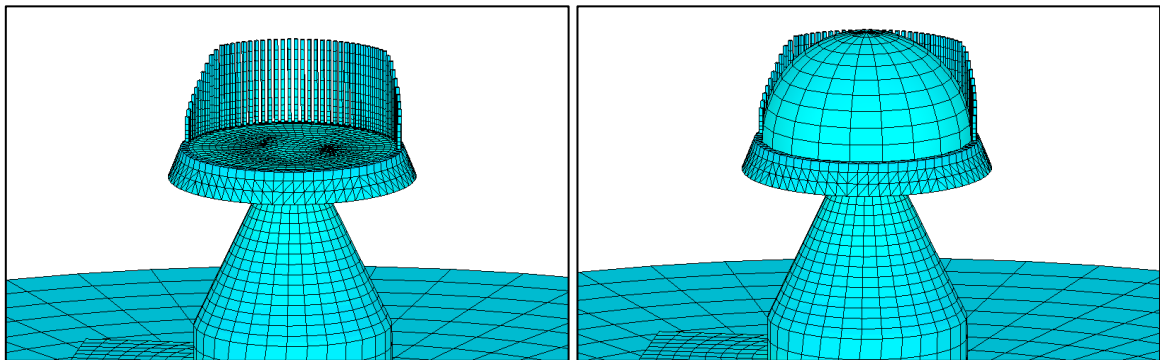
Figure 1 Conventional dome. EST "Close Configuration".

EST TELESCOPE ENVIRONMENT PRELIMINARY THERMAL ANALYSIS II	Page: 7 of 54 Date: November 13, 2014
Code: DM/TN-SNT/011v.1	File: DELIVERABLE70_4B.DOCX

This group contains three subgroups:

- a. Dome without thermal control (3 cases).
- b. Dome with thermal control at the outer Surface (3 cases).
- c. Dome with heat rejected effect (6 cases).

2. "Open Configuration with windshield". Telescope with a retractable dome



(Analysis 42 to 44).

Figure 2 Retractable dome. EST "Open Configuration" thermal analysis. Day (left) and night configuration (right).

EST TELESCOPE ENVIRONMENT PRELIMINARY THERMAL ANALYSIS II	Page: 8 of 54 Date: November 13, 2014
Code: DM/TN-SNT/011v.1	File: DELIVERABLE70_4B.DOCX

Case	Configuration	Site	Season	Wind	Time	Sun Orientation	Tair	T Ground
DOME								
30	DOME Building West	Izaña	Summer	5m/s North	Morning	70,9° North 13,9° Elev	15,5°C	14,2°C
31	DOME Building West	Izaña	Summer	5m/s North	Noon	214,3° North 83,8° Elev	24,5°C	34,1°C
32	DOME Building West	Izaña	Summer	5m/s North	Afternoon	286,1° North 20,1° Elev	23,1°C	26,1°C
DOME COOLING SYSTEM (T^a=T^aair)								
33	DOME Building West	Izaña	Summer	5m/s North	Morning	70,9° North 13,9° Elev	15,5°C	14,2°C
34	DOME Building West	Izaña	Summer	5m/s North	Noon	214,3° North 83,8° Elev	24,5°C	34,1°C
35	DOME Building West	Izaña	Summer	5m/s North	Afternoon	286,1° North 20,1° Elev	23,1°C	26,1°C
DOME + HEAT STOP								
36	DOME(Wind) Building West	Izaña	Summer	5m/s North	Morning	70,9° North 13,9° Elev	15,5°C	14,2°C
37	DOME(Wind) Building West	Izaña	Summer	5m/s North	Noon	214,3° North 83,8° Elev	24,5°C	34,1°C
38	DOME (Wind) Building West	Izaña	Summer	5m/s North	Afternoon	286,1° North 20,1° Elev	23,1°C	26,1°C
39	DOME (Air) Building West	Izaña	Summer	5m/s North	Morning	70,9° North 13,9° Elev	15,5°C	14,2°C
40	DOME (Air) Building West	Izaña	Summer	5m/s North	Noon	214,3° North 83,8° Elev	24,5°C	34,1°C
41	DOME (Air) Building West	Izaña	Summer	5m/s North	Afternoon	286,1° North 20,1° Elev	23,1°C	26,1°C
WIND SHIELD								
42	WINDSHIELD Building West	Izaña	Summer	5m/s North	Morning	70,9° North 13,9° Elev	15,7°C	14,6°C
43	WINDSHIELD Building West	Izaña	Summer	5m/s North	Noon	214,3° North 83,8° Elev	24,3°C	33,9°C
44	WINDSHIELD Building West	Izaña	Summer	5m/s North	Afternoon	286,1° North 20,1° Elev	21,1°C	23,5°C

The following table summarizes the cases analysed:

Table 2: Thermal analysis performed.

EST TELESCOPE ENVIRONMENT PRELIMINARY THERMAL ANALYSIS II	Page: 9 of 54 Date: November 13, 2014
Code: DM/TN-SNT/011v.1	File: DELIVERABLE70_4B.DOCX

2.1 WEATHER CONDITIONS

All models listed in this document have been analysed under the same weather conditions, according to RD.6, solar irradiance and air temperature in summer with a wind speed of 5 m / s from the North.

The following table shows the solar coordinates used in the models, measured at the geographical coordinates of the Canary Islands, 28.3 degrees north latitude and 16.51 degrees west longitude. The angle of elevation, has its origin in the zenith. (zenith = 0°) and the origin for the azimuth angle is the North.

HORA	ZENITH	AZIMUTH	HORA	ZENITH	AZIMUTH
5:55	94,1933	60,8624	13:25	6,21262	214,278
6:10	91,2844	62,7157	13:40	8,5498	234,367
6:25	88,3276	64,4894	13:55	11,4177	245,544
6:40	85,3277	66,1917	14:10	14,5032	252,462
6:55	82,2888	67,8305	14:25	17,6911	257,23
7:10	79,2149	69,4132	14:40	20,9324	260,801
7:25	76,1095	70,947	14:55	24,2037	263,652
7:40	72,9755	72,4389	15:10	27,4919	266,041
7:55	69,8159	73,8957	15:25	30,789	268,12
8:10	66,6333	75,3244	15:40	34,09	269,982
8:25	63,4299	76,732	15:55	37,391	271,692
8:40	60,208	78,1257	16:10	40,6893	273,292
8:55	56,9696	79,5135	16:25	43,9825	274,813
9:10	53,7167	80,9042	16:40	47,2685	276,278
9:25	50,451	82,3076	16:55	50,5454	277,705
9:40	47,1745	83,7355	17:10	53,8114	279,107
9:55	43,8888	85,202	17:25	57,0647	280,497
10:10	40,596	86,7251	17:40	60,3035	281,885
10:25	37,298	88,3279	17:55	63,5257	283,278
10:40	33,9974	90,0416	18:10	66,7295	284,686
10:55	30,6968	91,9097	18:25	69,9125	286,115
11:10	27,4002	93,9954	18:40	73,0725	287,572
11:25	24,1127	96,3947	18:55	76,2068	289,064
11:40	20,8423	99,2615	19:10	79,3126	290,598
11:55	17,6022	102,858	19:25	82,3869	292,182
12:10	14,4165	107,669	19:40	85,4261	293,822
12:25	11,335	114,668	19:55	88,4265	295,525
12:40	8,47621	126,013	20:10	91,3836	297,3
12:55	6,16202	146,441	20:25	94,2928	299,155
13:10	5,18501	180,507	20:40	97,1487	301,098
			20:55	99,9453	303,14

Table 3. Sun coordinates. Summer. – July 99. Latitude N 28.3/Longitude W 16.51°.

<p align="center">EST TELESCOPE ENVIRONMENT PRELIMINARY THERMAL ANALYSIS II</p>	<p>Page: 10 of 54 Date: November 13, 2014</p>
<p align="center">Code: DM/TN-SNT/011v.1</p>	<p>File: DELIVERABLE70_4B.DOCX</p>

Solar irradiance values, according to RD.6, (July 99) used in the models are shown in the following figure:

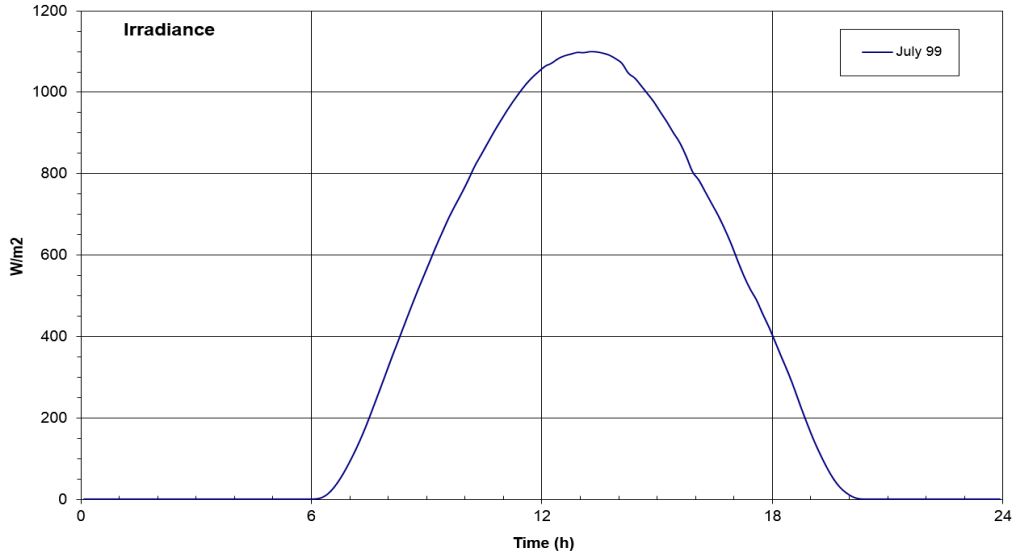


Figure: 3. Solar Irradiation (W/m^2) July 99. Latitude N 28.3/Longitude W 16.51°/Altitude=2400m

The next graph displays the evolution of the air temperature for a summer day, according to RD.6:

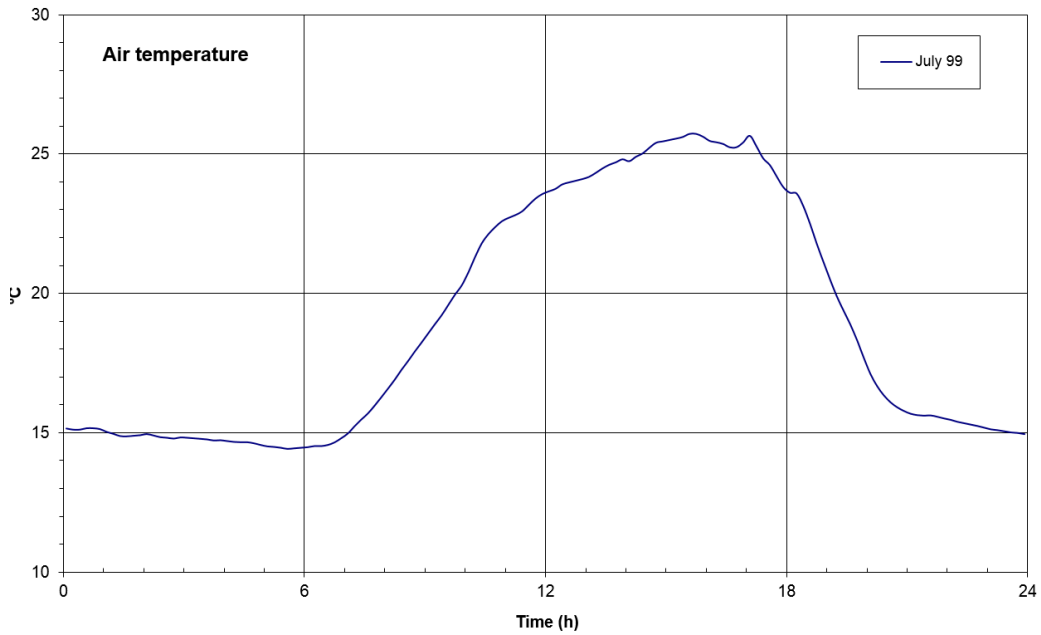


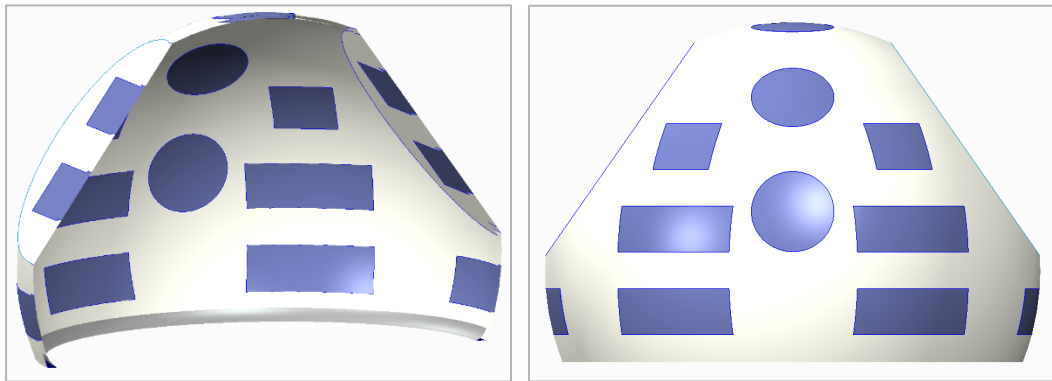
Figure 4: Air Temperature (°C) July 99.

EST TELESCOPE ENVIRONMENT PRELIMINARY THERMAL ANALYSIS II	Page: 11 of 54 Date: November 13, 2014
Code: DM/TN-SNT/011v.1	File: DELIVERABLE70_4B.DOCX

2.2 CLOSED CONFIGURATION

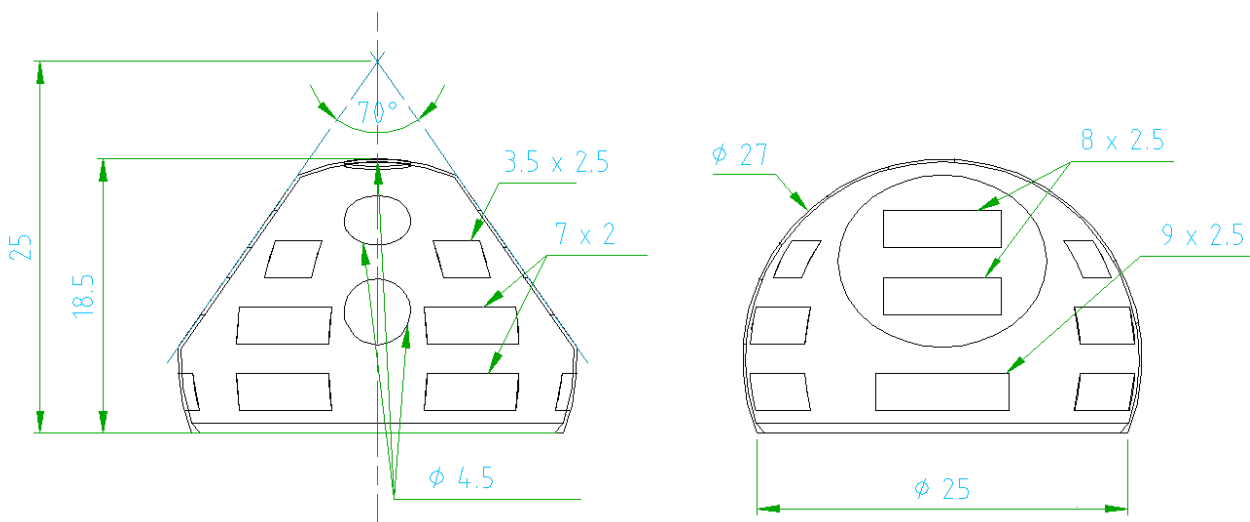
The analysis in "Closed Configuration" (cases 30 to 41) includes a conventional dome in the simplified design of the EST facilities and a cylindrical pier, in contrast with the conical design of the pier at "Open Configuration". The dome has eighteen rectangular windows radially distributed to allow air to circulate through the dome. Dome also contains 4 circular openings for observation distributed in the elevation plane of the telescope (Morning: 13.9 ° / Noon: 83.8 ° / Afternoon: 20.1 ° / Intermediate position:45°).

Ventilation windows and observation windows remain closed during thermal analysis to simulate a real opening which prevents radiation from entering inside, once the analysis is completed, ventilation windows are removed and the observation window that corresponds to the case analysed to perform the CFD



analysis, which allow air to circulate inside of the dome.

Figure 5: Conventional Dome. Top Left) Front view. Top Right) Section. Down) Main dimensions.



EST TELESCOPE ENVIRONMENT PRELIMINARY THERMAL ANALYSIS II	Page: 12 of 54 Date: November 13, 2014
Code: DM/TN-SNT/011v.1	File: DELIVERABLE70_4B.DOCX

Thermal analysis with conventional telescope dome is made for two consecutive days, the first day the dome remains static and rotates in the azimuth axis the second day according to Table 3.

A simplified model of the telescope including dome, pier, enclosure, telescope platform, service floor, building and ground structure was defined for the thermal analysis according to RD.1, based on the close configuration telescope concept.

The model used for the analysis corresponds to the geometry presented in the following figure:

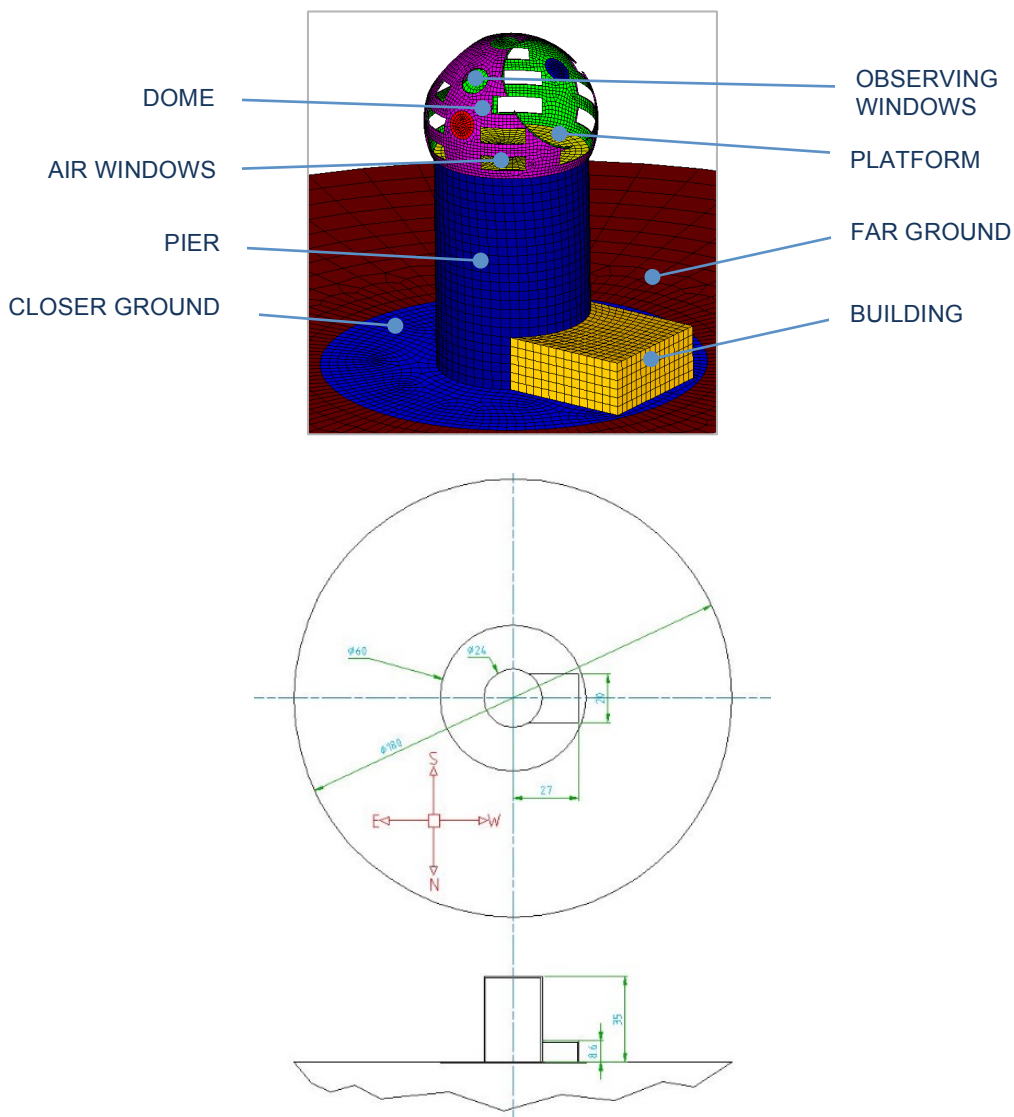


Figure 6: EST at "Close Configuration". Thermal analysis 3D model. Dome without thermal control and provided with windows to allow air flow inside (Up). Model main dimensions (Down).

EST TELESCOPE ENVIRONMENT PRELIMINARY THERMAL ANALYSIS II	Page: 13 of 54 Date: November 13, 2014
Code: DM/TN-SNT/011v.1	File: DELIVERABLE70_4B.DOCX

2.2.1 DOME WITHOUT THERMAL CONTROL.

Analysis with conventional dome without thermal control (cases 30 to 32) is performed following the above guidelines.

MODEL CONFIGURATION				
DOME WITHOUT THERMAL CONTROL				
	DESCRIPCION	SURFACE	CONVECTION	DIMENSIONS
DOME	1mm thick steel external surface / 198 mm isolation polyurethane foam / 1mm thick steel internal surface	External: White painted TiO2 (Abs= 0.28 / Emis= 0.87) Internal: White painted	Outside: Wind Inside: Wind	Ø _{DOME} = 27m Height= 18.5m
PIER	0.5 m thick concrete walls with 200mm external isolation and 150mm external concrete wall.	External: White painted TiO2 (Abs= 0.28 / Emis= 0.87) Internal: Concrete (Abs:0.6 / Emis=0.88)	Outside: Wind Inside: Air at 20° H= 5 W/m ² .K	Height= 35m Ø _{PIER} = 24m
BUILDING	0.2 thick concrete walls without isolation	External: White painted TiO2 (Abs= 0.28 / Emis= 0.87) Internal: Concrete (Abs:0.6 / Emis=0.88)	Outside: Wind Inside: Air at 20° H= 5 W/m ² .K	Width=20m Large=20m Height=8.6m
PLATFORM	5mm Steel plate/ 200mm isolation polyurethane foam/ 250mm concrete	White painted TiO2 (Abs= 0.28 / Emis= 0.87)	Upper Surface: Wind Down Surface: Air at 20° H= 5 W/m ² .K	Ø _{PLATFORM} = 25m
FAR GROUND	Soil – Rocky Field	Surface Moisture: Dry Bulk Moisture: Dry Abs=0.63 Core Temp=15°C		Ø _{FARG} = 60m
CLOSER GROUND	Concrete - Sidewalk	Abs= 0.27 Core Temp=15°C Wetness= Exposed normal		Ø _{CLOSERG} = 180m

The model used for the analysis has been calculated under the following conditions:

Table 4: Model configuration Dome Analysis.

EST TELESCOPE ENVIRONMENT PRELIMINARY THERMAL ANALYSIS II	Page: 14 of 54 Date: November 13, 2014
Code: DM/TN-SNT/011v.1	File: DELIVERABLE70_4B.DOCX

Name	Density (kg/ m³)	Conductivity (W/m.k)	Specific heat(J/Kg.k)
Polyurethane Foam	32	0.0389	2090
Steel	7769.98	52.019	460.967
Concrete	2200	1.28	880

Table 5: Materials Properties Dome Analysis

2.2.2 DOME WITH THERMAL CONTROL

Analysis with conventional dome and thermal control (cases 33 to 36) is performed similarly to the previous case (2.2.1), with respect to the geometry the general process followed for carrying out analysis..

To simulate the cooling system, temperature of the dome is restricted and is converged to the air temperature values, represented in the Figure 4, for summer conditions according to RD.6. Only the outer part of the dome has this restriction and thus the entire outer surface of the dome will keep air temperature throughout the day.

Thermal analysis with conventional telescope dome and thermal control is made for two consecutive days, the first day the dome remains static and rotates in the azimuth axis the second day according to Table 3. The cooling system remains active for two days.

The model used for the analysis is similar to Dome Analysis Model (2.2.1) and corresponds to the geometry presented in the Figure 6.

EST TELESCOPE ENVIRONMENT PRELIMINARY THERMAL ANALYSIS II	Page: 15 of 54 Date: November 13, 2014
Code: DM/TN-SNT/011v.1	File: DELIVERABLE70_4B.DOCX

The model used for the analysis has been calculated under the following conditions:

MODEL CONFIGURATION				
DOME WITH THERMAL CONTROL				
	DESCRIPCION	SURFACE	CONVECTION	DIMENSIONS
DOME	1mm thick steel external surface (back side isolated) / 99 mm isolation polyurethane foam / 1mm thick steel internal surface	External: White painted TiO2 (Abs= 0.28 / Emis= 0.87) Internal: White painted	Outside: Temp= Tair Inside: Wind	Ø _{DOME} = 27m Height= 18.5m
PIER	0.5 m thick concrete walls with 200mm external isolation and 150mm external concrete wall.	External: White painted TiO2 (Abs= 0.28 / Emis= 0.87) Internal: Concrete (Abs:0.6 / Emis=0.88)	Outside: Wind Inside: Air at 20° H= 5 W/m ² .K	Height= 35m Ø _{PIER} = 24m
BUILDING	0.2 thick concrete walls without isolation	External: White painted TiO2 (Abs= 0.28 / Emis= 0.87) Internal: Concrete (Abs:0.6 / Emis=0.88)	Outside: Wind Inside: Air at 20° H= 5 W/m ² .K	Width=20m Large=20m Height=8.6m
PLATFORM	5mm Steel plate/ 200mm isolation polyurethane foam/ 250mm concrete	White painted TiO2 (Abs= 0.28 / Emis= 0.87)	Upper Surface: Wind Down Surface: Air at 20° H= 5 W/m ² .K	Ø _{PLATFORM} = 25m
FAR GROUND	Soil – Rocky Field	Surface Moisture: Dry Bulk Moisture: Dry Abs=0.63 Core Temp=15°C	Wind	Ø _{FARG} = 60m
CLOSER GROUND	Concrete - Sidewalk	Abs= 0.27 Core Temp=15°C Wetness= Exposed normal	Wind	Ø _{CLOSERG} = 180m

Table 6: Model configuration Dome Analysis Thermal Control.

EST TELESCOPE ENVIRONMENT PRELIMINARY THERMAL ANALYSIS II	Page: 16 of 54 Date: November 13, 2014
Code: DM/TN-SNT/011v.1	File: DELIVERABLE70_4B.DOCX

Name	Density (kg/ m ³)	Conductivity (W/m.k)	Specific heat(J/Kg.k)
Polyurethane Foam	32	0.0389	2090
Steel	7769.98	52.019	460.967
Concrete	2200	1.28	880

Table 7: Materials Properties Dome Thermal Control Analysis.

2.2.3 DOME - HEAT STOP

EST is equipped with a four-meter diameter primary mirror and primary focal length of about six meters. This optical configuration generates an important thermal load that it needs to be considered at close configuration since the dome makes impossible that heat can be projected into the atmosphere.

A heat stop or a heat rejected, positioned at the primary focus, must be able to remove a heat load of 13,6 kW from the optic path. while maintaining its surfaces very close to room temperature to avoid the onset of seeing. Heat Stop Analysis evaluates the effects of using a "flat 45° inclined heat rejecter", that projects the thermal load into the dome, as the configuration as is shown in the following figure:

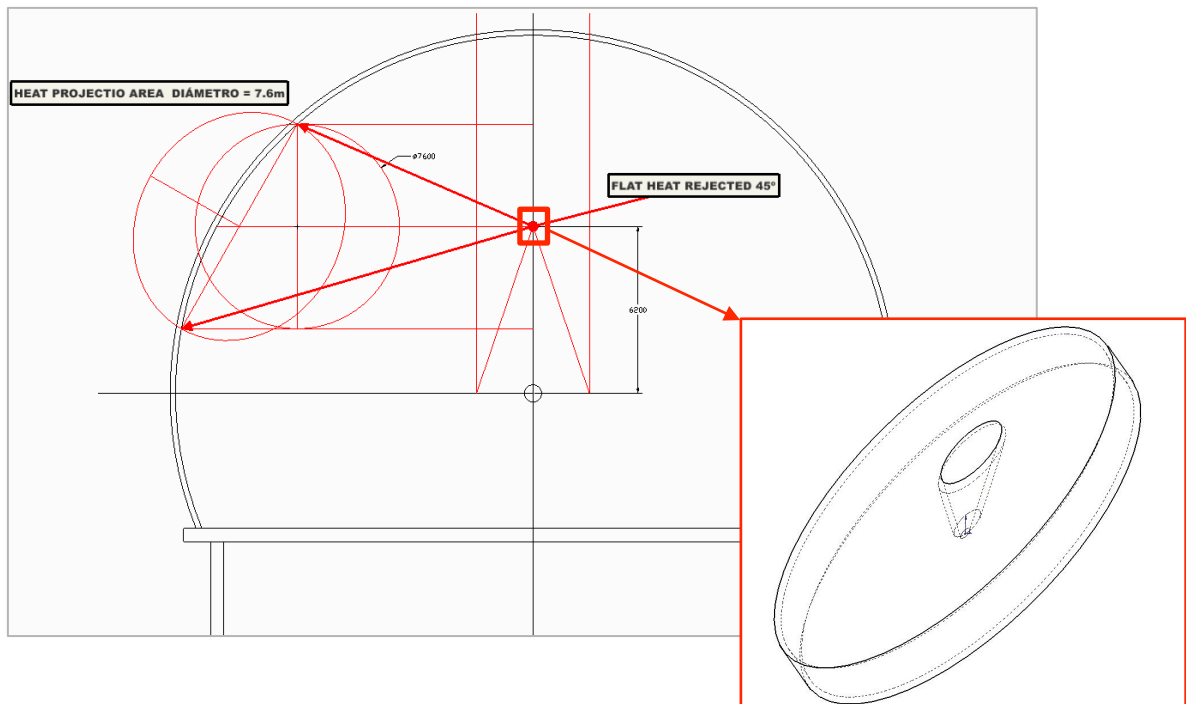


Figure 7: a) Heat projection into the dome rejected by the heat stop, 7.6m of diameter.

EST TELESCOPE ENVIRONMENT PRELIMINARY THERMAL ANALYSIS II	Page: 17 of 54 Date: November 13, 2014
Code: DM/TN-SNT/011v.1	File: DELIVERABLE70_4B.DOCX

b) Flat HR - the hole is a cone having the same aperture of the light beam (18°).

Heat Stop analysis (cases 36 to 41) is made for two consecutive days, in summer for North wind of 5m/s. During night hours the telescope platform was covered by the enclosure, enclosing the telescope chamber. The enclosure was removed at sunrise. For the analysis the enclosure was assumed at ambient temperature at the moment of being deployed. Second day results are considered the significant results of this analysis, assuming that during the first day is used to stabilize the model.

These analyses are divided in two groups, first group comprises the cases 36 to 38 and have been performed simulating stagnant air inside dome, second group, cases 39 to 41, has been analysed with wind condition not only outside of the dome, but also inside, rather than stagnant air as in the first group.

The following figures illustrate how heat projection heats up different parts of the inner dome during the day:

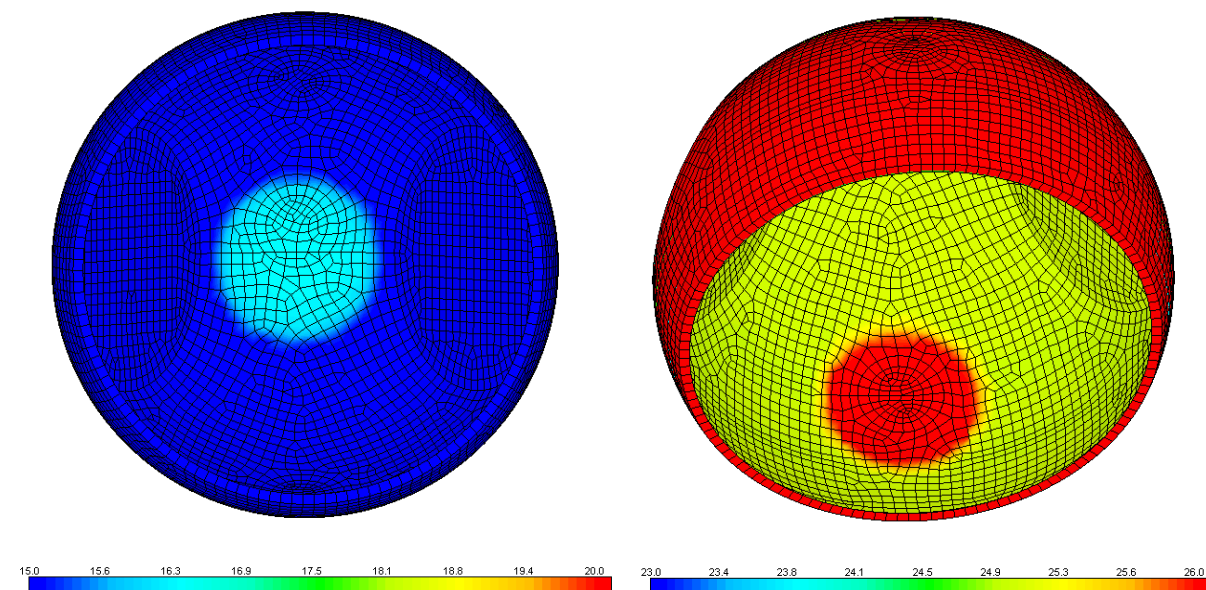


Figure 8: a) Heat projection at sunrise. B) Heat projection at noon.

The following table shows how heat collected by the primary mirror and reflected by the heat rejected is distributed inside dome, divided a total of 13,6 Kw among dome inner surface, platform and heat projection.

EST TELESCOPE ENVIRONMENT PRELIMINARY THERMAL ANALYSIS II	Page: 18 of 54 Date: November 13, 2014
Code: DM/TN-SNT/011v.1	File: DELIVERABLE70_4B.DOCX

	PLATFORM	DOME	HEAT PROJECTION
IMPOSED HEAT	2,586 KW	8,973 KW	2,040 KW
TOTAL HEAT REJECTED	13,6 KW		

Table 8: Calorific power distributed among the areas affected by the deflection of light at the "Heat Rejected".

The model used for the analysis is geometrically identical to the model presented in the previous analysis (Dome Analysis) and has been calculated under the following conditions:

MODEL CONFIGURATION				
DOME HEAT STOP - AIR INSIDE DOME AND WIND INSIDE DOME				
	DESCRIPCION	SURFACE	CONVECTION	DIMENSIONS
DOME	1mm thick steel external surface / 198 mm isolation polyurethane foam / 1mm thick steel internal surface	External: White painted TiO2 (Abs= 0.28 / Emis= 0.87) Internal: White painted	Outside: Temp= Wind Inside: Air at ambient temperature (cases 28,29 y 30) Wind (cases 31, 32 y 33).	$\varnothing_{\text{DOME}}= 27\text{m}$ Height= 18.5m
PIER	0.5 m thick concrete walls with 200mm external isolation and 150mm external concrete wall.	External: White painted TiO2 (Abs= 0.28 / Emis= 0.87) Internal: Concrete (Abs:0.6 / Emis=0.88)	Outside: Wind Inside: Air at 20° H= 5 W/m ² .K	Height= 35m $\varnothing_{\text{PIER}}= 24\text{m}$
BUILDING	0.2 thick concrete walls without isolation	External: White painted TiO2 (Abs= 0.28 / Emis= 0.87) Internal: Concrete (Abs:0.6 / Emis=0.88)	Outside: Wind Inside: Air at 20° H= 5 W/m ² .K	Width=20m Large=20m Height=8.6m
PLATFORM	5mm Steel plate/ 200mm isolation polyurethane foam/ 250mm concrete	White painted TiO2 (Abs= 0.28 / Emis= 0.87)	Upper Surface: Wind Down Surface: Air at 20° H= 5 W/m ² .K	$\varnothing_{\text{PLATFORM}}= 25\text{m}$

EST TELESCOPE ENVIRONMENT PRELIMINARY THERMAL ANALYSIS II	Page: 19 of 54 Date: November 13, 2014
Code: DM/TN-SNT/011v.1	File: DELIVERABLE70_4B.DOCX

FAR GROUND	Soil – Rocky Field	Surface Moisture: Dry Bulk Moisture: Dry Abs=0.63 Core Temp=15°C	Wind	$\varnothing_{\text{FARG}} = 60\text{m}$
CLOSER GROUND	Concrete - Sidewalk	Abs= 0.27 Core Temp=15°C Wetness= Exposed normal	Wind	$\varnothing_{\text{CLOSERG}} = 180\text{m}$

Table 9: Model configuration “Heat Stop Analysis”.

Name	Density (kg/ m ³)	Conductivity (W/m.k)	Specific heat(J/Kg.k)
Polyurethane Foam	32	0.0389	2090
Steel	7769.98	52.019	460.967
Concrete	2200	1.28	880

Table 10: Materials properties Heat Stop Analysis.

2.3 OPEN CONFIGURATION WITH WINDSHIELD

Thermal analysis of the telescope with the windshield (cases 42 to 44), which takes as its starting point the analysis of the open configuration telescope according to RD.2, evaluates the use of a new configuration for the platform telescope.

The analysis of the telescope environment has been performed for complete day-night cycles comprising two consecutive days in summer for North wind of 5 m/s. During night hours the telescope platform was covered by the enclosure, enclosing the telescope chamber. The enclosure was removed at sunrise. For the analysis the enclosure was assumed at ambient temperature at the moment of being deployed.

Second day results are considered the significant results of this analysis, assuming that during the first day is used to stabilize the model.

A simplified model of the telescope facilities including windshield, pier, enclosure, telescope platform, service floor, building and ground was defined for the thermal analysis according to RD.1, based on the open configuration telescope concept.

The model used for the analysis corresponds to the geometry presented in the following figure:

<p align="center">EST TELESCOPE ENVIRONMENT PRELIMINARY THERMAL ANALYSIS II</p>	<p>Page: 20 of 54 Date: November 13, 2014</p>
<p>Code: DM/TN-SNT/011v.1</p>	<p>File: DELIVERABLE70_4B.DOCX</p>

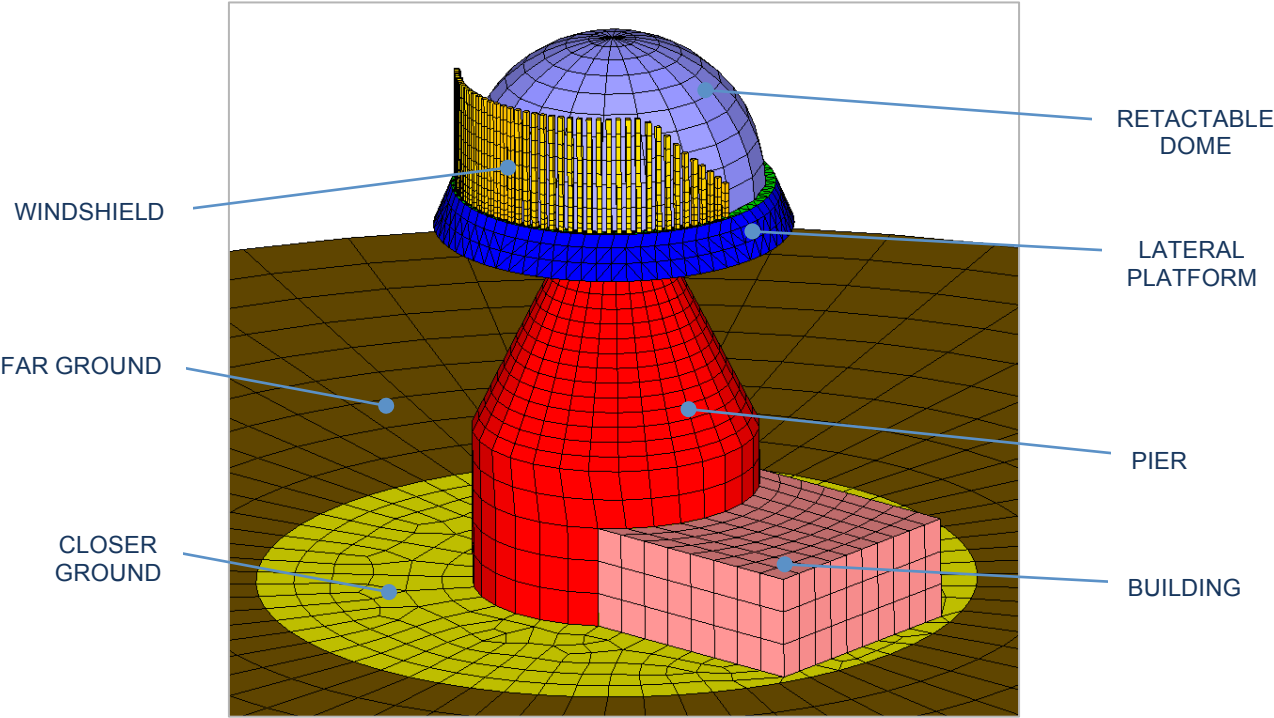


Figure 9. Windshield analysis thermal model at night configuration.

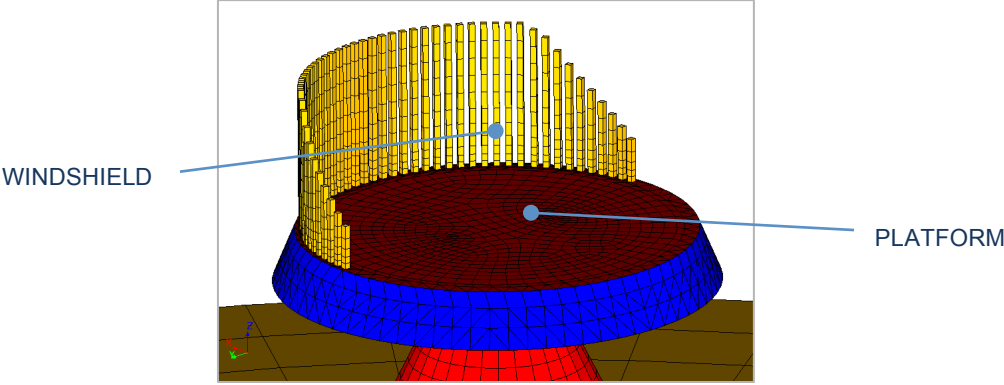


Figure 10: Windshield analysis thermal model at day configuration.

Windshield dimensions are shown in the following figure:

<p align="center">EST TELESCOPE ENVIRONMENT PRELIMINARY THERMAL ANALYSIS II</p>	<p>Page: 21 of 54 Date: November 13, 2014</p>
<p align="center">Code: DM/TN-SNT/011v.1</p>	<p>File: DELIVERABLE70_4B.DOCX</p>

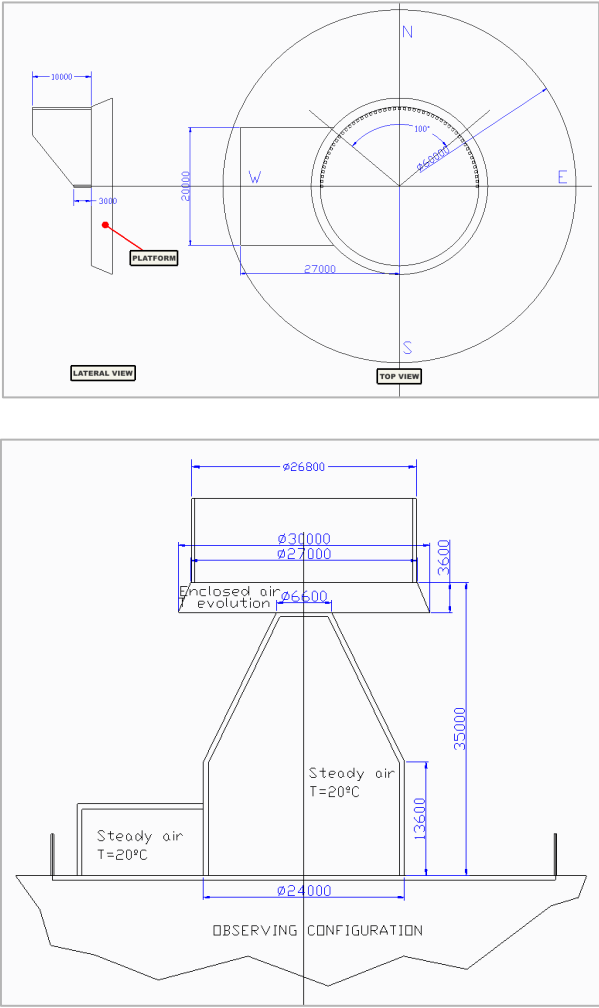


Figure 11: Windshield model dimensions.

EST TELESCOPE ENVIRONMENT PRELIMINARY THERMAL ANALYSIS II	Page: 22 of 54 Date: November 13, 2014
Code: DM/TN-SNT/011v.1	File: DELIVERABLE70_4B.DOCX

The model used for the analysis has been calculated under the following conditions:

MODEL CONFIGURATION				
WINDSHIELD				
	DESCRIPCION	SURFACE	CONVECTION	DIMENSIONS
WINDSHIELD	50 bars 0.05m thick steel square section. Stagnant air inside	External: White painted TiO2 (Abs= 0.28 / Emis= 0.87) Internal: Steel clean (Abs= 0.54 / Emis= 0.1)	Outside: Wind Inside: Air inside windshield – Stagnant air H= 1 W/m ² .K	Width=0.4m Large=0.4m Variable height
RETRACTABLE DOME	1.15m thick	External =Internal = Aluminium Paint (Abs= 0.22 / Emis= 0.21)	Outside: Wind Inside: Air inside dome –Stagnant air H= 1 W/m ² .K	Ø _{Dome} = 25m
BUILDING	0.2 thick concrete walls without isolation	External: White painted TiO2 (Abs= 0.28 / Emis= 0.87) Internal: Concrete (Abs:0.6 / Emis=0.88)	Outside: Wind Inside: Air at 20° H= 5 W/m ² .K	Width=20m Large=20m Height=8.6m
PLATFORM	5mm Steel plate/ 200mm isolation polyurethane foam/ 250mm concrete	White painted TiO2 (Abs= 0.28 / Emis= 0.87) Internal: : Steel clean (Abs= 0.54 / Emis= 0.1)	Outside: Wind Inside: Wind	Ø _{Upper Plat} = 27m Ø _{Lower Plat} = 30m
FAR GROUND	Soil – Rocky Field	Surface Moisture: Dry Bulk Moisture: Dry Abs=0.63 Core Temp=15°C	Wind	Ø _{FARG} = 60m
CLOSER GROUND	Concrete - Sidewalk	Abs= 0.27 Core Temp=15°C Wetness= Exposed normal	Wind	Ø _{CLOSERG} = 180m

Table 11: Model configuration “Windshield Analysis”.

EST TELESCOPE ENVIRONMENT PRELIMINARY THERMAL ANALYSIS II	Page: 23 of 54 Date: November 13, 2014
Code: DM/TN-SNT/011v.1	File: DELIVERABLE70_4B.DOCX

Name	Density (kg/ m ³)	Conductivity (W/m.k)	Specific heat (J/Kg.k)
Polyurethane Foam	32	0.0389	2090
Steel	7769.98	52.019	460.967
Concrete	2200	1.28	880
Dome Precontrait 1502	1300	0.009	-

Table 12: Materials properties Windshield Analysis.

3. RESULTS

3.1 Results summary

The objective of these analyses is to obtain the temperature maps for the telescope structure and the telescope environment during the day for different configurations under real environmental conditions in order to select the optimal configurations to minimize the local seeing degradation.

The difference between the air temperature and the average temperature of each part composing the model analysed, being this the most important factor to evaluate the thermal behaviour of each component, in terms of probability to create turbulence or air plumes that could reduce the optical quality of the observations, however CFD seeing analysis is required in order to evaluate properly thermal effects..

In cases involving parts in to the optical path the objective is to keep the surface of the structure as close as possible to the ambient temperature during all the observing time. As a preliminary value it is assumed $\pm 1^{\circ}\text{C}$ (TBC) with respect to the ambient air.

In the case of the telescope environment, including the telescope platform, which is below the telescope level, the requirement of temperature difference can be more relaxed depending of the distance from the optical path. It is considered that keeping the temperature of the surfaces during the observation a few degrees below the ambient temperature is effective to improve the local seeing, since it suppresses the ground layer, as presented in RD.5. The maximum positive temperature difference of the telescope platform over the ambient air in order to avoid effects of the boundary layer on the optical path is 1.5°C (TBC) according to the preliminary estimation presented in RD.1.

The following table summarizes the maximum and minimum differences ($^{\circ}\text{C}$) observed between the average temperature of each part and the ambient temperature during the observing hours (daytime). The results are compared for the second day of the analysis, assuming that the first day is used to stabilize the model. The spatial gradients along the elements can be seen in the next section of this report.

EST TELESCOPE ENVIRONMENT PRELIMINARY THERMAL ANALYSIS II	Page: 24 of 54 Date: November 13, 2014
Code: DM/TN-SNT/011v.1	File: DELIVERABLE70_4B.DOCX

TEMPERATURE DIFFERENCES T- Tair																
Season	Wind Speed	PARTS	FAR GROUND	CLOSER GROUND	BUILDING	PIER	PLATFORM	DOME OUT	DOME IN	HEAT PROJECTION	WINDSHIELD	LATERAL PLATFORM	LOWER PLATFORM			
														Summer	5m/s	°C
														CLOSED CONFIGURATION	DOME WITHOUT THERMAL CONTROL	ΔTmax
ΔTmin	-2,43	-3,64	-4,35	-2,09	-0,73	-2,74	-0,33	-								
DOME WITH THERMAL CONTROL	ΔTmax	9,88	1,91	4,25	3,33	0,93	0,28	0,48	-							
	ΔTmin	-2,43	-3,64	-4,35	-2,10	-0,68	-0,36	-0,16	-							
DOME HEAT STOP AIR INSIDE	ΔTmax	9,89	1,95	4,27	3,41	4,43	2,66	3,34	6,64							
	ΔTmin	-2,43	-3,63	-4,47	-2,38	-1,13	-2,78	-0,09	-0,03							
DOME HEAT STOP WIND INSIDE	ΔTmax	9,89	1,94	4,54	3,57	1,26	3,21	0,74	1,93							
	ΔTmin	-2,43	-3,64	-4,33	-2,16	-1,02	-2,78	-0,11	-0,06							
OPEN CONFIGURATION WITH WINDSHIELD	ΔTmax	9,87	2,17	3,84	2,98	3,12	0,00	-	-	2,24	1,33	2,28				
	ΔTmin	-3,12	-3,02	-4,61	-2,71	-1,92	-0,85	-	-	-2,00	-1,78	-0,41				

Table 13: Maximum temperature difference between air and parts of the model.

TEMPERATURE DIFFERENCES T- Tair																		
Season	Wind Speed	ELEMENTS	PLATFORM NORTH	PLATFORM SOUTH	PLATFORM EAST	PLATFORM WEST	DOME IN FRONT	DOME IN BACK	DOME OUT FRONT	DOME OUT BACK	PIER EAST	PIER WEST						
													Summer	5m/s	°C			
													CLOSED CONFIGURATION	DOME WITHOUT THERMAL CONTROL	ΔTmax	0,92	0,92	0,92
ΔTmin	-0,73	-0,73	-0,73	-0,73	-0,31	-0,33		-3,41	-3,47	-1,84	-3,99							
DOME WITH THERMAL CONTROL	ΔTmax	0,94	0,93	0,93	0,95	0,65	0,41		0,28	0,28	2,68	6,20						
	ΔTmin	-0,69	-0,69	-0,66	-0,69	-0,16	-0,18		-0,36	-0,36	-1,85	-4,00						
HEAT STOP AIR INSIDE	ΔTmax	4,42	4,42	4,42	4,42	3,24	4,14		5,24	2,57	2,76	5,61						
	ΔTmin	-1,08	-1,08	-1,08	-1,04	-0,19	-0,25		-3,42	-3,49	-1,87	-4,10						
HEAT STOP WIND INSIDE	ΔTmax	1,26	1,26	1,26	1,26	0,71	1,42		6,23	3,20	2,87	6,20						
	ΔTmin	-0,48	-0,48	-0,48	-0,48	-0,11	-0,11		-3,40	-3,47	-1,85	-3,97						
TEMPERATURE DIFFERENCES T- Tair																		
Season	Wind Speed	ELEMENTS	PIER EAST	PIER WEST	PLATFORM LATERAL NORTH	PLATFORM LATERAL EAST	PLATFORM LATERAL SOUTH	PLATFORM LATERAL WEST	WINDSHIEL NORTH	WINDSHIELD SOUTH	PLATFORM NORTH	PLATFORM EAST		PLATFORM SOUTH	PLATFORM WEST			
																Summer	5m/s	°C
																OPEN CONFIGURATION	WINDSHIELD	ΔTmax
ΔTmin	-2,29	-4,84	-1,78	-1,80	-1,78	-1,76	-2,36	-2,10	-1,32	-1,74	-2,21	-1,91						

Table 14: Maximum temperature difference between air and elements.

EST TELESCOPE ENVIRONMENT PRELIMINARY THERMAL ANALYSIS II	Page: 25 of 54 Date: November 13, 2014
Code: DM/TN-SNT/011v.1	File: DELIVERABLE70_4B.DOCX

3.2 Temperature Maps

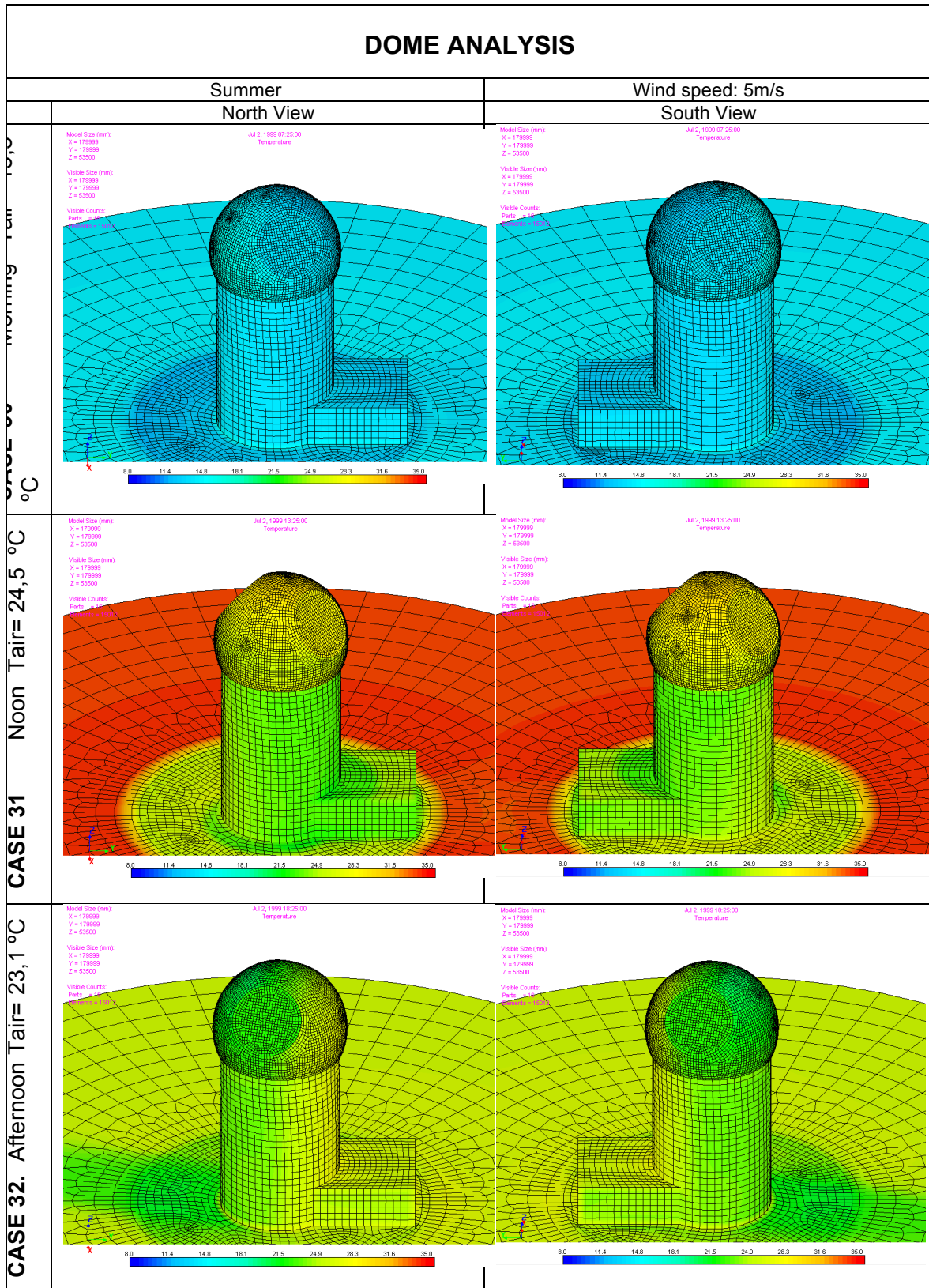
This section presents the temperature maps obtained in the thermal analyses of the different cases analysed for the EST facilities. Temperature maps are represented for three moments during the day: 90 minutes after sunrise, noon and 90 minutes before sunset, for summer conditions and wind speed of 5 m/s.

For each condition, the temperature maps are presented in two views of the telescope facilities, North and South.

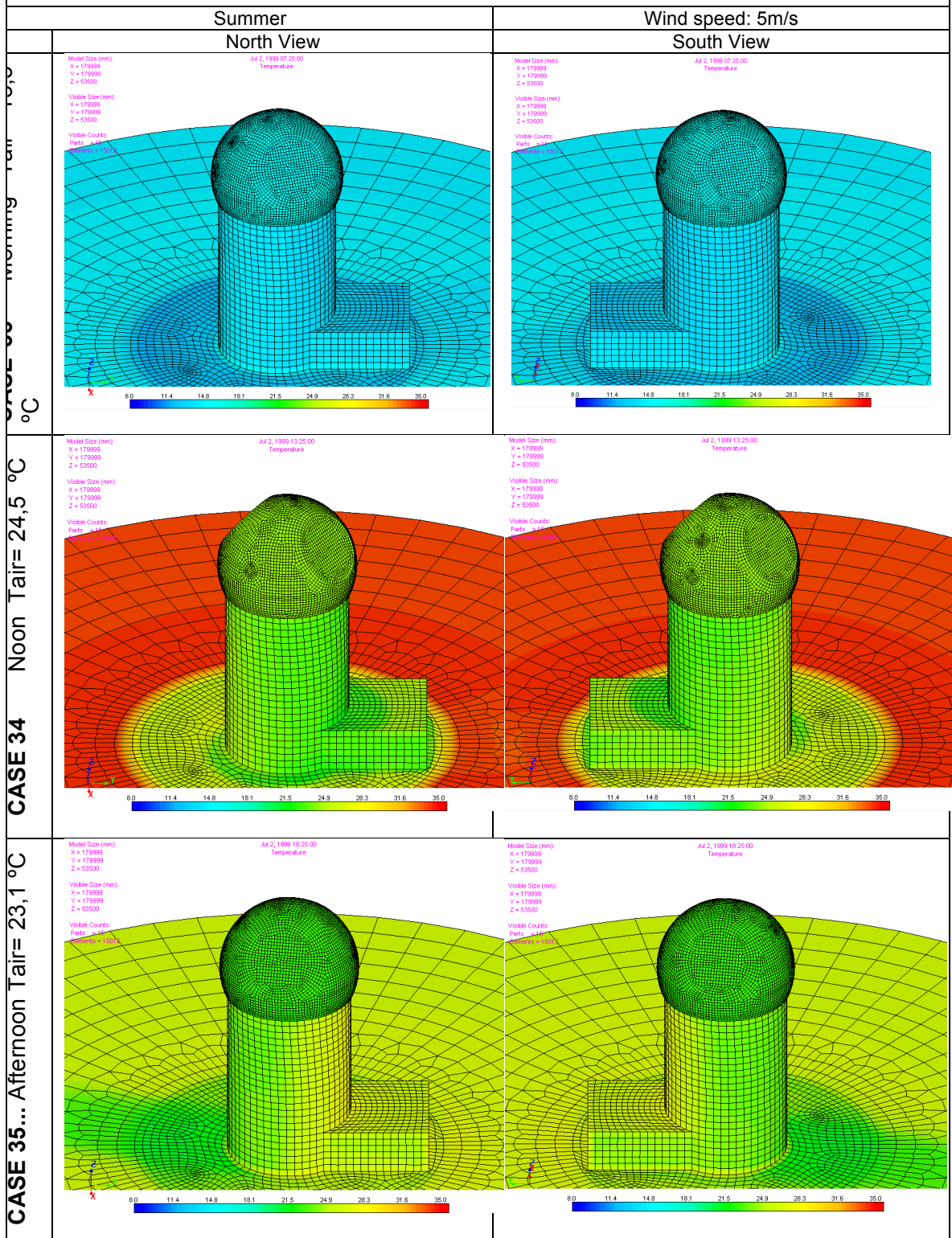
Cartesian frame of reference of each figure corresponds to the compass directions described below:

- X axis (red) corresponds to the north.
- Y axis (green) corresponds to the east.
- Z axis (blue) corresponds to the zenith.

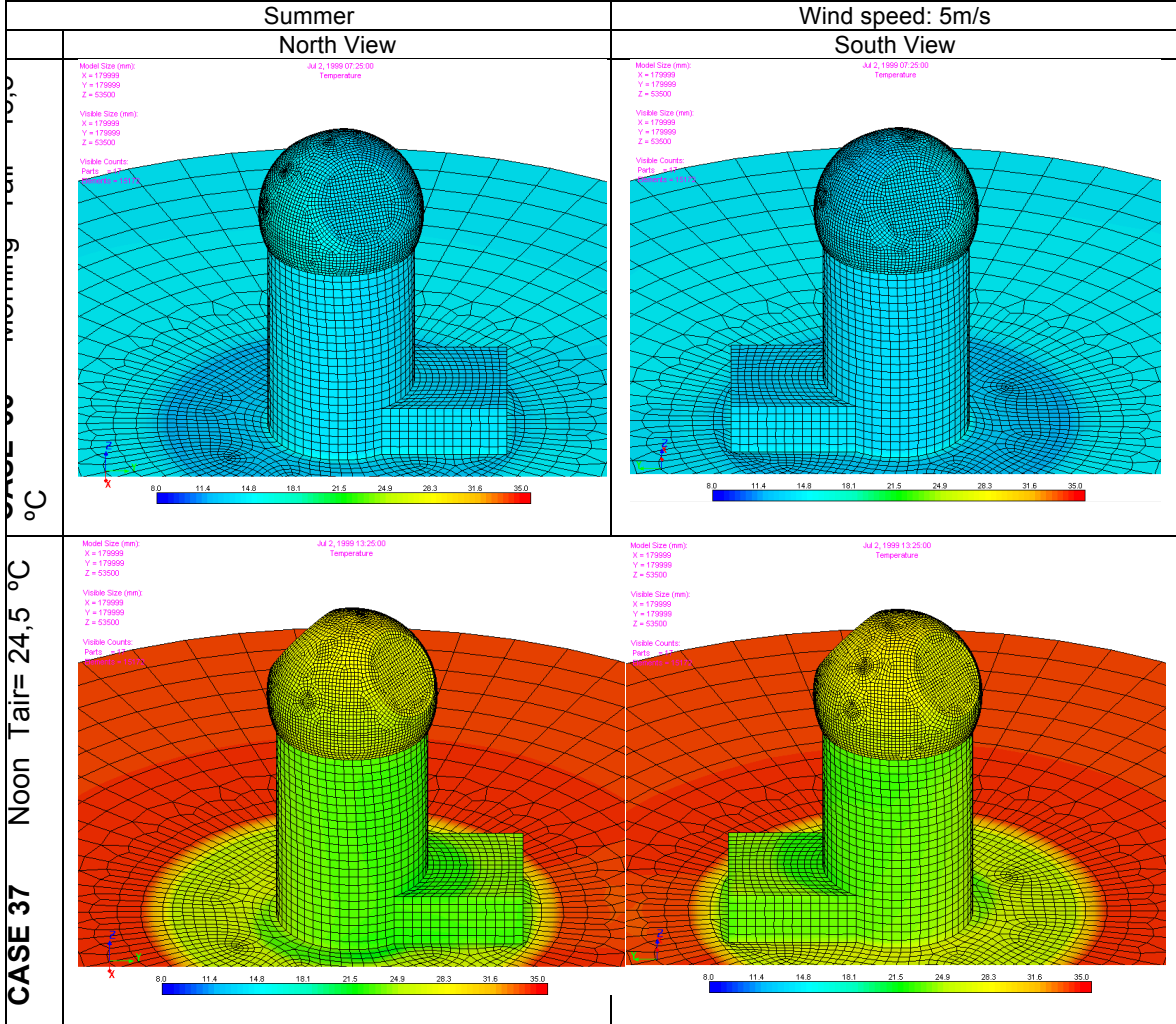
DOME ANALYSIS



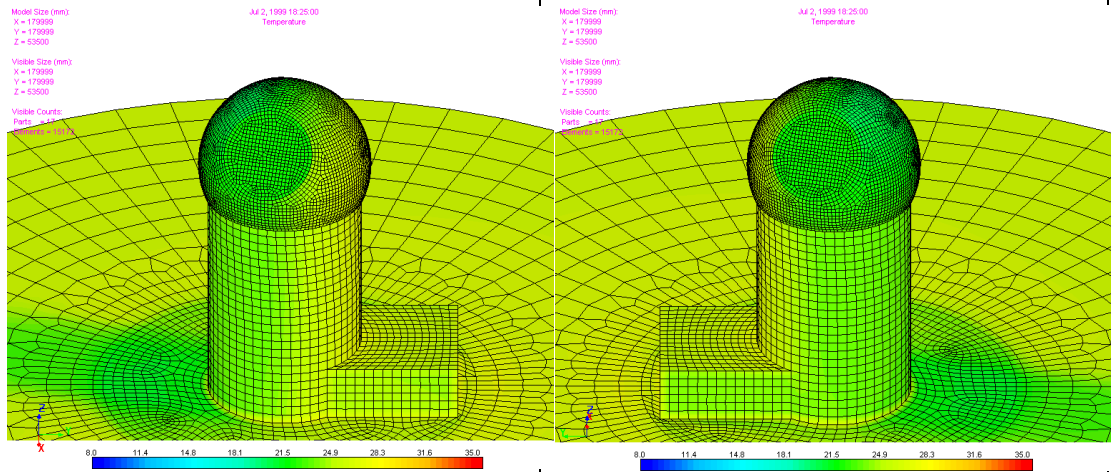
DOME THERMAL CONTROL ANALYSIS



HEAT STOP ANALYSIS – AIR INSIDE DOME



CASE 38... Afternoon Tair= 23,1 °C

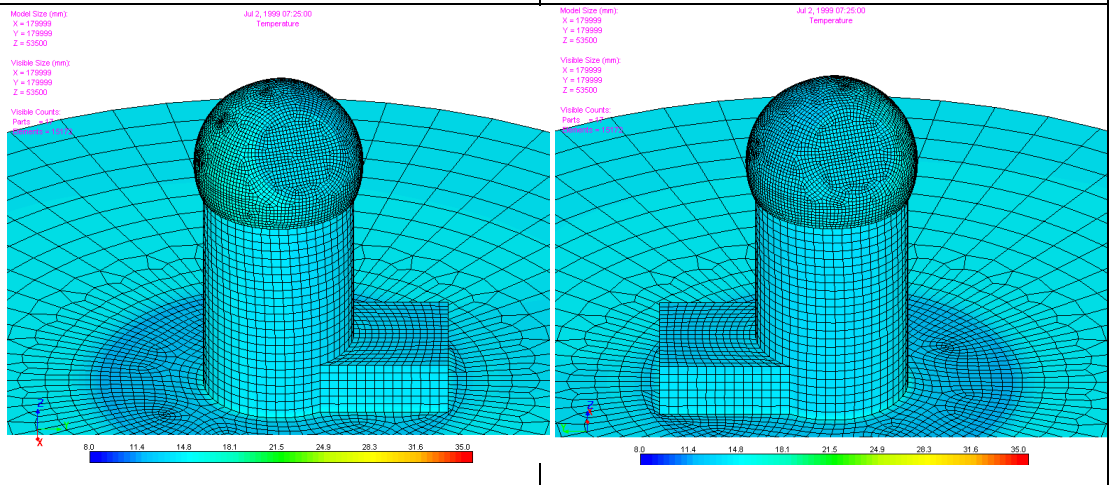


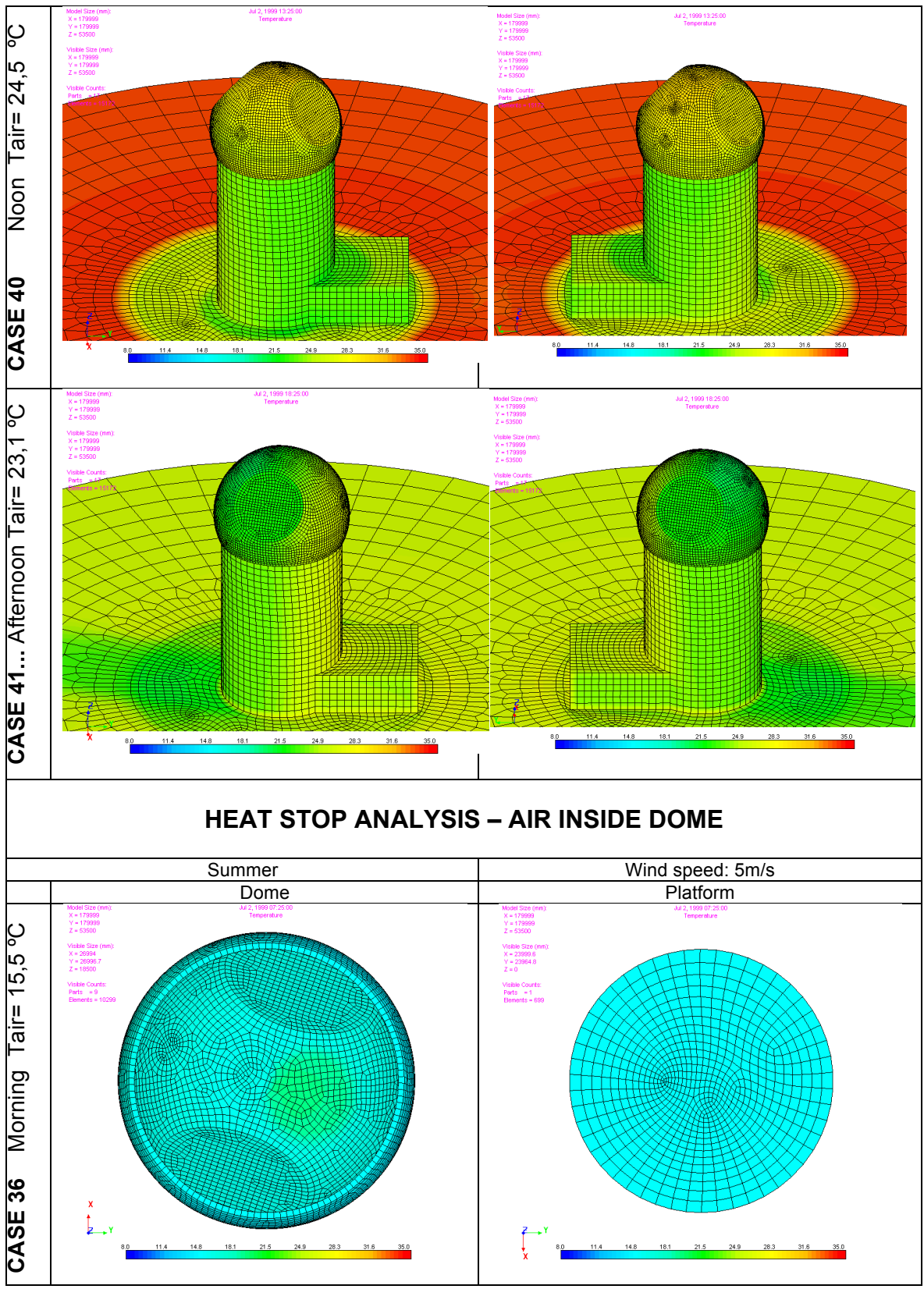
HEAT STOP ANALYSIS – WIND INSIDE DOME

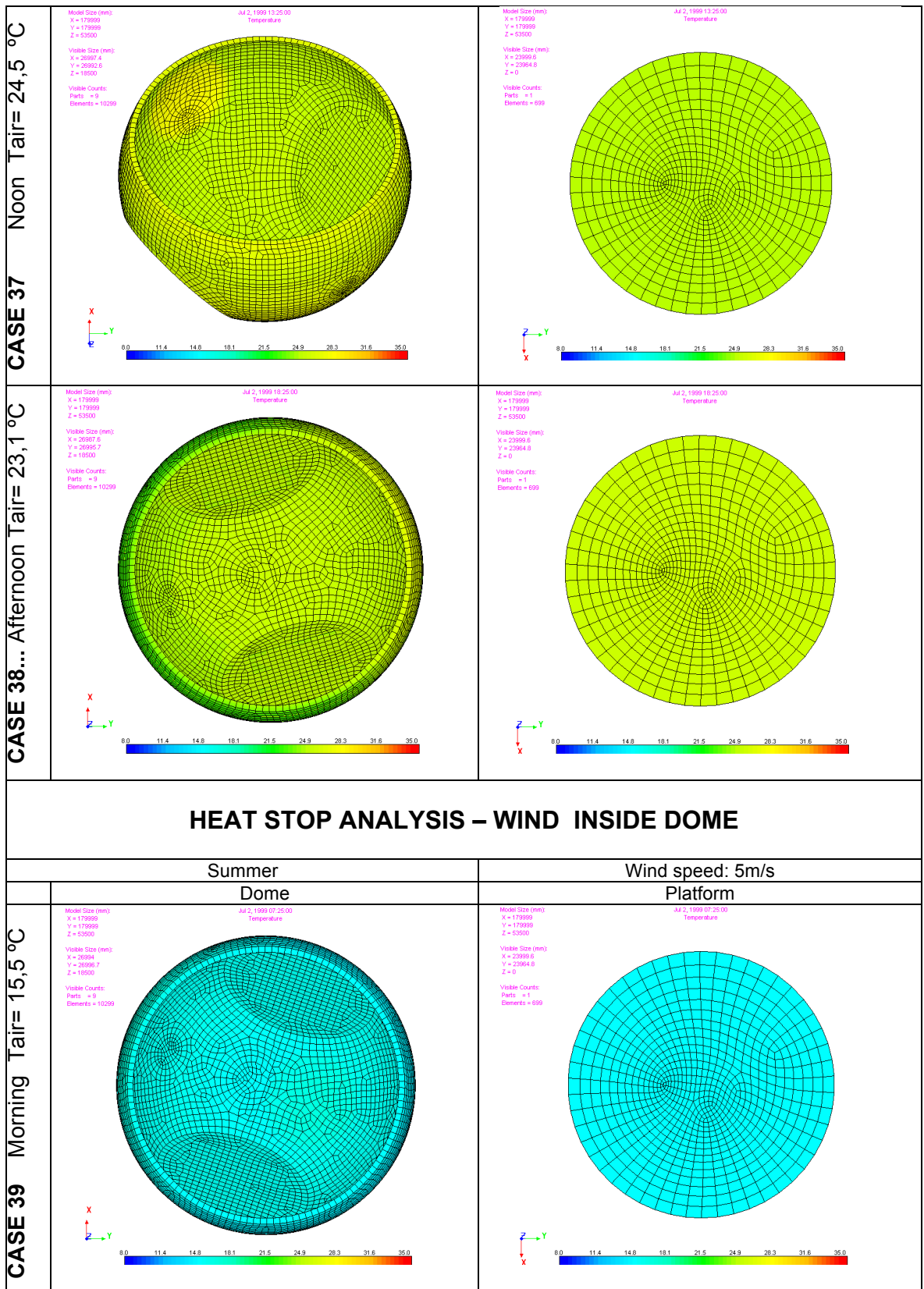
Summer
North View

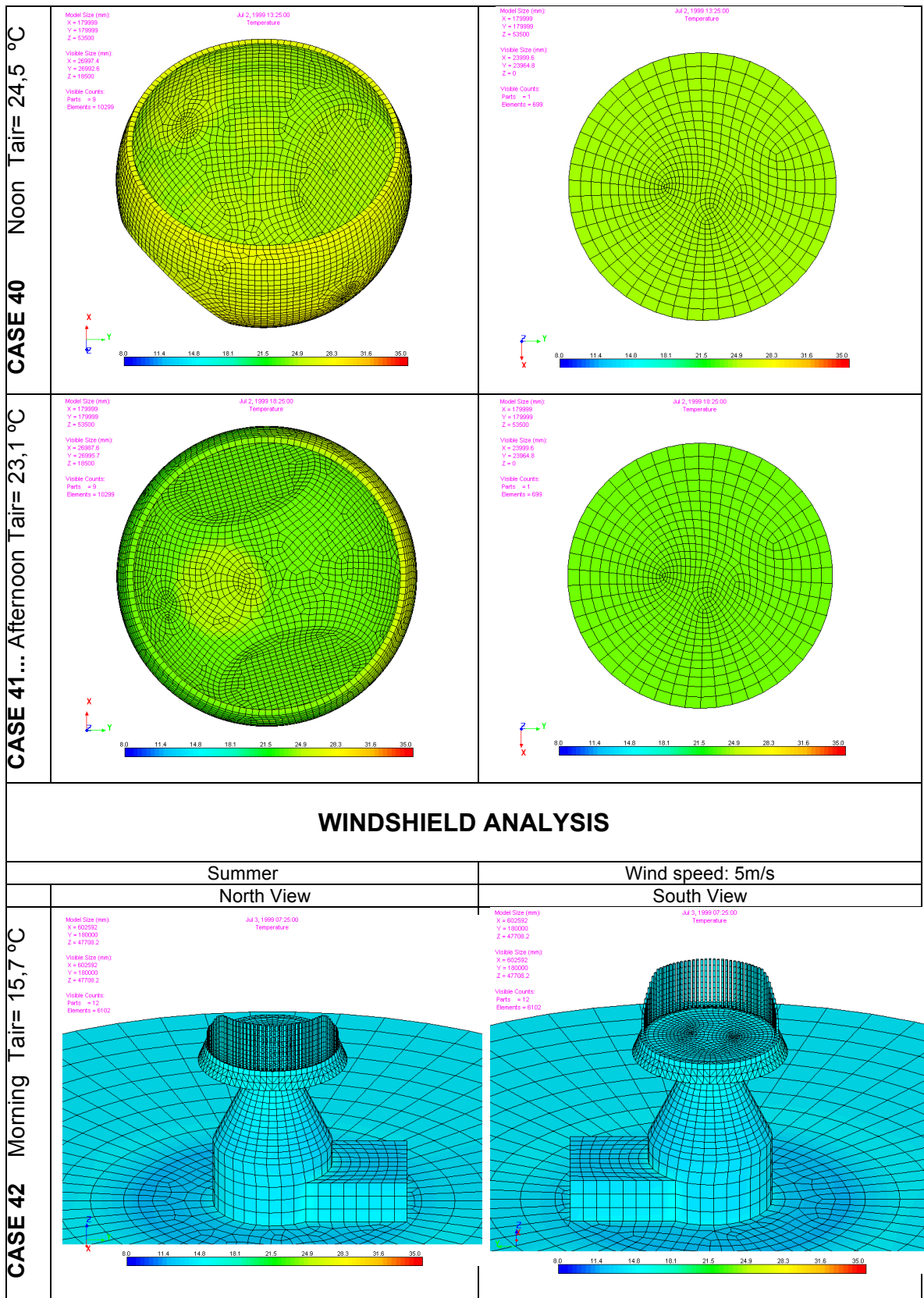
Wind speed: 5m/s
South View

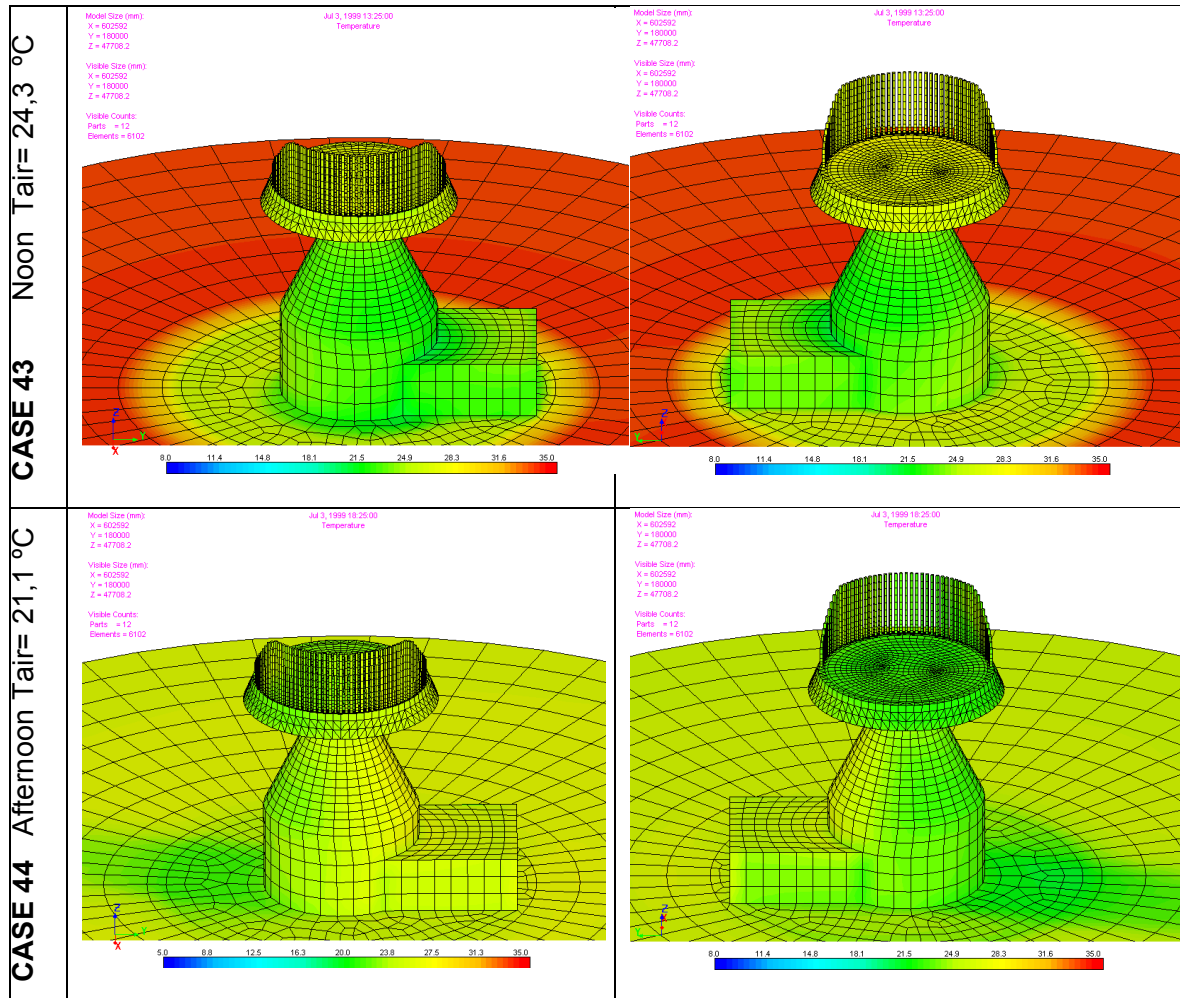
CASE 39 Morning Tair= 15,5 °C











3.3 Results analysis

In the following paragraphs the results are analysed in details, with a particular focus on the significant elements or conditions that differ between models.

The temperature of each part or element used is plotted as its difference with the air temperature, so long as we talk about degrees of difference will be referring to temperature difference relative to the air, if not otherwise specified..

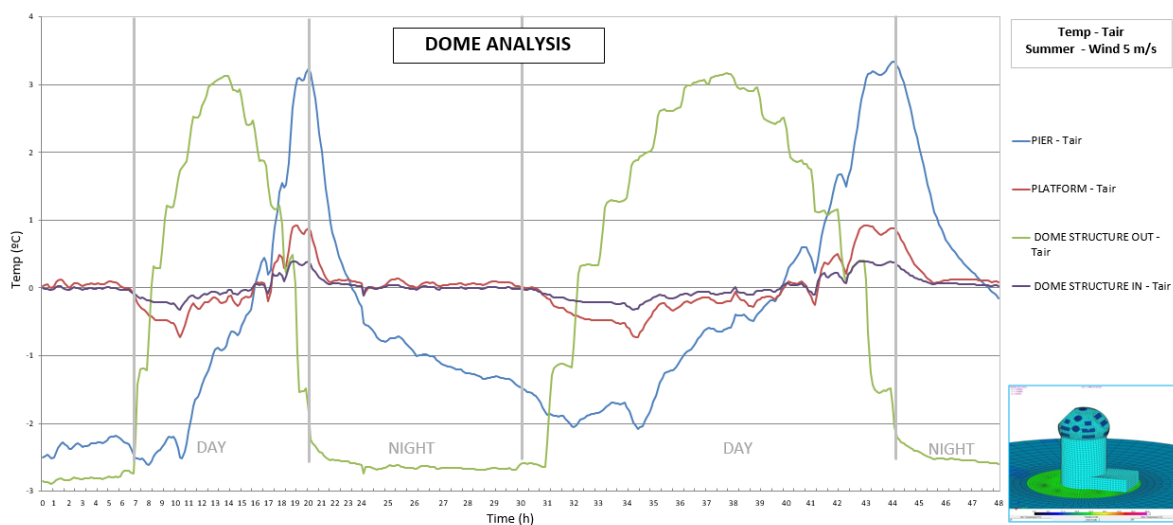
3.3.1 Closed Configuration

3.3.1.1 Dome without Thermal Control.

The average temperatures measured at "Dome Analysis" show that the interior elements (Dome Structure IN and Platform) keep a temperature close to the air temperature (+/-1°C), while the outer elements reach 2 to 3 degrees of difference with the ambient air.

EST TELESCOPE ENVIRONMENT PRELIMINARY THERMAL ANALYSIS II	Page: 34 of 54 Date: November 13, 2014
Code: DM/TN-SNT/011v.1	File: DELIVERABLE70_4B.DOCX

Inner elements (Dome Structure In and Platform) cool below ambient air during morning and afternoon, and show a minimum temperature difference 4,5 hours after sunrise, outer elements (Dome Structure Out and Pier) heat above ambient air during day. Dome shows a maximum temperature difference of 3.2°C at 14:00, when solar radiation is maximum and pier reaches the maximum temperature difference at 20:00 because of its higher thermal inertia. (See model configuration in Table 4). When the air temperature decreases, at evening, inner elements are not able to dissipate heat as rapidly as the air temperature decreases, and they are still hot nearly one degree respect to the ambient air temperature in



case of platform and 0.5°C in case of dome.

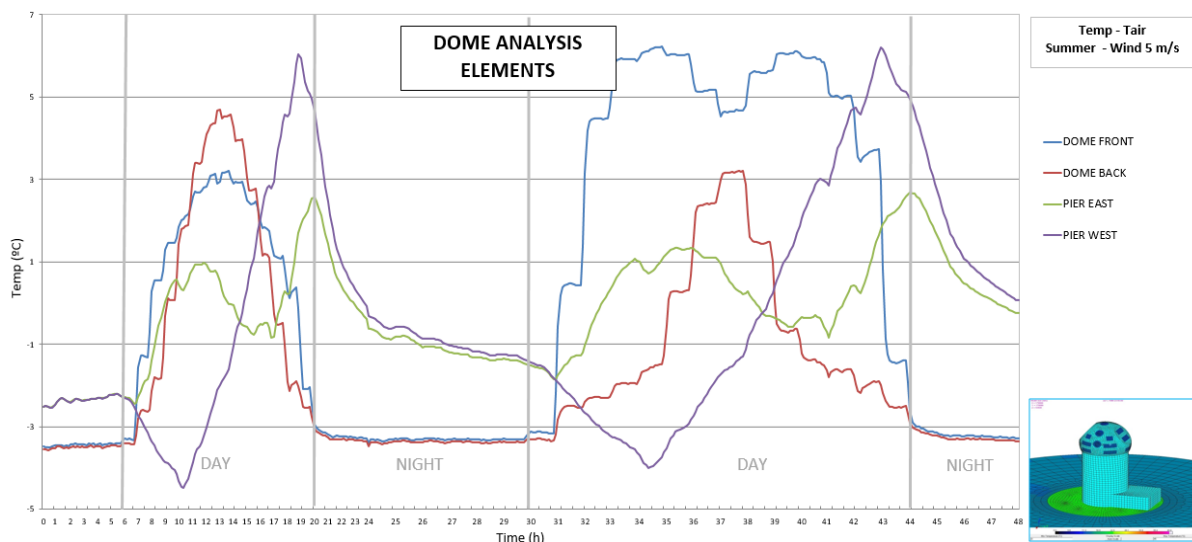
Figure 12: 48 hours evolution of the temperature difference between main elements (Platform, Dome Out, Dome In and Pier) and ambient air for 5 m/s wind in summer conditions. Dome Analysis.

EST TELESCOPE ENVIRONMENT PRELIMINARY THERMAL ANALYSIS II	Page: 35 of 54 Date: November 13, 2014
Code: DM/TN-SNT/011v.1	File: DELIVERABLE70_4B.DOCX

The following graph shows a look in details of what happens for the interior elements. During the first day of the test, the four elements remain static, each one oriented at the four points of the compass, north and south elements are located on the dome, and east and west elements on the pier, the second day the dome elements are rotating, so "Front Dome" element always faces the sun.

Notice how "Pier East" reaches two maximums, first during the morning up to 1.5 °C at 12:00 and second during evening, 2.7°C above air temperature at 20:00. "Pier West" element is sub cooling during the morning reaching a minimum of -4°C at 10:00, after this, the incident continuous radiation causes an increase in the temperature difference, reaching +6.2°C above the ambient temperature at 19:00. The behaviour of the elements located at the pier is similar during the first and second day.

Dome elements have very different behaviour during the first and second day. During the first day, the element that receives more radiation is "Dome Back", facing south, reaches +4.8°C difference at 13:00 and -3.5°C overnight, "Dome Front" element is sub cooling equally during night but during day reaches +3.2°C above the ambient air. The second day, once stabilized the model, the front of the dome has several degrees above the temperature of the air for most of the day. Two peaks are observed, one at 10:00 of +6.23°C and another of +6°C at 16:00, including a minimum of +4.5°C at 13:30 produced by an increase in the air temperature. The back side, "Dome Back" element, only for 4 hours (11:00-15:00) heats above



ambient air, and reaches a maximum at 14:00 of +3.2°C.

Figure 13: 48 hours evolution of the temperature difference between four elements and ambient air. "Dome Front" at the sun facing side of the dome, "Dome Back" at rear part of the dome, shadow side.

EST TELESCOPE ENVIRONMENT PRELIMINARY THERMAL ANALYSIS II	Page: 36 of 54 Date: November 13, 2014
Code: DM/TN-SNT/011v.1	File: DELIVERABLE70_4B.DOCX

“Pier East” located in the east of the pier and “West Pier” on the west side, both at half height. Dome Analysis.

EST TELESCOPE ENVIRONMENT PRELIMINARY THERMAL ANALYSIS II	Page: 37 of 54 Date: November 13, 2014
Code: DM/TN-SNT/011v.1	File: DELIVERABLE70_4B.DOCX

The following graph shows the interior elements, located on the platform and dome inner surface, all the elements remain within a temperature range of +/-1°C with ambient air, only during afternoon, the temperature difference increases slightly reaching +0.92°C at 19:00, in case of platform, and +0.42°C in case of the dome elements.

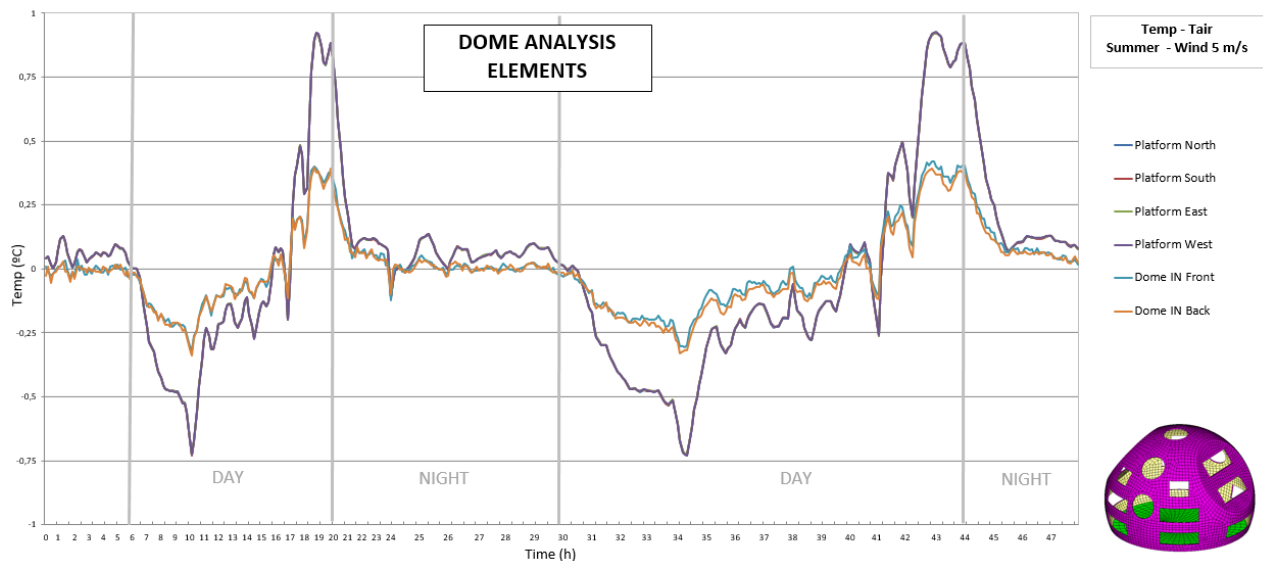


Figure 14: 48 hours evolution of the temperature difference between six elements at the inner part of the dome and ambient air. "Dome Front" at the sun facing side of the dome, "Dome Back" at rear part of the dome, shadow side. The remaining four elements are located on the platform at the four points of the compass, near the edge. Dome Analysis.

3.3.1.2 Dome with Thermal Control.

The average temperatures measured at "Dome Thermal Control Analysis" show a similar trend during test, except at "Dome Structure Out", which keeps temperature difference within a range of +/-1°C with respect to the air temperature, due to the thermal control at the outer surface of the dome.

During the day, dome temperature heats over ambient air temperature to a maximum of 0.28°C at 10:00, and reaches a minimum temperature difference of -0.35°C at 18:30.

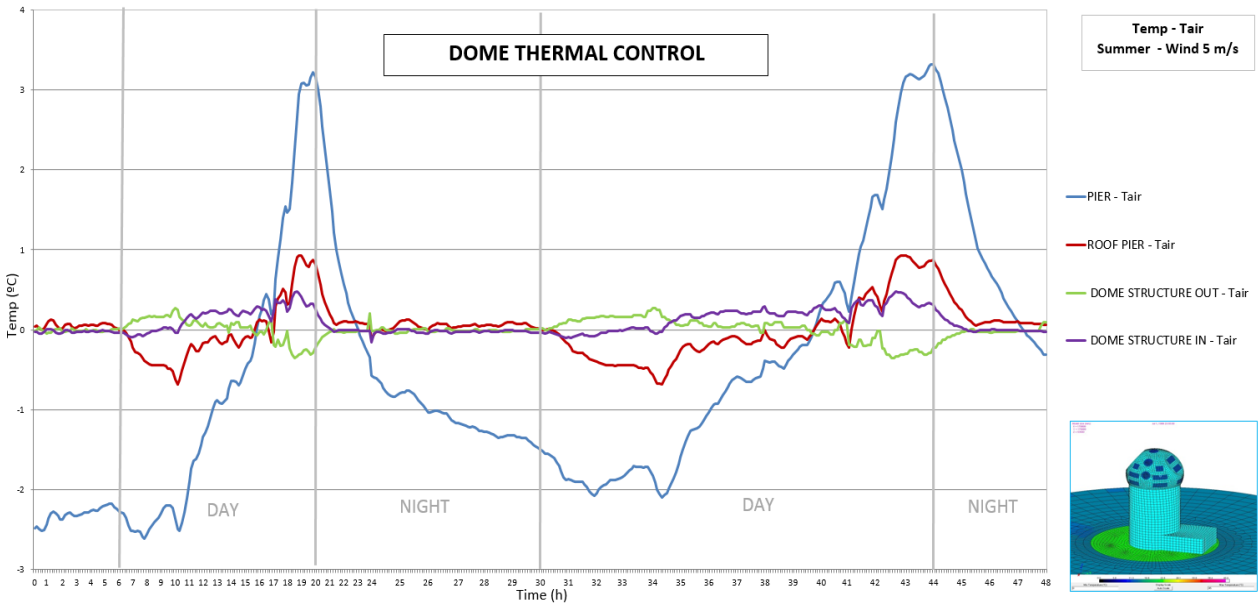
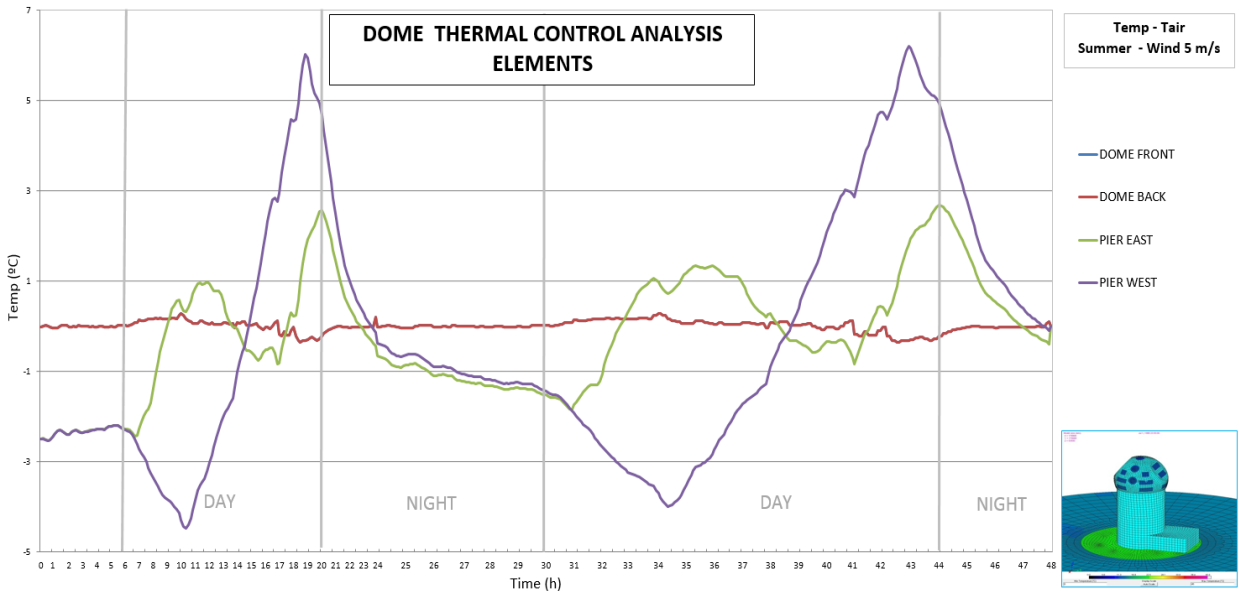


Figure 15: 48 hours evolution of the temperature difference between main elements (Platform, Dome Out, Dome In and Pier) and ambient air for 5 m/s wind in summer conditions. Dome Thermal Control Analysis.

There are not significant changes for the elements located at pier, however dome structure elements show how the thermal control stabilizes the dome temperature, keeping its temperature, both front and rear, very close to the air



temperature (+/- 0.2°C).

Figure 16: 48 hours evolution of the temperature difference between four elements and ambient air. "Dome Front" at the sun facing side of the dome, "Dome Back" at rear part of the dome ("Dome Front"

EST TELESCOPE ENVIRONMENT PRELIMINARY THERMAL ANALYSIS II	Page: 39 of 54 Date: November 13, 2014
Code: DM/TN-SNT/011v.1	File: DELIVERABLE70_4B.DOCX

and "Dome Back" are overlapped in the graph), shadow side. "Pier East" located in the east of the pier and "West Pier" on the west side, both at half height. Dome Thermal Control Analysis.

The interior elements, located on the platform, behave similarly to the results of the analysis without thermal control. The inner elements of the dome present some variations, mainly the "Dome IN Front" element which has an offset of +0.3°C comparing with the results of the previous analysis in which its temperature was similar to the back side element. This slight difference is probably due to the different configurations parameters of the dome, which produces heating in the front part of the dome relative to the rear.

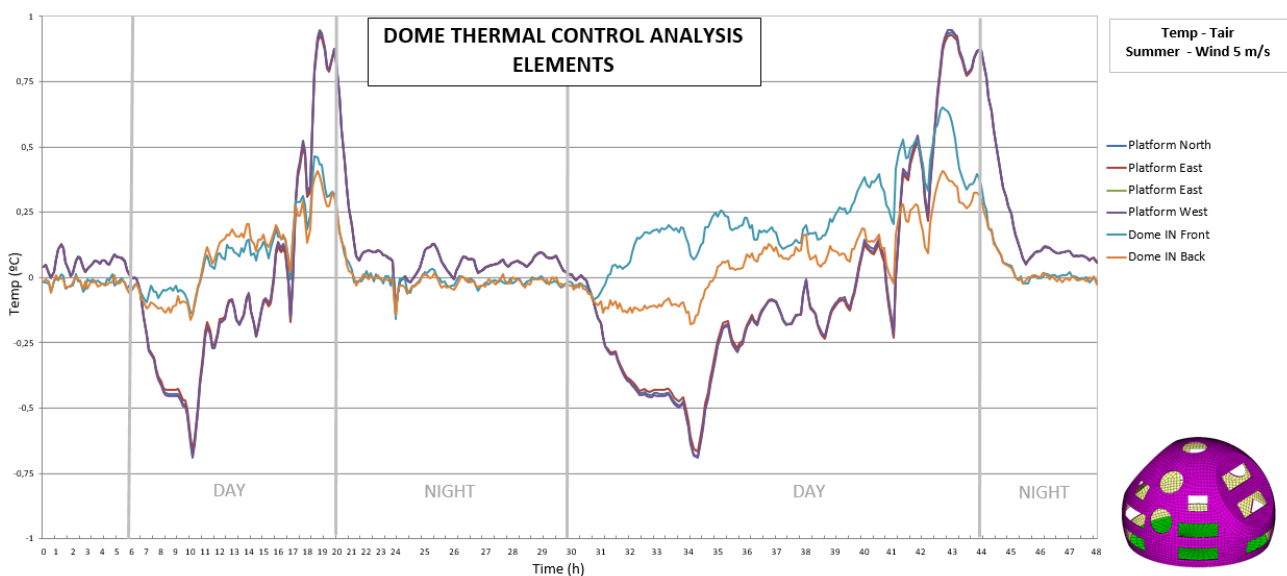


Figure 17: 48 hours evolution of the temperature difference between six elements at the inner part of the dome and ambient air. "Dome Front" at the sun facing side of the dome, "Dome Back" at rear part of the dome, shadow side. The remaining four elements are located on the platform at the four points of the compass, near the edge. Dome Thermal Control Analysis.

3.3.1.3 Dome Heat Stop.

"Heat Stop Analysis" simulate the effects of heat projected towards the inner surface of the dome. The following figure shows main temperatures of the analysis, performed with ambient air inside the dome. All the elements that receive part of the heat rejected, increase their temperature during the test.

The platform cools below ambient during morning until noon with a minimum of -1.08°C, and during the afternoon temperature increases to a maximum of +4.43°C at 20:00. Dome inner Surface heats over ambient temperature throughout the day and even during night with a maximum of +3.34°C at 20:00, and follows the same evolution as the "heat projection", this area is the most affected by the deflection of the light beam and the whole

EST TELESCOPE ENVIRONMENT PRELIMINARY THERMAL ANALYSIS II	Page: 40 of 54 Date: November 13, 2014
Code: DM/TN-SNT/011v.1	File: DELIVERABLE70_4B.DOCX

day remains overheated, with respect to the air. The maximum temperature difference is +6.64°C, observed at 20:00.

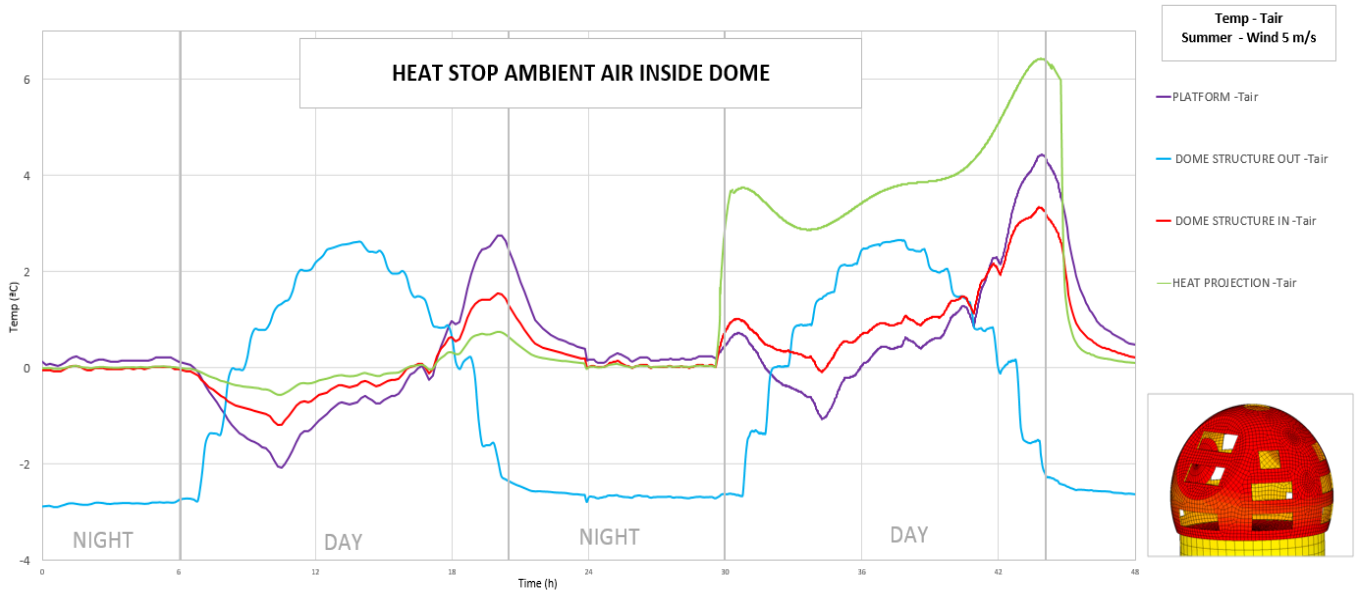
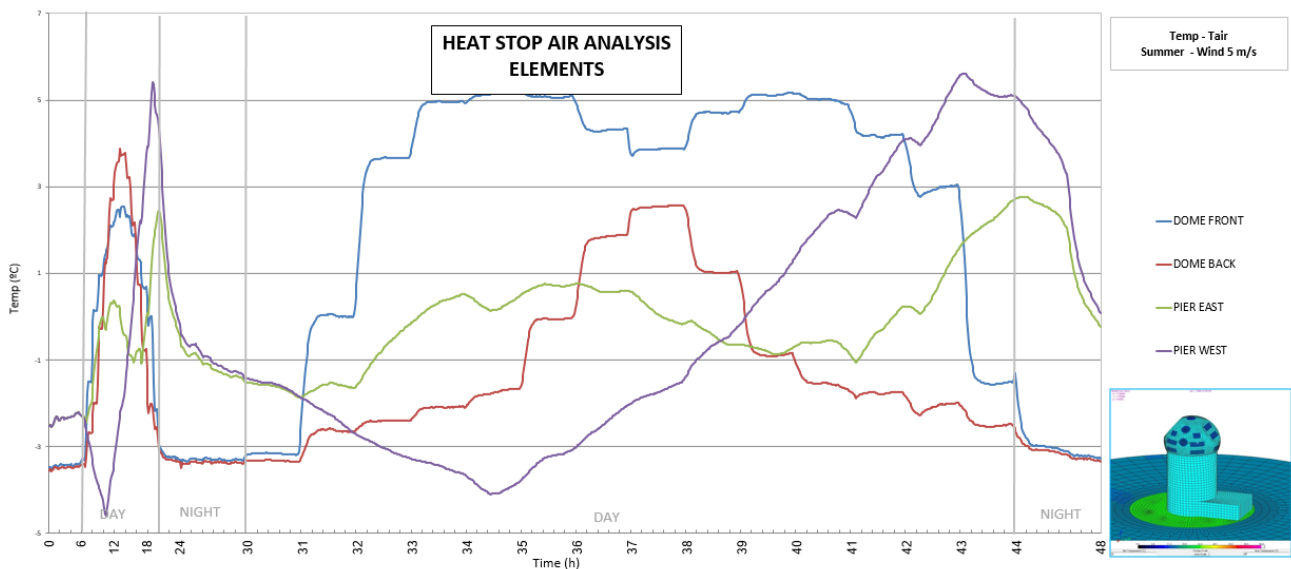


Figure 18: 48 hours evolution of the temperature difference between main elements (Platform, Dome Out, Dome In and Heat Projection) and ambient air for 5 m/s wind in summer conditions. Heat Stop Analysis – Air inside dome.

The analysis of the external elements, provides similar results to the initial analysis of the dome, "Analysis Dome". The most notable difference is the temperature for the outside of the dome, which reaches a maximum of 5,24 °C , instead of 6.23°C, caused by a higher temperature inside dome which reduces the



EST TELESCOPE ENVIRONMENT PRELIMINARY THERMAL ANALYSIS II	Page: 41 of 54 Date: November 13, 2014
Code: DM/TN-SNT/011v.1	File: DELIVERABLE70_4B.DOCX

difference with the air temperature.

Figure 19: 48 hours evolution of the temperature difference between four elements and ambient air. "Dome Front" at the sun facing side of the dome, "Dome Back" at rear part of the dome, shadow side. "Pier East" located in the east of the pier and "West Pier" on the west side, both at half height. Heat Stop Analysis-Air inside dome.

The following figure shows the variation of the temperature of the interior elements, among them "Dome Back" stands out, the element at the rear part of the dome affected by the heat projection during the midday. After 12:00 the temperature of this part of the dome heats up to a maximum of 4.14°C at 13:30, from this point is cooled to equalize the temperature of the dome.

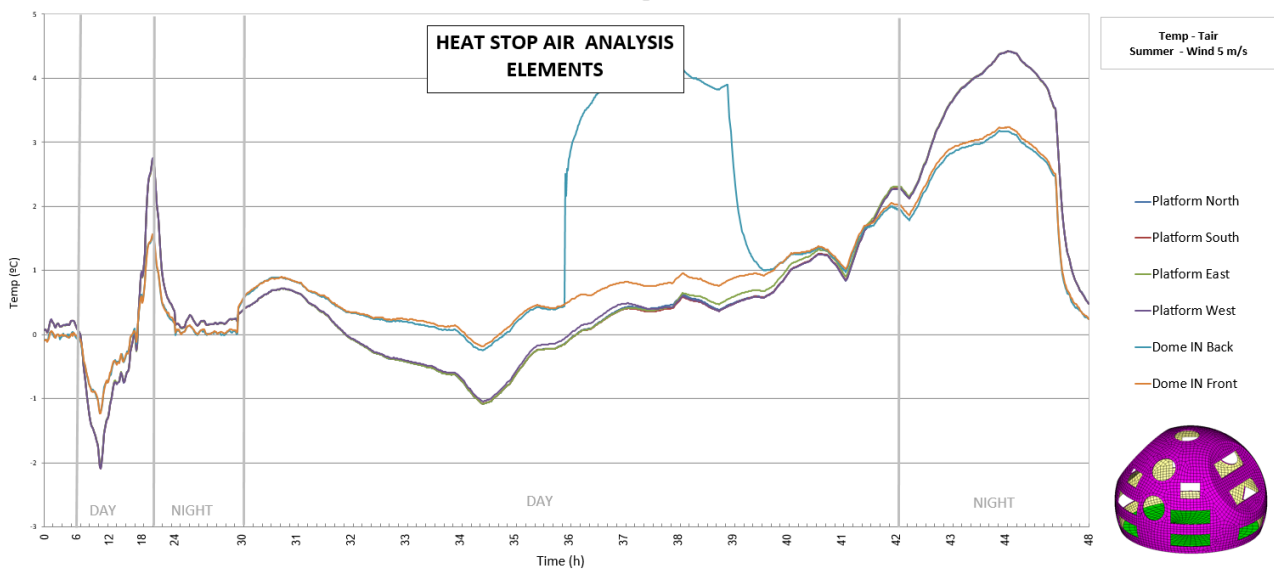


Figure 20: 48 hours evolution of the temperature difference between six elements at the inner part of the dome and ambient air. "Dome Front" at the sun facing side of the dome, "Dome Back" at rear part of the dome, shadow side. The remaining four elements are located on the platform at the four points of the compass, near the edge. Heat Stop Analysis-Air inside dome.

At "Heat Stop Wind" analysis, wind parameter is set inside the dome, thus facilitates heat transfer by convection. As shown in the graph below, the maximum temperatures differences for each element are greatly reduced. "Dome Structure In" heats over the ambient air temperature up to a maximum of +0.74°C, "Platform" reaches a maximum of +1.26°C at 20:00 and "Dome Structure In" only increases its temperature of +0.74°C above ambient air. The outside of the dome, "Dome Structure Out" acquires a temperature profile similar to the first analysis, "Dome Analysis".

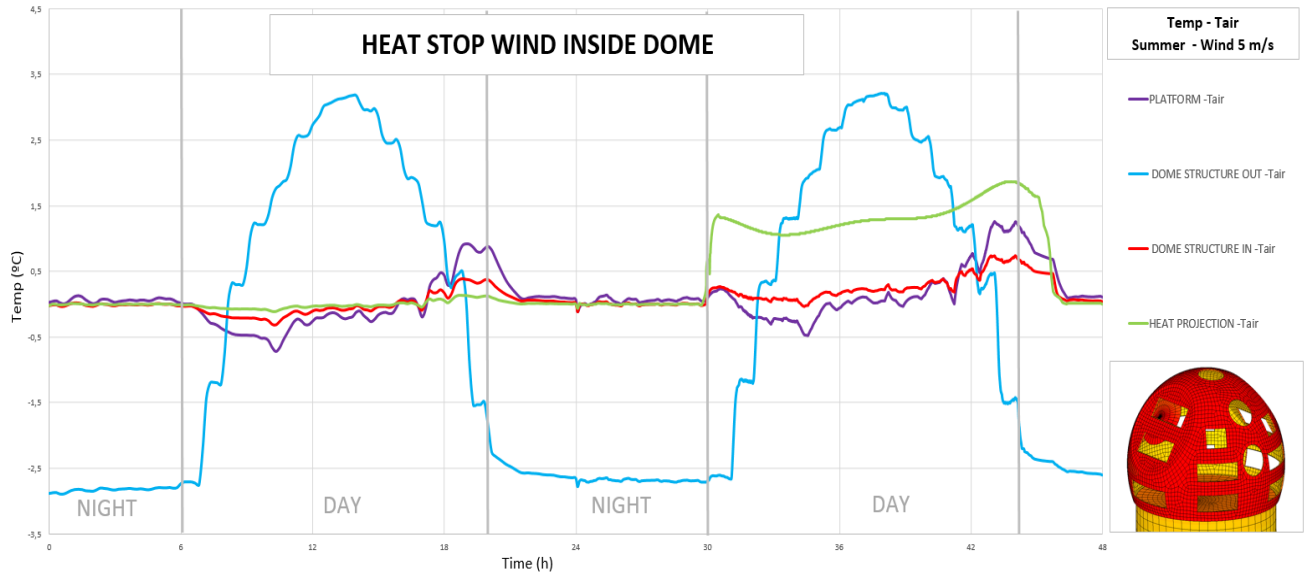
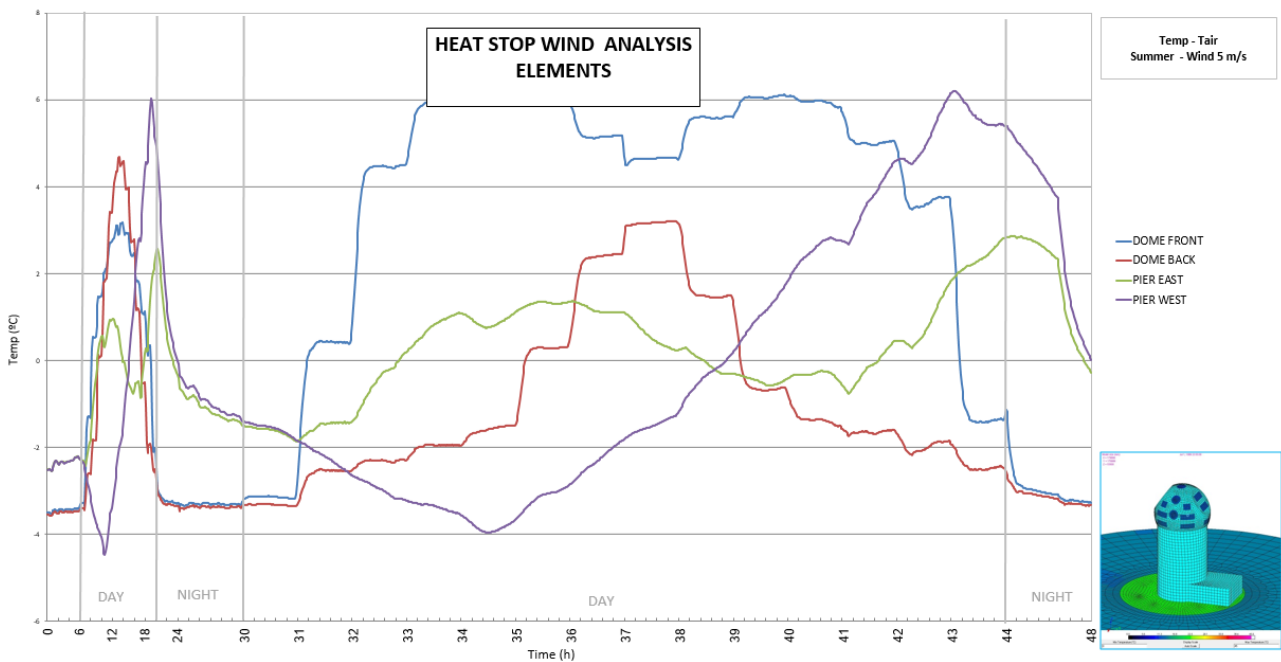


Figure 21: 48 hours evolution of the temperature difference between main elements (Platform, Dome Out, Dome In and Heat Projection) and ambient air for 5 m/s wind in summer conditions. Heat Stop Analysis-Wind inside dome.

The analysis of the outer elements (following figure) does not reveal significant changes in behaviour of the elements; it is similar to the reference

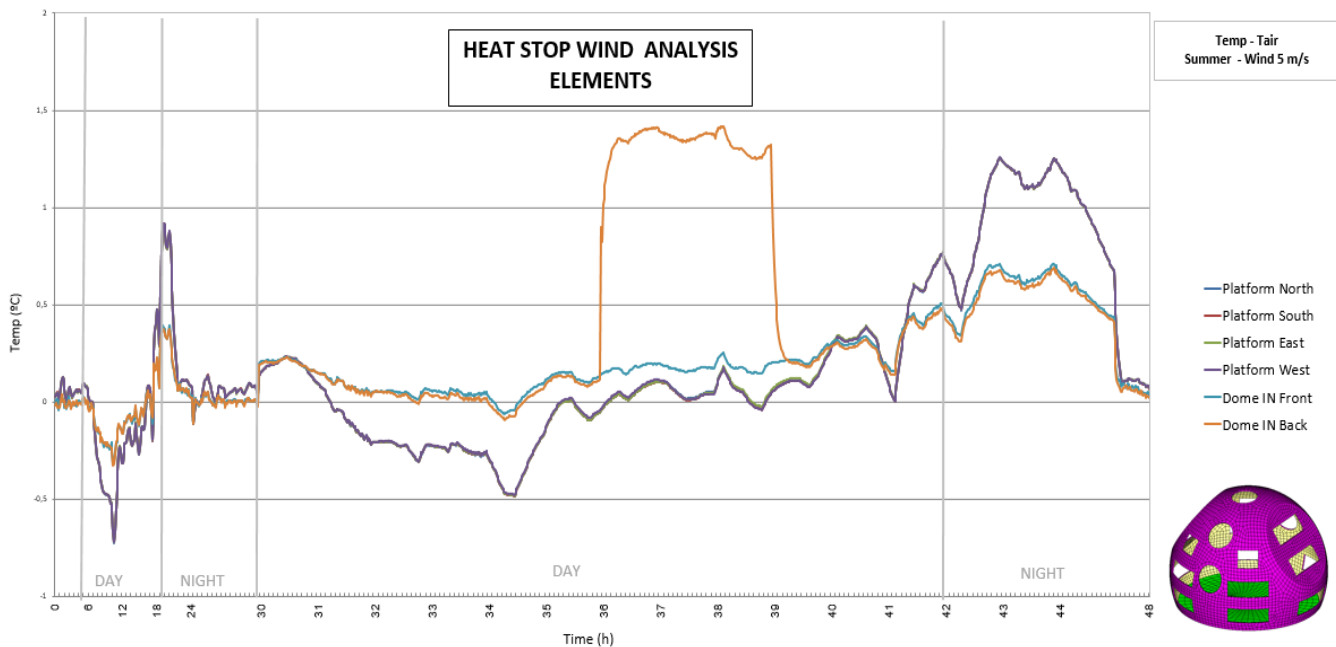


analysis, "Dome Analysis".

EST TELESCOPE ENVIRONMENT PRELIMINARY THERMAL ANALYSIS II	Page: 43 of 54 Date: November 13, 2014
Code: DM/TN-SNT/011v.1	File: DELIVERABLE70_4B.DOCX

Figure 22: 48 hours evolution of the temperature difference between four elements and ambient air. "Dome Front" at the sun facing side of the dome, "Dome Back" at rear part of the dome, shadow side. "Pier East" located in the east of the pier and "West Pier" on the west side, both at half height. Heat Stop Analysis-Wind inside dome.

The following figure shows the variation of the temperature of the interior elements. "Dome Back", the element at the rear part of the dome affected by the heat projection during the midday heats up to a maximum of +1.4°C for three hours, (12:00- 15:00), three degrees less than in the previous analysis, "Heat Stop Air". Not only this element is colder, the temperature difference of all elements has been



reduced about three degrees by increasing the thermal dissipation capacity.

Figure 23: 48 hours evolution of the temperature difference between six elements at the inner part of the dome and ambient air. "Dome Front" at the sun facing side of the dome, "Dome Back" at rear part of the dome, shadow side. The remaining four elements are located on the platform at the four points of the compass, near the edge. Heat Stop Analysis-Wind inside dome.

EST TELESCOPE ENVIRONMENT PRELIMINARY THERMAL ANALYSIS II	Page: 44 of 54 Date: November 13, 2014
Code: DM/TN-SNT/011v.1	File: DELIVERABLE70_4B.DOCX

3.3.2 Open Configuration with Windshield

The average temperatures measured at Windshield analysis are shown in the following figure. During most of the day the temperatures of all the elements with low thermal inertia reach 1 to 3°C of difference with the ambient air, and the elements with high thermal inertia reach similar differences just before sunset.

The highest difference is located at "Upper Platform", which reaches +3.12°C with respect to the ambient temperature. Temperature of the platform is a critical factor in terms of "local seeing" degradation, and this configuration keeps local seeing optimized only during a few hours after sunrise and before sunset, when its temperature is below the ambient air.

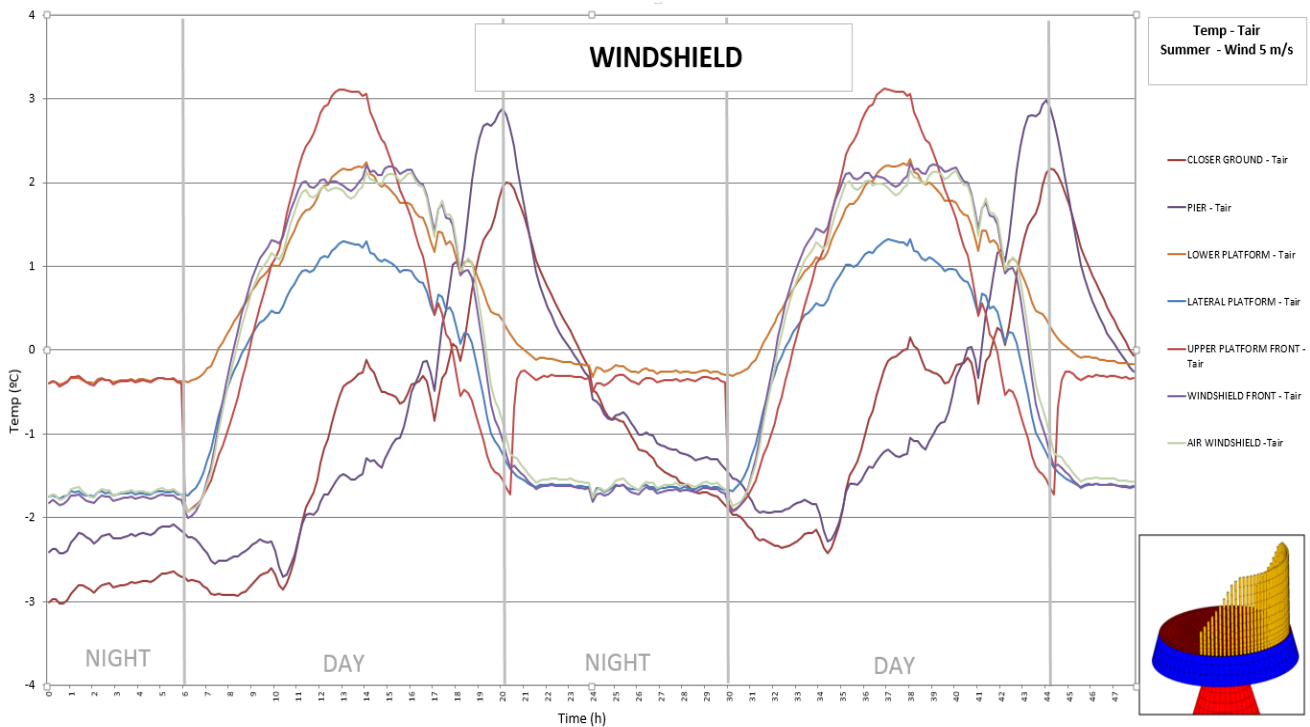


Figure 24: 48 hours evolution of the temperature difference between main elements (Platform, Windshield, Air Windshield and Pier) and ambient air, for 5 m/s wind in summer conditions. Windshield Analysis.

During night an enclosure covers the upper platform. This enclosure cools below air ambient during all night to a minimum of -0.8 °C, in summer conditions. The air inside this enclosure stays below air temperature with a temperature difference of -0.4 °C just before sunrise. The air inside windshield bars is very sensitive to temperature changes between day and night, during the night it cools below ambient air to a minimum of -1.75°C just after sunrise and reaches up to a maximum temperature difference of +2.2°C at noon.

EST TELESCOPE ENVIRONMENT PRELIMINARY THERMAL ANALYSIS II	Page: 45 of 54 Date: November 13, 2014
Code: DM/TN-SNT/011v.1	File: DELIVERABLE70_4B.DOCX

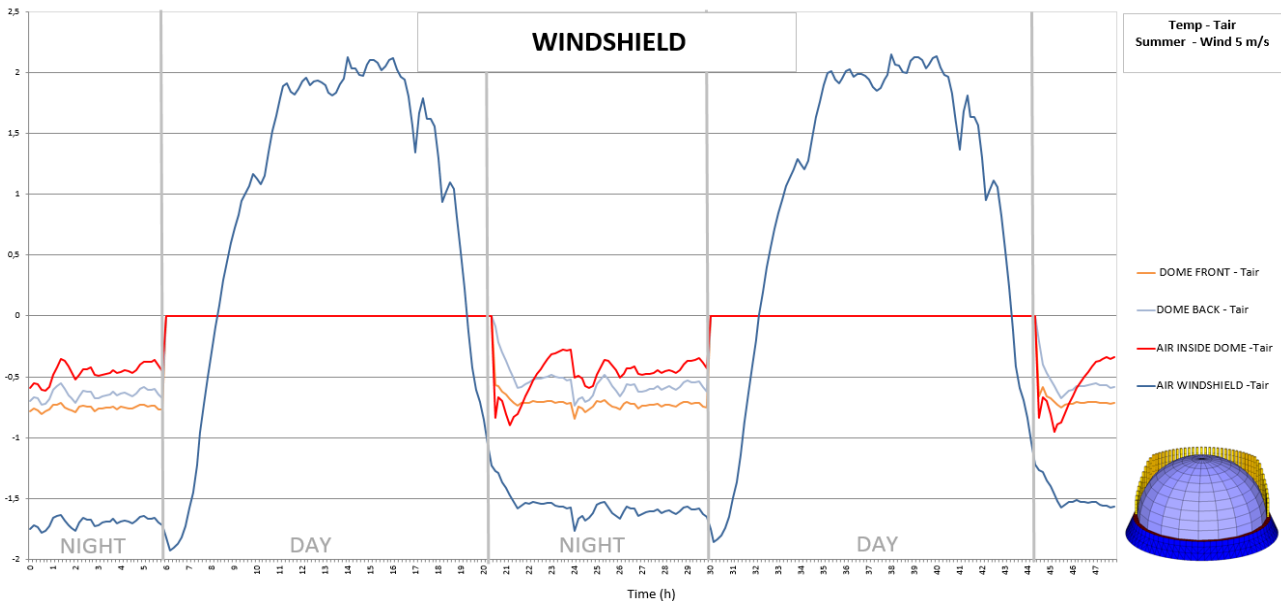


Figure 25: 48 hours evolution of the temperature difference between Retractable Dome (outer and inner side) and ambient air. The graphic also shows temperature difference between stagnant air (inside dome and windshield) and ambient air. Windshield Analysis

The following figure shows temperatures of different elements located at pier and lateral platform. As in the previous analysis, the western part of the pillar is heated much more than the eastern part, and in this case it reaches 4.81 ° above the air temperature. On the lateral platform, east and west sides reach higher temperatures, +2.77°C and +2.85°C respectively.

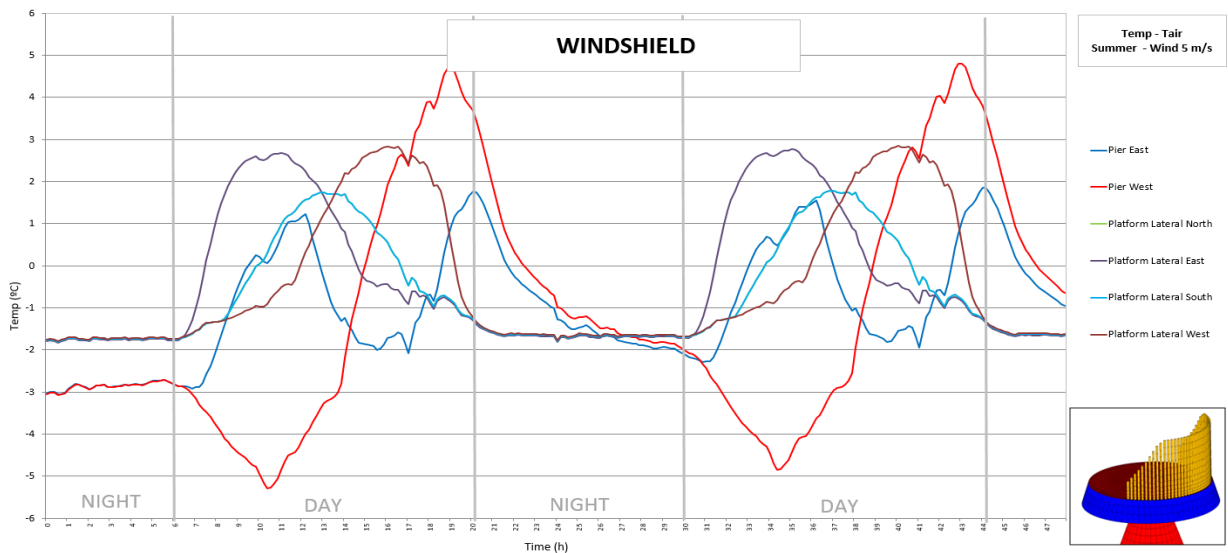
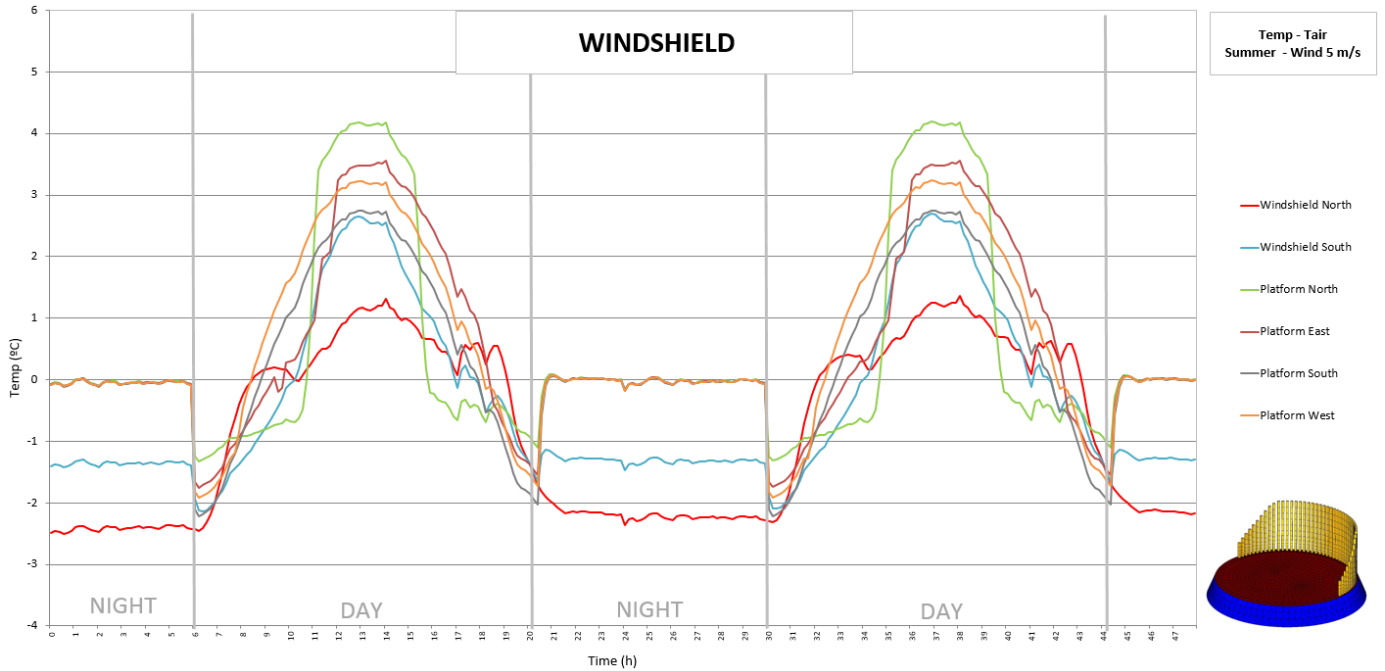


Figure 26: 48 hours evolution of the temperature difference between six elements and ambient air. "Pier East" and "Pier West" and four elements located on the lateral platform at the four points of the compass. Windshield Analysis.

EST TELESCOPE ENVIRONMENT PRELIMINARY THERMAL ANALYSIS II	Page: 46 of 54 Date: November 13, 2014
Code: DM/TN-SNT/011v.1	File: DELIVERABLE70_4B.DOCX

Looking in details at the state of windshield during analysis is seen as remains sub cooled two or three hours after sunrise and before sunset. With regard to the platform, stand out as the north side during morning is covered by the windshield and remains cooler than air until 11:00, from that moment increases its temperature quickly up to +4.19° at noon repeats the same behaviour that it had in



the morning.

Figure 27: 48 hours evolution of the temperature difference measured for six elements and ambient air. Two elements are located on the wind shield, one on the north side and one on the south side, both in the central part of the shield. The remaining four elements are located on the platform at the four points of the compass, near the edge. Windshield Analysis.

EST TELESCOPE ENVIRONMENT PRELIMINARY THERMAL ANALYSIS II	Page: 47 of 54 Date: November 13, 2014
Code: DM/TN-SNT/011v.1	File: DELIVERABLE70_4B.DOCX

4. CONCLUSIONS

The objective of these analyses is to obtain the temperature maps for the conventional dome and the telescope environment during the day for different configurations under the same environmental conditions as input data to performance CFD Seeing analysis.

Once obtained CFD results, a complete list of configurations for the telescope environment and their respective local seeing degradation will be available in order to select the optimal configuration to minimize the local seeing degradation.

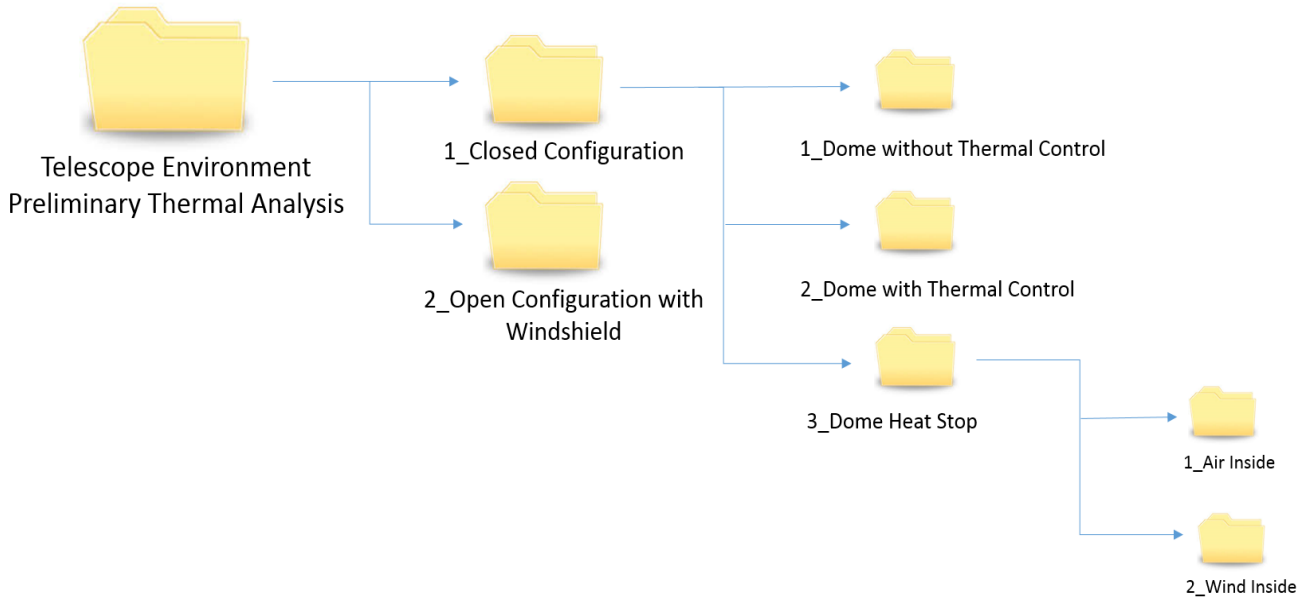
EST TELESCOPE ENVIRONMENT PRELIMINARY THERMAL ANALYSIS II	Page: 48 of 54 Date: November 13, 2014
Code: DM/TN-SNT/011v.1	File: DELIVERABLE70_4B.DOCX

5. ANNEXES

5.1 LIST OF REFERENCE DOCUMENTS

RD.1	TEN-GTC-9001 1.A Definition of preliminary thermal analysis for telescope and environment.
RD.2	RPT-GTC-9002 1.A Telescope Environment Preliminary Thermal Analysis
RD.3	RPT-GTC-9002 1.A Telescope Environment Preliminary Thermal Analysis - Annex I
RD.4	RPT-GTC-9001 1.A Telescope Structure Preliminary Thermal Analysis
RD.5	GREGOR Environmental Specification, O. von der Lühe, Gregor Specification GREKIS-SPE-0001
RD.6	GRE-KIS-SPE-0001-EnvironmentalSpec_11.xls
RD.7	Advanced Technology Solar Telescope lower enclosure thermal system, L.Phelps, M. Warner, SPIE proc. 7017 (2008).
RD.8	Thermal analysis of the Mechanical Structure of the Solar Telescope GREGOR

<p align="center">EST TELESCOPE ENVIRONMENT PRELIMINARY THERMAL ANALYSIS II</p>	<p>Page: 49 of 54 Date: November 13, 2014</p>
<p align="center">Code: DM/TN-SNT/011v.1</p>	<p>File: DELIVERABLE70_4B.DOCX</p>



5.2 LIST OF RADTHERM FILES

Figure 288: Folder tree Radtherm files.

EST TELESCOPE ENVIRONMENT PRELIMINARY THERMAL ANALYSIS II	Page: 50 of 54 Date: November 13, 2014
Code: DM/TN-SNT/011v.1	File: DELIVERABLE70_4B.DOCX

Analysis	Folder Name	Path	Rartherm Files
DOME WITHOUT THERMAL CONTROL	1_Dome without Thermal Control	<i>Telescope Environment Preliminary Thermal Analysis\1_Closed Configuration\1_Dome without Thermal Control</i>	EST_1_DOME_1_july_5wind0.tdf EST_1_DOME_1_july_5wind0B.tdf EST_1_DOME_1_july_5wind1.tdf EST_1_DOME_1_july_5wind2.tdf EST_1_DOME_1_july_5wind3.tdf EST_1_DOME_1_july_5wind4.tdf EST_1_DOME_1_july_5wind5.tdf EST_1_DOME_1_july_5wind6.tdf EST_1_DOME_1_july_5wind7.tdf EST_1_DOME_1_july_5wind8.tdf EST_1_DOME_1_july_5wind9.tdf EST_1_DOME_1_july_5wind10.tdf EST_1_DOME_1_july_5wind11.tdf EST_1_DOME_1_july_5wind12.tdf EST_1_DOME_1_july_5wind13.tdf EST_1_DOME_1_july_5wind14.tdf EST_1_DOME_1_july_5wind15.tdf EST_1_DOME_1_july_5wind16.tdf EST_1_DOME_1_july_5wind17.tdf EST_1_DOME_1_july_5wind18.tdf EST_1_DOME_1_july_5wind18.vfs

EST TELESCOPE ENVIRONMENT PRELIMINARY THERMAL ANALYSIS II	Page: 51 of 54 Date: November 13, 2014
Code: DM/TN-SNT/011v.1	File: DELIVERABLE70_4B.DOCX

Analysis	Folder Name	Path	Rartherm Files
DOME WITH THERMAL CONTROL	2_Dome with Thermal Control	<i>Telescope Environment Preliminary Thermal Analysis1_Closed Configuration2_Dome with Thermal Control</i>	EST_2_DOME_1_july_5wind.tdf EST_2_DOME_1_july_5wind0.tdf EST_2_DOME_1_july_5wind0B.tdf EST_2_DOME_1_july_5wind1.tdf EST_2_DOME_1_july_5wind2.tdf EST_2_DOME_1_july_5wind3.tdf EST_2_DOME_1_july_5wind4.tdf EST_2_DOME_1_july_5wind5.tdf EST_2_DOME_1_july_5wind6.tdf EST_2_DOME_1_july_5wind7.tdf EST_2_DOME_1_july_5wind8.tdf EST_2_DOME_1_july_5wind9.tdf EST_2_DOME_1_july_5wind10.tdf EST_2_DOME_1_july_5wind11.tdf EST_2_DOME_1_july_5wind12.tdf EST_2_DOME_1_july_5wind13.tdf EST_2_DOME_1_july_5wind14.tdf EST_2_DOME_1_july_5wind15.tdf EST_2_DOME_1_july_5wind16.tdf EST_2_DOME_1_july_5wind17.tdf EST_2_DOME_1_july_5wind18.tdf

EST TELESCOPE ENVIRONMENT PRELIMINARY THERMAL ANALYSIS II	Page: 52 of 54 Date: November 13, 2014
Code: DM/TN-SNT/011v.1	File: DELIVERABLE70_4B.DOCX

Analysis	Folder Name	Path	Rartherm Files
DOME HEAT STOP	3_Dome Heat Stop\2_Wind Inside	<i>Telescope Environment Preliminary Thermal Analysis\1_Closed Configuration\3_Dome Heat Stop\1_Air Inside</i>	EST_3_DOME_1_july_5wind.tdf EST_3_DOME_1_july_5wind0.tdf EST_3_DOME_1_july_5wind0B.tdf EST_3_DOME_1_july_5wind1.tdf EST_3_DOME_1_july_5wind1A.tdf EST_3_DOME_1_july_5wind2.tdf EST_3_DOME_1_july_5wind3.tdf EST_3_DOME_1_july_5wind4.tdf EST_3_DOME_1_july_5wind5.tdf EST_3_DOME_1_july_5wind6.tdf EST_3_DOME_1_july_5wind7.tdf EST_3_DOME_1_july_5wind8.tdf
	3_Dome Heat Stop\1_Air Inside	<i>Telescope Environment Preliminary Configuration\3_Dome Heat Stop\2_Wind Inside</i>	EST_3_DOME_1_july_5wind9.tdf EST_3_DOME_1_july_5wind10.tdf EST_3_DOME_1_july_5wind11.tdf EST_3_DOME_1_july_5wind12.tdf EST_3_DOME_1_july_5wind13.tdf EST_3_DOME_1_july_5wind14.tdf EST_3_DOME_1_july_5wind15.tdf EST_3_DOME_1_july_5wind16.tdf EST_3_DOME_1_july_5wind17.tdf

<p align="center">EST TELESCOPE ENVIRONMENT PRELIMINARY THERMAL ANALYSIS II</p>	<p>Page: 53 of 54 Date: November 13, 2014</p>
<p align="center">Code: DM/TN-SNT/011v.1</p>	<p>File: DELIVERABLE70_4B.DOCX</p>

Analysis	Folder Name	Path	Rartherm Files
<p align="center">OPEN CONFIGURATION WITH WINDSHIELD</p>	<p align="center">2_Open Configuration with Windshield</p>	<p><i>Telescope Environment Preliminary Thermal Analysis\2_Open Configuration with Windshield</i></p>	<p>EST_4_WINDSHIELD_2_july_5wind.tdf EST_4_WINDSHIELD_2_july_5wind1.tdf EST_4_WINDSHIELD_2_july_5wind2.tdf EST_4_WINDSHIELD_3_july_5wind3.tdf EST_4_WINDSHIELD_3_july_5wind4.tdf EST_4_WINDSHIELD_3_july_5wind5.tdf</p>

EST TELESCOPE ENVIRONMENT PRELIMINARY THERMAL ANALYSIS II	Page: 54 of 54 Date: November 13, 2014
Code: DM/TN-SNT/011v.1	File: DELIVERABLE70_4B.DOCX

5.3 LIST OF CFD INPUT FILES

ANALYSIS		NAME	NUMBER OF FILES
CLOSED CONFIGURATION	DOME WITHOUT THERMAL CONTROL	Caso30_July_Wind5_North70_9_Elev13_9.nas/stp/jpg	6 x .jpg
		Caso31_July_Wind5_North214_3_Elev83_8.nas/stp/jpg	3 x .nas
		Caso32_July_Wind5_North286_1_Elev20_1.nas/stp/jpg	3 x .stp
	DOME WITH THERMAL CONTROL	Caso33_July_Wind5_North70_9_Elev13_9.nas/stp/jpg	6 x .jpg
		Caso34_July_Wind5_North214_3_Elev83_8.nas/stp/jpg	3 x .nas
		Caso35_July_Wind5_North286_1_Elev20_1.nas/stp/jpg	3 x .stp
	DOME HEAT STOP	Caso36_July_Wind5_North70_9_Elev13_9.nas/stp/jpg	12 x .jpg 6 x .nas 6 x .stp
		Caso37_July_Wind5_North214_3_Elev83_8.nas/stp/jpg	
		Caso38_July_Wind5_North286_1_Elev20_1.nas/stp/jpg	
		Caso39_July_Wind5_North70_9_Elev13_9.nas/stp/jpg	
		Caso40_July_Wind5_North214_3_Elev83_8.nas/stp/jpg	
		Caso41_July_Wind5_North286_1_Elev20_1.nas/stp/jpg	
OPEN CONFIGURATION WITH WINDSHIELD	Caso42_July_Wind5_North72_Elev15_9.nas/jpg	3 x .jpg	
	Caso43_July_Wind5_North192_3_Elev84_6.nas/jpg	3 x .nas	
	Caso44_July_Wind5_North289_Elev13_8.nas/jpg	1 x .stp	
	EST_WINDSHIELD.stp		



IAC TECHNOLOGY DIVISION

DM/TN-SNT/018v.1

DMTNSNT_018V1

October 14, 2014

Project Ref.: 312495

PROJECT / DESTINATION:

SOLARNET

TITLE:

**EST THERMAL ANALYSIS - OBSERVATIONS OUT OF THE
SUN**

INSTITUTO DE ASTROFISICA DE CANARIAS

38200 La Laguna (Tenerife) - ESPAÑA - Phone (922)605200 - Fax (922)605210

EST THERMAL ANALYSIS - OBSERVATIONS OUT OF THE SUN	Page: 2 of 24 Date: November 13, 2014
Code: DM/TN-SNT/018v.1	File: DELIVERABLE70_4C.DOCX

AUTHOR LIST

Name	Function
Nauzet Vega Reyes	Mechanical Engineer

DOCUMENT CHANGE RECORD

Issue	Date	Change Description
01	09/21/2014	Initial Issue

APPROVAL CONTROL

Control	Name	Function
Revised by:	Lluís Cavaller	System Engineering
Approved by:	Christine Grivel	Project Manager
Authorised by:	Manuel Collados	Project Coordinator

EST THERMAL ANALYSIS - OBSERVATIONS OUT OF THE SUN	Page: 3 of 24 Date: November 13, 2014
Code: DM/TN-SNT/018v.1	File: DELIVERABLE70_4C.DOCX

SUMMARY

The aim of this document is to compare the effect of observations out of the sun between open configuration and closed configuration, for the EST telescope. In this document are described the results of the thermal analysis of the telescope structure and the secondary mirror, when the telescope is pointed out of the sun, either in nearby positions to the limb or in positions far away from the sun.

In the previous analysis with the telescope in open configuration, according to RD.1 and RD.2, arose important issues to take into account when the telescope is pointing to positions more distant from the sun than the effective size of the heat rejecter. The light from the sun reflected by M1 could reach directly M2 or the structure without passing through the heat rejecter. This situation would increase dramatically the heat load on the structure, if the incidence is produced close to the M1 focus.

From these findings, this analysis evaluates the influence of the dome when pointing off axis, hence this study is a continuation of the thermal analysis performed with the telescope at "Open Configuration", described at RD.1 and RD.2. It has studied a large number of positions covering an angle ranging from 0 ° (telescope pointed at the sun) to 45° (telescope pointing out of the sun) in order to identify areas that reduce the quality of observation, as well as the points that create a high risk to the telescope structure, for which safety systems should be implemented. RadTherm software has been used for the structure analysis and Ansys for the secondary mirror analysis.

EST THERMAL ANALYSIS - OBSERVATIONS OUT OF THE SUN	Page: 4 of 24 Date: November 13, 2014
Code: DM/TN-SNT/018v.1	File: DELIVERABLE70_4C.DOCX

TABLE OF CONTENTS

AUTHOR LIST	2
DOCUMENT CHANGE RECORD	2
APPROVAL CONTROL	2
SUMMARY	3
TABLE OF CONTENTS	4
LIST OF ABBREVIATIONS	4
1. INTRODUCTION	5
2. GEOMETRICAL ANALYSIS	5
3. STRUCTURE THERMAL ANALYSIS	11
4. M2 THERMAL ANALYSIS	13
A) THERMAL MODEL.....	14
B) RESULTS FOR DIFFERENT CONFIGURATIONS.....	15
5. CONCLUSIONS	16
ANNEXES	18
A. M2 THERMAL ANALYSIS RESULTS OPEN AND CLOSED CONFIGURATION	18
A) DIRECT ILLUMINATION AND THERMAL CONTROL:.....	18
B) DIRECT ILLUMINATION WITHOUT THERMAL CONTROL:.....	19
C) OPTICAL SURFACE ERROR.....	20
B. LIST OF REFERENCE DOCUMENTS	22
C. LIST OF APPLICABLE DOCUMENTS	23
D. LIST OF FILES	23

LIST OF ABBREVIATIONS

EST	European Solar Telescope
M1	Primary Mirror EST

EST THERMAL ANALYSIS - OBSERVATIONS OUT OF THE SUN	Page: 5 of 24 Date: November 13, 2014
Code: DM/TN-SNT/018v.1	File: DELIVERABLE70_4C.DOCX

M2	Secondary mirror EST
----	----------------------

1. INTRODUCTION

EST is an on-axis Gregorian telescope, equipped with a four-meter diameter primary mirror and primary focal length of about six meters. In such a large area solar telescope a considerable heat load (13 kW) is concentrated by the primary mirror on the focal plane image (of about 57 mm of diameter) and it is thus necessary to place a heat stop at the primary focus with the purpose of selecting the desired field of view (a few minutes of arc) and of preventing the remaining solar radiation (about 99 %) to reach the subsequent optics or parts of the telescope structure.

This document describes the consequences when the telescope is pointed to positions more distant from the sun than the effective size of the heat rejecter (200" from the solar limb) and the light from the sun reflected by M1 could reach directly M2 or the structure beams.

2. GEOMETRICAL ANALYSIS

Incident radiation in M1 has very different behaviours when the telescope is covered by a dome (closed configuration) or in open air configuration (open configuration). Opening dome greatly reduces heat at the primary mirror, reaching zero watts when the angle is 19°, on the other hand, the incident radiation remains constant when the telescope is in open configuration.

The following graph represents how incident radiation on M1 varies from on-axis observations to off-axis observations.

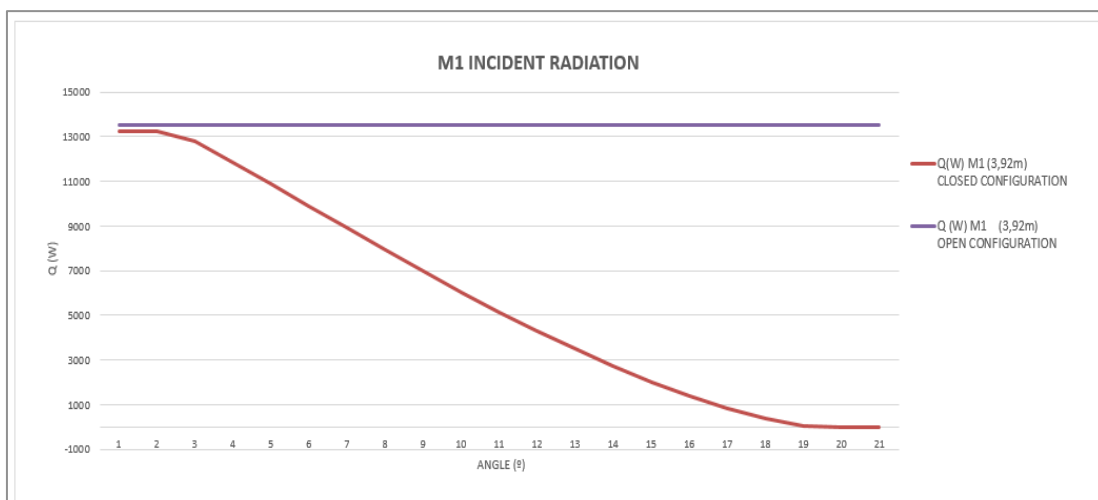
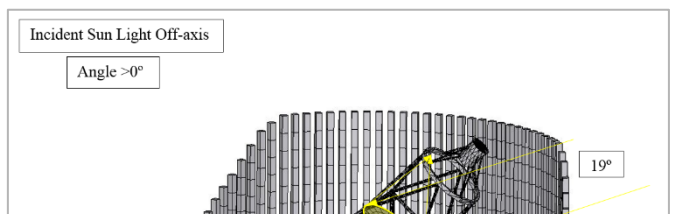
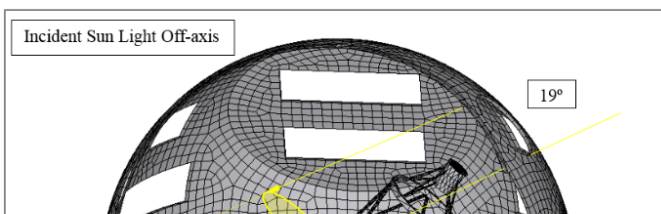
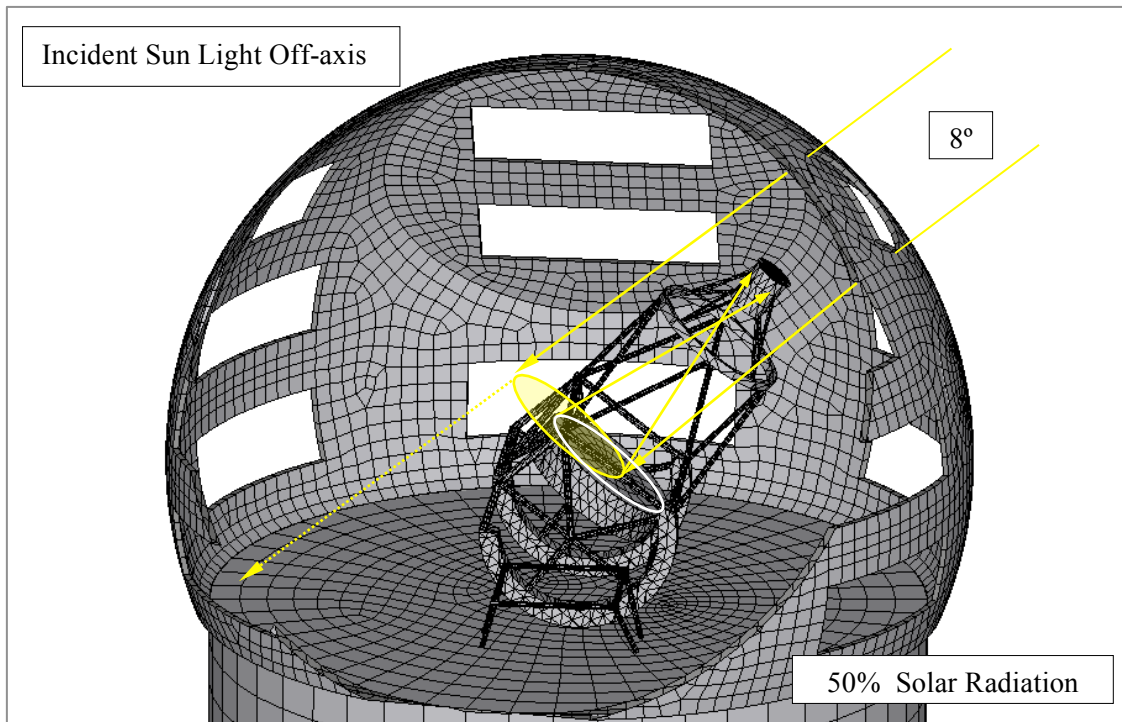
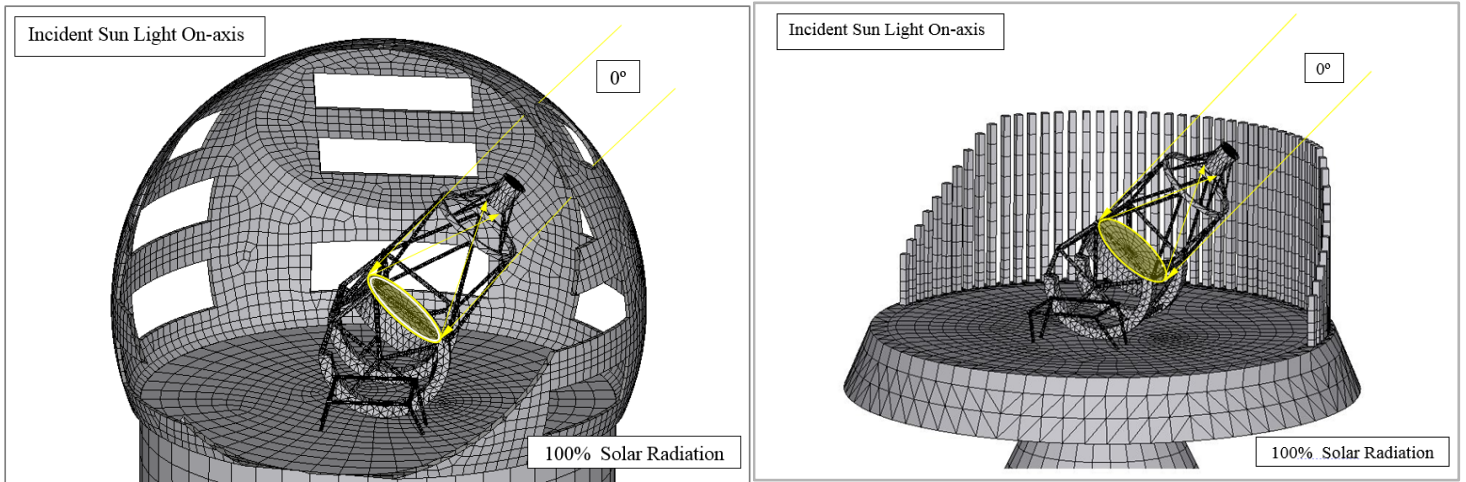


Figure 1. M1 incident radiation for Open and Closed Configuration.

The following figures show graphically how the telescope deviation from the sun light axis reduces the area illuminated on the primary mirror compared with open configuration in which the primary mirror remains fully lit. Influenced by the opening dome, the area illuminated on the primary mirror receives radiation in half its surface when the angle is 8°, and reaches zero when the angle is 19° off-axis. (Incident radiation inside the dome or the platform, their reflections and the thermal effects are not considered in this study).



EST THERMAL ANALYSIS - OBSERVATIONS OUT OF THE SUN	Page: 7 of 24 Date: November 13, 2014
Code: DM/TN-SNT/018v.1	File: DELIVERABLE70_4C.DOCX

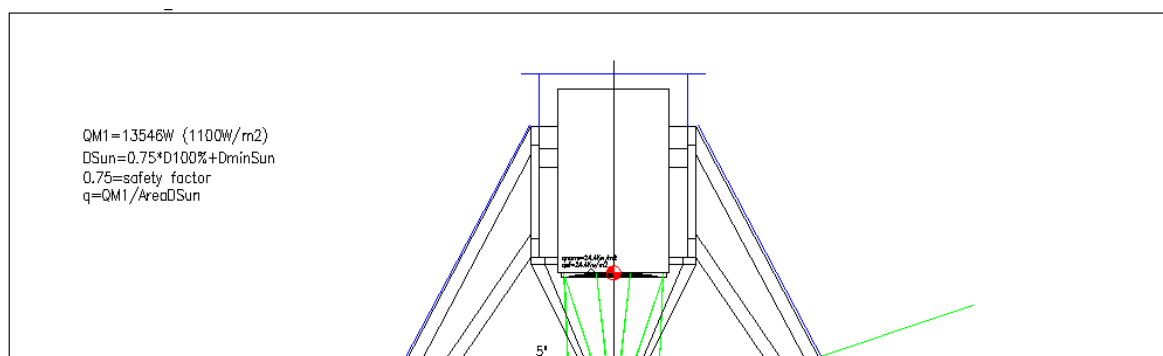
Figure 2. Incident radiation at the primary mirror for Closed Configuration and open configuration. First figure shows an on-axis observation, as in both configurations M1 receive 100% of the solar radiation. Second figure shows an intermediate case, when half of the primary mirror is illuminated, an off-axis observation with a deviation of 8° in close configuration. Last figure shows how the primary mirror does not receive solar radiation when the angle of observation is 19° (off-axis observation) and light falls directly on the platform and inner dome surface in close configuration. Solar radiation continues illuminating the entire surface of M1 in open configuration.

The heat density at the M1 focus decreases quickly while the sun is observed off-axis, passing from 5354KW/m² at the on-axis focus, to 7.1KW/m² at the image 45° off-axis at open configuration and from 5354KW/m² to 0KW/m² at closed configuration. The following table presents the off-axis position of the M1 focus (angle) and its equivalent heat density when the telescope is observing out of the sun, according to the current optical design.

	ANGLE (°)	Q Open Configuration ((W/m2)	Q Closed Configuration ((W/m2)
ENCIRCLED ENERGY OF THE IMAGE OF THE SOLAR DISK	5	13456	10176,5224
	10	13456	5346,8294
	20	13456	0
	30	13456	0
	45	13456	0
	ANGLE (°)	Q Open Configuration (KW/m2)	Q Closed Configuration (W/m2)
HEAT DENSITY OF THE IMAGE OF THE SOLAR DISK	5	1293	971
	10	468	184
	20	81	0
	30	26,5	0
	45	7,1	0

Table 1. Heat density of the solar disk for different angles observing out of the sun, for open and closed configuration.

The position of the M1 focus changes as the telescope pointing out of the sun, furthermore changes the focus size and its shape. The following figure shows the position of the M1 focus and the telescope structure. Red lines coming up from the bottom represent the observation offset angle from on-axis observations, the latter represented in green.



EST THERMAL ANALYSIS - OBSERVATIONS OUT OF THE SUN	Page: 8 of 24 Date: November 13, 2014
Code: DM/TN-SNT/018v.1	File: DELIVERABLE70_4C.DOCX

Figure 3 Position of the focus of the image of the solar disk for different off-axis position from 0° to 45°. The diameter containing 100% of the encircled energy of the image of the solar disk and the heat density are presented for each position, and for open and closed configuration.

As stated previously, the solar disk diameter changes not only in shape if not in size. A safety factor has been included to take into account the fact of changes on heat density through the solar disk surface. Inner part has a greater heat density that the outer part which receives less energy. The diameter calculated optically has been modified under the following expression:

$$D_{sun} = 0,75 * D_{100\%} + D_{minSun}$$

Where “D100%” is the diameter at each position, “DminSun” is the nominal diameter when the telescope operates on-axis and “Dsun” is the resulting diameter corrected for each position. (See RD.2).

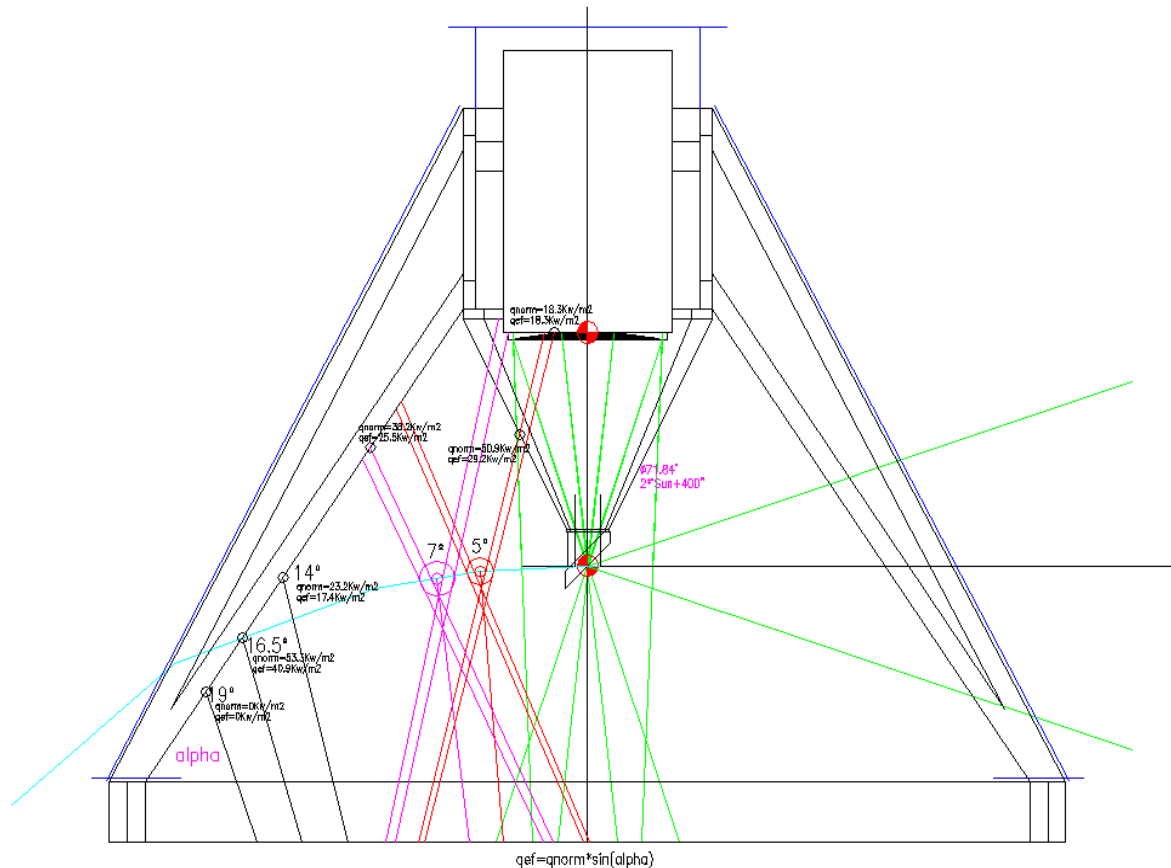
The following shows the solar diameters calculated for each angle, before (Diameter 100%) and after (Solar Disk Diameter) applying the safety factor. For both configurations, open and closed, are equal.

	ANGLE (°)	SOLAR DISK DIAMETER (mm)	DIAMETER 100% (mm)
SOLAR DISK DIAMETER	5	115,5	78
	10	192	180
	20	462	540
	30	807	1000
	45	1557	2000

Table 2. Solar disk diameter for different angles observing out of the sun.

EST THERMAL ANALYSIS - OBSERVATIONS OUT OF THE SUN	Page: 9 of 24 Date: November 13, 2014
Code: DM/TN-SNT/018v.1	File: DELIVERABLE70_4C.DOCX

In the following figure it is presented the heat density on different points of the structure for observing positions out of the solar disk. Two situations stand out because they would cause an unacceptable deterioration in the quality of the observations.



- Direct incidence on the secondary mirror:** in the case that the telescope is pointed to positions at certain distance from the sun, the light from the sun reflected by M1 could reach directly M2 without passing through the heat rejecter. This situation would increase the heat load on M2 from 40W/m^2 absorbed in nominal conditions up to 3600W/m^2 at Open Configuration and 2475W/m^2 in Closed Configuration. This situation occurs when the heat trap ceases to be effective (solar limb $+200''$) until 7° of deviation from telescope pointing on-axis (position where beam reflected by M1 is out of M2). The telescope cannot operate in this range because the deterioration of the surface quality of M2 is unacceptable. (See section 4. M2 Thermal Analysis).
- Solar disk at structure-spider:** pointing the telescope at 16.5° from the centre of the Sun, the focus of the image of the solar disk collides on the telescope spider (RD.2). This situation corresponds to the worst situation in open and closed configuration, since the collision is produced with the maximum heat density. 151KW/m^2 at Open Configuration and 40.9KW/m^2 at Closed Configuration.

EST THERMAL ANALYSIS - OBSERVATIONS OUT OF THE SUN	Page: 10 of 24 Date: November 13, 2014
Code: DM/TN-SNT/018v.1	File: DELIVERABLE70_4C.DOCX

Besides these critical situations mentioned above, four other positions are analysed. One analyses the incident heat on the spider that holds the heat trap at 5° (HS), and the remaining three analyse the heat that affects the M2 spider for different angles of observation out of the sun. All points analysed are represented in Figure 5.

The graph below shows the density of heat at each analysed point in open and closed configuration. The values have been measured in a normal plane to the light beam.

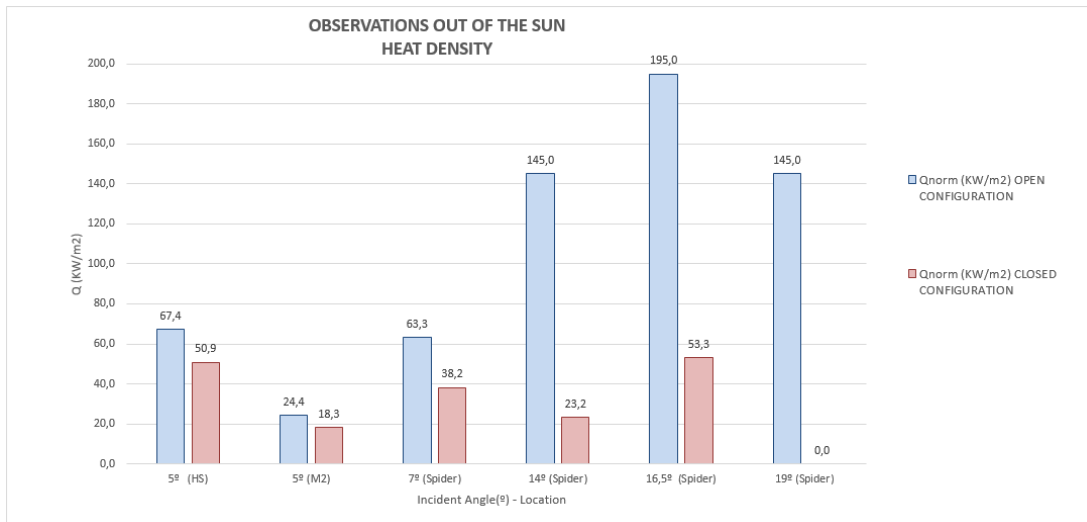
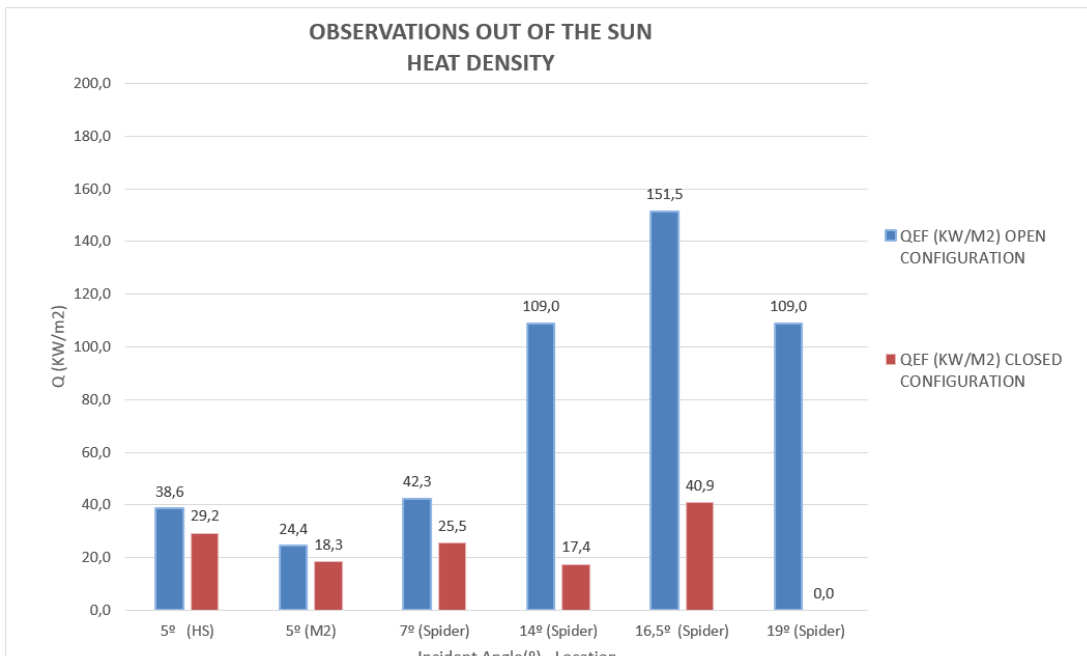


Figure 5 Heat density in different points of the telescope structure. Open configuration is represented in blue and closed configuration in red.

Since the surfaces on which the light strikes are not perpendicular to the light beam, the values have been corrected according to the angle of the receiving surface, to finally obtain the effective heat density received by each part of the structure according to the following expression:

$$q_{ef} = q_{norm} * \sin(\alpha)$$

Where “alpha” is the incidence angle and “qnorm” the heat density shown in the graph above. The corrected heat density, effective heat, is shown in the next figure.



EST THERMAL ANALYSIS - OBSERVATIONS OUT OF THE SUN	Page: 11 of 24 Date: November 13, 2014
Code: DM/TN-SNT/018v.1	File: DELIVERABLE70_4C.DOCX

Figure 6. Comparison of heat density in different points of the telescope between Open Configuration (blue) and Closed Configuration (red). Point 1) Angle 5° at Heat Stop Spider. Point 2) Angle 5° at M2. Point 3) Angle 7° at Spider. Point 4) Angle 14° at Spider. Point 5) Angle 16.5° at Spider. Point 6) Angle 19° at Spider.

In the most critical situation, direct illumination of the secondary mirror, a value of 18,3 KW/m² is obtained in closed configuration, 6.1 KW/m² less than in open configuration. The thermal analysis of M2 and its results are presented in section 4.

The difference is much greater for the incident heat in the spider of the secondary mirror, 151,5KW/m² in open configuration compared to 40,9 KW/m² in closed configuration. The next section describes the thermal analysis performed in this part of the structure.

As the graphic shows, the dome reduces the thermal load at any point of the telescope, even reaching zero in points with high thermal load in the open configuration and it greatly reduces the indirect radiation which produces the platform of the telescope and the telescope itself.

3. STRUCTURE THERMAL ANALYSIS

Direct incidence on the telescope spider is analysed in order to evaluate the temperatures reached on the structure under such thermal conditions.

Two cases are analysed: direct incidence on the steel spider without sunshade or provision of special aluminium sunshades in the lower face of the spider to protect the structure from this effect.

In the first case it is assumed an illuminated length of 400mm with reflectivity of 75%, receiving 50KW/m², so the absorbed heat is 12.5KW/m². The spider is assumed a steel tube 5mm thick, and the wind conditions are assumed 2m/s.

In the second case it is assumed a 2mm thick aluminium sunshade with reflectivity of 85%, producing an absorbed heat of 7.5KW/m².

In the first case the spider temperature rises to 202°C, in the second case the sunshade temperature rises to 62°C. Although these temperatures are far from the melting temperature for the spiders, it will affect the local seeing and it is necessary to introduce thermal control on the spider sunshades.

<p align="center">EST THERMAL ANALYSIS - OBSERVATIONS OUT OF THE SUN</p>	<p>Page: 12 of 24 Date: November 13, 2014</p>
<p>Code: DM/TN-SNT/018v.1</p>	<p>File: DELIVERABLE70_4C.DOCX</p>

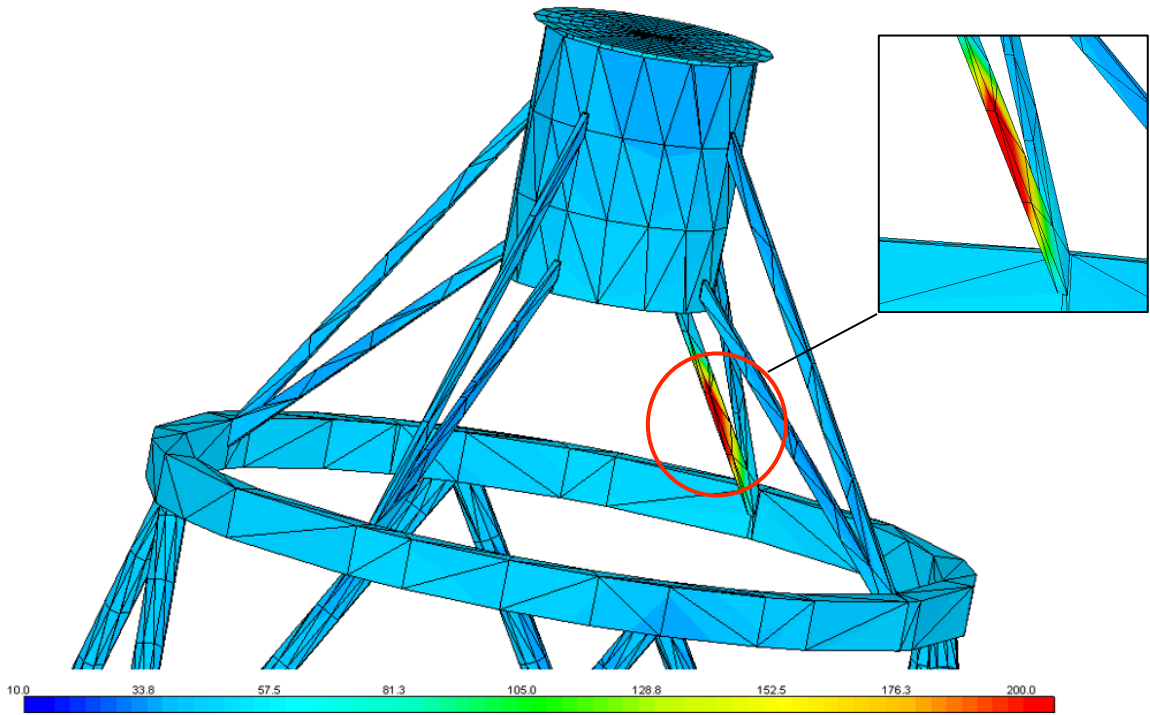
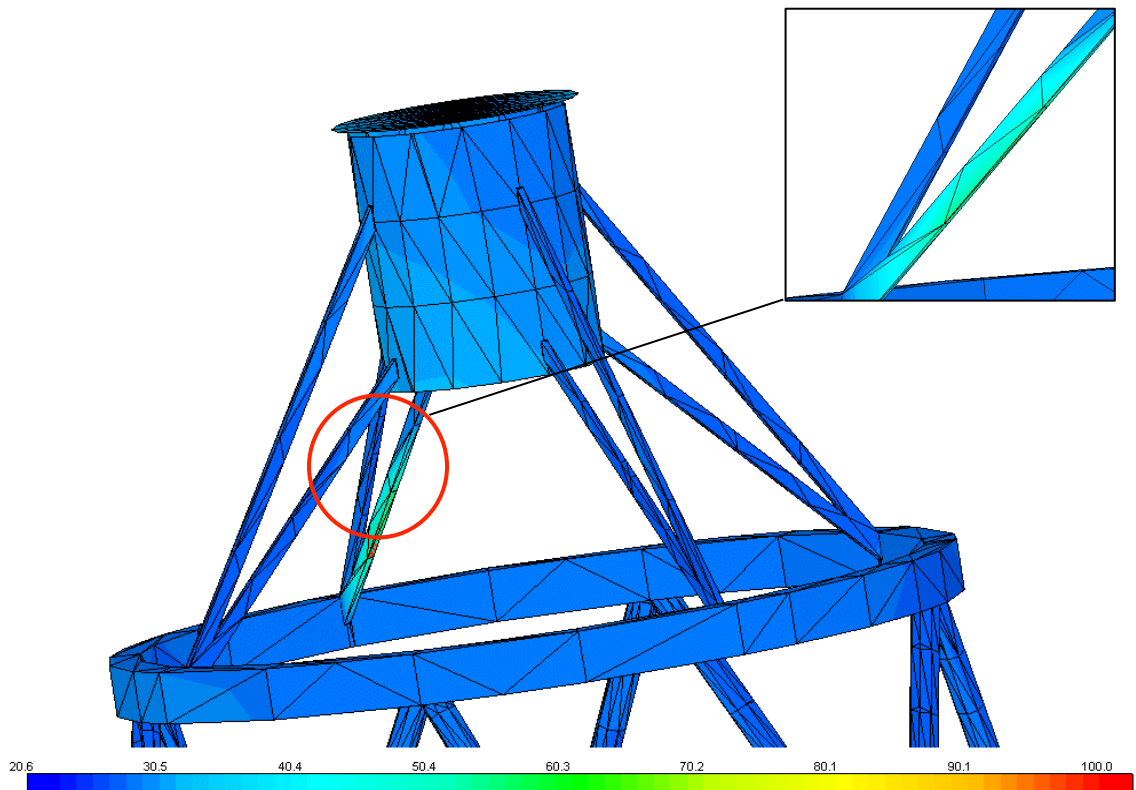


Figure 7. Temperature distribution on the spider due to concentrated heat from M1. Case without lower sunshade.



EST THERMAL ANALYSIS - OBSERVATIONS OUT OF THE SUN	Page: 13 of 24 Date: November 13, 2014
Code: DM/TN-SNT/018v.1	File: DELIVERABLE70_4C.DOCX

Figure 8. Temperature distribution on the spider due to concentrated heat from M1. Lower sunshade included.

The following table shows the temperatures of the structure in open and closed configurations. In closed configuration the temperature without sunshade is less than half (202°C) but still unacceptable. The same situation happen using sunshades, the temperature is not too high (62°C) but would generate significant thermal gradients near the optical path.

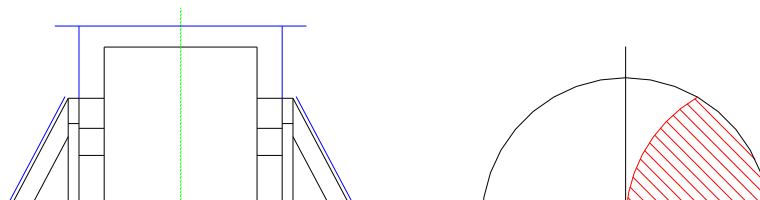
Pointing the telescope at 16,5°					
		OPEN CONFIGURATION			
CASE	REFLECTIVITY	LOAD	FINAL LOAD	IMPOSED HEAT	TEMPERATURE
Direct incidence on Steel (5mm thick) Spider	75%	160 KW/m2	40 Kw/m2	900W	436°C
		50KW/m2	12,5KW/m2	280 W	202 °C
		LOAD	FINAL LOAD	IMPOSED HEAT	TEMPERATURE
		CLOSED CONFIGURATION			

Pointing the telescope at 16,5°					
		OPEN CONFIGURATION			
CASE	REFLECTIVITY	LOAD	FINAL LOAD	IMPOSED HEAT	TEMPERATURE
Special aluminium (2mm thick) sunshades	85%	160 KW/m2	24 Kw/m2	540W	213°C
		50KW/m2	7,5KW/m2	170 W	62 °C
		LOAD	FINAL LOAD	IMPOSED HEAT	TEMPERATURE
		CLOSED CONFIGURATION			

Table 3. Structure Thermal Analysis. Parameters and final temperature of the spider without sunshades (top) and using aluminium sunshades (down). Comparison between open and closed configuration.

4. M2 THERMAL ANALYSIS

In the case that the telescope is pointed to positions at certain distance from the sun, the light from the sun reflected by M1 could reach directly M2 without passing through the heat rejecter. This situation would increase the heat load on M2 from 40W/m² absorbed in nominal conditions up to 2475 W/m² in Closed Configuration and 3600W/m² at Open Configuration. This situation cannot be produced in normal observation since the areas which could produce direct illumination of M2 shall be forbidden for observation. This case is analysed to evaluate the safety of M2 if direct illumination occurs by accident. The case of direct illumination is analysed in two conditions: with normal operation of the air impingement system and with air impingement system switched off.



<p align="center">EST THERMAL ANALYSIS - OBSERVATIONS OUT OF THE SUN</p>	<p>Page: 14 of 24 Date: November 13, 2014</p>
<p align="center">Code: DM/TN-SNT/018v.1</p>	<p>File: DELIVERABLE70_4C.DOCX</p>

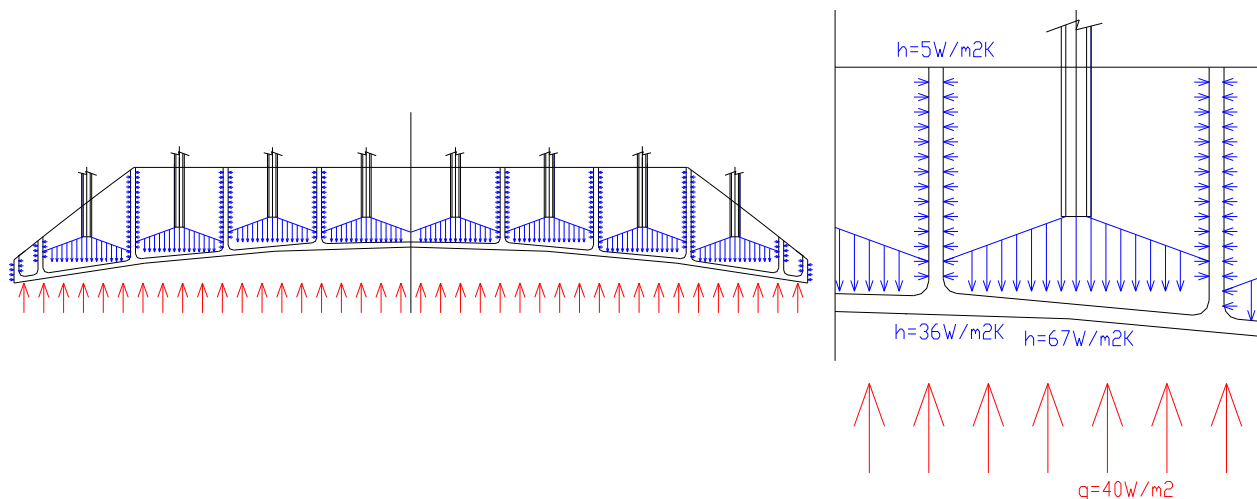
Figure 9. Fraction of M2 being directly illuminated by M1 without heat rejecter attenuation. The net heat absorbed by the illuminated area of M2 is estimated at 3600W/m², assuming a mirror reflectivity of 85%.

a) Thermal model

The thermal model includes the solar radiation absorbed by the optical surface, the forced convection produced by the air impingement system on the back surface and natural convection at the core walls.

During normal operation, the net heat absorbed on the optical surface is estimated at 40W/m², assuming a mirror reflectivity of 85% and natural convection through the front face. The forced convection coefficient inside the mirror core cells is assumed changing lineally from 67W/m²K at radius 15mm from the centre of the cell and 36W/m²K at radius 45mm, according to RD.3. The natural convection coefficient at the core walls is assumed 5W/m²K, corresponding to still air. The ambient temperature and the impinging air temperature assumed in this analysis is 293K.

The mirror temperature and thermal deformation of the surface are analysed in two conditions: normal operation of the air impingement system and air impingement system switched off.



EST THERMAL ANALYSIS - OBSERVATIONS OUT OF THE SUN	Page: 15 of 24 Date: November 13, 2014
Code: DM/TN-SNT/018v.1	File: DELIVERABLE70_4C.DOCX

Figure 10. Mirror thermal model.

b) Results for different configurations

The following table is a summary of the results of M2 thermal analysis under different conditions. “Q” represents the thermal load absorbed on the optical surface, ΔT is the maximum temperature difference with respect to the air, δ_{rmsZ2} is the surface deformation after extracting rigid body motion, δ_{rmsZ10} is the residual surface deformation after M1 compensation up to Z10 and σ is the maximum Von Misses stress.

	Conditions	q(W/m ²)	ΔT_{max} (K)	δ_{rmsZ2} (nm)	δ_{rmsZ10} (nm)	σ (MPa)
NOMINAL OBSERVATIONS IN THE SOLAR DISK	Nominal observation (85% reflectivity)	40	0.6	19	0.4	--
NOMINAL OBSERVATIONS IN THE SOLAR DISK HEAT REJECTED ALTERNATIVES	Nominal observation (85% reflectivity), no thermal control (h=5W/m ² K)	40	1.5	48	1.1	--
	Nominal observation (90% reflectivity), no thermal control (h=10W/m ² K)	30	0.6	19	0.8	--
OBSERVATIONS OUT OF THE SUN DIRECT INCIDENT M2 “ OPEN CONFIGURATION”	Direct illumination (85% reflectivity)	3600	46	5400	233	8
	Direct illumination (85% reflectivity), no thermal control (h=5W/m ² K)	3600	93	9500	310	12
OBSERVATIONS OUT OF THE SUN DIRECT INCIDENT M2 “ CLOSED CONFIGURATION”	Direct illumination (85% reflectivity)	2475	35	4100	174	6,3
	Direct illumination (85% reflectivity), no thermal control (h=5W/m ² K)	2475	72	7300	226	9.2

EST THERMAL ANALYSIS - OBSERVATIONS OUT OF THE SUN	Page: 16 of 24 Date: November 13, 2014
Code: DM/TN-SNT/018v.1	File: DELIVERABLE70_4C.DOCX

Table 4. Summary of results of the thermal analysis of the secondary mirror for both open and closed configuration.

In nominal conditions, when the telescope is pointing the sun, the situation is exactly the same with or without dome, so this case presents any difference between open and closed configuration.

In the worst case of illumination of a fraction of M2 directly by M1, with the thermal control switched off, M2 temperature increases up to 72°C above the ambient, 21°C more than in case of open configuration. This situation generates a maximum stress of 9.2 MPa. Switching on the thermal control, the temperature drops to 325K, 35°C above the ambient air.

The thermal deformation of the optical surface without thermal control is very high after compensation with M1 active optics ($\delta_{rmsZ10}=226nm$), far from the admissible limit according to AD.1, and after rigid body correction the situation is even worse, the error budgets sets a total maximum value of 115 nm and the value calculated is $\delta_{rmsZ2}=7300nm$. When the thermal control is switched on, the quality of the surface is improved but remains far from reaching an acceptable quality. After compensation with active optics reaches $\delta_{rmsZ10}=174nm$ and $\delta_{rmsZ2}=4100nm$ after extracting rigid body motion.

Observations out of the sun, both in open and closed configuration with M2 directly illuminated by M1, are absolutely unacceptable in order to keep the quality of M2 optical surface and therefore quality observations.

5. CONCLUSIONS

Closed Configuration reduces thermal loads in both structure and secondary mirror due to the dome aperture which reduces the incoming light energy from the sun when the telescope is pointing off-axis but neither the thermal analysis of the structure nor the secondary mirror has achieved an acceptable situation for some areas of observations.

The thermal analysis of the spider shows that closed configuration reduce more than a half the temperatures reached by the structure, the goal is to keep the temperature as near as possible to the ambient air temperature and a gradient of more than 60 degrees at less than two meters of the light path is considered as a weak point to keep an air turbulence as low as possible. Although the thermal load is lower in closed configuration, cooling by liquid refrigerant systems is still necessary. In order to analyse deeply this phenomenon it is needed a CFD analysis to evaluate the influence of this temperature gradient under different boundary conditions (ambient temperature, wind speed, wind direction, telescope orientation,...).

The secondary mirror has a decisive influence on the optical quality of the telescope and its surface quality must be within narrow limits set in the error budget (AD.1). From the results we can determine what range is not acceptable when the telescope is pointing off axis, and hence in which can operate normally.

<p align="center">EST THERMAL ANALYSIS - OBSERVATIONS OUT OF THE SUN</p>	<p>Page: 17 of 24 Date: November 13, 2014</p>
<p align="center">Code: DM/TN-SNT/018v.1</p>	<p>File: DELIVERABLE70_4C.DOCX</p>

When the telescope is pointed 200 arcsec beyond the limb of the sun the heat trap is no longer effective, from this position the light reflected by M1 is sent directly to the secondary mirror and thermal effects produced on the mirror make unacceptable the operation of the telescope in this area. Only when the angle is greater than 7 degrees, it becomes possible to observe because the M2 is no longer illuminated, but the structure is. In the range from 7 degrees to 14, the observations are possible because the spider gets a low thermal load, but from 14 degrees to 19 degrees, the telescope re-enters a critical area because the heat density on the structure increases in excess.

The following figure shows these safety ranges of operation:

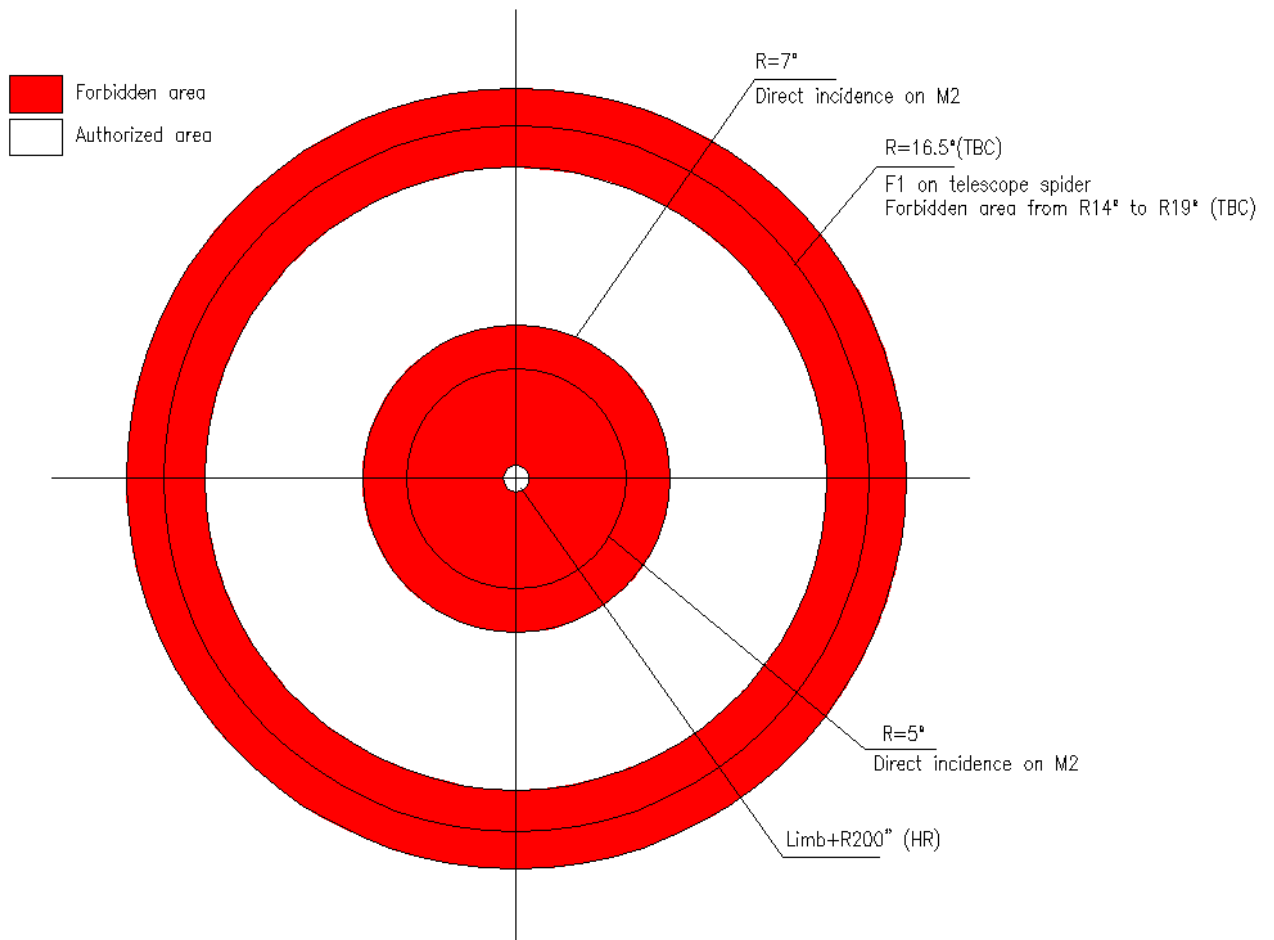


Figure 11. Forbidden observation areas (red areas).

ANNEXES

A. M2 THERMAL ANALYSIS RESULTS OPEN AND CLOSED CONFIGURATION

a) Direct illumination and thermal control:

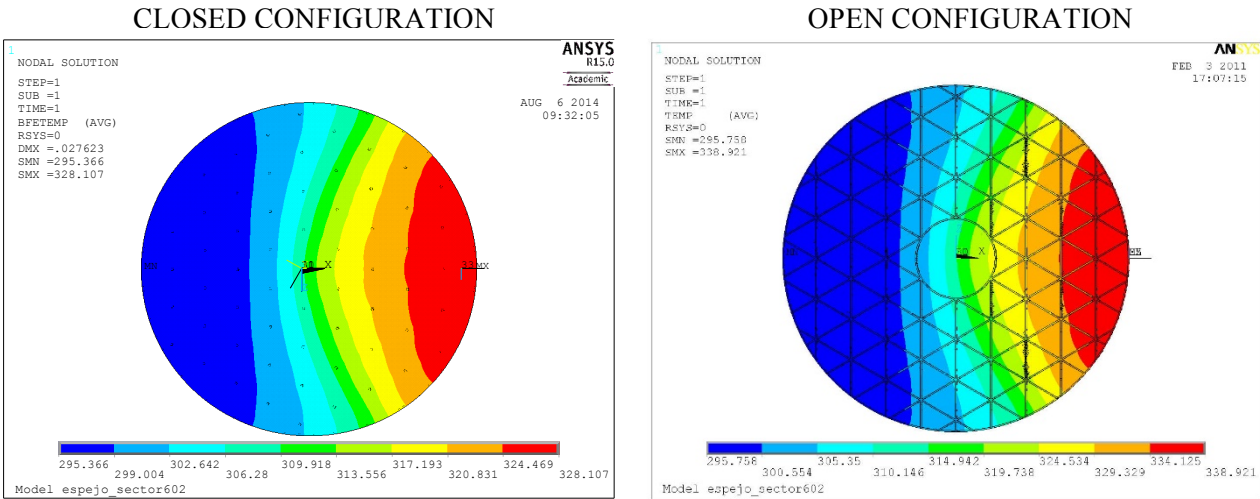


Figure 12. Temperature distribution for direct incidence of light path coming from M1 on a fraction of the optical surface without being attenuated by the heat rejecter (Mirror reflectivity 85% / Q incident closed configuration= 2475W/m^2 / Q incident open configuration= 3600W/m^2) Air impingement system in operation. The temperatures difference between the mirror and the ambient ranges from 2.3 to 35°C in closed configuration and from 2,7°C to 46°C in open configuration.

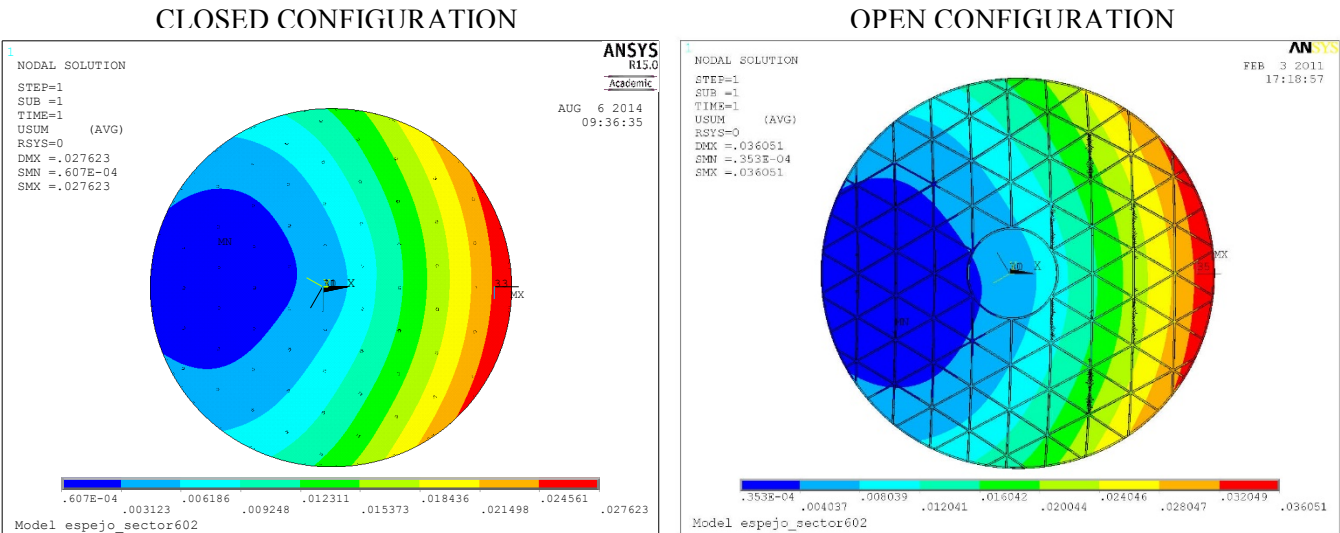
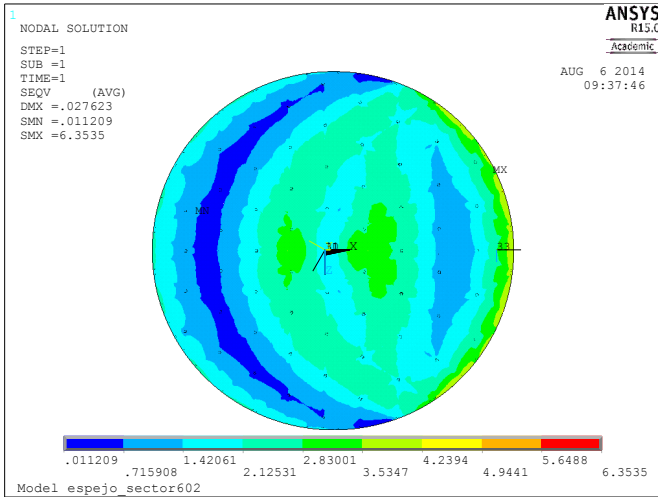


Figure 13. Total raw displacement for direct incidence of light path coming from M1 on a fraction of the optical surface without being attenuated by the heat rejecter. Air impingement system in operation. The maximum displacement is 27,6 microns in closed configuration and 36 microns in open configuration.

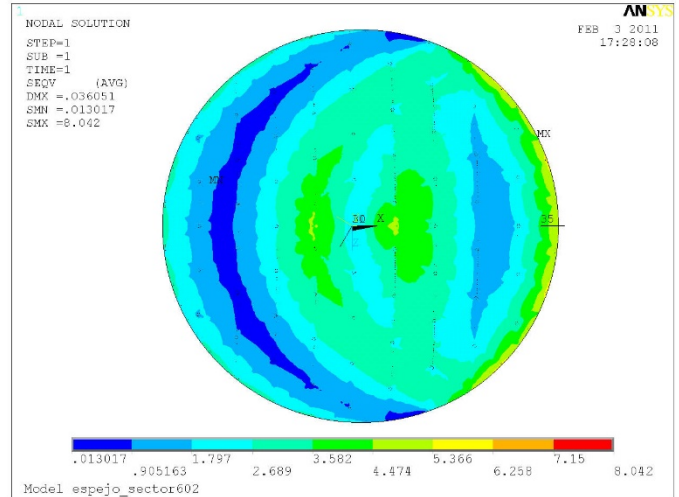
EST THERMAL ANALYSIS - OBSERVATIONS OUT OF THE SUN	Page: 19 of 24 Date: November 13, 2014
Code: DM/TN-SNT/018v.1	File: DELIVERABLE70_4C.DOCX

EST THERMAL ANALYSIS - OBSERVATIONS OUT OF THE SUN	Page: 20 of 24 Date: November 13, 2014
Code: DM/TN-SNT/018v.1	File: DELIVERABLE70_4C.DOCX

CLOSED CONFIGURATION



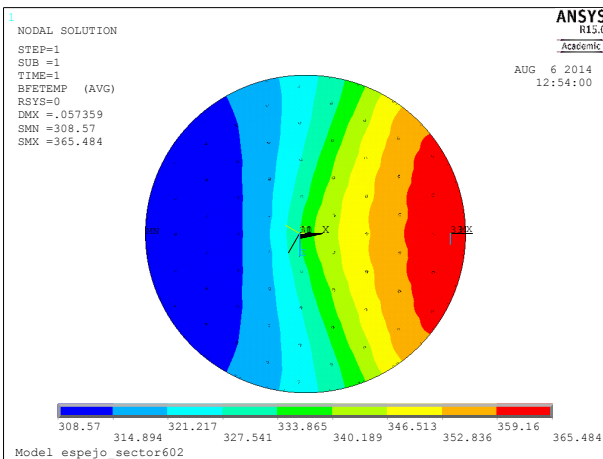
OPEN CONFIGURATION



of light path coming from M1 on a fraction of the optical surface without being attenuated by the heat rejecter. Air impingement system in operation. The maximum stress is 6.3 MPa in closed configuration and 8 MPa in open configuration. (Tensile strength 50-70 MPa)

b) Direct illumination without thermal control:

CLOSED CONFIGURATION



OPEN CONFIGURATION

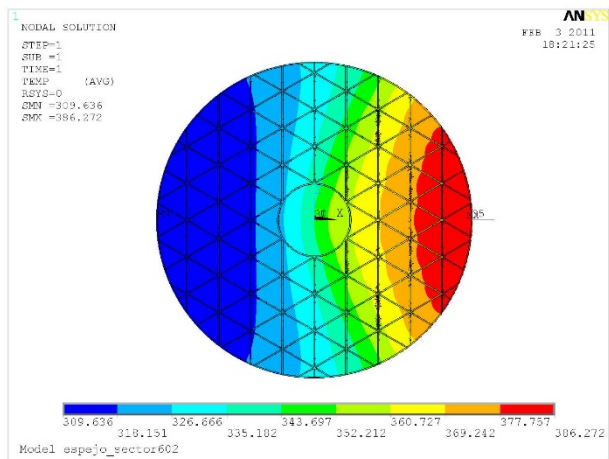


Figure 15. Temperature distribution for direct incidence of light path coming from M1 on a fraction of the optical surface without being attenuated by the heat rejecter (Mirror reflectivity 85%, $q=2475\text{W/m}^2$), without air impingement system, assuming natural convection ($h=5\text{W/m}^2\text{K}$) on all the mirrors surfaces. The temperature difference between the mirror and the ambient ranges from 15.5 to 72°C in closed configuration and from 16.6°C to 93°C in open configuration.

EST THERMAL ANALYSIS - OBSERVATIONS OUT OF THE SUN	Page: 21 of 24 Date: November 13, 2014
Code: DM/TN-SNT/018v.1	File: DELIVERABLE70_4C.DOCX

CLOSED CONFIGURATION

OPEN CONFIGURATION

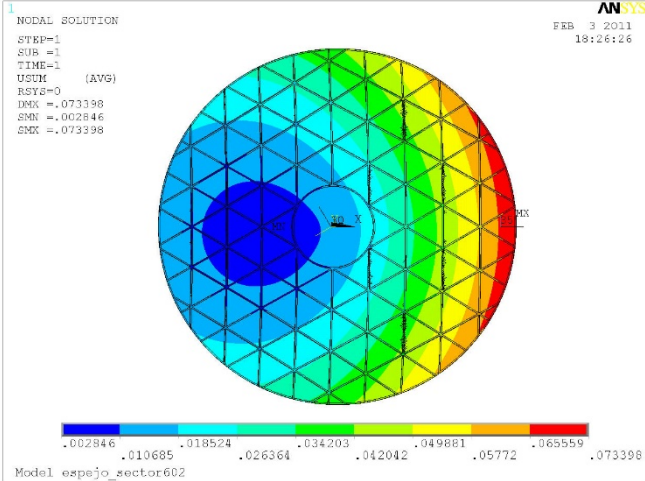
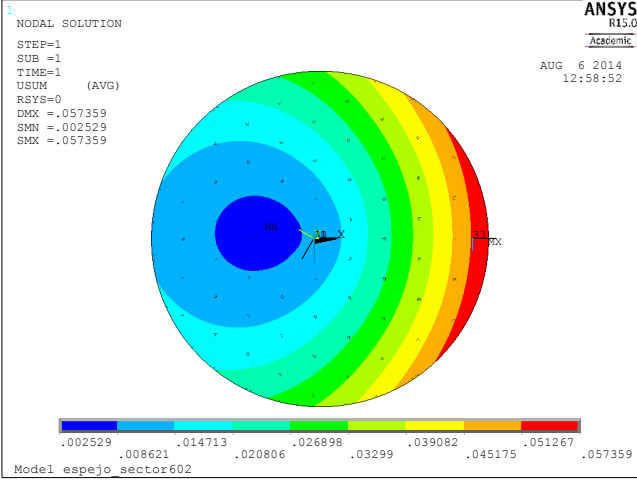


Figure 16. Total raw displacement for direct incidence of light path coming from M1 on a fraction of the optical surface without being attenuated by the heat rejecter. Air impingement system off. The maximum displacement is 57.3 microns in closed configuration and 73.3 microns in open configuration.

CLOSED CONFIGURATION

OPEN CONFIGURATION

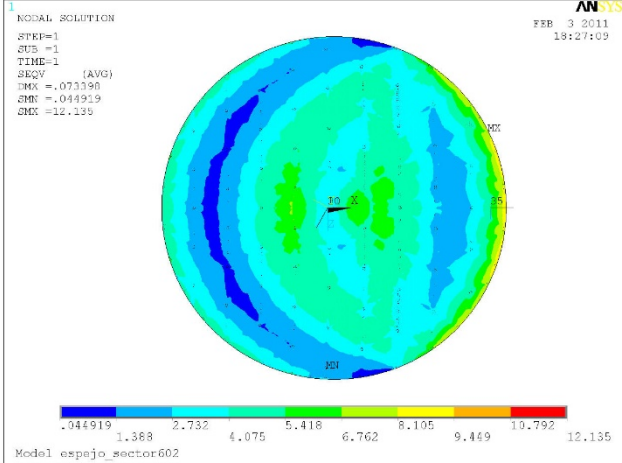
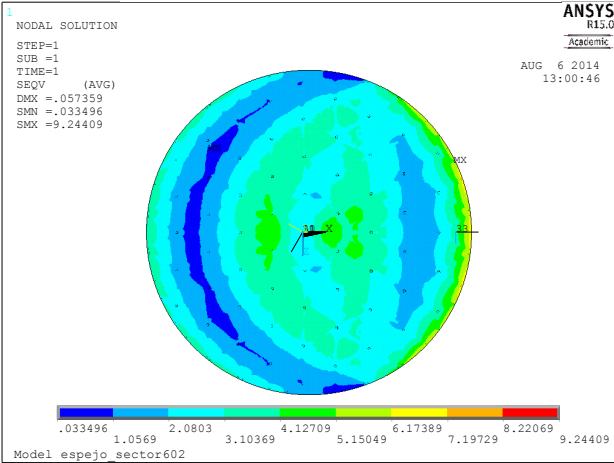


Figure 17. Von Mises Stress distribution for direct incidence of light path coming from M1 on a fraction of the optical surface without being attenuated by the heat rejecter. Air impingement system off. The maximum stress is 9.2 MPa in closed configuration and 12.13 MPa in open configuration. (Tensile strength 50-70 MPa)

EST THERMAL ANALYSIS - OBSERVATIONS OUT OF THE SUN	Page: 22 of 24 Date: November 13, 2014
Code: DM/TN-SNT/018v.1	File: DELIVERABLE70_4C.DOCX

c) Optical surface error.

From the obtained surface deformations in thermal analysis, superficial errors in the optical surface have been calculated in two different cases, correcting up to $Z = 2$ and $Z = 10$.

a) Direct illumination and thermal control.

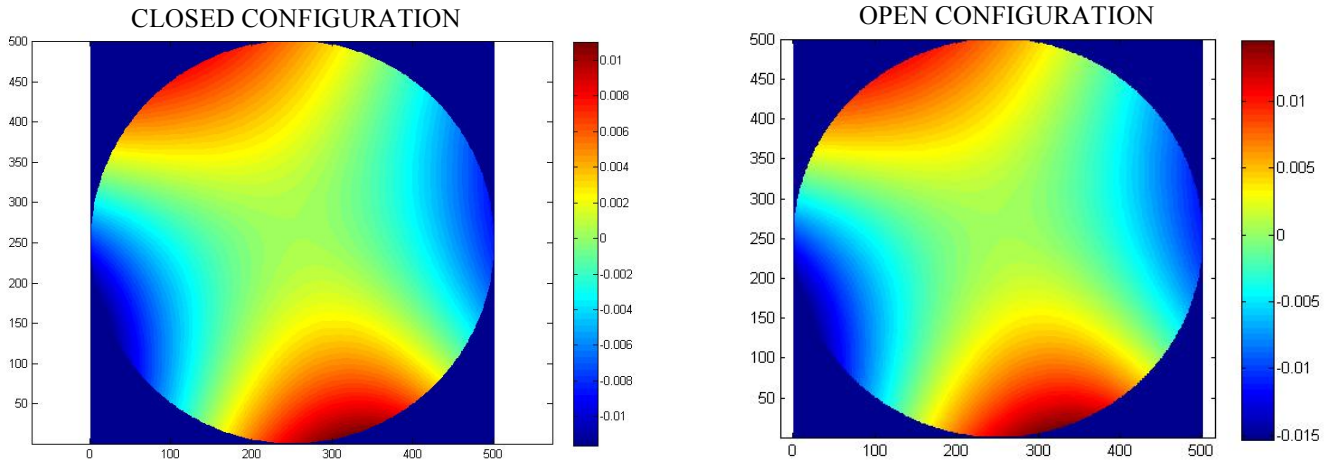


Figure 18. Left) Closed configuration: RMS-Z2= 4100 nm first two Zernike polynomials subtracted. Right) Open configuration: RMS-Z2=5400nm First two Zernike polynomials subtracted.

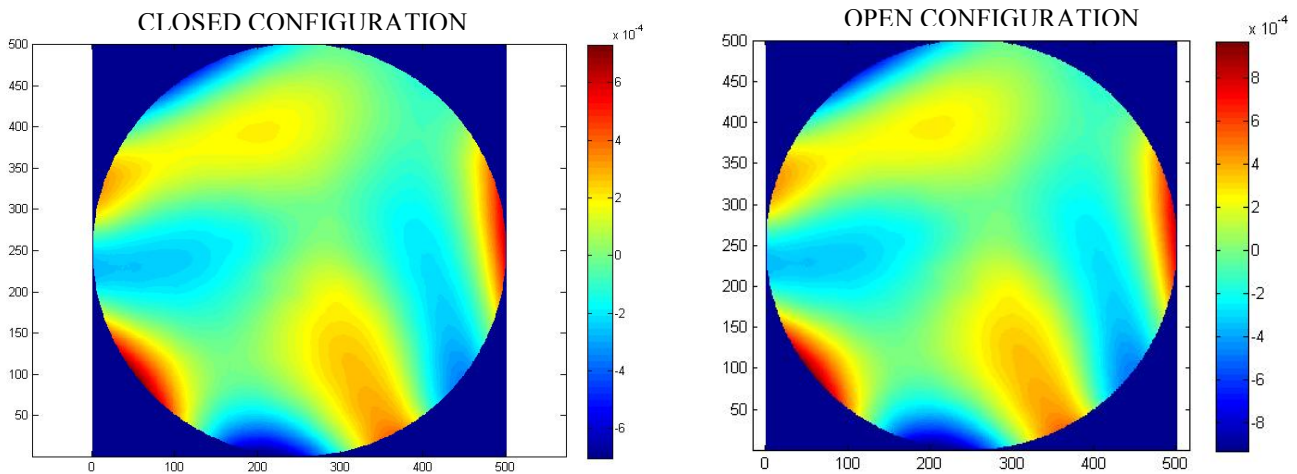
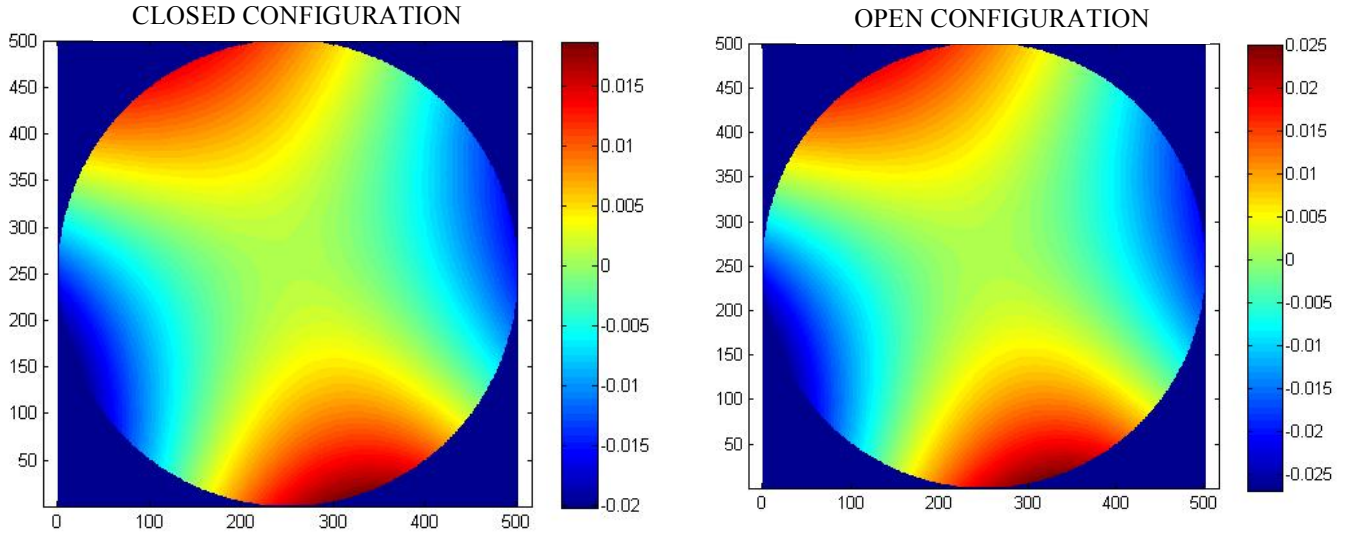


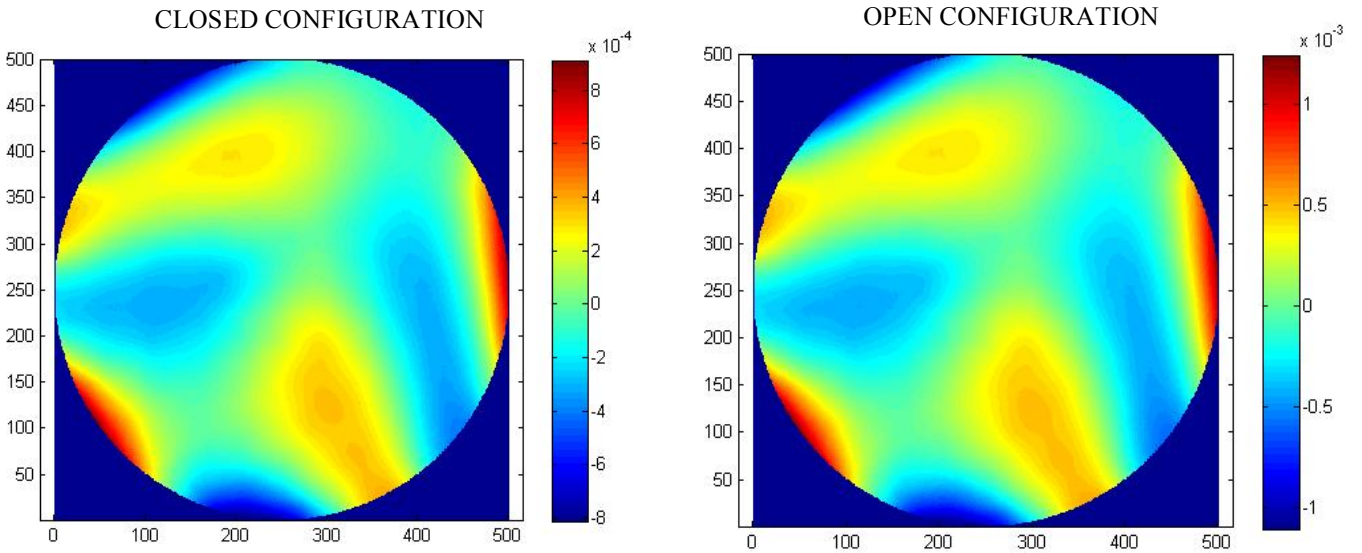
Figure 19. Left) Closed configuration: RMS-Z10= 1/4 nm first ten Zernike polynomials subtracted. Right) Open configuration: RMS-Z10=233nm First ten Zernike polynomials subtracted.

EST THERMAL ANALYSIS - OBSERVATIONS OUT OF THE SUN	Page: 23 of 24 Date: November 13, 2014
Code: DM/TN-SNT/018v.1	File: DELIVERABLE70_4C.DOCX

b) Direct illumination without thermal control:



configuration: RMS-Z2=5400nm First two Zernike polynomials subtracted. Right) Open configuration: RMS-Z2=5400nm First two Zernike polynomials subtracted.



configuration: RMS-Z10=310 nm First ten Zernike polynomials subtracted.

EST THERMAL ANALYSIS - OBSERVATIONS OUT OF THE SUN	Page: 24 of 24 Date: November 13, 2014
Code: DM/TN-SNT/018v.1	File: DELIVERABLE70_4C.DOCX

B. LIST OF REFERENCE DOCUMENTS

RD.1	RPTGTC50012A SECONDARY MIRROR PRELIMINARY DESIGN
RD.2	RPTGTC90011A TELESCOPE STRUCTURE PRELIMINARY THERMAL ANALYSIS
RD.3	RPT-NTE-5001, 1.A, EST M2 unit Phase II report

C. LIST OF APPLICABLE DOCUMENTS

AD.1	RPTEST30051A EST ERROR BUDGETS
AD.2	RPT-EST-2001 SCIENCE REQUIREMENTS DOCUMENT

D. LIST OF FILES

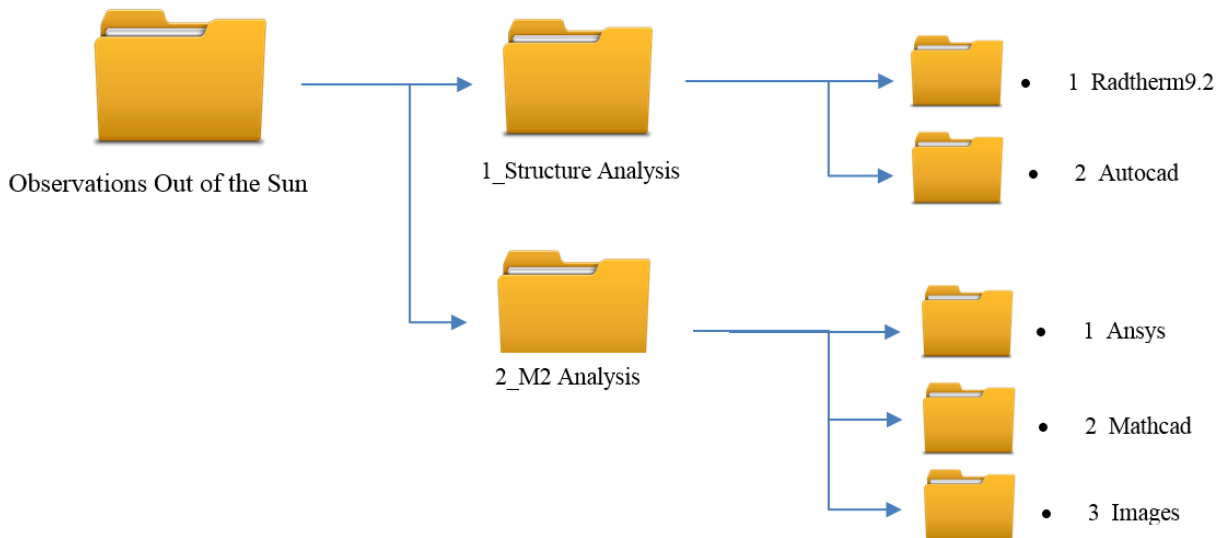


Figure 22. Out of the Sun Analysis - Folder tree.

EST THERMAL ANALYSIS - OBSERVATIONS OUT OF THE SUN	Page: 25 of 25 Date: November 13, 2014
Code: DM/TN-SNT/018v.1	File: DELIVERABLE70_4C.DOCX

Analysis	Folder Name	Sub-Folder Name	Path	Files
OBSERVATION OUT OF THE SUN	2_M2_ANALYSIS	2_AUTOCAD	<i>Observations Out of the Sun\1_Structure Analysis\2_Autocad</i>	- Out_of_the_sun.dwg
		1_RADTHERM9.2	<i>Observations Out of the Sun\1_Structure Analysis\1_Radtherm9.2</i>	- 9_est_spider_2wind.tdf - 9_est_spider_2wind_3.tdf
	1_STRUCTURE ANALYSIS	3_IMAGES	<i>Observations Out of the Sun\2_M2 Analysis\1_Ansys Files</i>	- Displacements - Von Misses - Hconv - Zernike
		2_MATHCAD	<i>Observations Out of the Sun\2_M2 Analysis\2_Mathcad Files</i>	- RESULT_M2Term7A.txt - RESULT_M2Term6A.txt - Zernike.m
		1_ANSYS	<i>Observations Out of the Sun\2_M2 Analysis\1_Ansys Files\2_Code</i>	- Espejo_sector602.anf - 1_EST-M2_nominal_observation40wm2_Conv - 2_EST-M2_Hcn=10_Q=30wm2_Hcf=0 - 2_EST-M2_nominal_observation40wm2_NoConv - 4_EST-M2_Direct_illumination_3600wm2_hcn=5+Hcf - 5_EST-M2_Direct_illumination_3600wm2_Hcn=5_Hcf=0 - 6_EST-M2_Direct_illumination_2745wm2_hcn=5+Hcf



IAC TECHNOLOGY DIVISION

DM/TN-SNT/022V.1

DMTNSNT_022V1

November 13, 2014

Project Ref.: 312495

PROJECT / DESTINATION:

SOLARNET

TITLE:

EST TELESCOPE STRUCTURE - ANALYSIS REPORT

INSTITUTO DE ASTROFISICA DE CANARIAS

38200 La Laguna (Tenerife) - ESPAÑA - Phone (922)605200 - Fax (922)605210

EST TELESCOPE STRUCTURE - ANALYSIS REPORT	Page: 2 of 54 Date: November 13, 2014
Code: DM/TN-SNT/022V.1	File: DELIVERABLE70_4D.DOCX

AUTHOR LIST

Name	Function
Miguel A. Esteves Pérez	Mechanical Engineer

APPROVAL CONTROL

Control	Name	Function
Revised by:	Lluís Cavaller Marqués	System Engineer
Approved by:	Christine Grivel	System Engineer
Authorised by:	Manuel Collados Vera	Principal Investigator

DOCUMENT CHANGE RECORD

Issue	Date	Change Description
01	09/22/2014	Initial Issue

EST TELESCOPE STRUCTURE - ANALYSIS REPORT	Page: 3 of 54 Date: November 13, 2014
Code: DM/TN-SNT/022V.1	File: DELIVERABLE70_4D.DOCX

SUMMARY

This document covers main developments made in the field of the telescope structure, showing current state of progress from the previous conceptual design study, i.e., EST-2008/2011.

The analyses have been performed considering the models studied in the previous stage, i.e., **Rocking-Chair** and **Gantry** Models, as well as the **Yoke** Model, an alternative not studied in details in the first study.

Model performance is valued according to dynamic behaviour, as well as the errors due to gravity and wind loads acting on the structure.

An alternative configuration for the upper section of the telescope tube is also considered, as well as the possibility of changing current Nasmyth platform position from the right side of the telescope to the rear side.

EST TELESCOPE STRUCTURE - ANALYSIS REPORT	Page: 4 of 54 Date: November 13, 2014
Code: DM/TN-SNT/022V.1	File: DELIVERABLE70_4D.DOCX

TABLE OF CONTENTS

AUTHOR LIST.....	2
APPROVAL CONTROL.....	2
DOCUMENT CHANGE RECORD.....	2
SUMMARY	3
TABLE OF CONTENTS	4
1. DESIGN ALTERNATIVES	7
2. DYNAMIC ANALYSIS	9
2.1 ROCKING-CHAIR WITH R-GUIDES	9
2.2 GANTRY WITH R-GUIDES AND EL MOTORS IN THE EL-AXIS TRUNNION	10
2.3 GANTRY WITH R-GUIDES AND EL MOTORS ON TELESCOPE WHEELS PERIPHERY	11
2.4 YOKE WITH R-GUIDES AND EL MOTORS ON TELESCOPE WHEELS PERIPHERY ...	12
2.5 YOKE WITH ROLLER BEARING AND EL MOTORS ON TELESCOPE WHEELS PERIPHERY	14
2.6 DYNAMIC ANALYSIS CONCLUSIONS	15
3. GRAVITY DEFORMATIONS ANALYSIS	17
3.1 RESULTS OF FE CALCULATIONS.....	17
3.1.1 <i>Rocking-Chair Model</i>	18
3.1.2 <i>Gantry Model</i>	18
3.1.3 <i>Yoke Model</i>	19
3.2 SENSITIVITY MATRICES.....	20
3.2.1 <i>General</i>	20
3.2.2 <i>Resulting Gravity Induced Pointing Errors</i>	21
3.2.2.1 <i>Rocking-Chair Model</i>	21
3.2.2.2 <i>Gantry Model</i>	22
3.2.2.3 <i>Yoke Model</i>	24
3.3 GRAVITY DEFORMATIONS ANALYSIS CONCLUSIONS	25
4. WIND ANALYSIS.....	26
4.1 WIND DRAG FORCES ON THE STRUCTURE	26
4.2 STEADY STATE WIND ANALYSIS.....	29
4.2.1 <i>Mirror Displacements due to Structural Deformations</i>	29
4.2.1.1 <i>Rocking-Chair Model</i>	29
4.2.1.2 <i>Gantry Model</i>	29
4.2.1.3 <i>Yoke Model</i>	30
4.2.2 <i>Steady State Wind Induced Errors due to Structural Deformations</i>	31
4.2.2.1 <i>Rocking-Chair Model</i>	31
4.2.2.2 <i>Gantry Model</i>	31
4.2.2.3 <i>Yoke Model</i>	32
4.3 DYNAMIC WIND ANALYSIS	32
4.3.1 <i>Mirror Displacements due to Structural Deformations</i>	32
4.3.2 <i>Dynamic Wind Induced Errors due to Structural Deformations</i>	32
4.3.2.1 <i>Rocking-Chair Model</i>	33

EST TELESCOPE STRUCTURE - ANALYSIS REPORT	Page: 5 of 54 Date: November 13, 2014
Code: DM/TN-SNT/022V.1	File: DELIVERABLE70_4D.DOCX

4.3.2.2	Gantry Model.....	33
4.3.2.3	Yoke Model	33
4.3.3	<i>Structural Deformations Errors including the Resonant Effect</i>	34
4.3.3.1	Methodology.....	34
4.3.3.2	Rocking-Chair Model	38
4.3.3.3	Gantry Model.....	39
4.3.3.4	Yoke Model	39
4.3.4	<i>Wind Shake on Axes Errors</i>	40
4.3.4.1	Methodology.....	40
4.3.4.2	Rocking-Chair Model	42
4.3.4.3	Gantry Model.....	42
4.3.4.4	Yoke Model	43
4.4	WIND ANALYSIS CONCLUSIONS.....	43
5.	TELESCOPE UPPER TUBE OPTIMIZATION	45
5.1	ALTERNATIVE TUBE CONFIGURATION ANALYSIS	45
5.2	CURRENT UPPER TUBE OPTIMIZATION ANALYSIS.....	47
5.3	TELESCOPE UPPER TUBE OPTIMIZATION CONCLUSIONS	49
6.	NASMYTH PLATFORM POSITION ANALYSIS	50
7.	GENERAL CONCLUSIONS	52
A.	ANNEXES	54

EST TELESCOPE STRUCTURE - ANALYSIS REPORT	Page: 7 of 54 Date: November 13, 2014
Code: DM/TN-SNT/022V.1	File: DELIVERABLE70_4D.DOCX

1. DESIGN ALTERNATIVES

For the telescope structure and its mechanics, the following alternatives described in RD.3 were considered:

- 1- **Rocking-Chair.** This model was provided with R-Guides for the AZ-Axis, and four EL motors placed on Telescope Wheels Periphery.
- 2- **Gantry.** For this model, the following cases were considered:
 - Two EL motors placed in the EL-Axis Trunnion, and R-Guides for the AZ-Axis.
 - Four EL Motors placed on Telescope Wheels Periphery, and R-Guides for the AZ-Axis.
- 3- **Yoke.** For this model, the following cases were considered:
 - Four EL Motors placed on Telescope Wheels Periphery, and R-Guides for the AZ-Axis.
 - Four EL Motors placed on Telescope Wheels Periphery, and Roller Bearing for the AZ-Axis.

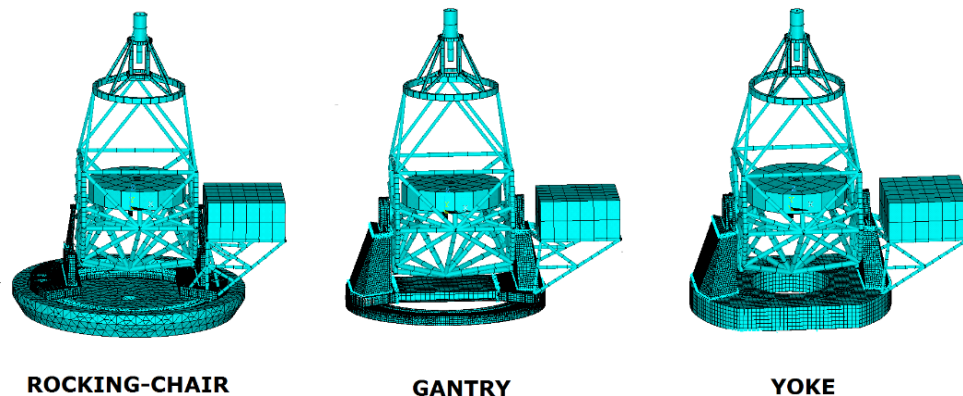


Fig. 1. Design Alternatives FE Models.

For Rocking-Chair and Gantry configurations, the fact of improving the performance by increasing the Telescope Wheel Stiffness was tested by means of valuing the dynamical behaviour. The rigidity was increased using a 1.0 cm iron plate glued to the radii of the wheels.

The Yoke configuration with roller bearing in the AZ-Axis allows the use of conventional bearings. The analysis was performed considering two diameters (5.0 m and 6.0 m). Both diameters are feasible from RotheERDE or other large roller bearing manufacturers. In this case, the tilt stiffness was determined scaling the tilt stiffness from the ALMA antenna AZ Bearing ($k_{\phi_ALMA}=1.26 \cdot 10^{11}$ Nm/rad, $\phi_{ALMA}=3.4$ m), using the following rule:

$$k_{\phi_brg} = \left[\frac{\phi_{brg}}{\phi_{ALMA}} \right]^3 \cdot k_{\phi_ALMA}$$

For those cases where the R-Guides were used for the AZ-Axis (Rocking-Chair, Gantry and Yoke Models with R-Guides), the tilt stiffness is given by the axial stiffness of each trolley ($k_{axial}=1.0 \cdot 10^6$ N/mm taken from THK), and its distance to the axis (Global Y axis).

In this case, the bearing is composed by an inner and an outer track, whose diameters vary depending on the configuration.

For all the cases, a total of 32 trolleys were allocated in the tracks as depicted in the following picture.

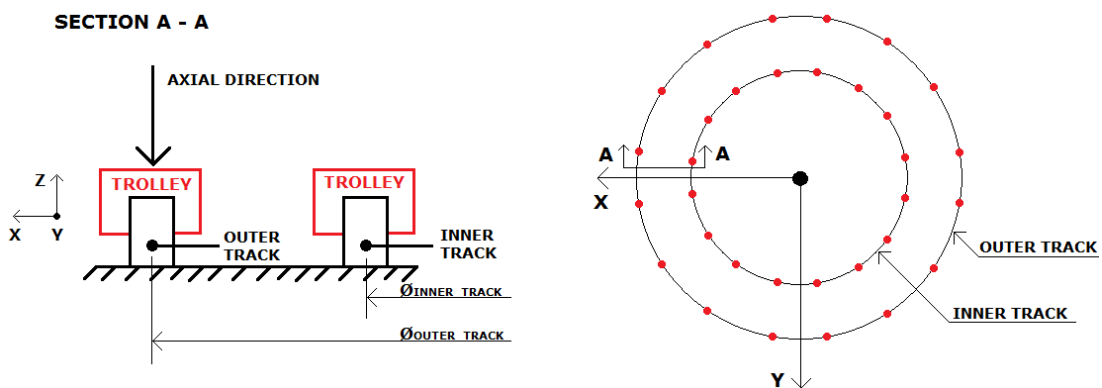


Fig. 2. R-Guides Axial Stiffness

The following table summarises the tilt stiffness obtained for the R-Guides and the Roller Bearings used in the analysis.

	ROCKING-CHAIR	GANTRY	YOKE (R-GUIDES)
\varnothing_{ext} [m]	10.00	10.00	6.00
\varnothing_{int} [m]	8.00	8.00	4.00
k_{θ} [Nm/rad]	8.30E+09	8.30E+09	2.07E+09

YOKE (ROLLER BEARING)	
\varnothing [m]	k_{θ} [Nm/rad]
5.00	4.01E+11
6.00	6.92E+11

Table 1. Tilt Stiffness for AZ Bearing.

As dynamic structural behaviour is related to the structural rigidity, all the models were first dynamically valued, choosing those models with a better behaviour for later analysis.

FE Models do not include the pier in order to avoid any kind of modes or deformations related to it, and distortions inherent to the mirrors are not considered.

EST TELESCOPE STRUCTURE - ANALYSIS REPORT	Page: 9 of 54 Date: November 13, 2014
Code: DM/TN-SNT/022V.1	File: DELIVERABLE70_4D.DOCX

2. DYNAMIC ANALYSIS

The following results are obtained from the Dynamic Analysis of the FE Models. Results belong to the Lowest Locked Rotor Modes and the analyses were performed with the telescope pointing to the Horizon and pointing to the Zenith.

2.1 Rocking-Chair with R-Guides

For this model, the Lowest Locked Rotor Modes are summarized in the following table:

TELESCOPE POINTING TO HORIZON			TELESCOPE POINTING TO ZENITH		
MODE N°	Frq. [Hz]	MODE DESCRIPTION	MODE N°	Frq. [Hz]	MODE DESCRIPTION
01	8.34	Nasmyth	01	8.33	Nasmyth
02	9.98	EL	02	9.36	EL
03	10.29	XEL	03	11.33	XEL
04	14.92	Spider	04	14.92	Spider
05	17.65	Tube Mode	05	19.14	Tube Mode
06	18.84	AZ	07	21.65	AZ

Table 2. Lowest Locked Rotor Modes for Rocking-Chair with R-Guides Model.

The modes highlighted are modes of special interest. Particularly, the Elevation (EL) and the Azimuth (AZ) modes are modes coupled with the main axis (EL-Axis and AZ-Axis) and therefore, are accessible to pointing correction. These modes define the bandwidth for the drives and hence, the correction capability.

On the contrary, XEL mode is a rotation along an axis perpendicular to the EL-Axis, not being coupled with none of the main axis. This mode makes shift the telescope tube; and the mirrors mounted on it, along global X axis. Hence, the beam path remains the same and it does not produce image motion. Therefore, this is a mode of less importance.

Finally, the Spider Mode is a local subsystem mode not related to the overall structural layout, and independent of the EL position. The thickness of the spiders was elevated to 40 mm maximum in order to minimize optical path obstruction.

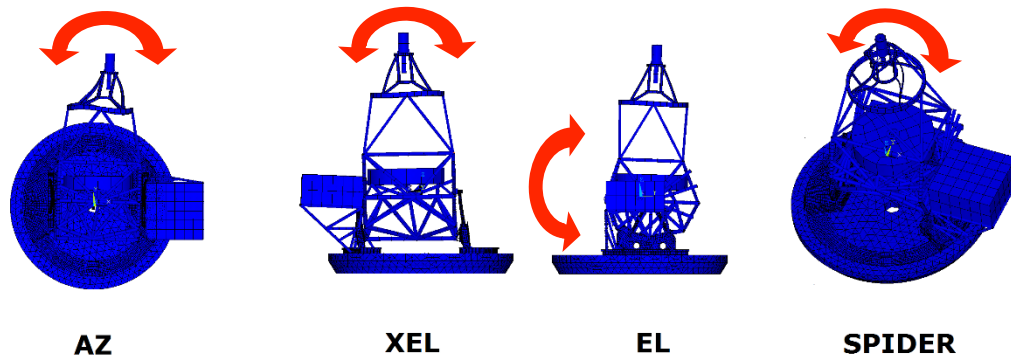


Fig. 3. Rocking-Chair Locked Rotor Modes.

EST TELESCOPE STRUCTURE - ANALYSIS REPORT	Page: 10 of 54 Date: November 13, 2014
Code: DM/TN-SNT/022V.1	File: DELIVERABLE70_4D.DOCX

The following table summarizes the results obtained for the case where the wheels are reinforced with the plate.

TELESCOPE POINTING TO HORIZON			TELESCOPE POINTING TO ZENITH		
MODE N°	Frq. [Hz]	MODE DESCRIPTION	MODE N°	Frq. [Hz]	MODE DESCRIPTION
01	8.33	Nasmyth	01	8.33	Nasmyth
02	9.87	EL	02	9.37	EL
03	10.01	XEL	03	10.94	XEL
04	14.92	Spider	04	14.92	Spider
05	15.57	Wheel Plate	05	15.16	Wheel Plate
10	18.87	AZ	11	21.63	AZ

Table 3. Lowest Locked Rotor Modes for Rocking-Chair with R-Guides and Reinforced Wheels Model.

As it can be seen comparing the tables 2 and 3, the fact of adding a reinforcement on the telescope wheels does not cause significant differences in the dynamic behaviour, mainly because this extra stiffness is being loosed through the EL motors supports, which have a low rigidity.

2.2 Gantry with R-Guides and EL motors in the EL-Axis Trunnion

The main advantage of this model is the possibility to use out-of-the-shelf direct drives installed on the trunnions.

The following table summarises the results obtained for this model.

TELESCOPE POINTING TO HORIZON			TELESCOPE POINTING TO ZENITH		
MODE N°	Frq. [Hz]	MODE DESCRIPTION	MODE N°	Frq. [Hz]	MODE DESCRIPTION
01	5.89	EL	01	5.72	EL
02	8.91	XEL	02	9.21	XEL
03	14.92	Spider	03	14.92	Spider
04	18.78	Complex Mode	04	18.11	Complex Mode
05	20.09	AZ	05	18.55	Tube Mode
			12	24.66	AZ

Table 4. Lowest Locked Rotor Modes for Gantry with R-Guides and EL motors in the EL-Axis Trunnion Model.

This model exhibits an EL frequency lower than the one obtained for Rocking-Chair denoting poor stiffness. This is related to the low stiffness of the EL Wheels and the lower lever arm for the EL motors in comparison to the Rocking-Chair model, in which the motors are placed on the Telescope Wheels Periphery, increasing the lever arm.

The results for the case where telescope wheel is reinforced with the plate are shown in the following table:

EST TELESCOPE STRUCTURE - ANALYSIS REPORT	Page: 11 of 54 Date: November 13, 2014
Code: DM/TN-SNT/022V.1	File: DELIVERABLE70_4D.DOCX

TELESCOPE POINTING TO HORIZON		
MODE N°	Frq. [Hz]	MODE DESCRIPTION
01	8.12	XEL
02	14.92	Spider
03	17.94	EL
04	19.88	AZ
05	20.31	Tube Mode

TELESCOPE POINTING TO ZENITH		
MODE N°	Frq. [Hz]	MODE DESCRIPTION
01	8.39	XEL
02	14.92	Spider
03	17.17	EL
04	18.93	Tube Mode
05	19.30	Complex Mode
11	24.15	AZ

Table 5. Lowest Locked Rotor Modes for Gantry with R-Guides, EL motors in the EL-Axis Trunnion and Reinforced Wheels Model.

As it can be noticed, the EL mode increases its resonant frequency considerably obtaining a frequency even better than the one obtained for Rocking-Chair. Thus, in case of choosing this configuration for Gantry or Yoke model, it is important to modify the wheel structure making it stiffer in order to gain global telescope stiffness.

2.3 Gantry with R-Guides and EL motors on Telescope Wheels Periphery

Results obtained for this model are presented in the following table:

TELESCOPE POINTING TO HORIZON		
MODE N°	Frq. [Hz]	MODE DESCRIPTION
01	9.12	XEL
02	14.00	EL
03	14.92	Spider
04	18.49	AZ
05	18.67	Tube Mode

TELESCOPE POINTING TO ZENITH		
MODE N°	Frq. [Hz]	MODE DESCRIPTION
01	9.47	XEL
02	12.96	EL
03	14.92	Spider
04	19.11	Complex Mode
05	19.61	Complex Mode
10	23.75	AZ

Table 6. Lowest Locked Rotor Modes for Gantry with R-Guides and EL motors on Telescope Wheels Periphery Model.

This model has a better behaviour in comparison to the ones obtained for Rocking-Chair and Gantry without wheel reinforcement, making it one of the best options for next steps.

If the wheel is reinforced with a plate, the results become the ones shown in the following table:

TELESCOPE POINTING TO HORIZON		
MODE N°	Frq. [Hz]	MODE DESCRIPTION
01	8.39	XEL
02	13.69	EL
03	14.92	Spider
04	17.76	AZ
05	18.70	Trans. along Global Z

TELESCOPE POINTING TO ZENITH		
MODE N°	Frq. [Hz]	MODE DESCRIPTION
01	8.70	XEL
02	12.61	EL
03	14.92	Spider
04	19.09	Complex Mode
05	19.84	Tube Mode
11	23.37	AZ

Table 7. Lowest Locked Rotor Modes for Gantry with R-Guides, EL motors on Telescope Wheels Periphery and Reinforced Wheels Model.

EST TELESCOPE STRUCTURE - ANALYSIS REPORT	Page: 12 of 54 Date: November 13, 2014
Code: DM/TN-SNT/022V.1	File: DELIVERABLE70_4D.DOCX

As the EL motors are placed on Telescope Wheels Periphery, the wheel rigidity does not add useful global stiffness, on the contrary, the results are slightly worse. Thus, in case of choosing this configuration, it is not useful to reinforce the wheels.

2.4 Yoke with R-Guides and EL motors on Telescope Wheels Periphery

This configuration is analysed considering the EL motors placed on the Telescope Wheels Periphery.

Due to the location of the EL motors on the Wheels Periphery, it is not useful to reinforce the EL Wheels. Hence, the model is analysed only for the case where the wheels are not reinforced.

Furthermore, as EL frequency is lower in the case where the telescope is pointing to the Zenith, this position is taken as a reference for the analysis.

The following results belong to the model in the case where the R-Guides are used for the AZ-Axis. In this case, a total of 32 trolleys were allocated over a 4.0 m diameter inner track and a 6.0 m diameter outer track, giving a total tilt stiffness of 2.0710^9 Nm/rad.

TELESCOPE POINTING TO ZENITH		
MODE N°	Frq. [Hz]	MODE DESCRIPTION
01	8.26	XEL
02	10.84	EL
03	14.92	Spider
04	18.83	Complex Mode
05	19.52	Tube Mode
08	21.69	AZ

Table 8. Lowest Locked Rotor Modes for Yoke with R-Guides and EL motors on Telescope Wheels Periphery Model.

As it was expected, those results are worse than the ones obtained for Gantry model. The main difference between Yoke (with R-Guides or Roller Bearing), and Gantry model lies in the AZ-Axis diameter, which is smaller in the case of Yoke Model, and therefore, the tilt stiffness is normally lower.

Additionally, the fact of having a smaller diameter for the tracks (or for the roller bearing) implies that there is an annular section of the platform that is not being withstand, causing this section to be in bending against the tube loads, which implies larger deformations.

<p align="center">EST TELESCOPE STRUCTURE - ANALYSIS REPORT</p>	<p>Page: 13 of 54 Date: November 13, 2014</p>
<p>Code: DM/TN-SNT/022V.1</p>	<p>File: DELIVERABLE70_4D.DOCX</p>

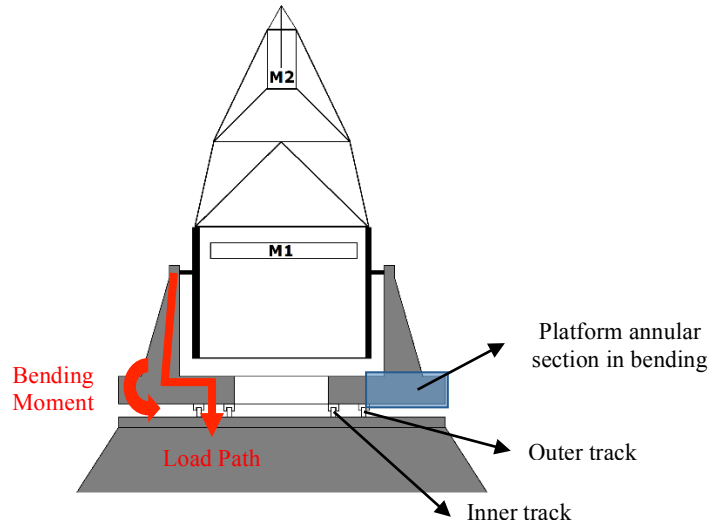


Fig. 4. Yoke Load Path from Telescope Tube to Pier.

To withstand the loads coming from the yokes, it is designed a **reinforced box beam of 1.0 cm thickness**, as shown in the following picture:

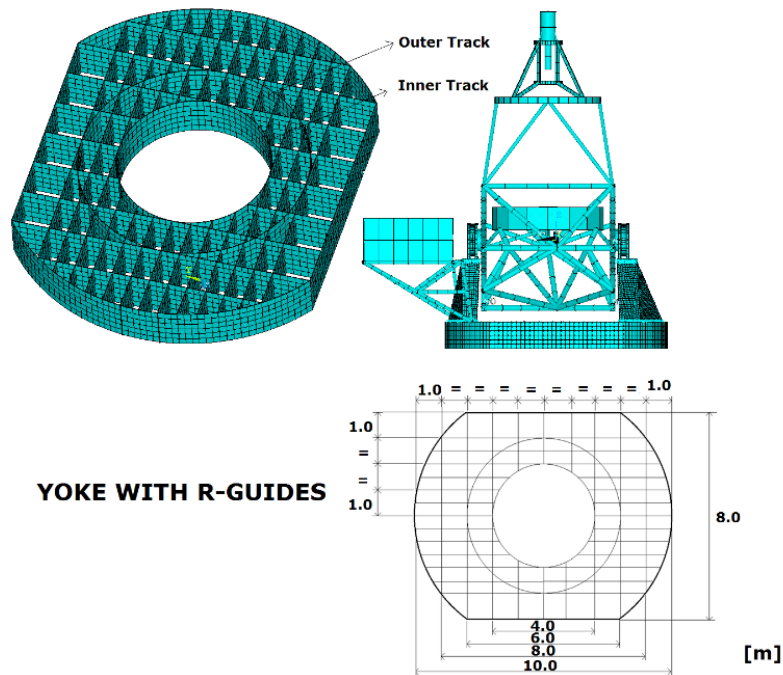


Fig. 5. Yoke with R-Guides FE Model.

As the centre of the platform does not work (the bending moment is compensated by the pair of tracks), it is left empty. The platform height is set to **1.2 m** in order to gain inertia against the bending moment.

2.5 Yoke with Roller Bearing and EL motors on Telescope Wheels Periphery

In this case, as only one bearing is disposed instead of two tracks, it is necessary to fill the centre of the platform in order to compensate loads coming from the yokes. To do that, a similar reinforced box beam has been designed, keeping the thicknesses and height of previous model as shown in the following picture:

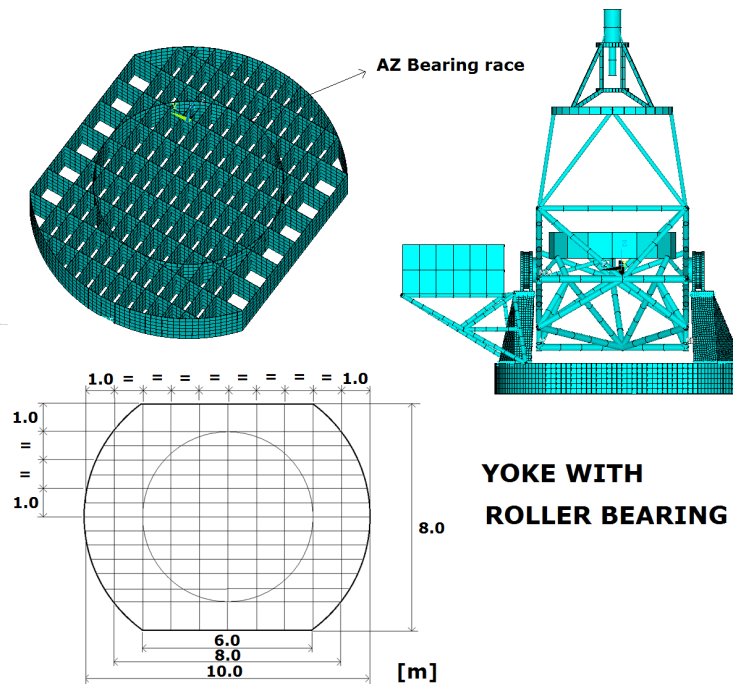


Fig. 6. Yoke with Roller Bearing FE Model.

This model has been tested using a **5.0 m** diameter ($k_{\phi}=4.01 \cdot 10^{11}$ Nm/rad) and a **6.0 m** diameter ($k_{\phi}=6.92 \cdot 10^{11}$ Nm/rad) **conventional roller bearing**, obtaining the following results:

TELESCOPE POINTING TO ZENITH $\phi_{\text{bearing}} = 6.0$ m			TELESCOPE POINTING TO ZENITH $\phi_{\text{bearing}} = 5.0$ m		
MODE N°	Frq. [Hz]	MODE DESCRIPTION	MODE N°	Frq. [Hz]	MODE DESCRIPTION
01	9.13	XEL	01	8.70	XEL
02	12.06	EL	02	11.23	EL
03	14.92	Spider	03	14.92	Spider
04	18.95	Complex Mode	04	18.88	Complex Mode
05	19.69	Tube Mode	05	19.57	Tube Mode
10	23.51	AZ	08	22.40	AZ

Table 9. Lowest Locked Rotor Modes for Yoke with Roller Bearing and EL motors on Telescope Wheels Periphery Model.

As it can be seen, the results are better than the ones obtained with R-Guides (table 8.0), maybe because of the higher tilt stiffness provided by the roller bearings in comparison to the R-Guides.

EST TELESCOPE STRUCTURE - ANALYSIS REPORT	Page: 15 of 54 Date: November 13, 2014
Code: DM/TN-SNT/022V.1	File: DELIVERABLE70_4D.DOCX

Although those results are slightly worse than the ones obtained for Gantry model (table 6), the Yoke configuration has several advantages in relation to the Gantry. As we have a smaller AZ bearing, the use of conventional bearings is feasible from RotheERDE or other large bearing manufacturers. At the same time, the smaller diameter allows the allocation for transfer optics and cable wrap subsystem in separated compartments, unlike the Gantry model, in which the bigger diameter requires both subsystems to be in a common compartment, making the design more complicated.

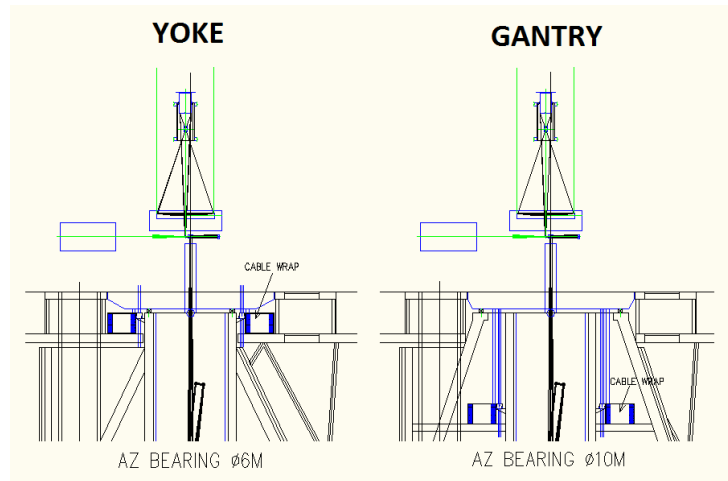


Fig. 6. Cable Wrap and Transfer Optics Subsystems for Yoke and Gantry Models.

That are the main reasons why this model is considered to be one of the best options for EST, being considered for next analysis.

2.6 Dynamic Analysis Conclusions

Results obtained in the Dynamic Analysis, considering the case where the telescope is pointing to the zenith, are summarized in the following table:

MODEL	CONFIGURATION	EL [Hz]	AZ [Hz]
ROCKING CHAIR	R-GUIDES	9.36	21.65
	R-GUIDES AND WHEELS REINFORCED	9.37	21.63
GANTRY	R-GUIDES AND EL MOTORS ON EL-AXIS TRUNNION	5.72	24.66
	R-GUIDES, EL MOTORS ON EL-AXIS TRUNNION AND WHEEL REINFORCED	17.17	24.15
	R-GUIDES AND EL MOTORS ON TELESCOPE WHEELS PERIPHERY	12.96	23.75
	R-GUIDES, EL MOTORS ON TELESCOPE WHEELS PERIPHERY AND WHEELS R.	12.61	23.37
YOKE	R-GUIDES AND EL MOTORS ON TELESCOPE WHEELS PERIPHERY	10.84	21.69
	ROLLER BEARING (Ø 6.0 m) AND EL MOTORS ON TELESCOPE WHEELS PERIPHERY	12.06	23.51
	ROLLER BEARING (Ø 5.0 m) AND EL MOTORS ON TELESCOPE WHEELS PERIPHERY	11.23	22.40

Table. 10. Frequency Summary for Principal Modes of Analysed Models. Telescope pointing to Zenith.

EST TELESCOPE STRUCTURE - ANALYSIS REPORT	Page: 16 of 54 Date: November 13, 2014
Code: DM/TN-SNT/022V.1	File: DELIVERABLE70_4D.DOCX

As it can be seen, the main differences occur for the EL mode, while the AZ mode remains approximately constant whatever the model considered. Therefore, this is the criteria followed to value the performance of the models.

Attending to the EL mode frequency, the best model is **Gantry**, for the case where the EL motors are placed in the EL-Axis Trunnion (17.17 Hz), followed by the case where the motors are placed on the Telescope Wheels Periphery (12.96 Hz).

The main advantage of the configuration with the EL motors in the EL-Axis Trunnion is the possibility to use conventional direct drives (in this case, out-of-the-shelve) instead of customs. On the contrary, this model requires the EL wheels to be reinforced in order to gain global stiffness, which is not necessary in case of placing the EL motors in the EL Wheels Periphery, because of the higher lever arm.

The configuration considered in next analysis for Gantry model correspond to the case where the EL motors are placed on the EL Wheels Periphery.

Following with the comparison, the next model with better behaviour is the **Yoke** model under the configuration with conventional Roller Bearing for the AZ-Axis instead of R-Guides (12.06 Hz). In comparison to the Gantry model with the equivalent configuration (El motors on Telescope Wheels Periphery), this model has a close frequency (12.06 Hz Vs 12.96 Hz), offering also a set of mechanical advantages, mostly related to the mechanical design for the transfer optics and cable wrap subsystems and the possibility to use conventional roller bearing. Therefore, it is considered one of the best option for EST.

Finally, the EL frequency for **Rocking-Chair** model remains constant whatever the rigidity of the wheel because the EL motors are placed on the EL Wheels Periphery. In this case, the elevation resonant frequency is 9.36 Hz.

EST TELESCOPE STRUCTURE - ANALYSIS REPORT	Page: 17 of 54 Date: November 13, 2014
Code: DM/TN-SNT/022V.1	File: DELIVERABLE70_4D.DOCX

3. GRAVITY DEFORMATIONS ANALYSIS

The following section covers the analysis for the structural deformations due to gravity acting on the telescope structure.

The analysis is made considering **Rocking-Chair**, **Gantry** and **Yoke** models with the configuration described below:

- **Rocking-Chair.** With R-Guides for AZ-Axis and EL wheels not reinforced.
- **Gantry.** With R-Guides for AZ-Axis, EL wheels not reinforced and EL motors on Telescope Wheels Periphery.
- **Yoke.** With Roller Bearing for AZ-Axis, EL wheels not reinforced and EL motors on Telescope Wheels Periphery.

Image motion due to gravity deformations is also computed considering M1 to M4 mirror displacements.

3.1 Results of FE Calculations

In regard of gravity, only the changing deformations of the elevation part when moving from Zenith to Horizon have influence on the pointing. The gravity deformations of the azimuth part are constant and hence, do not have influence.

The objective of this analysis is to obtain the deformations induced by gravity, converting them later into image motion in the focal, plane using the sensitivity matrix described in the following section.

For the analysis, the following **Loads Cases** are considered:

- **GH:** Gravity, with telescope pointing to Horizon
- **GZ:** Gravity, with telescope pointing to Zenith

Results are presented in a local coordinate system that moves with the EL structure, as shown in the following picture:

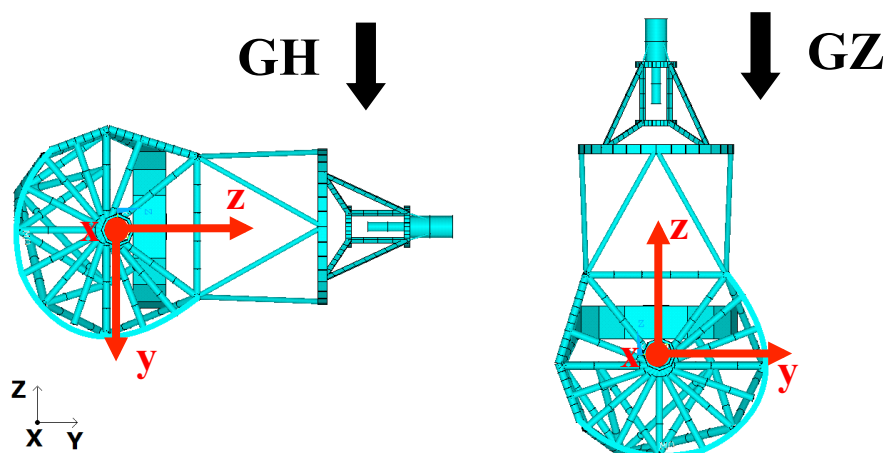


Fig. 7. Local Coordinate System for Gravity Deformations Results.

3.1.1 Rocking-Chair Model

Figure 9 and table 11 show the calculation results for Rocking-Chair with R-Guides.

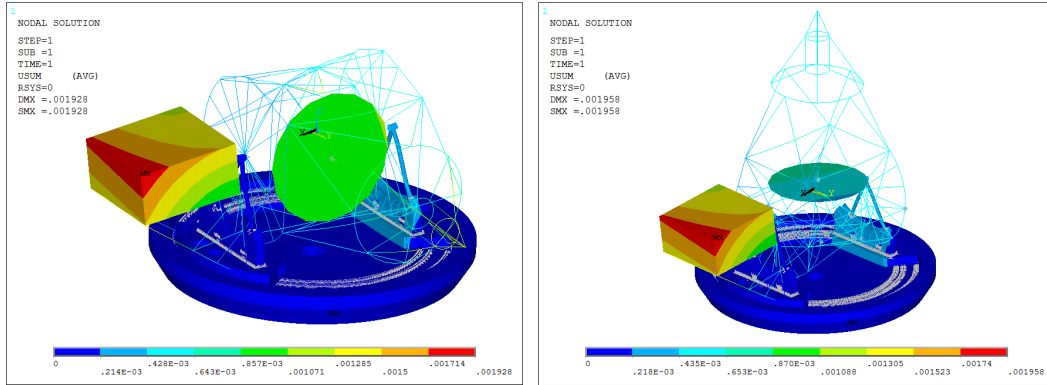


Fig. 9. Gravity Deformations. Rocking-Chair Model.

LOAD C.	MIRROR	UX [mm]	UY [mm]	UZ [mm]	ROTX [mrad]	ROTY [mrad]	ROTZ [mrad]
GH	M1	0.008	1.008	-0.108	0.052	-0.002	-0.021
	M2	-0.032	1.140	0.070	-0.015	-0.003	-0.024
	M3	0.011	1.070	-0.108	0.058	-0.002	-0.021
	M4	0.013	1.070	-0.102	0.058	-0.002	-0.021

LOAD C.	MIRROR	UX [mm]	UY [mm]	UZ [mm]	ROTX [mrad]	ROTY [mrad]	ROTZ [mrad]
GZ	M1	-0.041	0.127	-0.568	0.072	-0.026	-0.006
	M2	-0.279	0.054	-0.580	-0.004	-0.027	0.000
	M3	-0.012	0.208	-0.568	0.072	-0.026	-0.006
	M4	-0.011	0.208	-0.561	0.072	-0.026	-0.006

Table. 11. Gravity Induced Translations and Rotations. Rocking-Chair Model.

3.1.2 Gantry Model

Figure 10 and table 12 show the calculation results for Gantry with R-Guides for AZ-Axis and EL motors on Telescope Wheels Periphery Model.

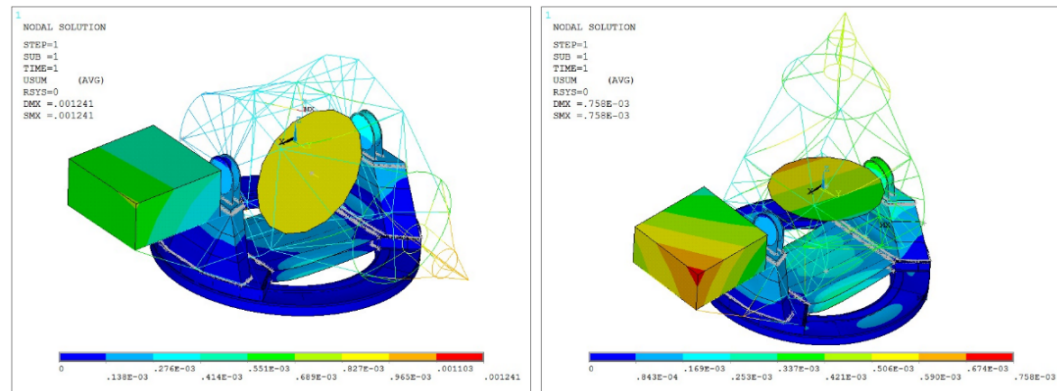


Fig. 10. Gravity Deformations. Gantry Model.

LOAD C.	MIRROR	UX [mm]	UY [mm]	UZ [mm]	ROTX [mrad]	ROTY [mrad]	ROTZ [mrad]
GH	M1	0.195	0.853	-0.098	0.049	-0.002	-0.008
	M2	0.181	1.062	0.069	-0.026	-0.001	-0.012
	M3	0.197	0.911	-0.098	0.054	-0.002	-0.008
	M4	0.198	0.911	-0.093	0.054	-0.002	-0.008

LOAD C.	MIRROR	UX [mm]	UY [mm]	UZ [mm]	ROTX [mrad]	ROTY [mrad]	ROTZ [mrad]
GZ	M1	0.137	0.146	-0.415	0.067	-0.011	-0.004
	M2	0.062	0.096	-0.416	-0.007	-0.009	0.001
	M3	0.149	0.221	-0.415	0.067	-0.011	-0.004
	M4	0.149	0.221	-0.408	0.066	-0.011	-0.004

Table 12. Gravity Induced Translations and Rotations. Gantry Model

3.1.3 Yoke Model

Figure 11 and table 13 show the calculation results for Yoke with Roller bearing for AZ-Axis and EL motors on Telescope Wheels Periphery Model.

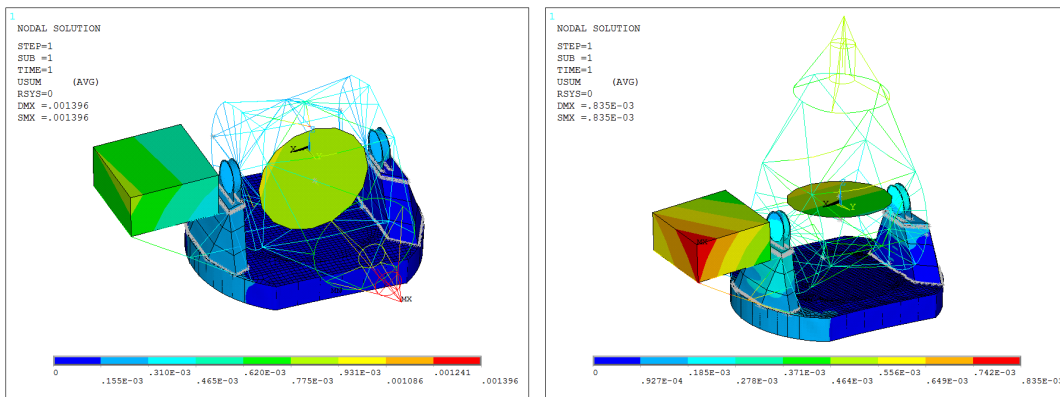


Fig. 11. Gravity Deformations. Yoke Model.

LOAD C.	MIRROR	UX [mm]	UY [mm]	UZ [mm]	ROTX [mrad]	ROTY [mrad]	ROTZ [mrad]
GH	M1	0.168	0.883	-0.047	0.033	-0.001	0.012
	M2	0.145	1.341	0.124	-0.030	-0.002	0.007
	M3	0.169	0.924	-0.047	0.039	-0.001	0.012
	M4	0.168	0.924	-0.043	0.039	-0.001	0.012

LOAD C.	MIRROR	UX [mm]	UY [mm]	UZ [mm]	ROTX [mrad]	ROTY [mrad]	ROTZ [mrad]
GZ	M1	0.138	0.186	-0.411	0.058	0.006	-0.003
	M2	0.198	0.170	-0.411	-0.013	0.006	0.001
	M3	0.131	0.250	-0.411	0.057	0.006	-0.003
	M4	0.131	0.250	-0.405	0.057	0.006	-0.003

Table 13. Gravity Induced Translations and Rotations. Yoke Model.

EST TELESCOPE STRUCTURE - ANALYSIS REPORT	Page: 20 of 54 Date: November 13, 2014
Code: DM/TN-SNT/022V.1	File: DELIVERABLE70_4D.DOCX

3.2 Sensitivity Matrices

3.2.1 General

For the calculation of the image motion induced by the deviations of the mirrors, a sensitivity matrix is used. This sensitivity matrix is defined in AD.1 and is based on the AZ platform fixed coordinate system, as shown in the following picture:

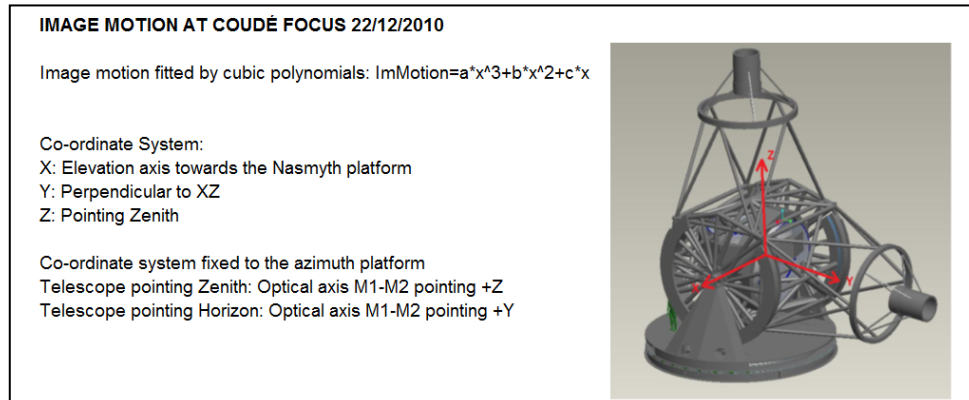


Fig. 12 Coordinate System for Sensitivity Matrix (AD.1)

Due to the fixed coordinate system, there are two matrices. One for horizontal telescope position and another for the case where the telescope is pointing to zenith.

As the FE calculation is defined using a local coordinate system (fig. 7), displacements must be translated into the focal plane coordinate system before doing the operation using the following cross-references:

MAGNITUDE	AD.1 ZENITH		AD.1 HORIZONTAL	
	FEM	FOCAL PLANE	FEM	FOCAL PLANE
X Displacement	dx	-dx	dx	-dx
Y Displacement	dy	-dy	dy	dz
Z Displacement	dz	dz	dz	-dy
X Rotation	rotx	-rotx	rotx	-rotx
Y Rotation	roty	-roty	roty	rotz
Z Rotation	rotz	rotz	rotz	-roty

Table. 14. Cross-References between Coordinate Systems

Sensitivity matrix contains the parameters for all the 7 mirrors, and is fitted with an up-to third order polynomial. The following evaluations are performed considering all fitting matrix parameters, and deformations related to M1 up to M4 mirrors.

EST TELESCOPE STRUCTURE - ANALYSIS REPORT	Page: 21 of 54 Date: November 13, 2014
Code: DM/TN-SNT/022V.1	File: DELIVERABLE70_4D.DOCX

3.2.2 Resulting Gravity Induced Pointing Errors

3.2.2.1 Rocking-Chair Model

Using the calculated gravity deformations of table 11 and the sensitivity matrix of AD.1, the following pointing errors for the defined load cases are obtained.

GRAVITY DEFORMATIONS		ROCKING CHAIR (R-GUIDES)									
		GRAVITY ZENITH					GRAVITY HORIZON				
MIRROR	MAG.	FEM	FOCAL PLANE	IMG. MOTION AT COUDE			FEM	FOCAL PLANE	IMG. MOTION AT COUDE		
				x [mm]	y [mm]	z [mm]			x [mm]	y [mm]	z [mm]
M1	δx [mm]	-0.041	0.041	1.342	0.079	-0.003	0.008	-0.008	-0.016	0.273	0.003
	δy [mm]	0.127	-0.127	0.245	-4.156	-0.074	1.008	-0.108	0.070	0.050	112.456
	δz [mm]	-0.568	-0.568	0.379	0.270	609.373	-0.108	-1.008	32.828	1.926	-1.596
	θx [mrad]	0.072	-0.072	-0.871	15.232	-0.009	0.052	-0.052	10.502	0.618	-0.426
	θy [mrad]	-0.026	0.026	5.473	0.313	-0.028	-0.002	-0.021	0.000	0.000	0.000
	θz [mrad]	-0.006	-0.006	0.000	0.000	0.000	-0.021	0.002	-0.045	0.509	0.006
M2	δx [mm]	-0.279	0.279	-10.260	-0.605	-0.109	-0.032	0.032	-0.070	1.183	0.013
	δy [mm]	0.054	-0.054	-0.119	2.019	0.020	1.140	0.070	0.046	0.033	74.041
	δz [mm]	-0.580	-0.580	-0.367	-0.261	-589.325	0.070	-1.140	-41.898	-2.483	-1.907
	θx [mrad]	-0.004	0.004	0.017	-0.287	-0.004	-0.015	0.015	-1.112	-0.066	-0.018
	θy [mrad]	-0.027	0.027	1.914	0.115	-0.003	-0.003	-0.024	0.000	0.000	0.000
	θz [mrad]	0.000	0.000	0.000	0.000	0.000	-0.024	0.003	-0.010	0.242	0.003
M3	δx [mm]	-0.012	0.012	0.000	0.000	0.000	0.011	-0.011	0.000	0.000	0.000
	δy [mm]	0.208	-0.208	0.054	-0.878	3.697	1.070	-0.108	-0.452	-0.026	1.927
	δz [mm]	-0.568	-0.568	0.148	-2.403	10.111	-0.108	-1.070	4.478	0.256	-19.087
	θx [mrad]	0.072	-0.072	0.011	-0.183	-0.001	0.058	-0.058	-0.145	-0.009	0.000
	θy [mrad]	-0.026	0.026	-0.033	-0.002	0.000	-0.002	-0.021	-0.002	0.026	0.000
	θz [mrad]	-0.006	-0.006	-0.008	0.000	0.000	-0.021	0.002	0.000	-0.003	0.000
M4	δx [mm]	-0.011	0.011	0.047	0.003	0.197	0.013	-0.013	-0.003	0.056	-0.234
	δy [mm]	0.208	-0.208	-0.875	-0.053	-3.706	1.070	-0.102	0.000	0.000	0.000
	δz [mm]	-0.561	-0.561	0.000	0.000	0.000	-0.102	-1.070	0.279	-4.531	19.067
	θx [mrad]	0.072	-0.072	-0.004	0.061	0.000	0.058	-0.058	0.048	0.003	0.000
	θy [mrad]	-0.026	0.026	-0.001	0.022	0.000	-0.002	-0.021	0.002	-0.035	0.000
	θz [mrad]	-0.006	-0.006	0.011	0.001	0.000	-0.021	0.002	-0.002	0.000	0.000
		TOTAL	[mm]	-2.897	9.286	30.136	TOTAL	[mm]	4.498	-1.979	184.247
		ZENITH	[arcsec]	-3.074	9.852		HORIZON	[arcsec]	-2.100	-4.772	

Table 15. Rocking-Chair Gravity Induced Pointing Error in Zenith and Horizontal Positions.

As deformations depend on the elevation angle of the structure, intermediate values can be derived from the ones obtained for horizontal and zenith positions as a function of the EL angle (θ_{EL}), applying the following formulas:

$$\mathbf{X}(\theta_{EL}) = X_H \cdot \cos(\theta_{EL}) + X_Z \cdot \sin(\theta_{EL}) \quad \text{and} \quad \mathbf{Y}(\theta_{EL}) = Y_H \cdot \cos(\theta_{EL}) + Y_Z \cdot \sin(\theta_{EL})$$

EST TELESCOPE STRUCTURE - ANALYSIS REPORT	Page: 22 of 54 Date: November 13, 2014
Code: DM/TN-SNT/022V.1	File: DELIVERABLE70_4D.DOCX

The following table contains the values obtained for a set of discrete angle positions in the range:

EL [°]	X [arcsec]	Y [arcsec]	Z [mm]
0	-2.100	-4.772	184.247
15	-2.824	-2.060	185.768
30	-3.356	0.793	174.630
45	-3.659	3.592	151.591
60	-3.712	6.146	118.222
75	-3.513	8.281	76.796
90	-3.074	9.852	30.136
Max-Min	1.612	14.625	155.632
xy [arcsec]	14.713		

Table 16. Rocking-Chair Gravity Induced Pointing Error as a function of EL Angle.

Total image motion is 14.713 arcsec and is obtained as the difference between the maximum and minimum value in the range. Using look-up tables, it is feasible to compensate this error by a factor of 90%, hence, the error would be 1.471 arcsec.

Fixing the origin of the table at the centre of the correction span. The maximum error can be limited to **0.736 arcsec**, i.e., 50% of the total error range (1.471arcsec). Hence, Rocking-Chair image motion due to gravity deformations (0.736 arcsec) is higher than the value specified in AD.1 (0.500 arcsec).

3.2.2.2 Gantry Model

Using the calculated gravity deformations of table 12 and the sensitivity matrix of AD.1, the following pointing errors for the defined load cases are obtained.

GRAVITY DEFORMATIONS		GANTRY (R-GUIDES)									
		GRAVITY ZENITH					GRAVITY HORIZON				
MIRROR	MAG.	FEM	FOCAL PLANE	IMG. MOTION AT COUDE			FEM	FOCAL PLANE	IMG. MOTION AT COUDE		
				x [mm]	y [mm]	z [mm]			x [mm]	y [mm]	z [mm]
M1	δx [mm]	0.137	-0.137	-4.448	-0.262	-0.026	0.195	-0.195	-0.377	6.400	0.018
	δy [mm]	0.146	-0.146	0.282	-4.794	-0.090	0.853	-0.098	0.064	0.045	102.119
	δz [mm]	-0.415	-0.415	0.274	0.195	440.605	-0.098	-0.853	27.779	1.630	-1.146
	θx [mrad]	0.067	-0.067	-0.807	14.110	0.005	0.049	-0.049	9.855	0.580	-0.394
	θy [mrad]	-0.011	0.011	2.252	0.129	-0.006	-0.002	-0.008	0.000	0.000	0.000
	θz [mrad]	-0.004	-0.004	0.000	0.000	0.000	-0.008	0.002	-0.038	0.429	0.005
M2	δx [mm]	0.062	-0.062	2.297	0.135	-0.007	0.181	-0.181	0.396	-6.722	-0.129
	δy [mm]	0.096	-0.096	-0.210	3.557	0.029	1.062	0.069	0.045	0.032	72.744
	δz [mm]	-0.416	-0.416	-0.266	-0.189	-427.072	0.069	-1.062	-39.035	-2.312	-1.653
	θx [mrad]	-0.007	0.007	0.032	-0.527	-0.007	-0.026	0.026	-1.854	-0.109	-0.031
	θy [mrad]	-0.009	0.009	0.664	0.040	-0.001	-0.001	-0.012	0.000	0.000	0.000
	θz [mrad]	0.001	0.001	0.000	0.000	0.000	-0.012	0.001	-0.003	0.063	0.001

EST TELESCOPE STRUCTURE - ANALYSIS REPORT	Page: 23 of 54 Date: November 13, 2014
Code: DM/TN-SNT/022V.1	File: DELIVERABLE70_4D.DOCX

M3	δx [mm]	0.149	-0.149	0.000	0.000	0.000	0.197	-0.197	0.000	0.000	0.000
	δy [mm]	0.221	-0.221	0.058	-0.935	3.936	0.911	-0.098	-0.411	-0.024	1.751
	δz [mm]	-0.415	-0.415	0.108	-1.754	7.382	-0.098	-0.911	3.815	0.218	-16.260
	θx [mrad]	0.067	-0.067	0.010	-0.169	-0.001	0.054	-0.054	-0.137	-0.008	0.000
	θy [mrad]	-0.011	0.011	-0.014	-0.001	0.000	-0.002	-0.008	-0.001	0.010	0.000
	θz [mrad]	-0.004	-0.004	-0.004	0.000	0.000	-0.008	0.002	0.000	-0.003	0.000
M4	δx [mm]	0.149	-0.149	-0.628	-0.038	-2.660	0.198	-0.198	-0.052	0.837	-3.524
	δy [mm]	0.221	-0.221	-0.931	-0.056	-3.946	0.911	-0.093	0.000	0.000	0.000
	δz [mm]	-0.408	-0.408	0.000	0.000	0.000	-0.093	-0.911	0.238	-3.859	16.237
	θx [mrad]	0.066	-0.066	-0.003	0.056	0.000	0.054	-0.054	0.046	0.003	0.000
	θy [mrad]	-0.011	0.011	-0.001	0.009	0.000	-0.002	-0.008	0.001	-0.014	0.000
	θz [mrad]	-0.004	-0.004	0.006	0.000	0.000	-0.008	0.002	-0.002	0.000	0.000
TOTAL		[mm]	-1.327	9.505	18.142	TOTAL	[mm]	0.329	-2.802	169.737	
ZENITH		[arcsec]	-1.408	10.085		HORIZON	[arcsec]	-2.973	-0.349		

Table 17. Gantry Gravity Induced Pointing Error in Zenith and Horizontal Positions.

The image motion as a function of the angle is:

EL [°]	X [arcsec]	Y [arcsec]	Z [mm]
0	-2.973	-0.349	169.737
15	-3.237	2.273	168.649
30	-3.279	4.740	156.067
45	-3.098	6.884	132.850
60	-2.706	8.559	100.580
75	-2.130	9.651	61.455
90	-1.408	10.085	18.142
Max-Min	1.871	10.434	151.595
xy [arcsec]	10.601		

Table 18. Gantry Gravity Induced Pointing Error as a function of EL Angle.

Applying all compensation factors, total image motion is **0.530 arcsec**, which is close to the values given in AD.1 (**0.500 arcsec**).

EST TELESCOPE STRUCTURE - ANALYSIS REPORT	Page: 24 of 54 Date: November 13, 2014
Code: DM/TN-SNT/022V.1	File: DELIVERABLE70_4D.DOCX

3.2.2.3 Yoke Model

Using the calculated gravity deformations of table 13 and the sensitivity matrix of AD.1, the following pointing errors for defined load cases are obtained.

GRAVITY DEFORMATIONS		YOKE (ROLLER BEARING)									
		GRAVITY ZENITH					GRAVITY HORIZON				
MIRROR	MAG.	FEM	FOCAL PLANE	IMG. MOTION AT COUDE			FEM	FOCAL PLANE	IMG. MOTION AT COUDE		
				x [mm]	y [mm]	z [mm]			x [mm]	y [mm]	z [mm]
M1	δx [mm]	0.138	-0.138	-4.488	-0.265	-0.027	0.168	-0.168	-0.326	5.527	0.022
	δy [mm]	0.186	-0.186	0.359	-6.094	-0.125	0.883	-0.047	0.030	0.022	49.017
	δz [mm]	-0.411	-0.411	0.271	0.193	436.383	-0.047	-0.883	28.755	1.688	-1.227
	θx [mrad]	0.058	-0.058	-0.695	12.157	0.023	0.033	-0.033	6.665	0.392	-0.248
	θy [mrad]	0.006	-0.006	-1.344	-0.077	-0.001	-0.001	0.012	0.000	0.000	0.000
	θz [mrad]	-0.003	-0.003	0.000	0.000	0.000	0.012	0.001	-0.011	0.128	0.002
M2	δx [mm]	0.198	-0.198	7.297	0.430	-0.063	0.145	-0.145	0.317	-5.383	-0.095
	δy [mm]	0.170	-0.170	-0.372	6.314	0.032	1.341	0.124	0.082	0.058	131.397
	δz [mm]	-0.411	-0.411	-0.262	-0.186	-421.285	0.124	-1.341	-49.313	-2.925	-2.647
	θx [mrad]	-0.013	0.013	0.057	-0.955	-0.012	-0.030	0.030	-2.185	-0.129	-0.037
	θy [mrad]	0.006	-0.006	-0.439	-0.026	0.000	-0.002	0.007	0.000	0.000	0.000
	θz [mrad]	0.001	0.001	0.000	0.000	0.000	0.007	0.002	-0.007	0.166	0.002
M3	δx [mm]	0.131	-0.131	0.000	0.000	0.000	0.169	-0.169	0.000	0.000	0.000
	δy [mm]	0.250	-0.250	0.065	-1.059	4.455	0.924	-0.047	-0.198	-0.011	0.843
	δz [mm]	-0.411	-0.411	0.107	-1.738	7.313	-0.047	-0.924	3.866	0.221	-16.478
	θx [mrad]	0.057	-0.057	0.009	-0.146	-0.001	0.039	-0.039	-0.097	-0.006	0.000
	θy [mrad]	0.006	-0.006	0.008	0.000	0.000	-0.001	0.012	0.001	-0.015	0.000
	θz [mrad]	-0.003	-0.003	-0.004	0.000	0.000	0.012	0.001	0.000	-0.001	0.000
M4	δx [mm]	0.131	-0.131	-0.551	-0.033	-2.336	0.168	-0.168	-0.044	0.709	-2.986
	δy [mm]	0.250	-0.250	-1.054	-0.064	-4.465	0.924	-0.043	0.000	0.000	0.000
	δz [mm]	-0.405	-0.405	0.000	0.000	0.000	-0.043	-0.924	0.241	-3.911	16.456
	θx [mrad]	0.057	-0.057	-0.003	0.048	0.000	0.039	-0.039	0.032	0.002	0.000
	θy [mrad]	0.006	-0.006	0.000	-0.005	0.000	-0.001	0.012	-0.001	0.020	0.000
	θz [mrad]	-0.003	-0.003	0.006	0.000	0.000	0.012	0.001	-0.001	0.000	0.000
		TOTAL	[mm]	-1.032	8.494	19.892	TOTAL	[mm]	-12.193	-3.447	174.021
		ZENITH	[arcsec]	-1.095	9.013		HORIZON	[arcsec]	-3.658	12.937	

Table 19. Yoke Gravity Induced Pointing Error in Zenith and Horizontal Positions.

EST TELESCOPE STRUCTURE - ANALYSIS REPORT	Page: 25 of 54 Date: November 13, 2014
Code: DM/TN-SNT/022V.1	File: DELIVERABLE70_4D.DOCX

The image motion as a function of the angle is:

EL [°]	X [arcsec]	Y [arcsec]	Z [mm]
0	-3.658	12.937	174.021
15	-3.816	14.829	173.240
30	-3.715	15.710	160.652
45	-3.361	15.521	137.117
60	-2.777	14.273	104.237
75	-2.005	12.054	64.254
90	-1.095	9.013	19.892
Max-Min	2.721	6.697	154.129
xy [arcsec]	7.229		

Table 20. Yoke Gravity Induced Pointing Error as a function of EL Angle.

Applying all compensation factors, total image motion is **0.361 arcsec**, which is lower than the value given in AD.1 (**0.500 arcsec**).

3.3 Gravity Deformations Analysis Conclusions

The following table contains the gravity induced pointing errors obtained for the models considered in the analysis. The results include the compensation factors.

MODEL	IMAGE MOTION [arcsec]	REQUIRED AD.1 [arcsec]
ROCKING-CHAIR	0.736	0.500
GANTRY	0.530	
YOKE	0.361	

Table 21. Gravity Induced Pointing Errors for the Models Considered in the Analysis.

As it can be seen, only Gantry and Yoke configurations exhibit a feasible performance to meet AD.1 requirements.

As it was expected according to the dynamic analysis of the previous chapter, Rocking-Chair has a worse performance, not enough to meet AD.1 requirement.

EST TELESCOPE STRUCTURE - ANALYSIS REPORT	Page: 26 of 54 Date: November 13, 2014
Code: DM/TN-SNT/022V.1	File: DELIVERABLE70_4D.DOCX

4. WIND ANALYSIS

The following section covers the analysis for the structural deformations due to wind forces acting on the telescope structure.

The analysis is performed for the same models and the same configurations considered in the Gravitational Analysis, i.e.,

- **Rocking-Chair.** With R-Guides for the AZ-Axis and wheels not reinforced.
- **Gantry.** With R-Guides for the AZ-Axis, wheels not reinforced and EL motors placed on Telescope Wheels Periphery.
- **Yoke.** With Roller Bearing for the AZ-Axis, wheels not reinforced and EL motors placed on Telescope Wheels Periphery.

Image motion due to the wind forces on the telescope structure is computed considering M1 to M4 mirror movements, using the sensitivity matrix described in AD.1.

4.1 Wind Drag Forces on the Structure

The wind induced drag forces on the telescope structure depends on the far field wind pressure q_0 , the exposed area A , and the drag coefficient C_{drag} according to the following formula:

$$F_{drag} = C_{drag} \cdot A \cdot q_0$$

The far field wind pressure depends on the wind speed V and the air density ρ_{air} according to:

$$q_0 = \frac{1}{2} \rho_{air} \cdot V^2$$

As wind speed V is composed by an static component $V_{st.}$ and a dynamic component $V_{dyn.}$ q_0 can be divided into a component due to the static wind and a component due to dynamic wind:

$$q_0 = \frac{1}{2} \rho_{air} \cdot (V_{st.} + V_{dyn.})^2 = \frac{1}{2} \rho_{air} \cdot (V_{st.}^2 + V_{dyn.}^2 + 2 \cdot V_{st.} \cdot V_{dyn.}) \approx \frac{1}{2} \rho_{air} (V_{st.}^2 + 2 \cdot V_{st.} \cdot V_{dyn.})$$

$$q_{0_st.} = \frac{1}{2} \rho_{air} \cdot V_{st.}^2$$

$$q_{0_dyn.} = \rho_{air} \cdot V_{st.} \cdot V_{dyn.}$$

Static wind velocity is set to **11.5 m/s** and the dynamic component as a 30 % of the static component according to AD.2, i.e., **3.5 m/s**, which result in a total wind speed of **15 m/s** including the static and dynamic component.

For the analysis, a value of **1.5 kg/m³** for air density is considered, which is equivalent to have a safety factor of approximately 1.5 (1.0 kg/m³ is the air density for a place on a site at ~ 3000 m and 20 °).

EST TELESCOPE STRUCTURE - ANALYSIS REPORT	Page: 27 of 54 Date: November 13, 2014
Code: DM/TN-SNT/022V.1	File: DELIVERABLE70_4D.DOCX

Considering those values, the far field wind pressure for the static wind component and dynamic wind component is:

$$q_{0_st.} = \frac{1}{2} \rho_{air} \cdot V_{st.}^2 = 99.187 \left[\frac{N}{m^2} \right]; q_{0_dyn.} = \rho_{air} \cdot V_{st.} \cdot V_{dyn.} = 60.375 \left[\frac{N}{m^2} \right]$$

Wind forces on the telescope depend on the elevation angle and the angle of attack of the wind in combination with the azimuth angle. The following four extreme load cases were considered in the analysis:

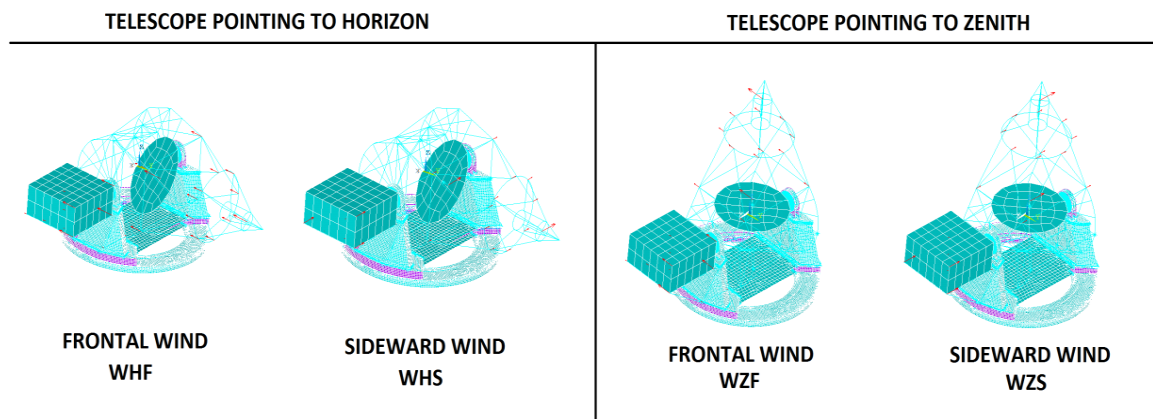


Fig. 13. Considered Load Cases for Wind Analysis

For each load case, the wind drag force was determined considering the areas given by M1 and M2 mirrors, as well as the upper part of the tube and the Nasmyth platform, including its supporting structure.

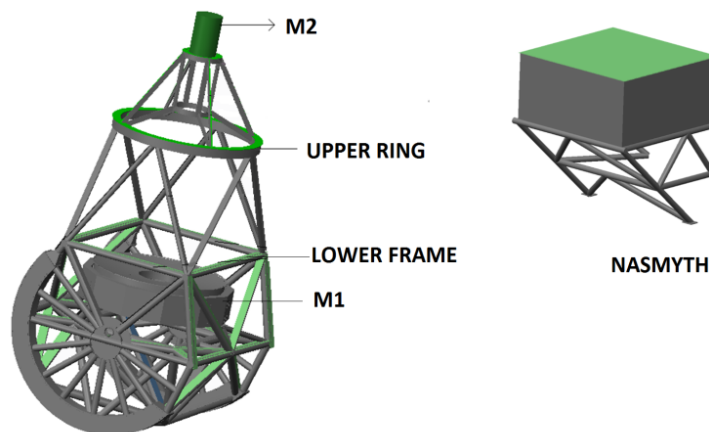


Fig. 14. Considered Areas for Wind Drag Forces Calculation

The following table contains the effective areas as well as the resulting drag forces over telescope tube:

EST TELESCOPE STRUCTURE - ANALYSIS REPORT	Page: 28 of 54 Date: November 13, 2014
Code: DM/TN-SNT/022V.1	File: DELIVERABLE70_4D.DOCX

FRONTAL WIND. TELESCOPE POINTING TO HORIZON (WHF)			
SECTION	EFFECTIVE AREA [m ²]	F _{DRAG} [N]	
		STATIC WIND	DYNAMIC WIND
M1	20.74	2057.46	1252.37
M2	3.91	387.37	235.79
UPPER RING	22.18	2200.21	1339.26
LOWER FRAME	13.92	1381.05	840.64
TOTAL:	60.75	6026.09	3668.05

FRONTAL WIND. TELESCOPE POINTING TO ZENITH (WZF)			
SECTION	EFFECTIVE AREA [m ²]	F _{DRAG} [N]	
		STATIC WIND	DYNAMIC WIND
M1	5.73	568.64	346.13
M2	6.14	608.61	370.46
UPPER RING	16.69	1655.53	1007.72
LOWER FRAME	8.30	823.55	501.29
TOTAL:	36.86	3656.33	2225.60

SIDEWARD WIND. TELESCOPE POINTING TO HORIZON (WHS)			
SECTION	EFFECTIVE AREA [m ²]	F _{DRAG} [N]	
		STATIC WIND	DYNAMIC WIND
M1	5.73	568.64	346.13
M2	6.14	608.61	370.46
UPPER RING	16.25	1611.77	981.08
LOWER FRAME	7.24	718.51	437.35
TOTAL:	35.36	3507.53	2135.02

SIDEWARD WIND. TELESCOPE POINTING TO ZENITH (WZS)			
SECTION	EFFECTIVE AREA [m ²]	F _{DRAG} [N]	
		STATIC WIND	DYNAMIC WIND
M1	5.73	568.64	346.13
M2	6.14	608.61	370.46
UPPER RING	16.25	1611.77	981.08
LOWER FRAME	7.24	718.51	437.35
TOTAL:	35.36	3507.53	2135.02

Table 22. Effective Areas and Static/Dynamic Wind Drag Forces over Telescope Tube.

Values are the same regardless the model considered because the telescope tube is not related to the configuration unlike the Nasmyth platform, whose values are different depending on the model considered. This is because the support structure varies between the Rocking-Chair, Gantry or Yoke model. On the contrary, Nasmyth areas and forces are independent of the elevation angle. Values are showed in the following table:

MODEL	EFFECTIVE AREAS [m ²]		STATIC WIND DRAG FORCES [N]		DYNAMIC WIND DRAG FORCES [N]	
	FRONTAL WIND	SIDEWARD WIND	FRONTAL WIND	SIDEWARD WIND	FRONTAL WIND	SIDEWARD WIND
ROCKING-CHAIR	25.56	23.06	2535.37	2287.38	1543.27	1392.32
GANTRY	22.65	20.44	2247.02	2026.91	1367.75	1233.77
YOKE	22.65	20.44	2247.02	2026.91	1367.75	1233.77

Table 23. Effective Areas and Static/Dynamic Wind Drag Forces over the Nasmyth

Forces coming from telescope tube are distributed between FEM nodes of M1, M2, Upper Ring and Lower Frame, and forces coming from Nasmyth platform are distributed between the nodes of the platform and support structure.

EST TELESCOPE STRUCTURE - ANALYSIS REPORT	Page: 29 of 54 Date: November 13, 2014
Code: DM/TN-SNT/022V.1	File: DELIVERABLE70_4D.DOCX

4.2 Steady State Wind Analysis

4.2.1 Mirror Displacements due to Structural Deformations

4.2.1.1 Rocking-Chair Model

LOAD CASE	MIRROR	UX [mm]	UY [mm]	UZ [mm]	ROTX [mrad]	ROTY [mrad]	ROTZ [mrad]
WHF	M1	-0.001	-0.006	-0.024	0.007	0.000	0.000
	M2	-0.001	-0.063	-0.039	0.006	0.000	0.000
	M3	0.000	0.002	-0.024	0.007	0.000	0.000
	M4	0.000	0.002	-0.023	0.007	0.000	0.000

LOAD CASE	MIRROR	UX [mm]	UY [mm]	UZ [mm]	ROTX [mrad]	ROTY [mrad]	ROTZ [mrad]
WHS	M1	-0.025	0.000	-0.001	0.000	-0.002	-0.001
	M2	-0.094	-0.001	-0.001	0.000	0.006	0.000
	M3	-0.023	0.001	-0.001	0.000	-0.002	-0.001
	M4	-0.023	0.001	-0.001	0.000	-0.002	-0.001

LOAD CASE	MIRROR	UX [mm]	UY [mm]	UZ [mm]	ROTX [mrad]	ROTY [mrad]	ROTZ [mrad]
WZF	M1	-0.001	-0.043	-0.001	0.009	0.000	0.000
	M2	-0.004	-0.187	-0.002	0.003	0.000	0.000
	M3	-0.001	-0.033	-0.001	0.009	0.000	0.000
	M4	-0.001	-0.033	0.000	0.009	0.000	0.000

LOAD CASE	MIRROR	UX [mm]	UY [mm]	UZ [mm]	ROTX [mrad]	ROTY [mrad]	ROTZ [mrad]
WZS	M1	-0.021	-0.002	-0.001	0.000	-0.001	-0.001
	M2	-0.087	-0.005	-0.001	0.000	0.006	0.000
	M3	-0.019	-0.001	-0.001	0.000	-0.001	-0.001
	M4	-0.019	-0.001	-0.001	0.000	-0.001	-0.001

Table 24. Static Wind Induced Translations and Rotations. Rocking-Chair with R-Guides.

4.2.1.2 Gantry Model

LOAD CASE	MIRROR	UX [mm]	UY [mm]	UZ [mm]	ROTX [mrad]	ROTY [mrad]	ROTZ [mrad]
WHF	M1	0.000	-0.002	-0.013	0.004	0.000	0.000
	M2	0.003	-0.031	-0.028	0.003	0.000	0.000
	M3	-0.001	0.003	-0.013	0.004	0.000	0.000
	M4	-0.001	0.003	-0.013	0.004	0.000	0.000

LOAD CASE	MIRROR	UX [mm]	UY [mm]	UZ [mm]	ROTX [mrad]	ROTY [mrad]	ROTZ [mrad]
WHS	M1	-0.030	-0.001	0.000	0.000	-0.001	0.000
	M2	-0.096	-0.001	0.000	0.000	0.007	0.001
	M3	-0.029	0.000	0.000	0.000	-0.001	0.000
	M4	-0.029	0.000	0.000	0.000	-0.001	0.000

EST TELESCOPE STRUCTURE - ANALYSIS REPORT	Page: 30 of 54 Date: November 13, 2014
Code: DM/TN-SNT/022V.1	File: DELIVERABLE70_4D.DOCX

LOAD CASE	MIRROR	UX [mm]	UY [mm]	UZ [mm]	ROTX [mrad]	ROTY [mrad]	ROTZ [mrad]
WZF	M1	0.000	-0.021	0.000	0.004	0.000	-0.001
	M2	-0.001	-0.115	-0.001	-0.003	0.000	-0.001
	M3	0.000	-0.016	0.000	0.004	0.000	-0.001
	M4	0.000	-0.016	0.001	0.004	0.000	-0.001

LOAD CASE	MIRROR	UX [mm]	UY [mm]	UZ [mm]	ROTX [mrad]	ROTY [mrad]	ROTZ [mrad]
WZS	M1	-0.024	0.000	0.000	0.000	0.000	-0.001
	M2	-0.079	0.001	0.000	0.000	0.008	0.000
	M3	-0.024	0.000	0.000	0.000	0.000	-0.001
	M4	-0.024	0.000	0.000	0.000	0.000	-0.001

Table 25. Static Wind Induced Translations and Rotations. Gantry with R-Guides Model.

4.2.1.3 Yoke Model

LOAD CASE	MIRROR	UX [mm]	UY [mm]	UZ [mm]	ROTX [mrad]	ROTY [mrad]	ROTZ [mrad]
WHF	M1	-0.016	-0.003	-0.004	0.001	0.001	-0.004
	M2	-0.038	-0.033	-0.008	0.000	0.001	-0.004
	M3	-0.015	0.002	-0.007	0.002	0.001	-0.004
	M4	-0.015	0.002	-0.007	0.002	0.001	-0.004

LOAD CASE	MIRROR	UX [mm]	UY [mm]	UZ [mm]	ROTX [mrad]	ROTY [mrad]	ROTZ [mrad]
WHS	M1	-0.032	0.000	0.001	0.000	-0.001	0.000
	M2	-0.125	0.001	0.001	0.000	0.007	0.001
	M3	-0.031	0.000	0.001	0.000	-0.001	0.000
	M4	-0.031	0.000	0.001	0.000	-0.001	0.000

LOAD CASE	MIRROR	UX [mm]	UY [mm]	UZ [mm]	ROTX [mrad]	ROTY [mrad]	ROTZ [mrad]
WZF	M1	0.000	-0.025	0.001	0.004	0.000	-0.001
	M2	-0.001	-0.125	0.000	-0.001	0.000	-0.001
	M3	0.000	-0.020	0.001	0.004	0.000	-0.001
	M4	0.000	-0.020	0.001	0.004	0.000	-0.001

LOAD CASE	MIRROR	UX [mm]	UY [mm]	UZ [mm]	ROTX [mrad]	ROTY [mrad]	ROTZ [mrad]
WZS	M1	-0.028	0.000	0.000	0.000	-0.001	-0.001
	M2	-0.104	0.001	0.000	0.000	0.015	0.000
	M3	-0.027	0.001	0.000	0.000	-0.001	-0.001
	M4	-0.027	0.001	0.000	0.000	-0.001	-0.001

Table 26. Static Wind Induced Translations and Rotations. Yoke with Roller Bearing Model.

EST TELESCOPE STRUCTURE - ANALYSIS REPORT	Page: 31 of 54 Date: November 13, 2014
Code: DM/TN-SNT/022V.1	File: DELIVERABLE70_4D.DOCX

4.2.2 Steady State Wind Induced Errors due to Structural Deformations

Considering the structural deformations induced by the static wind and sensibility matrices as defined in AD.1, pointing errors due to static component wind are determined following the same methodology as described in the static analysis. This time, it is considered that a **90 % compensation factor** is feasible for the image motion correction, as it is a quasi-static effect. However, it is no desirable to have to use all this percentage in order to meet AD.1 error budgets, because that means a more complex corrective system.

4.2.2.1 Rocking-Chair Model

The following table shows the static wind induced pointing error for Rocking-Chair with R-Guides model

IMG. MOTION DUE TO STRUCTURAL DEFORMATIONS INDUCED BY STATIC WIND				
LOAD CASE	x [arcsec]	y [arcsec]	xy [arcsec]	z [mm]
WHF	0.289	-4.133	4.143	-15.377
WHS	2.666	0.052	2.667	0.383
WZF	0.318	-3.470	3.485	-0.917
WZS	-2.753	-0.182	2.759	0.262

	TOTAL	COMPENSATED
Max [arcsec]	4.143	0.414
LOAD CASE	WHF	

Table 27. Static Wind Induced Pointing Error. Rocking-Chair with R-Guides Model.

4.2.2.2 Gantry Model

The following table shows the static wind induced pointing error for Gantry Model with R-Guides and EL motors on Telescope Wheels.

IMG. MOTION DUE TO STRUCTURAL DEFORMATIONS INDUCED BY STATIC WIND				
LOAD CASE	x [arcsec]	y [arcsec]	xy [arcsec]	z [mm]
WHF	-0.165	-2.150	2.156	-15.363
WHS	2.314	0.090	2.315	0.402
WZF	0.281	-3.088	3.100	-1.090
WZS	-2.720	-0.112	2.722	0.305

	TOTAL	COMPENSATED
Max [arcsec]	3.100	0.310
LOAD CASE	WZF	

Table 28. Static Wind Induced Pointing Error. Gantry with R-Guides Model.

EST TELESCOPE STRUCTURE - ANALYSIS REPORT	Page: 32 of 54 Date: November 13, 2014
Code: DM/TN-SNT/022V.1	File: DELIVERABLE70_4D.DOCX

4.2.2.3 Yoke Model

The following table shows the static wind induced pointing error for Yoke Model with conventional Roller Bearing and EL motors on Telescope Wheels.

IMG. MOTION DUE TO STRUCTURAL DEFORMATIONS INDUCED BY STATIC WIND				
LOAD CASE	x [arcsec]	y [arcsec]	xy [arcsec]	z [mm]
WHF	0.718	-1.314	1.498	-4.109
WHS	3.392	0.236	3.400	0.444
WZF	0.310	-3.064	3.080	-1.089
WZS	-4.048	-0.192	4.053	0.345

	TOTAL	COMPENSATED
Max [arcsec]	4.053	0.405
LOAD CASE	WZS	

Table 29. Static Wind Induced Pointing Errors. Yoke Model with Roller Bearing Model.

4.3 Dynamic Wind Analysis

Dynamic wind has two effects on the image motion. One related to the errors due to the structural deformations, like the one studied in the static case, but including the resonant effect, and another related to the errors due to wind shake over the axles. This section covers the analysis for both effects.

4.3.1 Mirror Displacements due to Structural Deformations

As the FE Model is analysed as a **static-linear** case, it is possible to obtain the structural deformations due to dynamic wind scaling the structural deformations obtained for the static wind case, applying the relation between dynamic and static wind forces.

The relation between static and dynamic wind forces is:

$$F_{\text{drag_st.}} = \frac{1}{2} C_{\text{drag}} \cdot A \cdot \rho_{\text{air}} \cdot V_{\text{st.}}^2$$

$$F_{\text{drag_dyn.}} = C_{\text{drag}} \cdot A \cdot \rho_{\text{air}} \cdot V_{\text{st.}} \cdot V_{\text{dyn.}}$$

$$\frac{F_{\text{drag_dyn.}}}{F_{\text{drag_st.}}} = 2 \cdot \frac{V_{\text{st.}}}{V_{\text{dyn.}}} = 2 \cdot \frac{3.5}{11.5} = \mathbf{0.6087}$$

Therefore, the structural deformations due to dynamic wind are obtained from tables 24 (Rocking-Chair Model), 25 (Gantry Model) and 26 (Yoke Model) applying the 0.6087 scaling factor.

4.3.2 Dynamic Wind Induced Errors due to Structural Deformations

Considering the structural deformations induced by dynamic wind forces and sensibility matrices as defined in AD.1, errors are determined following the same methodology as described in the static wind case.

EST TELESCOPE STRUCTURE - ANALYSIS REPORT	Page: 33 of 54 Date: November 13, 2014
Code: DM/TN-SNT/022V.1	File: DELIVERABLE70_4D.DOCX

4.3.2.1 Rocking-Chair Model

The following table shows the dynamic wind induced pointing error due to structural deformations for Rocking-Chair with R-Guides Model.

IMG. MOTION DUE TO STRUCTURAL DEFORMATIONS INDUCED BY DYNAMIC WIND				
LOAD CASE	x [arcsec]	y [arcsec]	xy [arcsec]	z [mm]
WHF	0.176	-2.516	2.522	-9.391
WHS	1.623	0.032	1.623	0.236
WZF	0.194	-2.112	2.121	-0.544
WZS	-1.676	-0.111	1.679	0.162

Table 30. Dynamic Wind Induced Pointing Errors due to Structural Deformations. Rocking-Chair with R-Guides Model.

4.3.2.2 Gantry Model

The following table shows the dynamic wind induced pointing error due to structural deformations for Gantry with R-Guides and EL motors on Telescope Wheels Periphery Model.

IMG. MOTION DUE TO STRUCTURAL DEFORMATIONS INDUCED BY DYNAMIC WIND				
LOAD CASE	x [arcsec]	y [arcsec]	xy [arcsec]	z [mm]
WHF	-0.101	-1.309	1.313	-9.366
WHS	1.408	0.055	1.409	0.248
WZF	0.171	-1.879	1.887	-0.658
WZS	-1.656	-0.068	1.657	0.188

Table 31. Dynamic Wind Induced Pointing Errors due to Structural Deformations. Gantry with R-Guides Model.

4.3.2.3 Yoke Model

The following table shows the dynamic wind induced pointing error due to structural deformations for Yoke Model with Roller Bearing and EL motors on Telescope Wheels Periphery Model.

IMG. MOTION DUE TO STRUCTURAL DEFORMATIONS INDUCED BY DYNAMIC WIND				
LOAD CASE	x [arcsec]	y [arcsec]	xy [arcsec]	z [mm]
WHF	0.437	-0.800	0.912	-2.501
WHS	2.065	0.144	2.070	0.276
WZF	0.189	-1.865	1.874	-0.657
WZS	-2.464	-0.117	2.467	0.214

Table 32. Dynamic Wind Induced Pointing Errors due to Structural Deformations. Yoke with Roller Bearing Model.

EST TELESCOPE STRUCTURE - ANALYSIS REPORT	Page: 34 of 54 Date: November 13, 2014
Code: DM/TN-SNT/022V.1	File: DELIVERABLE70_4D.DOCX

4.3.3 Structural Deformations Errors including the Resonant Effect

In the previous section, the image motion due to dynamic wind structural deformations is obtained as a static case. This section extends the analysis including the resonant effect on the image motion and the correction of the dynamic disturbances.

4.3.3.1 Methodology

The errors due to structural deformations induced by dynamic wind component are analysed from the wind velocity power spectral density function S_v .

The S_v function is constructed in the 0.001 to 100 Hz range following **Davenport** and **Kolmogorov** models. The results obtained for $V_{st.} = 11.5 \text{ m/s}$ and $V_{dyn.} = 3.5 \text{ m/s}$ are depicted in the following picture:

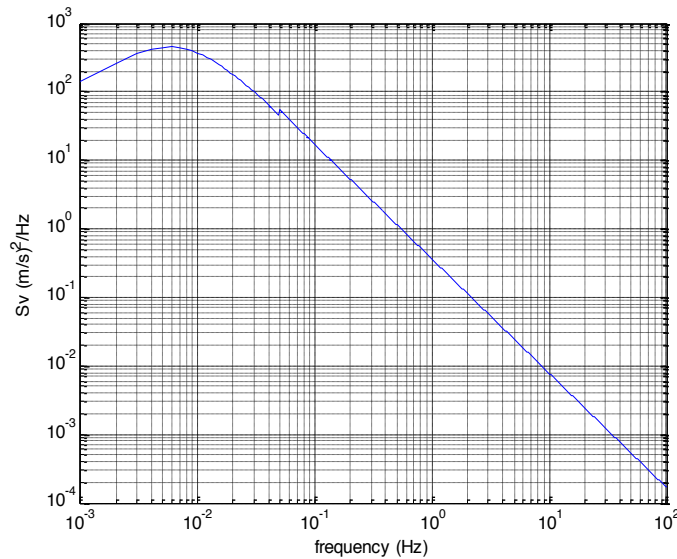


Fig. 15. Wind Spectra S_v for $V_{st.}=11.5 \text{ m/s}$ and $V_{dyn.} = 3.5 \text{ m/s}$ following Davenport ($<0.05 \text{ Hz}$) and Kolmogorov ($>0.05 \text{ Hz}$) Models.

Once obtained this function, the next step is to obtain the equivalent function for deformations as follows:

$$S_{def} = \left(\frac{def}{V_{dyn}} \right)^2 \cdot S_v$$

In this equation, **def** is the image motion due to dynamic wind component, obtained as a static case, i.e., the errors obtained in the previous section for dynamic wind (tables 30, 31 and 32), **considering all load cases and without applying correction factors.**

Taking as reference a value of 0.500 arcsec for the image motion, and the wind spectra obtained before, the following S_{def} is obtained:

EST TELESCOPE STRUCTURE - ANALYSIS REPORT	Page: 35 of 54 Date: November 13, 2014
Code: DM/TN-SNT/022V.1	File: DELIVERABLE70_4D.DOCX

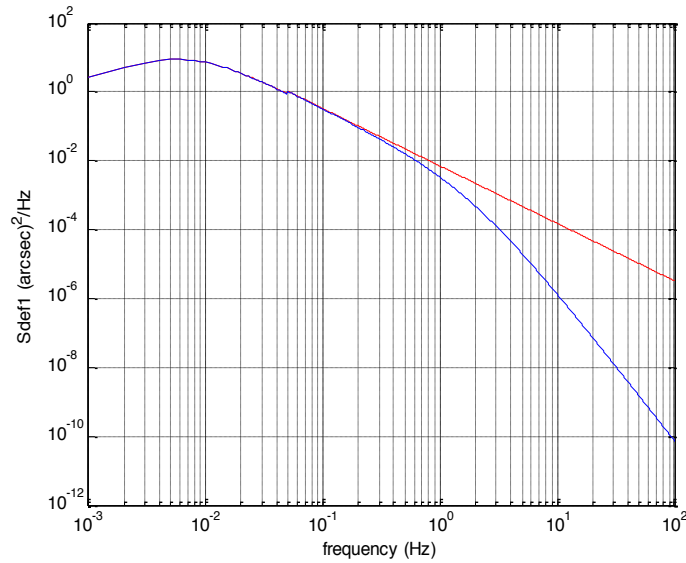


Fig. 16. Spectra Function for Dynamic Wind Deformations. The blue line represents the function including the Aerodynamic Attenuation Factor X.

The blue line represents the spectra including the aerodynamic attenuation factor X, which takes into account the differences in the pressure profile as a function of the area.

$$X = \frac{1}{1 + \left(\frac{2 \cdot f \cdot \sqrt{A}}{V_{st.}} \right)^{4/3}}$$

$$S_{def_aten} = S_{def} \cdot X^2$$

The aerodynamic attenuation factor varies with the frequency and area. An area of 10 m², is supposed for all the cases, that is a conservative approach.

In order to take into account the **structural resonance** in the image motion, the following transfer function is constructed:

$$H = \frac{1}{\sqrt{\left[1 - \left(\frac{f}{f_n} \right)^2 \right]^2 + \left[2 \cdot \zeta \cdot \frac{f}{f_n} \right]^2}}$$

$$S_{def_aten_res} = S_{def_aten} \cdot H^2$$

H is a mechanical unit transfers function whose unitary profile is modified attending to the structural dynamic properties of resonant frequencies f_n and structural damping factor ζ , as shown in the following picture:

EST TELESCOPE STRUCTURE - ANALYSIS REPORT	Page: 36 of 54 Date: November 13, 2014
Code: DM/TN-SNT/022V.1	File: DELIVERABLE70_4D.DOCX

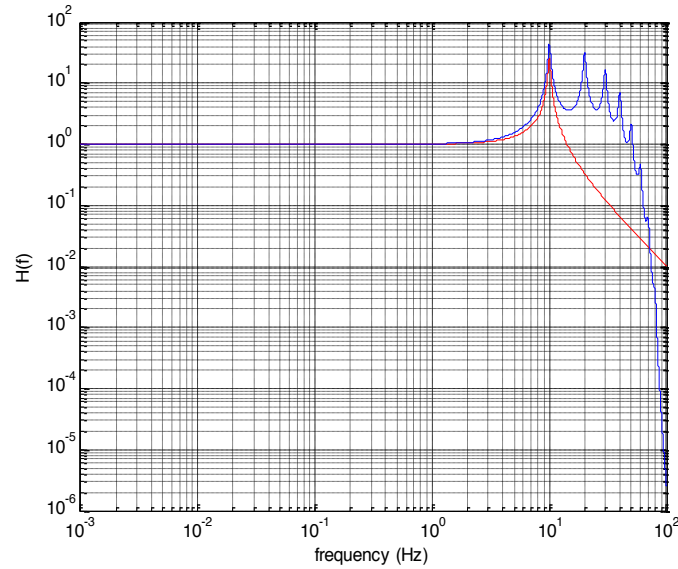


Fig. 17. Mechanical Unit Transfer Function including the effect of one Resonant Mode (red) or several Resonant Modes (blue)

This function has as many peaks as resonant frequencies considered. Here, the analysis is performed considering the effect of one resonant mode per case (red), being the cases considered those related to the modes associated with the telescope main axis, i.e., AZ and EL modes. The structural damping factor is set to 2.0 %, which is a typical value for metallic structures.

The effect of including the resonant frequency on the structural deformations can be seen in the following picture. As a consequence of the 10 Hz resonant frequency considered for the example, the error spectral function raises in the proximity of the peak:

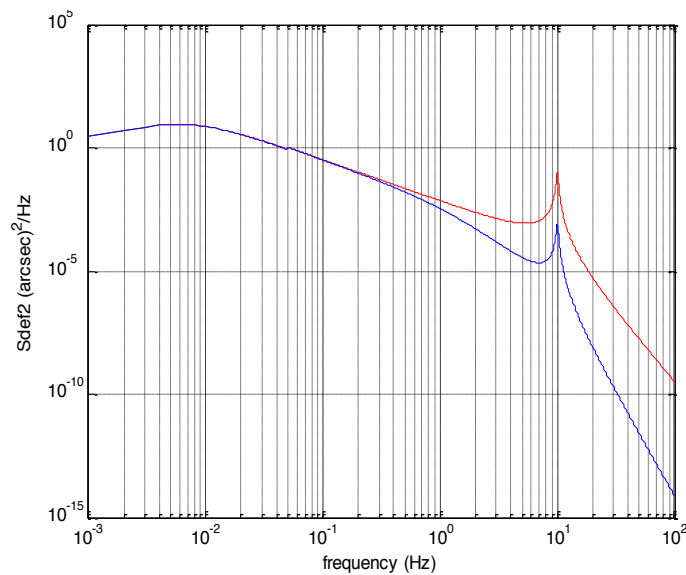


Fig. 18. S_{def} including the effect of one Resonant Mode (10Hz). Red: without Aerodynamic Attenuation. Blue: including the Aerodynamic Attenuation.

EST TELESCOPE STRUCTURE - ANALYSIS REPORT	Page: 37 of 54 Date: November 13, 2014
Code: DM/TN-SNT/022V.1	File: DELIVERABLE70_4D.DOCX

If more than one resonant mode per case is included, S_{def} rises in the proximity of all those resonant frequencies. This effect should be considered in future analyses.

Once obtained the spectra for the deformations including the resonant effect, the next step is to apply Flexible Body Correction Techniques (**FBC**) in order to know how much the errors can be reduced.

FBC is a set of techniques focused in the reduction of part of the structural deformations induced by dynamic effects like the wind, which is made acting on the telescope main axis drives using a closed-loop control system.

This system has to be capable to read the variable disturbances, which requires the use of additional sensors like inclinometers, accelerometers,...in order to feed the control system which acts on main axis drives correcting the errors.

To do that, a unitary transfer function for FBC is corrected applying a correction of **1.0 Db/dec** and **2.0 Db/dec** according to the following limits:

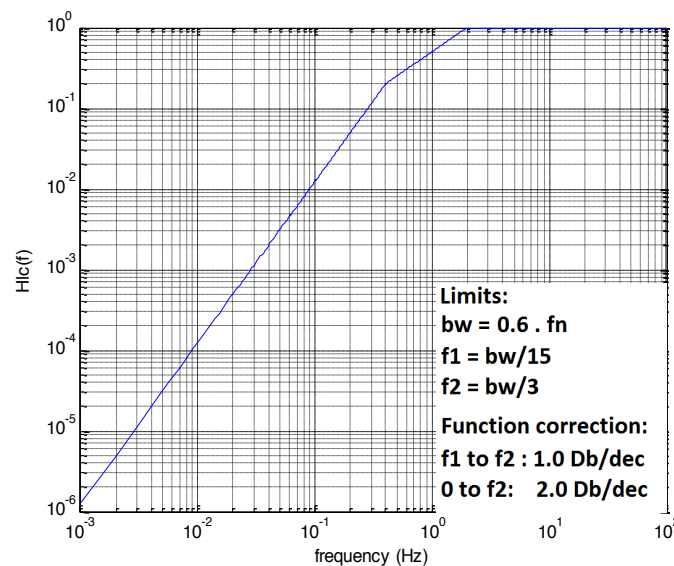


Fig. 19. FBC Transfer Function (H_{FBC}).

And then, the deformations are determined as follows:

$$S_{def_FBC} = S_{def} \cdot H_{FBC}^2$$

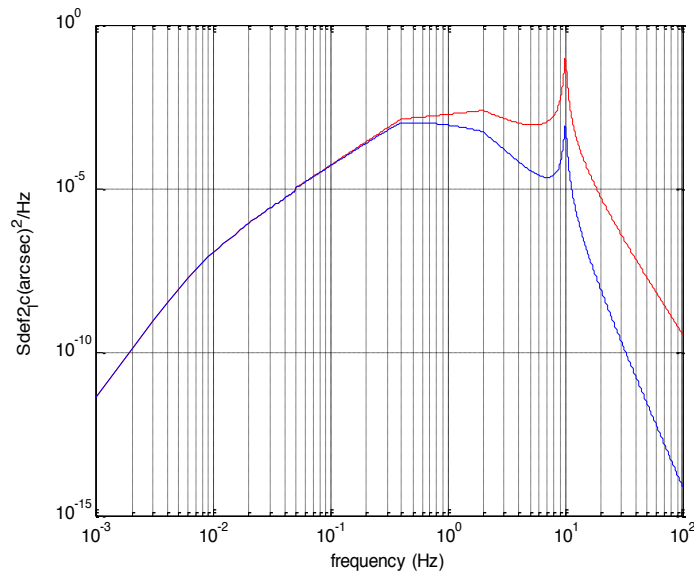


Fig. 20. S_{def} applying FBC. Red: without Attenuation. Blue: including Attenuation.

As it can be seen, errors are only reduced in the region included under defined limits.

All the analysis are repeated for every case obtaining the critical case. Cases considered in this analysis include the four load cases for wind analysis (WZF,WZS,WHF,WHs) and, for each load case, two resonant frequencies are considered (AZ and EL) obtaining a total of eight cases per model. Results obtained are shown in the following section.

4.3.3.2 Rocking-Chair Model

The following results are obtained for Rocking-Chair with R-Guides model.

CASE	FRQ. [Hz]	IMG. MOT. DUE TO DYN. WIND	STRUCTURAL DEF. ERRORS INCLUDING RESONANT EFFECT			
			W/O FBC CORRECTION		FBC CORRECTION	
			NOT ATTEN.	ATTENUATED	NOT ATTEN.	ATTENUATED
WHF -- EL	9.977	2.522	2.805	2.445	1.319	0.250
WHS -- EL	9.977	1.623	1.805	1.573	0.849	0.161
WZF -- EL	9.359	2.121	2.368	2.057	1.133	0.224
WZS -- EL	9.359	1.679	1.875	1.628	0.897	0.178
WHF -- AZ	18.836	2.522	2.711	2.441	1.067	0.130
WHS -- AZ	18.836	1.623	1.745	1.571	0.687	0.083
WZF -- AZ	21.651	2.121	2.267	2.053	0.857	0.094
WZS -- AZ	21.651	1.679	1.794	1.625	0.678	0.074
	MAX:	2.522	2.805	2.445	1.319	0.250

Table 33. Structural Deformations errors including Resonant Effect. Rocking-Chair Model.

The critical case is **WHF** with **EL** as the resonant mode. If FBC is not applied, the error remains in the same order (2.522 arcsec to 2.445 arcsec), while it can be reduced in an

EST TELESCOPE STRUCTURE - ANALYSIS REPORT	Page: 39 of 54 Date: November 13, 2014
Code: DM/TN-SNT/022V.1	File: DELIVERABLE70_4D.DOCX

order of magnitude applying FBC (2.522 arcsec to 0.250 arcsec). Thus, the assumption made in the static wind section of applying a **compensation factor of 90%** is correct.

4.3.3.3 Gantry Model

The following results are obtained for Gantry with R-Guides and EL motors on Telescope Wheels Periphery Model.

CASE	FRQ. [Hz]	IMG. MOT. DUE TO DYN. WIND	STRUCTURAL DEF. ERRORS INCLUDING RESONANT EFFECT			
			W/O FBC CORRECTION		FBC CORRECTION	
			NOT ATTEN.	ATTENUATED	NOT ATTEN.	ATTENUATED
WHF -- EL	14.008	1.313	1.432	1.272	0.613	0.092
WHS -- EL	14.008	1.409	1.536	1.365	0.658	0.099
WZF -- EL	12.964	1.887	2.066	1.828	0.904	0.143
WZS -- EL	12.964	1.657	1.814	1.605	0.794	0.126
WHF -- AZ	18.485	1.313	1.413	1.271	0.559	0.069
WHS -- AZ	18.485	1.409	1.516	1.364	0.600	0.074
WZF -- AZ	23.746	1.887	2.009	1.827	0.739	0.076
WZS -- AZ	23.746	1.657	1.764	1.604	0.649	0.066
	MAX:	1.887	2.066	1.828	0.904	0.143

Table 34. Structural Deformations errors including Resonant Effect. Gantry Model.

The critical case is **WZF** with **EL** as the resonant mode. If FBC is not applied, the error remains in the same order (1.887 arcsec to 1.828 arcsec), while it can be reduced in more than an one order of magnitude if FBC is applied (1.887 arcsec to 0.143 arcsec).

4.3.3.4 Yoke Model

The following results are obtained for Yoke with Roller bearing and EL motors on Telescope Wheels Periphery Model.

CASE	FRQ. [Hz]	IMG. MOT. DUE TO DYN. WIND	STRUCTURAL DEF. ERRORS INCLUDING RESONANT EFFECT			
			W/O FBC CORRECTION		FBC CORRECTION	
			NOT ATTEN.	ATTENUATED	NOT ATTEN.	ATTENUATED
WHF -- EL	12.618	0.912	1.000	0.883	0.441	0.071
WHS -- EL	12.618	2.070	2.270	2.005	1.001	0.162
WZF -- EL	12.077	1.875	2.060	1.815	0.920	0.153
WZS -- EL	12.077	2.467	2.712	2.390	1.211	0.201
WHF -- AZ	17.041	0.912	0.985	0.883	0.399	0.052
WHS -- AZ	17.041	2.070	2.235	2.004	0.906	0.118
WZF -- AZ	23.508	1.874	1.996	1.814	0.737	0.076
WZS -- AZ	23.508	2.467	2.628	2.388	0.970	0.100
	MAX:	2.467	2.712	2.390	1.211	0.201

Table 35. Structural Deformations errors including Resonant Effect. Yoke Model.

EST TELESCOPE STRUCTURE - ANALYSIS REPORT	Page: 40 of 54 Date: November 13, 2014
Code: DM/TN-SNT/022V.1	File: DELIVERABLE70_4D.DOCX

The critical case for structural deformations is **WZS** with **EL** as the resonant mode. If FBC is not applied, the error remains in the same order (2.467arcsec to 2.390 arcsec), while it can be reduced in more than one order of magnitude if FBC is applied (2.467 arcsec to 0.201 arcsec).

4.3.4 Wind Shake on Axes Errors

The following section covers the analysis for the errors induced by dynamic wind shake over the axles, describing the methodology and the results obtained for the models.

4.3.4.1 Methodology

From the wind spectra S_V and Dynamic Wind Locked Rotor Torques obtained from FEM, it is determined the torque spectra S_{torque} as follows:

$$S_{torque} = \left(\frac{\text{torque}}{V_{din}} \right)^2 \cdot S_V$$

$$S_{torque_{aten}} = S_{torque} \cdot X^2$$

Considering a torque of 20000 Nm and the wind spectra obtained in the previous section, the following torque spectra is obtained:

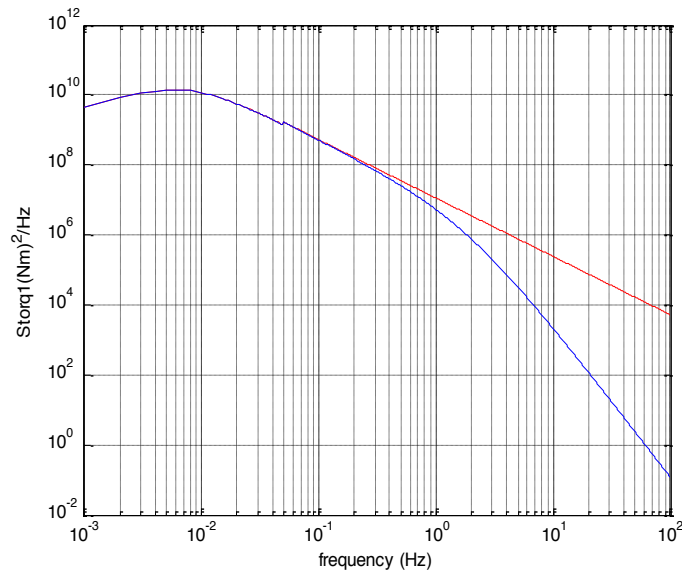


Fig. 21. Spectra S_{torque} . Red, without Attenuation. Blue, including Attenuation.

It is also determined the inertial axis response in closed loop $H_{inertial}$ according to the following equation:

$$H_{inertial} = \left[\frac{180 \cdot 3600}{\pi} \right] \cdot \left[\frac{1}{J_T} \right] \cdot \left[\frac{1}{(2 \cdot \pi \cdot f)^2} \right]$$

The mass moment of torsional inertia J_T is set to **1.4.10⁶ kgm²** for the EL-axis and **3.0.10⁶ kgm²** for the AZ-Axis.

EST TELESCOPE STRUCTURE - ANALYSIS REPORT	Page: 41 of 54 Date: November 13, 2014
Code: DM/TN-SNT/022V.1	File: DELIVERABLE70_4D.DOCX

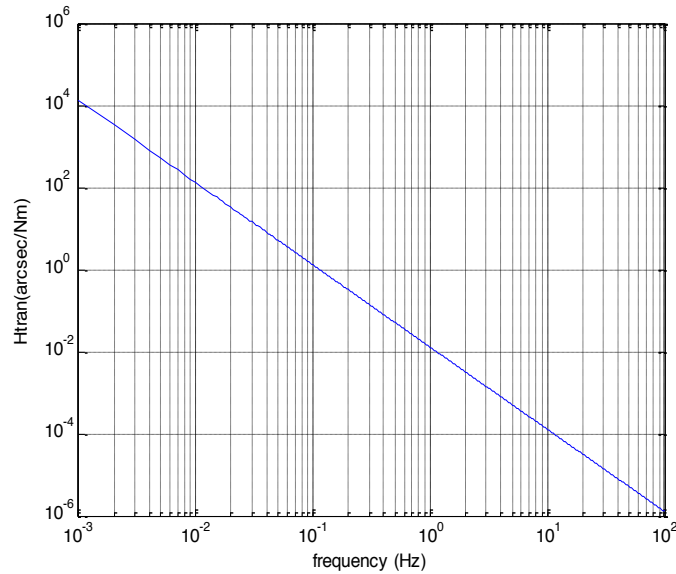


Fig. 22. Inertial Axis Response ($H_{inertial}$) as a frequency function ($J_1=4.0 \cdot 10^5 \text{ Kgm}^2$).

This function is modified in order to include FBC using the same limits as for structural deformations.

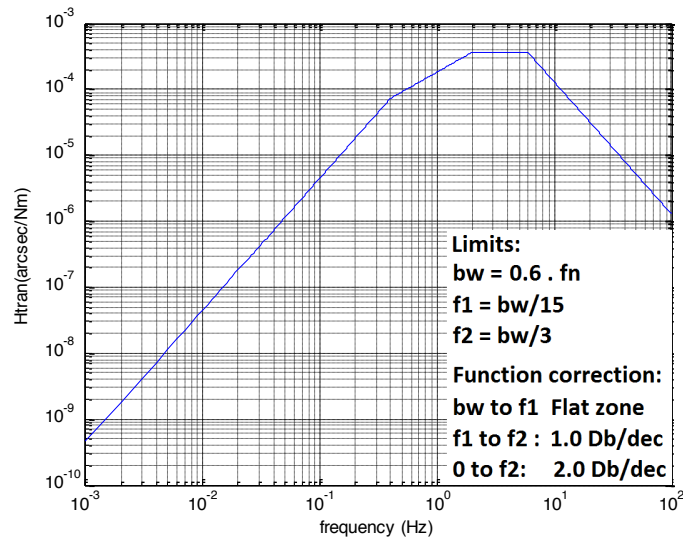


Fig. 23. Inertial Axis Response function with FBC Correction.

And the image motion due to the wind shake on axes is:

$$S_{wind_Axle_beat_FBC} = S_{torque_aten} \cdot H_{LC}^2$$

This methodology has to be applied for each case, and final results added to the structural deformations errors, i.e., total dynamic wind errors is equal to the addition of the errors due to structural deformations, considering the resonant effect, and the errors due to wind shake on axes.

EST TELESCOPE STRUCTURE - ANALYSIS REPORT	Page: 42 of 54 Date: November 13, 2014
Code: DM/TN-SNT/022V.1	File: DELIVERABLE70_4D.DOCX

4.3.4.2 Rocking-Chair Model

The following results are obtained for Rocking-Chair with R-Guides model.

CASE	FRQ. [Hz]	IMG. MOT. DUE TO DYN. WIND	WIND SHAKE ON AXES ERRORS	
			FBC CORRECTION	
			NOT ATTEN.	ATTENUATED
WHF -- EL	9.977	2.522	0.083	0.042
WHS -- EL	9.977	1.623	0.002	0.001
WZF -- EL	9.359	2.121	0.164	0.085
WZS -- EL	9.359	1.679	0.011	0.006
WHF -- AZ	18.836	2.522	0.029	0.010
WHS -- AZ	18.836	1.623	0.042	0.015
WZF -- AZ	21.651	2.121	0.020	0.006
WZS -- AZ	21.651	1.679	0.001	0.000
	MAX:	2.522	0.164	0.085

Table 36. Wind Shake on Axes Errors. Rocking-Chair Model.

The critical case is **WZF** with **EL** as the resonant mode, giving an error of **0.085 arcsec**.

4.3.4.3 Gantry Model

The following results are obtained for Gantry with R-Guides and EL motors on Telescope Wheels Periphery Model.

CASE	FRQ. [Hz]	IMG. MOT. DUE TO DYN. WIND	WIND SHAKE ON AXES ERRORS	
			FBC CORRECTION	
			NOT ATTEN.	ATTENUATED
WHF -- EL	14.008	1.313	0.006	0.002
WHS -- EL	14.008	1.409	0.000	0.000
WZF -- EL	12.964	1.887	0.220	0.096
WZS -- EL	12.964	1.657	0.001	0.000
WHF -- AZ	18.485	1.313	0.021	0.007
WHS -- AZ	18.485	1.409	0.019	0.007
WZF -- AZ	23.746	1.887	0.012	0.004
WZS -- AZ	23.746	1.657	0.001	0.000
	MAX:	1.887	0.220	0.096

Table 37. Wind Shake on Axes Errors. Gantry Model.

The critical case is **WZF** with **EL** as the resonant mode, giving an error of **0.096 arcsec**.

EST TELESCOPE STRUCTURE - ANALYSIS REPORT	Page: 43 of 54 Date: November 13, 2014
Code: DM/TN-SNT/022V.1	File: DELIVERABLE70_4D.DOCX

4.3.4.4 Yoke Model

The following results are obtained for Yoke with Roller bearing and EL motors on Telescope Wheels Periphery Model.

CASE	FRQ. [Hz]	IMG. MOT. DUE TO DYN. WIND	WIND SHAKE ON AXES ERRORS	
			FBC CORRECTION	
			NOT ATTEN.	ATTENUATED
WHF -- EL	12.618	0.912	0.007	0.003
WHS -- EL	12.618	2.070	0.000	0.000
WZF -- EL	12.077	1.874	0.260	0.118
WZS -- EL	12.077	2.467	0.001	0.000
WHF -- AZ	17.041	0.912	0.042	0.016
WHS -- AZ	17.041	2.070	0.054	0.020
WZF -- AZ	23.508	1.874	0.019	0.006
WZS -- AZ	23.508	2.467	0.001	0.000
	MAX:	2.467	0.260	0.118

Table 38. Wind Shake on Axes Errors. Yoke Model.

The critical case is **WZF** with **EL** as the resonant mode, giving an error of **0.118 arcsec**.

4.4 Wind Analysis Conclusions

The following table summarizes the results obtained for wind analysis considering each load case and the addition for pointing and tracking error comparison to AD.1.

IMAGE MOTION DUE TO WIND LOADS [arcsec]. ROCKING-CHAIR MODEL					
LOAD	STATIC WIND	DYNAMIC WIND		TRACKING ERROR	POINTING ERROR
CASE	ST. DEFORMATIONS	ST. DEFORMATIONS	WIND SHAKE		
WHF	0.414	0.250	0.042	0.292	0.706
WHS	0.267	0.161	0.001	0.162	0.429
WZF	0.348	0.224	0.085	0.309	0.657
WZS	0.276	0.178	0.006	0.184	0.459
				0.309	0.706

IMAGE MOTION DUE TO WIND LOADS [arcsec]. GANTRY MODEL					
LOAD	STATIC WIND	DYNAMIC WIND		TRACKING ERROR	POINTING ERROR
CASE	ST. DEFORMATIONS	ST. DEFORMATIONS	WIND SHAKE		
WHF	0.216	0.092	0.002	0.094	0.310
WHS	0.232	0.099	0.000	0.099	0.330
WZF	0.310	0.143	0.096	0.239	0.549
WZS	0.272	0.126	0.000	0.126	0.398
				0.239	0.549

EST TELESCOPE STRUCTURE - ANALYSIS REPORT	Page: 44 of 54 Date: November 13, 2014
Code: DM/TN-SNT/022V.1	File: DELIVERABLE70_4D.DOCX

IMAGE MOTION DUE TO WIND LOADS [arcsec]. YOKE MODEL					
LOAD CASE	STATIC WIND	DYNAMIC WIND		TRACKING ERROR	POINTING ERROR
	ST. DEFORMATIONS	ST. DEFORMATIONS	WIND SHAKE		
WHF	0.150	0.071	0.003	0.074	0.224
WHS	0.340	0.162	0.000	0.162	0.502
WZF	0.308	0.153	0.118	0.271	0.578
WZS	0.405	0.201	0.000	0.202	0.607
				0.271	0.607

Table 39. Image Motion due to Wind Loads summary (FBC correction applied)

Taking into account that the error allocated in AD.1 for pointing is **2.000 arcsec**, and **0.800 arcsec** for tracking, it can be concluded that all models meet the requirements. However, this is only possible if FBC is applied. Otherwise, those results would be approximately an order of magnitude higher and hence, too far above the requirements.

The comparison between the models leads to a conclusion similar to the one obtained for Dynamic and Gravity Deformations Analysis, i.e., Gantry is the model with the best performance, followed by Yoke and Rocking-Chair in the last place.

Notes:

- Tracking Error is the error due to Dynamic Wind Loads. It is obtained as the addition of the errors due to the structural deformations, and the errors due to the wind shake on axes induced by dynamic wind loads.
- Pointing Error is the error due to Static and Dynamic Wind Loads. It is obtained as the addition of the errors due to the structural deformations, induced by static and dynamic wind loads, and the errors due to wind shake on axes, induced by dynamic wind loads.
- Results included the compensation factor due to FBC, which can reduce the errors in up to a 90 %.

EST TELESCOPE STRUCTURE - ANALYSIS REPORT	Page: 45 of 54 Date: November 13, 2014
Code: DM/TN-SNT/022V.1	File: DELIVERABLE70_4D.DOCX

5. TELESCOPE UPPER TUBE OPTIMIZATION

The objective of this analysis is to optimize the structure of the upper section of the telescope tube.

An alternative configuration has been developed and several design variables of current model have been parameterized in order to value possibly design modifications within the limits imposed by restrictions.

5.1 Alternative Tube Configuration Analysis

The study of an alternative configuration in which certain elements were suppressed was carried out. The objective of this simplification was to reduced wind loads on the upper section of the tube, i.e., to reduce the loads affecting M2 gaining stability, especially against dynamic loads as wind, which will always have a less correctable effect than those related to static cases, such as gravity.

Particularly, it has been developed a model in which the upper ring has been suppressed, holding M2 housing directly by means of rectangular bars that end in the corners of the rectangular frame, as showed in the following picture:

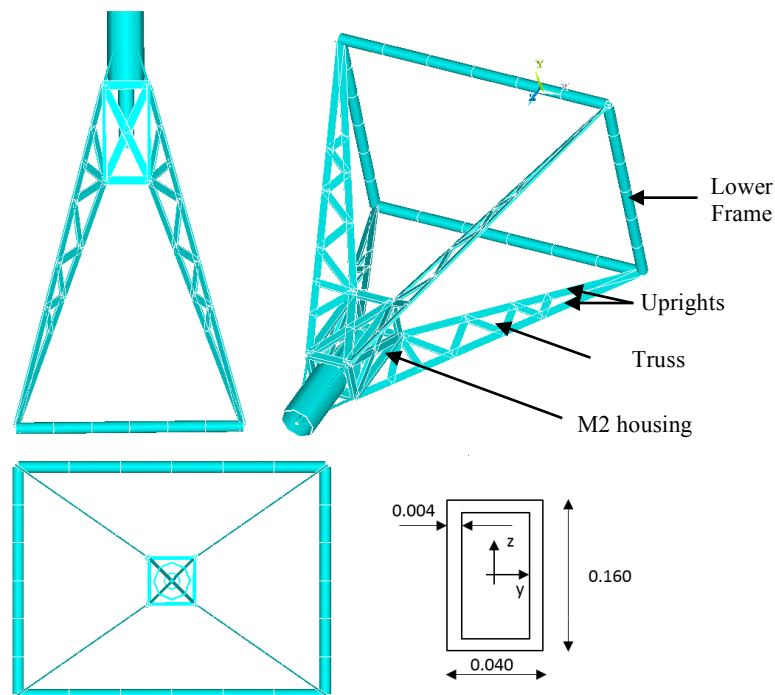


Fig. 24. Alternative Upper Tube Configuration Model.

The width of the uprights has been left in **40 mm width** in order not to let increase beam shadows. The model has been developed considering also the addition of a truss between uprights obtaining the following results.

EST TELESCOPE STRUCTURE - ANALYSIS REPORT	Page: 46 of 54 Date: November 13, 2014
Code: DM/TN-SNT/022V.1	File: DELIVERABLE70_4D.DOCX

MODE	WITH TRUSS		W/O TRUSS	
	Frq. [Hz]	DESCRIPTION	Frq. [Hz]	DESCRIPTION
01	5.15	Spider	7.29	Spider
02	8.30	Uprights Mode	9.20	XEL
03	8.60	Uprights Mode	12.37	EL
04	8.74	Uprights Mode	18.92	Mode Tube
05	9.30	XEL	19.14	Mode Tube
06	12.33	Uprights Mode	20.31	Complex Mode
07	12.62	EL	22.49	Complex Mode
08	17.47	Uprights Mode	23.55	AZ
09	18.98	Complex Mode	24.71	Complex Mode
10	20.31	Complex Mode		

Table 40. Dynamic Analysis for Alternative Tube. Results correspond to the Vertical Model.

Taking into account that this model has been constructed using Yoke with Roller Bearing and EL motors on Telescope Wheels Periphery Model, dynamic performance turns out to be better than the one obtained with the classical tube configuration (table 9.0), except the spider mode, which falls down, even more for the case with the truss.

The addition of a truss between uprights does not bring more useful torsional stiffness. On the contrary, it is just adding mass and consequently, torsional frequency decreases.

Any case, resonant frequencies for principal modes (EL and AZ), which are the important in relation to the image motion remains the same, being considered for the error analysis.

The following results are obtained for the model without truss including vertical and horizontal positions:

YOKE - ALTERNATIVE TUBE -- HORIZONTAL			YOKE - ALTERNATIVE TUBE -- VERTICAL		
MODE	Frq. [Hz]	MODE DESCRIPTION	MODE	Frq. [Hz]	MODE DESCRIPTION
01	7.37	Spider	01	7.29	Spider
02	8.88	XEL	02	9.20	XEL
03	13.06	EL	03	12.37	EL
04	18.54	Mode Tube	04	18.92	Mode Tube
05	19.22	AZ	05	19.14	Mode Tube
06	19.77	Mode Tube	06	20.31	Complex Mode
07	21.12	Complex Mode	07	22.49	Complex Mode
08	22.49	Complex Mode	08	23.55	AZ
09	22.53	Complex Mode	09	24.71	Complex Mode
10	24.80	Nasmyth	10		

Table 37. Dynamic Analysis for Alternative Tube without Truss.

EST TELESCOPE STRUCTURE - ANALYSIS REPORT	Page: 47 of 54 Date: November 13, 2014
Code: DM/TN-SNT/022V.1	File: DELIVERABLE70_4D.DOCX

The errors obtained with this model are the following:

EFFECT	FEM MODEL [arcsec]	ERROR ALLOCATED AD.1 [arcsec]
GRAVITY (POINTING)	0.412	0.500
WIND (POINTING)	0.871	2.000
WIND (TRACKING)	0.348	0.800

UPPER TUBE ALTERNATIVE CONFIGURATION					
LOAD CASE	STATIC WIND	DYNAMIC WIND		TRACKING ERROR	POINTING ERROR
	ST. DEFORMATIONS	ST. DEFORMATIONS	WIND SHAKE		
WHF	0.144	0.066	0.001	0.067	0.211
WHS	0.151	0.069	0.000	0.069	0.220
WZF	0.523	0.254	0.094	0.348	0.871
WZS	0.210	0.102	0.000	0.102	0.312
				0.348	0.871

Table 38. Upper Tube Alternative Configuration Errors.

Although the frequencies for principal modes are similar, this model loses some stiffness and wind loads do not fall as much as expected in comparison to the original model because the drag coefficient is higher for non-circular sections.

Consequently, although the errors meet AD.1 requirements, they are higher than the ones obtained with current upper tube design (table 40) Thus, this model does not represent a real structural advantage and it is discarded.

EFFECT	IMAGE MOTION [arcsec]		ERROR ALLOCATED IN AD.1 [arcsec]
	CURRENT TUBE	ALTERNATIVE TUBE	
GRAVITY (POINTING)	0.361	0.412	0.500
WIND (POINTING)	0.607	0.871	2.000
WIND (TRACKING)	0.271	0.348	0.800

Table 39. Image Motion comparison as a function of the Upper Tube Model. Results are based on Yoke with Roller Bearing and EL motors on Telescope Wheels Periphery Model.

5.2 Current Upper Tube Optimization Analysis

In order to improve the performance of current tube design, several test have been done varying the upper ring position in relation to the lower frame (H) as well as the M2 housing length (h), as shown in the following picture.

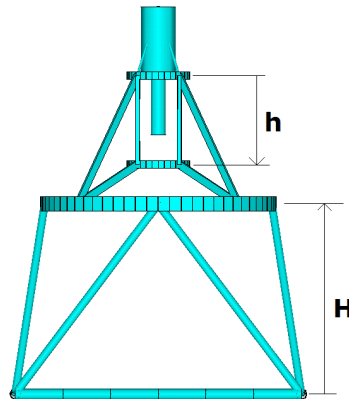


Fig. 25. Parameterized Variables for the Analysis.

The following results were obtained varying the height of the upper ring H.

H [m]	MODE [Frq. Hz]		
	XEL	EL	SPIDER
2.85	9.12	11.79	11.93
3.35	9.13	12.05	13.36
3.85	9.13	12.08	15.04
4.66	9.12	12.00	17.29
5.56	9.11	11.75	18.64
6.46	9.09	11.30	18.36

Table 40. Resonant Frequencies varying the Upper Ring Height.

As it can be seen, the upper ring position seems to have influence only on the spider mode, which is maximum for H=5.56 m, i.e., when M2 housing is centred with the ring. However, EL and AZ modes practically do not vary with the height and, as spider is not a principal mode, it is not an advantage to centre the upper ring because that would increase the loads at a higher distance, decreasing the performance.

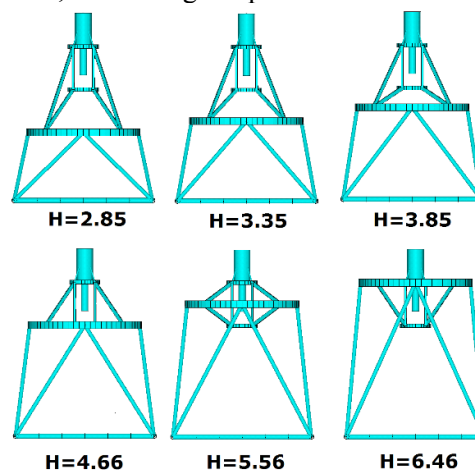


Fig. 26. Set of Upper Ring Heights considered in the Analysis.

EST TELESCOPE STRUCTURE - ANALYSIS REPORT	Page: 49 of 54 Date: November 13, 2014
Code: DM/TN-SNT/022V.1	File: DELIVERABLE70_4D.DOCX

Current housing height is set to 1.8 m, and it is only feasible to rise it and not to decrease because of the heat trap subsystem.

It has been made an analysis rising h up to 3.0 m obtaining the following results.

h [m]	MODE [Frq. Hz]		
	X TRANSLATION	EL	SPIDER
1.80	9.13	12.08	15.04
3.00	9.12	12.02	12.66

Table 41. Influence of the Housing Height (h) on the Dynamic Behaviour

Far from improving, the results are worse. Thus, it is better to left h as it is in the current design.

5.3 Telescope Upper Tube Optimization Conclusions

Although pointing and tracking errors obtained with the upper tube alternative are compliant with the errors allocated in AD.1, they are higher than the ones obtained with the current tube design, not representing a real structural advantage and hence, is discarded.

The position for the upper ring and M2 housing length for current model have influence only on the Spider mode. According to the analysis, best results are obtained using current design parameters.

In conclusion, the structure of the upper section of the telescope tube proposed until now is confirmed for EST design

EST TELESCOPE STRUCTURE - ANALYSIS REPORT	Page: 50 of 54 Date: November 13, 2014
Code: DM/TN-SNT/022V.1	File: DELIVERABLE70_4D.DOCX

6. NASMYTH PLATFORM POSITION ANALYSIS

Nasmyth platform is usually disposed on one of the lateral sides of the telescope, or in both sides, depending on the quantity of platforms. However, for Gantry and Yoke configurations, this platform is affected by the telescope translation mode XEL, which makes the platform rotates, causing large distortions on the beam.

Since the previous EST Conceptual Design Study, it has been pointed out the importance of valuing the convenience of placing the Nasmyth platform in the rear position. In that way, an increment in the telescope XEL frequency would be being favoured, as well as a freeing for the Nasmyth platform frequencies, which would not be linked to telescope frequencies.

Moreover, this change would allow to have a Nasmyth focus corrected by M6 (Tip-Tilt mirror) and M7 (Deformable mirror) because the beam pass throw them. Finally, the new rear Nasmyth would be less exposed to wind loads, which is a real advantage, especially for opened configurations.

First, the influence of the platform (3000 kg) over telescope XEL mode is studied. The results with and without the platform are shown in the following table:

MODE Nº	YOKE WITH NASMYTH		YOKE WITHOUT NASMYTH	
	Frq. [Hz]	DESCRIPTION	Frq. [Hz]	DESCRIPTION
01	9.13	XEL	9.69	XEL
02	12.08	EL	12.19	EL
03	15.04	Spider	15.04	Spider
04	18.95	Complex Mode	19.50	Tube Mode
05	19.48	Tube Mode	20.30	Tube Mode
06	20.24	Complex Mode	21.53	Complex Mode
07	20.37	Complex Mode	22.49	Complex Mode
08	22.49	Complex Mode	22.72	Mode Tube
09	22.72	Mode Tube		
10	23.51	AZ		

Table 42. Nasmyth Platform influence on Telescope Modes

As it can be seen, the resonant frequencies are in general higher, although not so much. So, it can be concluded that telescope resonant frequencies do not depend on the Nasmyth platform presence.

If the Nasmyth platform is located in the rear position, it implies a subsystem which sends the beam from the telescope to the Nasmyth Platform or to the Coude room. Several alternatives are to be studied: one could be a subsystem which makes M6/M7 integrally rotate about an axis parallel to the EL-Axis, sending the beam to the rear Nasmyth, another one could be the insertion of a mirror after M7 (localisation TBD) to send the light to the rear Nasmyth.

EST TELESCOPE STRUCTURE - ANALYSIS REPORT	Page: 51 of 54 Date: November 13, 2014
Code: DM/TN-SNT/022V.1	File: DELIVERABLE70_4D.DOCX

As mirrors from M6 onwards are joined to the platform and not to the tube, the design of the lower part of the tube has to be studied in detail in order to avoid any kind of interferences with the mirrors and its subsystems while the telescope tube is moving on EL. To achieve that goal, it is better to lower the beam height as much as possible and so, the second option is preferred. For this analysis, the Nasmyth is located at a rear position at a height of **1.5 m** measured from the top of the AZ platform to the centre of the Nasmyth platform.

The Nasmyth position in height, the subsystem to send the light to the Nasmyth and the design of the lower part of the telescope tube will be studied in detail in a next step.

The following model has been constructed obtaining the results showed in table 43.

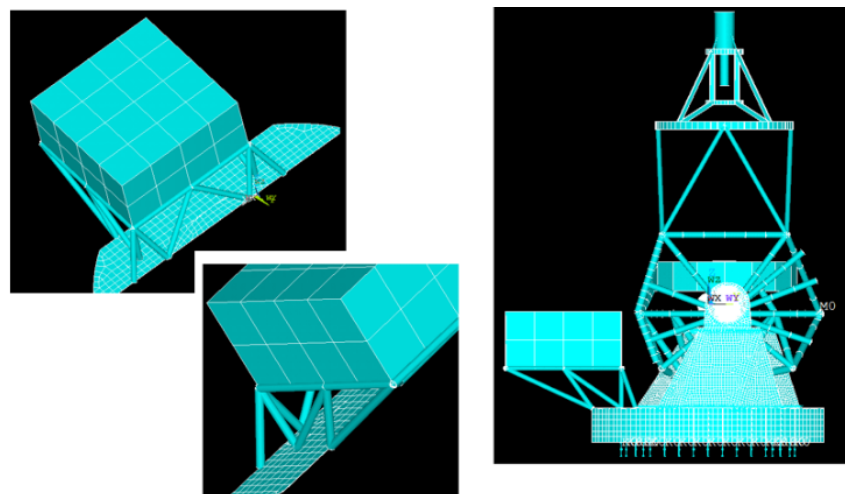


Fig. 27. Alternative Configuration for Nasmyth Platform on Rear Position

MODE	ROCKING-CHAIR		YOKE			
	LATERAL NASMYTH		LATERAL NASMYTH		REAR NASMYTH	
	FRQ [Hz]	DESCRIPTION	FRQ [Hz]	DESCRIPTION	FRQ [Hz]	DESCRIPTION
01	8.33	NASMYTH	9.13	XEL/NASMYTH	9.69	XEL
02	9.36	EL	12.08	EL	12.20	EL
03	11.33	XEL	15.04	Spider	15.04	Spider
04	14.92	Spider	18.95	Complex Mode	17.26	NASMYTH
05	19.14	Tube Mode	19.48	Tube Mode	19.50	Tube Mode

Table 43. Results obtained for proposed Rear Nasmyth Model

As it can be seen, the resonant Nasmyth frequency is almost the double in comparison to the lateral model and, this time, the Nasmyth frequency is independent of the telescope modes.

The table also shows the values for Rocking-Chair model. This case, despite of being an independent mode (Rocking-Chair Nasmyth joined to the platform), with this new configuration, the resonant frequency can be increased by almost twice. From this aspect, it seems convenient to locate the Nasmyth platform in the rear side.

EST TELESCOPE STRUCTURE - ANALYSIS REPORT	Page: 52 of 54 Date: November 13, 2014
Code: DM/TN-SNT/022V.1	File: DELIVERABLE70_4D.DOCX

7. GENERAL CONCLUSIONS

According to the Dynamic Analysis, the models which exhibit a better behaviour are the followings:

- **Gantry.** With R-Guides for the AZ-Axis, EL motors on EL-Axis Trunnion and Telescope Wheels Reinforced.
- **Gantry.** With R-Guides for the AZ-Axis and EL motors on Telescope Wheels Periphery.
- **Yoke.** With conventional Roller Bearing for the AZ-Axis and EL motors on Telescope Wheels Periphery.

And the Rocking-Chair would be on the last place. The reason why this model has a poorer performance is mainly related to the fact that the mounting for the R-Guides, as EL Bearings, has a low rigidity, and this is so because of the necessary mounting of the R-Guides in cantilever.

The following table summarises the results obtained for Gravitational and Wind Analysis, including the compensation factor for Gravitational Errors, and FBC for Wind Errors.

EFFECT	ROCKING-CHAIR	GANTRY	YOKE	REQUIRED AD.1
GRAVITY (POINTING)	0.736	0.530	0.361	0.500
WIND (POINTING)	0.706	0.549	0.607	2.000
WIND (TRACKING)	0.309	0.239	0.271	0.800

Table 44. Gravity and Wind induced error summary. Values are in arcsec.

Considering the Gravitational errors, it can be concluded that only Gantry and Yoke models have a performance that meets AD.1 requirements, especially considering that they have been tested using the configuration with the EL motors on the Telescope Wheels Periphery, which has a less performance in comparison to the case where the EL motors are placed on the EL-Axis Trunnion with the EL Wheels are reinforced.

Considering the Wind Errors, it can be seen that all models have a performance that meets the requirements, but only if FBC is applied. Otherwise, those errors would be approximately an order of magnitude higher, and hence, too far above the requirements.

According to wind analysis, FBC is able to compensate approximately a 90% of dynamic disturbances, and the minimum compensation percentage to meet the requirements are, approximately:

- Rocking-Chair: 75 % of FBC correction
- Yoke: 70 % of FBC correction
- Gantry: 65 % of FBC correction

The bigger the limit is, the complex the control system is. Once again, Gantry and Yoke are better than Rocking-Chair, and next analysis for EST should be based on them.

EST TELESCOPE STRUCTURE - ANALYSIS REPORT	Page: 53 of 54 Date: November 13, 2014
Code: DM/TN-SNT/022V.1	File: DELIVERABLE70_4D.DOCX

Continuing with the others analysis, an alternative configuration for the upper part of the telescope tube was studied and not retained as the current tube design has a better behaviour, according to static and dynamic analysis.

The attempts to optimize the current upper tube model by varying the upper ring position as well as the M2 housing length lead to changes only for the spider mode, which is not a relevant mode. In conclusion, the current upper structure of the telescope tube (proposed at the end of EST Conceptual Design Study) is still retained as baseline for EST design.

Finally, structural analysis underline that the Nasmyth platform placed on the rear side (instead of the lateral side, as proposed until now) is a better mechanical solution for EST. The Nasmyth mode is independent of the telescope ones and its frequency has been raised by almost the double.

Studies are needed in the future on how to send the light to the Nasmyth platform and the configuration for the lower part of the telescope tube in order to avoid interferences while moving on EL.

EST TELESCOPE STRUCTURE - ANALYSIS REPORT	Page: 54 of 54 Date: November 13, 2014
Code: DM/TN-SNT/022V.1	File: DELIVERABLE70_4D.DOCX

A. ANNEXES

LIST OF APPLICABLE DOCUMENTS	
AD.1	RPT-EST-3005 1.A EST ERROR BUDGETS
AD.2	RPT-EST-3001 2.A ENVIRONMENTAL CONDITIONS

LIST OF REFERENCE DOCUMENTS	
RD.1	RPT-MTM-5003 1.A POINTING AND TRACKING ERROR ANALYSIS
RD.2	RPT-EST-0001 1.A EUROPEAN SOLAR TELESCOPE: CONCEPTUAL DESIGN STUDY REPORT
RD.3	RPT-MTM-5004 1.A DETAILED DESIGN CONCEPT FOR THE STRUCTURE
RD.4	RPT-GTC-3003 1.A PRELIMINARY DYNAMIC ANALYSIS